

YEAR-END TECHNICAL REPORT

September 29, 2019 to September 28, 2020

Environmental Remediation Science and Technology

Date submitted:

December 6, 2020

Principal Investigator:

Leonel E. Lagos, Ph.D., PMP®

Florida International University Collaborators:

Yelena Katsenovich, Ph.D.

Ravi Gudavalli, Ph.D.

John Dickson, Ph.D.

Shambhu Kandel, Ph.D.

Muhammad Alam, Ph.D.

Angelique Lawrence, M.S., GISP

Yan Zhou, Ph.D.

DOE Fellows

Submitted to:

U.S. Department of Energy

Office of Environmental Management

Under Cooperative Agreement # DE-EM0000598



Applied Research Center

FLORIDA INTERNATIONAL UNIVERSITY

Addendum:

This document represents one (1) of five (5) reports that comprise the Year End Reports for the period of September 29, 2019 to September 28, 2020 prepared by the Applied Research Center at Florida International University for the U.S. Department of Energy Office of Environmental Management (DOE-EM) under Cooperative Agreement No. DE-EM0000598. Incremental funding under this cooperative agreement resulted in FIU having to execute carryover scope, which was completed in November 2019. The technical information for the carryover scope from FIU Performance Year 9 has therefore also been included in these reports.

The complete set of FIU's Year End Reports for this reporting period includes the following documents:

- Project 1: Chemical Process Alternatives for Radioactive Waste
Document number: FIU-ARC-2019-800006470-04b-270
- Project 2: Environmental Remediation Science and Technology
Document number: FIU-ARC-2019-800006471-04b-267
- Project 3: Waste and D&D Engineering and Technology Development
Document number: FIU-ARC-2019-800006472-04b-256
- Project 4: DOE-FIU Science & Technology Workforce Development Initiative
Document number: FIU-ARC-2019-800006473-04b-306
- Project 5: DOE-FIU Science & Technology Workforce Development Initiative for Office of Legacy Management
Document number: FIU-ARC-2019-800012253-04b-003

Each document will be submitted to OSTI separately under the respective project title and document number as shown above. In addition, the documents are available at the DOE Research website for the Cooperative Agreement between the U.S. Department of Energy Office of Environmental Management and the Applied Research Center at Florida International University: <https://doeresearch.fiu.edu>

DISCLAIMER

This report was prepared as an account of work sponsored by an agency of the United States government. Neither the United States government nor any agency thereof, nor any of their employees, nor any of its contractors, subcontractors, nor their employees makes any warranty, express or implied, or assumes any legal liability or responsibility for the accuracy, completeness, or usefulness of any information, apparatus, product, or process disclosed, or represents that its use would not infringe upon privately owned rights. Reference herein to any specific commercial product, process, or service by trade name, trademark, manufacturer, or otherwise does not necessarily constitute or imply its endorsement, recommendation, or favoring by the United States government or any other agency thereof. The views and opinions of authors expressed herein do not necessarily state or reflect those of the United States government or any agency thereof.

TABLE OF CONTENTS

TABLE OF CONTENTS..... i

LIST OF FIGURES iii

LIST OF TABLES ix

PROJECT 2 OVERVIEW 1

MAJOR TECHNICAL ACCOMPLISHMENTS 5

TASK 1: REMEDIATION RESEARCH AND TECHNICAL SUPPORT FOR THE HANFORD SITE 9

Task 1: Executive Summary 9

Subtask 1.1: Remediation Research of Ammonia Gas for Uranium Treatment 9

Subtask 1.2: Re-oxidation of Redox Sensitive Contaminants Immobilized by Strong Reductants (NEW)..... 19

Subtask 1.3: Evaluation of Competing Attenuation Processes for Mobile Contaminants in Hanford Sediments 46

Subtask 1.4: Experimental Support of Lysimeter Testing..... 57

TASK 2: REMEDIATION RESEARCH AND TECHNICAL SUPPORT FOR SAVANNAH RIVER SITE 66

Task 2: Executive Summary 66

Subtask 2.1: Environmental Factors Controlling the Attenuation and Release of Contaminants in the Wetland Sediments at Savannah River Site (NEW)..... 66

Subtask 2.2: Humic Acid Batch Sorption Experiments with SRS Soil..... 75

TASK 3: CONTAMINANT FATE AND TRANSPORT MODELING IN THE TIMS BRANCH WATERSHED 89

Task 3: Executive Summary 89

TASK 5: REMEDIATION RESEARCH AND TECHNICAL SUPPORT FOR THE WASTE ISOLATION PILOT PLANT 115

Task 5: Executive Summary 115

Subtask 5.2: Fate of actinides in the presence of ligands in high ionic strength systems ... 115

TASK 6: HYDROLOGY MODELING FOR WIPP (NEW) 130

Task 6: Executive Summary 130

Subtask 6.1: Digital Elevation Model and Hydrologic Network..... 131

Subtask 6.2: Model Development 148

ACKNOWLEDGEMENTS 168
CONFERENCE PARTICIPATION, PUBLICATIONS & AWARDS 169
APPENDIX..... 172

LIST OF FIGURES

Figure 1. Selected area electron diffraction (SAED) image patterns of the crystalline aluminosilicate minerals (illite, top; montmorillonite, bottom) for untreated minerals (a and d), treated with 95% N₂/5% NH₃ gas for 30-day contact time in SGW solution (7.2 mM) at pH 12 (b and e) and aerated-treated at pH 8 (c and f). Bottom right show inset micrographs of Transmission Electron Microscope (TEM) images at 100 and 200 nm resolution. 13

Figure 2. (a) Infrared spectra of aluminosilicate minerals (illite-blue and montmorillonite-red) showing (a) the effect of ammonia intercalation at ~ 3334 symmetric stretching vibration of N-H groups at ~ 3334 cm⁻¹. 14

Figure 3. SEM images of (a) untreated illite mineral taken in backscatter mode, (b) illite treated with 95% N₂/5% NH₃ gas treatment at pH 12, and (c) post treatment in secondary mode for 30-day contact time in SGW solution (7.2 mM). 15

Figure 4. Reductive removal of technetium over time in aerobic and anaerobic conditions via different reductants. 23

Figure 5. Reductive removal of technetium over time in aerobic and anaerobic conditions via different reductants. 24

Figure 6. Technetium reduction and reoxidation behavior in calcium polysulfide samples using LSC. The results present data for 0.5% calcium polysulfide samples in the ground water simulant measured via ICP-MS. 25

Figure 7. Measured total iron via ICP-MS for samples in perched water simulant. 26

Figure 8. Measured total iron via ICP-MS for samples in ground water simulant. 27

Figure 9. Measured oxidation reduction potential for batches containing perched water simulant. 28

Figure 10. Measured oxidation reduction potential for batches containing ground water simulant. 28

Figure 11. SEM-EDS images of Hepure ZVI treated sediment samples. 32

Figure 12. SEM-EDS images of sulfur modified ZVI treated sediment samples. 33

Figure 13. SEM-EDS images of calcium polysulfide treated sediment samples. 33

Figure 14. Sulfur modified ZVI, XRD patterns from triplicate samples in artificial ground water. 34

Figure 15. Hepure ZVI XRD patterns from triplicate samples in artificial ground water. 36

Figure 16. Calcium polysulfide XRD patterns from triplicate samples in artificial ground water. 38

Figure 17. Sulfur modified ZVI XRD patterns from triplicate samples in synthetic perched water. 40

Figure 18. Hepure ZVI XRD patterns from triplicate samples in synthetic perched water. 41

Figure 19. Calcium polysulfide XRD patterns from triplicate samples in synthetic perched water. 43

Figure 20. Pristine Hepure ZVI and sulfur modified ZVI. 45

Figure 21. Sediment samples in an end-over-end tube revolver at 30 rpm 50

Figure 22. BET surface areas for Hanford formation sediment fractions (0.5-0.063 mm, 0.063-0.02 mm, and ≤ 0.02 mm)..... 51

Figure 23. Results for XRD measurements on 0.5 mm-0.063 mm Hanford Formation sediments 53

Figure 24. Results for XRD measurements on 63 μm -20 μm Hanford Formation sediments 53

Figure 25. Results for XRD measurements on less than 20 μm Hanford Formation sediments .. 53

Figure 26. A: SEM-EDS analysis of Hanford sediment. B: EDS elemental distribution for Hanford sediment. 54

Figure 27. Cr batch adsorption experiment: Concentration of Cr(VI) in solution vs Time (hours) 55

Figure 28. mg/g of Cr on solid vs mg/L Cr in solution..... 55

Figure 29. The release rates for B from ORLEC28 glass at 25 °C, 40 °C, 70 °C and 90 °C, utilizing pH 12 buffer (control) as a leachate in R1 and grout-contacted solution as the leachate (R2 and R3). The x-axis represents temperature (°C) and the y-axis represents the normalized release rate ($\text{g m}^{-2} \text{d}^{-1}$)..... 61

Figure 30. The release rates for Re from ORLEC28 glass at 25 °C, 40 °C, 70 °C, and 90 °C, utilizing pH 12 buffer (control) as a leachate in R1 and grout-contacted solution as the leachate (R2 and R3). The x-axis represents temperature (°C) and the y-axis represents the normalized release rate ($\text{g m}^{-2} \text{d}^{-1}$)..... 61

Figure 31. SEM micrograph of pristine glass (ORLEC28) (A) and a magnified crystal of a used glass sample at 25 oC in the presence of grout contacted solution (B). 63

Figure 32. SEM micrographs of glass residue at 90 °C experiment from reactor 2 (x1500) (A) and a magnified image (x13,000) of white precipitate (inside a white circle) (B)..... 64

Figure 33. SRS soil samples being dried in the oven. 68

Figure 34. Bulk fraction mineralogy. Red - Quartz; Blue- Kaolinite; Green - Goethite 70

Figure 35. Sand fraction mineralogy. Red - Quartz, Blue - Kaolinite 70

Figure 36. Silt fraction mineralogy. Red - Quartz; Blue - Kaolinite 71

Figure 37. Silt + clay mineralogy. Red - Quartz; Blue - Kaolinite, Green - Gibbsite 71

Figure 38. Scanning Electron Microscope image from particle from the bulk fraction of the SRS soil, with three separate points selected for XRF analysis..... 72

Figure 39. Scanning Electron Microscope image from particle from sand fraction of the SRS soil, with three separate points selected for XRF analysis. 72

Figure 40. Scanning Electron Microscope image from particle from silt fraction of the SRS soil, with three separate points selected for XRF analysis. 73

Figure 41. FTIR Spectra of mod-HA and Huma-K. 78

Figure 42. Zeta potential of mod-HA (●) and Huma-K (■). 79

Figure 43. Hydrodynamic sizes of mod-HA (top) and Huma-K (bottom). 80

Figure 44. Potentiometric titration of mod-HA. 81

Figure 45. Effect of pH for humate substances (a) mod-HA (b) Huma-K and Mod-HA comparison. 82

Figure 46. Kinetic Studies for Humate Substances (a) mod-HA (b) Huma-K. 83

Figure 47. Isotherm of mod-HA with 200 mg SRS sediment..... 83

Figure 48. Desorption of Mod-HA with pH. 84

Figure 49. Effect of desorption cycles on Mod-HA and Huma-K (mg/kg)..... 84

Figure 50. (a) Uranium Precipitation (b) Effect of pH on Uranium Sorption. 85

Figure 51. Uranium Sorption Kinetic Studies mod-HA vs Huma-K..... 86

Figure 52. Uranium Sorption Equilibrium Studies. 86

Figure 53. Desorption of Uranium (mg/kg) (a) mod-HA (b) Huma-K..... 87

Figure 54. Tims Branch watershed study area within the Savannah River Site, showing significant features including: watershed boundary (model domain), ponded areas, A-014 tributary, A/M Area, precipitation gauge, groundwater wells and stream stages. 93

Figure 55. SRNL collaborators, Drs. Brian Looney, Mike Paller and Hansell Gonzalez-Raymat, assisting the FIU team with the reinstallation of the HOBO remote monitoring device for recording water level in Tims Branch. 95

Figure 56. FIU and SRNL collaborators positioning the sensor/probe at the end of the PVC piping prior to placement in the stream..... 95

Figure 57. Protective wire mesh installed to prevent fouling of the water level sensor by sediment or debris. 96

Figure 58. Diagram of an integrated hydrologic model showing the MIKE SHE land model including evapotranspiration (ET), overland flow (OL), and flow in the unsaturated zone (UZ) and saturated zone (SZ), MIKE 11 stream hydrodynamic model (M11 HD), and contaminant transport components including the MIKE 11 Advection Dispersion (M11 AD) module. 97

Figure 59. Flow and sediment transport modules/components included in the Tims Branch model. 100

Figure 60. Model calibration result showing precipitation (bar from top), simulated (markers) and monitored discharge time series (solid line). 101

Figure 61. Model calibration evaluated using FITEVAL showing (a) regression of computed vs observed discharge, (b) FITEVAL plot of cumulative probability of NSE and its median, (c) FITEVAL goodness of fit evaluation including hypothesis test results, outliers, and the sensitivity

of the indicators to model bias, and (d) scatter plot showing fit between computed vs observed discharge in order of the series. 101

Figure 62. Predicted subsurface groundwater elevation time series represented by solid line contrasted against historical records represented as boxplots at the depth of 9.1 meters. 102

Figure 63. Design rainfall scenarios used in storm analysis. Note: 1) each column represents events with the same rainfall duration, 6h, 12h, 24h, and 96h, respectively from left to right; 2) each row represents events with the same rainfall temporal distribution out of four quartiles, 1st, 2nd, 3rd, and 4th, respectively from top to bottom; 3) each individual figure includes two groups of curves showing 10% and 90% percent of duration, while each group of curves represents design rainfall events with different ARIs, 5y, 10y, 25y, 100y and 500y, respectively from top to bottom..... 103

Figure 64. Spatial distribution of bed shear stress for locations downstream of the A014 confluence under various design rainfall scenarios. Note: 1) each column represents results under events with the same rainfall duration, 6h, 12h, 24h, and 96h, respectively from left to right; 2) each row represents results under events with the same rainfall temporal distribution out of four quartiles, 1st, 2nd, 3rd, and 4th, respectively from top to bottom; 3) each individual figure includes two groups of curves showing results under 10% and 90% percent of duration while each group of curves represents results under design rainfall events with different ARIs, 5y, 10y, 25y, 100y and 500y, respectively from top to bottom; 4) each vertical reference line represents pond downstream of the A014 confluence including Beaver Pond 2, Steed Pond, Beaver Pond 3, 4 and 5, left to right respectively. 104

Figure 65. Bed shear stress at Steed Pond as a response to the design rainfall events. Note: 1) each column represents results under events with the same rainfall duration, 6h, 12h, 24h, and 96h, respectively from left to right; 2) each row represents results under events with the same rainfall temporal distribution out of four quartiles, 1st, 2nd, 3rd, and 4th, respectively from top to bottom; 3) each individual figure includes two groups of curves showing results under 10% and 90% percent of duration, while each group of curves represents results under events with different rainfall ARIs, 5y, 10y, 25y, 100y and 500y, respectively from top to bottom. 105

Figure 66. Simulated discharge hydrographs for the area below Steed Pond (left) and the outlet (right) of Tims Branch watershed. 107

Figure 67. Simulated suspended sediment concentrations for the area below Steed Pond (left) and the outlet (right) of Tims Branch watershed. 108

Figure 68. Critical duration peak flows and suspended sediment loads for all frequencies of design storm events at the outlet of the Tims Branch watershed. 111

Figure 69. Critical duration peak flows and cumulative suspended sediment loads for all frequencies of design storm events at the outlet of the Tims Branch watershed..... 111

Figure 70. A rendered layout of the Waste Isolation Pilot Plant, near Carlsbad New Mexico (Tracy, 2019). 116

Figure 71. Drilling activities within the geologic formation of the WIPP site (Tracy, 2019). ... 116

Figure 72. Dissolution of dolomite (5 g/L) with time as a function of EDTA and separation methods in 0.1 M NaNO₃ (A, B), 1.0 M NaNO₃ solutions (C, D). Error bars are based on one standard deviation of triplicate samples..... 121

Figure 73. Dissolution of dolomite (5 g/L) with time as a function of EDTA and separation methods in in high ionic strength 5.0 M NaNO₃ (A, B) and 5.0 M CaCl₂ solutions (C, D). Error bars are based on one standard deviation of triplicate samples. 122

Figure 74. Dissolution of dolomite (5 g/L) with time as a function of EDTA and separation methods in 1.0 M Na₂SO₄. Error bars are based on one standard deviation of triplicate samples. 123

Figure 75. Dissolution of dolomite (5 g/L) with time as a function of EDTA and separation methods in 1.0 M Na₂SO₄. Error bars are based on one standard deviation of triplicate samples. 124

Figure 76. Dissolution of dolomite (5 g/L) over time as a function of EDTA and separation methods (unfiltered -A; Filtered – B) in 1.0 M CsCl solution. Error bars are based on one standard deviation of triplicate samples 125

Figure 77. Aqueous Ca (A) and Mg (B) dissolved from dolomite (5 g/L) over time in 1.0 M CsCl solution. Error bars are based on one standard deviation of triplicate samples 126

Figure 78. Photogrammetry workflow to produce bare ground DEMs from a point cloud of the study area using RGB-based vegetation indices and machine learning technology..... 132

Figure 79. Ray cloud generated in Pix4D after importing aerial images taken in Basin 6, Carlsbad, NM. 133

Figure 80. 2D orthomosaic and 3D DSM generated when Basin 6 aerial images were imported into Pix4D. 133

Figure 81. Coverage of aerial survey (in red) conducted by FIU in Basin 6, Carlsbad, NM. 135

Figure 82. FIU team marking ground control points using a Trimble GPS receiver in Basin 6, taking note of surface hydrological features of interest including brine lakes, sinkholes, and gullies. 135

Figure 83. Drone images captured during the aerial survey conducted by FIU in Basin 6, Carlsbad, NM. 136

Figure 84. Waste Management Symposium 2020 poster being presented by DOE Fellow Gisselle Gutierrez based on the hydrological modeling research being conducted for the WIPP by FIU ARC. 137

Figure 85. Location of 87 measured ground control points (GCPs) shown as blue-cross markers. 137

Figure 86. Location of 15 check points (CPs) shown as light blue markers vs. ground control points (GCPs) shown as dark blue markers. 138

Figure 87. Matches of GCP (1a) and images (DJI_0145- DJI_0167). 139

Figure 88. Marking of GCPs in the rayCloud on Pix4D..... 140

Figure 89. Automated point cloud classification showing land surface in brown, low vegetation in light green, high vegetation in dark green, road surface in grey and structure in red..... 141

Figure 90. Reflectance/classified index maps showing vegetation vs. bare ground based on seven different RGB-based vegetation indices. 143

Figure 91. Rasters/DEMs created using ArcGIS tools after point cloud classification using an RGB-based method and a machine learning method..... 144

Figure 92. DEM of the surveyed area in Basin 6 adjacent to the WIPP..... 145

Figure 93. Land features shown on both DEM and aerial images..... 146

Figure 94. DEM artifacts visible at the seam between image sets..... 147

Figure 95. Error of GCPs and CPs in meters for x-, y-, and z-axes..... 147

Figure 96. Model structure..... 151

Figure 97. Visualization of the example model showing vertical Darcy velocity on the top and the saturation at the bottom..... 153

Figure 98. Figure from the CLM5. 155

Figure 99. Figure from NOAH-MP. 157

Figure 100. WRF-Hydro physics permutations. 159

Figure 101. WRF-Hydro physics components..... 160

Figure 102. Schematic of the WRF-Hydro modeling framework displaying several categories of the model components. 160

Figure 103. WRF-Hydro implementation workflow. 161

Figure 104. WRF-Hydro setup workflow..... 161

Figure 105. Figure from ParFlow. 163

Figure 106. Study area in Black Sea Region 165

LIST OF TABLES

Table 1. Synthetic groundwater (SGW) composition for batch protocol (7.2 mM total ionic strength).....	12
Table 2. PH readings post 5% NH ₃ /95% N ₂ injection (~30 d) and post aeration step (24 h).....	12
Table 3. Descriptive Statistics (ANOVA: two-factor with replication) and particle size measurements of illite ammonia- and aerated- treated samples taken from magnification 1000x SEM images.....	15
Table 4. Recipes for Prepared Simulants.....	20
Table 5. Fraction Analysis of Hanford Soil.....	23
Table 6. Phase 1 Perched Water Averages in the Anaerobic Conditions (~10ppb Tc, ~pH8.2)..	29
Table 7. Phase 2 Perched Water Averages in Aerobic Conditions (~10ppb Tc, ~pH8.2).....	29
Table 8. Phase 1 Ground Water Averages in Anaerobic Conditions (~420 ppb Tc, ~pH 7.8).....	30
Table 9. Phase 2 Ground Water Averages in Aerobic Conditions (~420 ppb Tc, ~pH 7.8).....	30
Table 10. SEM-EDS Results for Artificial Ground Water Batches.....	31
Table 11. Solid Phases Matched in 1% Sulfur Modified ZVI Treated Sediment in Artificial Ground Water.....	34
Table 12. Matched Solid Phases for 1% Hepure ZVI Treated Sediment in Artificial Ground Water.....	36
Table 13. Solid Phases Identified in Sediment Treated with 5% Calcium Polysulfide in Artificial Ground Water.....	38
Table 14. Solid Phases for Identified in Sulfur Modified ZVI Treated sediment Samples prepared with Synthetic Perched Water.....	40
Table 15. Solid Phases for 1% Hepure ZVI Treated Sediment in Synthetic Perched Water.....	42
Table 16. Solid Phases Identified in 5% Calcium Polysulfide Treated Sediment iSamples Prepared with Synthetic Perched Water.....	43
Table 17. Solid Phases Identified in Pristine Iron.....	45
Table 18. AGW formulation.....	49
Table 19. Concentrations of each contaminant used in experiments ^{11,12}	49
Table 20. Measured percent mass composition of ORLEC28 glass (Neeway et al., 2018).....	58
Table 21. Measured percent elemental composition of grout-treated glass and precipitated grout solution. Only major constituents are reported. (Note: Averages and standard deviations from reactors R2 and R3).....	62
Table 22. Measurement Conditions of XRD scans.....	68
Table 23. Average and Standard Deviation of Soil Fractions. Mass of each fraction was divided by total mass of the sample. The values were then combined into one average value.....	69

Table 24. Summary of XRD results. Percentage of each mineral found in found in each fraction of soil..... 70

Table 25. BET Surface Area Analysis results of triplicate samples of bulk fraction sediment.... 71

Table 26. Summary of results from SEM-XRF analysis. Results of each spectra, average of the three spectra and the standard deviation are shown..... 73

Table 27. Summary of the calibration parameters from both the MIKE SHE land model (MSHE) and MIKE 11 stream hydrodynamic model (M11), including initial values and calibrated values. 99

Table 28. Verification of Sediment Transport Model..... 106

Table 29. Suspended Sediment Concentrations and Sediment Loads at the Downstream End of Steed Pond and the Outlet of the Tims Branch Watershed for Various Design Storm Events .. 109

Table 30. Critical Duration Suspended Sediment Concentrations and Sediment Loads with Associated Precipitation Depths at the Outlet of the Tims Branch Watershed 110

Table 31. Vegetation Indices Applied to Pix4D-generated Reflectance Maps 134

Table 32. History of discharge..... 150

Table 33. Key Processes in CLM 155

Table 34. Key processes in Noah-MP..... 157

Table 35. Primary Output data..... 159

Table 36. Key processes in WRF-Hydro 161

Table 37. Key processes in ParFlow..... 163

PROJECT 2 OVERVIEW

This project focuses on environmental remediation of contaminated soil and groundwater at Hanford, Savannah River Site, Oak Ridge Reservation and the Waste Isolation Pilot Plant (WIPP). The aim is to reduce the potential for contaminant mobility or toxicity in the surface and subsurface through the development and application of state-of-the-art environmental remediation technologies at DOE sites. In FIU Year 10, FIU ARC provided research and technical support on contaminant remediation efforts at the Hanford Site under Task 1, at SRS under Tasks 2 and 3, and at the WIPP under Tasks 5 & 6. This research involves laboratory-scale studies which utilize novel analytical methods and microscopy techniques for characterization of various mineral and microbial samples. Tasks also include the implementation of hydrological models, which help to predict the behavior and fate of existing and potential contaminants in the surface and subsurface. The research also involves the application of photogrammetry for development of high-resolution digital elevation models in support of the hydrological model development.

The following tasks are included in this FIU Year 10 report:

- Task 1: Remediation Research and Technical Support for the Hanford Site
 - Subtask 1.1 - Remediation Research of Ammonia Gas for Uranium Treatment
 - Subtask 1.2 - Re-oxidation of Redox Sensitive Contaminants Immobilized by Strong Reductants (NEW)
 - Subtask 1.3 - Evaluation of Competing Attenuation Processes for Mobile Contaminants in Hanford Sediments (NEW)
 - Subtask 1.4 - Experimental Support of Lysimeter Testing
- Task 2: Remediation Research and Technical Support for the Savannah River Site
 - Subtask 2.1 - Environmental Factors Controlling the Attenuation and Release of Contaminants in the Wetland Sediments at Savannah River Site (NEW)
 - Subtask 2.2 - Humic Acid Batch Sorption Experiments with SRS Soil
- Task 3: Contaminant Fate and Transport Modeling in the Tims Branch Watershed
- Task 5: Remediation Research and Technical Support for WIPP
 - Subtask 5.2 - Fate of Actinides in the Presence of Ligands in High Ionic Strength Systems
- Task 6: Hydrology Modeling for the Waste Isolation Pilot Plant (WIPP)
 - Subtask 6.1 - Digital Elevation Model and Hydrologic Network
 - Subtask 6.2 - Model Development

DOE Fellows supporting this project include Silvina Di Pietro (graduate, Ph.D., chemistry), Juan Morales (graduate, Ph.D., public health), Katherine De La Rosa (undergraduate, environmental engineering), Alexis Vento (graduate, M.S. environmental engineering), Amanda Yancoskie (graduate, environmental engineering), Gisselle Gutierrez (graduate, M.S. environmental engineering), Nathalie Tuya (undergraduate, environmental engineering), Mariah Doughman (graduate, Ph.D., chemistry), Phuong Pham (graduate, Ph.D., chemistry), Alicia Maratos (undergraduate, environmental engineering), and Stevens Charles (undergraduate, civil

engineering). Graduate student, Jonathan Williams, from the BME Departemnt also supported this research.

Task 1: Remediation Research and Technical Support for the Hanford Site

Production of atomic weapons at the Hanford Site from 1944 through the late 1980s has left a legacy of radionuclide contamination in soil and groundwater that poses technically complex environmental cleanup challenges that are unique to EM. Today, this waste contains about 195 million curies of radioactivity and 220,000 metric tons of chemicals. Of the 177 tanks onsite, sixty-seven have leaked about 3800 cubic meters (1 million gallons) of liquids into the underlying sediment (Gephart, 2003). Most of this residual waste is in or near the 200 Area. These releases have created plumes that threaten groundwater quality due to potential downward migration through the unsaturated vadose zone (VZ) sediment. The fastest-moving contaminants in the subsurface are technetium-99, iodine-129, chromium, uranium and nitrate (Gephart, 2003).

This end of year report presents an overview of tasks supporting the cleanup mission at the Hanford Site that can complement ongoing work at PNNL for a better understanding of the long-term behavior of contaminants in the subsurface, including:

1. Ammonia Gas Injection for In Situ Immobilization of Uranium
2. Re-oxidation of Redox Sensitive Contaminants Immobilized by Strong Reductants (New)
3. Evaluation of Competing Attenuation Processes for Mobile Contaminants in Hanford Sediments (New)
4. Experimental Support of Lysimeter Testing

Task 2. Remediation Research and Technical Support for Savannah River Site

There is a need for the Savannah River Site to gather results to supplement permit requirements associated with the Area Completion Project (ACP), including the Phase 2 strategy to evaluate the performance of Phase 1 including "...downgradient of the F-Area inactive process sewer line and at Four Mile Branch". Per permitting requirements delineated in the corrective action plan, ¹²⁹I concentrations must be below groundwater standards in the Four Mile Branch by October 31, 2025, and in the F-Area plume in surface water at the seepline by October 31, 2030. Because the DOE has no approved technology for remediation of subsurface iodine, it is essential to understand its long-term fate in plumes at the Savannah River Site. In addition, DOE-EM requires additional study of the fate of co-mingled contaminant plumes due to their complexity (McCabe, D., *et al.*, 2017). The experiments delineated in this subtask will contribute to both our understanding of the interactions of U, Tc, and I with organic materials, as well as the potential for remediation of U via injection of commercial humic materials providing essential data for fulfillment of the abovementioned permitting requirements and goals for DOE-EM.

Savannah River Site (SRS) is also conducting synergistic research, funded by the Department of Energy Environmental Management Office of Soil and Groundwater Remediation (EM-12), as part of the Attenuation-Based Remedies for the Subsurface Applied Field Research Initiative (ABRS AFRI). This applied research is geared to develop science-based approaches to clean and close sites contaminated with combinations of metals, radionuclides, and other contaminants of concern. A primary objective of this program is to develop approaches for attenuation-based remedies, in this case, to investigate and validate the use of humate for subsurface stabilization of metals in contaminated groundwater plumes. SRS successfully conducted a field campaign that

demonstrated the viability of dissolving and then injecting low cost agricultural humate into the subsurface and proposed that it is a viable attenuation-based remedy for uranium and potentially suitable for I-129. Humic acid, which carries a large number of functional groups, provides an important function in ion exchange and as a metal complexing ligand with a high complexation capacity, being able to affect the mobility of radionuclides in natural systems. Different types of humic substances such as unrefined humic acid, modified humic acid, and commercial humic acid, will be used in this research to study their effect on uranium removal.

Task 3: Contaminant Fate and Transport Modeling in the Tims Branch Watershed

This research involves the development of an integrated, fully distributed hydrology and contaminant transport model, which will be used as a tool to address the knowledge gaps related to the fate and transport of sediment-bound contaminants at DOE EM sites. Implementation of a tin-based mercury remediation technology in the Tims Branch watershed has provided records of the quantity and timing of the tin released. This subsequently presented a unique opportunity for the tin to serve as a potential tracer for modeling sedimentation and particle transport processes in the stream, making Tims Branch an ideal testbed for evaluating the effectiveness of wetland treatment and tin (II) - based mercury treatment at the SRS site. DOE EM has highlighted the need to track the tin and to understand the impact of frequent or extreme atmospheric events on its redistribution in Tims Branch. FIU intends to utilize the data available from the tin-based remediation technology to develop a hydrological and contaminant transport model that can in future be extended to investigate other heavy metal and radionuclide contaminants of concern (e.g., mercury, uranium and nickel). Knowledge acquired from this research will also assist in developing cost-effective remediation plans integrated into the SRS Area Completion Project (ACP) and accelerate progress of the DOE EM environmental restoration mission.

Task 5: Research and Technical Support for WIPP

The Waste Isolation Pilot Plant (WIPP) geologic repository is characterized by high ionic strength porewaters (up to 7.4M), requiring better understanding of the mobility of actinides and lanthanides in the presence of metal chelating ligands in relevant conditions for development of accurate risk assessment models. In a current Performance Assessment Inventory Report (Van Soest, 2018), ethylenediaminetetraacetic acid (EDTA), which forms strong, stable complexes with the lanthanides and actinides, is reported with a high concentration in the WIPP waste (7.9×10^{-5} M), making it the largest concern for impact on contaminant mobility (Dunagan et al., 2007; Brush, 1990). Additional ligands of interest include degradation products such as gluconate, a cement additive, which has been identified in the hyperalkaline conditions expected in cementitious repositories (Gaona et al., 2008). Current Performance Assessment (PA) models do not include gluconate due to the expected low impact in WIPP-relevant conditions. However, additional experimental support of the conservatism in the models will provide better understanding of potential impacts from these ligands. In this study, FIU ARC collaborated with Dr. Donald Reed, a team leader of the Actinide Chemistry and Repository Science (ACRSP), in support of Los Alamos National Laboratory's field office located at the Carlsbad Environmental Monitoring and Research Center (CEMRC) in Carlsbad, New Mexico. The goal of this study is to generate accurate sorption data for the actinides to minerals and under conditions relevant to the Waste Isolation Pilot Plant as previous risk assessment models are based on conservative assumptions.

Task 6: Hydrology Modeling for WIPP

This task was developed by FIU's Applied Research Center in collaboration with DOE personnel at Pacific Northwest National Laboratory (PNNL) and the Carsbad Field Office (CBFO) to support research and development activities at the WIPP site by developing a groundwater-basin model for the WIPP site using the DOE-developed Advanced Simulation Capability for Environmental Management (ASCEM) modeling toolset. There is a need for an improved understanding of the regional water balance, particularly the relation between Culebra recharge and the intense, episodic precipitation events typical of the monsoon. This relationship is essential for understanding the rate of propagation of the shallow dissolution front, and the impact of land-use changes around the WIPP facility on water levels in compliance-monitoring wells. The model developed will help to compute the regional water balance and derive estimates of groundwater recharge in the post-closure phase. As ASCEM cannot currently account for land surface hydrology, which is essential for computing the water balance, a regional land surface model is also needed to account for surface water routing. Coupling of the LSM with the ASCEM GWMs leads to more accurate predictions of groundwater flow patterns, including horizontal flow. This multi-year effort will benefit DOE-EM by providing improved estimates of the spatial and temporal patterns of recharge, so that better predictions of halite dissolution and propagation of the shallow dissolution front can be made possible to assess and quantify the potential impact on the WIPP repository performance.

MAJOR TECHNICAL ACCOMPLISHMENTS

Task 1: Remediation Research and Technical Support for the Hanford Site

- Investigated phyllosilicate clay mineral alteration in ammonia gas alkaline treatment. Results showed significant dissolution and mineral alternation occur upon exposure of phyllosilicate clay minerals to highly alkaline (pH > 11) treatment. These observations suggest secondary precipitation may be an effective method for sequestration of contaminants within newly formed, low solubility minerals.
- Successfully collaborated with the Department of Environmental Engineering and Earth Sciences at Clemson University to characterize Hanford sediments and phyllosilicates minerals via TEM-EDS. Results demonstrated that U was not detected on the surface of the minerals; however, this is due to low U-loading content on the solid phase.
- Currently collaborating with the solid-state Nuclear Magnetic Resonance (NMR) spectroscopy lab at Lawrence Livermore National Laboratory to detect the neighboring atoms of the Si and Al atoms in ammonia and aerated treated illite samples. The data interpretation and results will be included in the manuscript under preparation.
- Published a paper: Di Pietro, S.A., Emerson, H.P, Katsenovich, Y, Qafoku, N. P, and J. E.Szecsody. Phyllosilicate mineral dissolution upon alkaline treatment under aerobic and anaerobic conditions, 2020. *Applied Clay Science*, v.189, p.105520
- Studied technetium (Tc-99) reoxidation following reduction in the presence of strong reductants, Hepure ZVI, sulfur modified iron and calcium polysulfide (CPS). FIU performed experiments using Hanford sediment by doing sediment size fraction analysis, XRD, and BET characterizations. The study will help to determine reoxidation rates of pertechnetate after sediment samples prepared with the synthetic perched and groundwater were exposed to the aerobic conditions. FIU also initiated SEM-EDS and XRD analyses on reductant-treated samples.
- Completed investigation of the effect of variable pH and silica concentrations on the incorporation of iodate co-located with chromate in calcium carbonate and evaluated the release of incorporated iodate and chromate during calcite dissolution. These findings were included in the manuscript titled “*Silicon concentration and pH controls over competitive or simultaneous incorporation of iodate and chromate into calcium carbonate phases*” that is under peer-review in the *Applied Geochemistry* journal.
- Completed physical characterization of uncontaminated Hanford Formation sediment fractions. This includes measurement of the surface area via Brunauer–Emmett–Teller (BET), evaluation of mineralogy via X-ray Powder Diffraction (XRD) and elemental composition via Scanning Electron Microscopy with Energy Dispersive Spectroscopy (SEM/EDS) and X-ray fluorescence (XRF). Results show the presence of quartz and albite as dominant minerals in all fractions. Silicon was also the dominant element in all fractions. However, the presence of magnesium, aluminum, calcium, iron, and sodium was also detected in these fractions. These elements (notably iron) will more actively participate in the adsorption mechanisms of contaminants being studied.

- Initiated batch adsorption experiment of Cr(VI) to Hanford Formation sediment (<2 mm/bulk phase) at a high sediment-to-water ratio of 1.5:1. Concentrations of Cr(VI) used in the studies were modeled after values found in Hanford 2018 Groundwater Monitoring Report and 2018 Pump and Treat Report. Although this experiment will be repeated, a general idea of where equilibrium conditions are attained was established and significant sorption was observed after 72 hours.
- Completed the glass dissolution experiments via a single-pass flow-through (SPFT) experiment using grout-contacted solutions prepared in DIW at 25°C, 40°C, 70°C and 90°C. These experiments were conducted in support of the Hanford Lysimeter Test Facility (FLTF). The dissolution rate of the glass was lower in experiments using grout-contacted solution as the leachate when compared to a buffer solution with the same pH. The lowered dissolution rate may be due to a common ion effect occurring due to the presence of dissolved species from the grout in the leachate, however further work is ongoing to interpret and understand the controlling mechanisms.

Task 2. Remediation Research and Technical Support for Savannah River Site

- Completed characterization of SRS wetland sediment using various techniques such as XRD, SEM-XRF, BET. This characterized wetland sediment will be used in future experiments.
- Investigated KW15-modified humics (known as modified humic acid) to facilitate uranium adsorption onto SRS sediment to control the mobility of uranium in acidic SRS groundwater. Studied the sorption and desorption of uranium onto humate-coated SRS sediment.

Task 3: Contaminant Fate and Transport Modeling in the Tims Branch Watershed

- Field Research: Postdoctoral Associate, Dr. Yan Zhou, and 2 DOE Fellows (Amanda Yancoskie and Juan Morales) visited SRS from Dec. 16-18, 2019 to conduct fieldwork activities that support the Tims Branch hydrological model development. The team performed routine maintenance and calibration of 3 remote monitoring devices deployed in Tims Branch which record water level timeseries data. This data is required for hydrological model calibration and validation in order to increase confidence in the ability of the hydrology model being developed for Tims Branch to estimate flow depth and velocity, as well as contaminant spatial distribution over time. The FIU team was assisted by Drs. Brian Looney and Mike Paller from SRNL and Dr. John Seaman from SREL.
- Tims Branch MIKE SHE/ MIKE 11 model recalibration: FIU conducted a thorough review of the MIKE SHE/ MIKE 11 model parameterization. FIU updated the model boundary conditions and some most influential model parameters (e.g., hydraulic conductivity of geological layers, spatial variation of initial hydraulic head, and leakage coefficient) based on a literature review and best modeling practices. The restructured model was finally recalibrated to a 2018 flow hydrograph estimated at the outlet of the watershed.
- Extreme event simulation: Flow hydrographs at key locations in Tims Branch were simulated for the 5-, 10-, 25-, 100- and 500-year Average Recurrence Interval (ARI) events for storm durations of 6, 12, 24 and 96 hours. A range of temporal distributions as recommended by NOAA's Precipitation Frequency Data Server (PFDS) was considered in the model runs. The bed shear stress and flow velocity hydrographs were also estimated

from the results of ensemble runs. This study will be significantly useful in quantifying and characterizing stream flows to provide informed decisions related to the sediment remobilization study within the main branch.

- **Sediment transport module development and verification:** A cohesive sediment transport (CST) model was developed using the MIKE 11 AD (advection-dispersion) module available in the MIKE ZERO modeling platform. The CST model was plugged into the Tims Branch MIKE SHE/MIKE 11 modeling framework. The CST model was parameterized and verified utilizing available suspended sediment concentration data.
- **Sediment transport modeling under design storm events:** The integrated sediment transport and MIKE SHE/MIKE 11 model was implemented for simulating the sediment transport process under 1-, 5-, 10-, 25-, 100- and 500-year ARI events with a range of storm durations and temporal patterns as mentioned in NOAA's PFDS. The suspended sediment concentrations and sediment loads at the downstream end of Steed Pond and near the outlet of the watershed were estimated. This study will reinforce the understanding of sediment remobilization criteria and intensities under various extreme events and support the contaminant fate and transport modeling efforts.
- **Publications:** FIU submitted a full length paper and delivered an oral presentation entitled "*Contaminant Transport Modeling for Technology Evaluation and Long-Term Monitoring in the Tims Branch Testbed, SC*" at the 2020 Waste Management Symposia based on the Tims Branch hydrology model development. Two full length papers have also been submitted to the upcoming WM 2021 conference. Both papers will be published in the conference proceedings and were accepted for oral presentations. In addition, DOE Fellow Stevens Charles will present his recent work on the sediment transport process within Steed Pond during the WM2021 student poster competition.

Task 5: Research and Technical Support for WIPP

- Completed dolomite dissolution batch experiments to investigate impact of ionic strength and EDTA on mineral dissolution behavior.
- Initiated batch sorption investigation of the impact of gluconate and ionic strength on the sorption of Nd(III), Th(IV), and U(VI) to iron oxides.

Task 6: Hydrology Modeling for WIPP

- Postdoctoral Associate Dr. Yan Zhou and DOE Fellow Gisselle Gutierrez travelled to Carlsbad, NM in February 2020 to collect aerial imagery using a UAV for a pilot study in a representative basin (Basin 6) of the WIPP and surrounding region. The images were collected for a subset of Basin 6 adjacent to the WIPP along both sides of Road 128 that cover most of the topographical and surface hydrological features of interest including brine lakes, sinkholes, roads, pumping wells, etc. The imagery was processed using photogrammetry software and GIS tools to generate a high resolution DEM that will be used for delineation of significant hydrographical features such as sinkholes, brine lakes, gulleys, etc., and for development of a regional land surface model.
- FIU completed the processing of the drone imagery collected in the pilot study area of Basin 6 adjacent to the WIPP and has generated a digital elevation model (DEM) of the surveyed area at a resolution of 0.17 meters. The high-resolution DEM generated allows several land features to be easily identified, such as gullies, brine lakes, and land sinks.

- The FIU hydrologic team has completed preliminary training on the ASCEM modeling toolset, which will be used to develop a regional groundwater model for the WIPP and surrounding areas in order to simulate the fluctuation of groundwater levels in response to climate variability and pumping activities. It was agreed that FIU's PNNL and CBFO collaborators would conduct the training remotely instead of on-site at FIU due to health and safety concerns and travel restrictions imposed due to the coronavirus (COVID-19) pandemic, as well as FIU's transition of most of its employees to remote work. To date, FIU has succeeded in reproducing and visualizing the hydrologic response of test models; however, further training is needed to accommodate contaminant transport simulation test cases and to provide guidance and improve exception-handling capabilities. The ongoing ASCEM training designed and executed by PNNL to support Basin 6 ASCEM model development will be reactive in nature, as it will be based on the technical needs of FIU.
- FIU conducted a literature review on open-source land surface models including the Community Land Model (CLM), Noah MP, WRF-Hydro, and ParFlow. CLM has been successfully coupled with the LBNL-developed ParFlow, and the UCAR-developed Noah and Noah-Multi-parameterization (Noah-MP) models. Noah-MP has been successfully coupled with the Weather Research and Forecasting (WRF) Model and used to predict the water cycle components including precipitation, soil moisture, snowpack, groundwater, streamflow, and inundation. Both the CLM and Noah-MP LSMs can be run as standalone codes, generating output that can be used to force ASCEM groundwater models while work is done within the ASCEM program to couple the LSM and GWMs. Coupling of a LSM with the ASCEM GWMs will lead to more accurate predictions of groundwater flow patterns in the WIPP region, including horizontal flow (e.g., potentiometric surface, flow direction, vertical flow into transmissive units, and the effect of density on flow direction). With improved estimates of the spatial and temporal patterns of recharge to force the GWM, predictions of halite dissolution and propagation of the shallow dissolution front will be made possible and the potential impact on repository performance quantified.

TASK 1: REMEDIATION RESEARCH AND TECHNICAL SUPPORT FOR THE HANFORD SITE

Task 1: Executive Summary

DOE EM has a critical need to understand the biogeochemical processes influencing the behavior of contaminants (U, I, Tc, and Cr) in Hanford Site's deep vadose zone that can impact groundwater quality. This research studies solutions that may reduce the long-term costs of environmental stewardship at the Hanford site by transforming the more than 200,000 kg of mobile U released to the vadose zone into low solubility precipitates. It is directly applicable to plans to develop incremental technologies for treatment of subsurface contamination and 'gaining a better understanding of ... biogeochemical processes that influence contaminant behavior' as outlined for 2017-2021 (DOE EM, 2016). Further, this effort is in alignment with DOE EM's plans to quantify the effect of co-mingled contaminant plumes (McCabe, D., *et al.*, 2017) and targets Tc-99, uranium, iodate and chromate, which are high priority contaminants.

Subtasks under Task 1 are performed with guidance from the Pacific Northwest National Laboratory.

Subtask 1.1: Remediation Research of Ammonia Gas for Uranium Treatment

Subtask 1.1: Introduction

The dissolution and alteration of minerals under alkaline solutions is studied in several fields including geochemistry and materials science for the characterization and remediation of contaminated sites. Alkaline technologies are being implemented for remediation of acidic plumes created by heap leach mining processes, sulfide-rich mine drainage, and acidic waste releases (Doye & Duchesne, 2003; Fernández et al., 2014; Mason et al., 1997). Yet, remediation and treatment with ammonia (NH₃) gas is a lesser studied treatment option that requires further study (Zhong et al., 2015). The use of a gas phase is seldom explored as a tool for remediation purposes, although it can be cost-effective, simpler to distribute, and less impactful to the vadose zone than aqueous solutions. NH₃ quickly partitions into subsurface porewater due to its low Henry's constant ($K_H = 0.016 \text{ atm/mol}$) (Tro et al., 2017) and prevents the addition of liquids that may increase contaminant mobility in unsaturated sediments. Moreover, 99% of the NH₃-mass is expected to partition to solution at 1.0% porewater content (Szecsody et al., 2012). NH₃ gas technology has the potential to sequester inorganic cations and radionuclides within solid phases in the subsurface. It has been shown to increase mineral dissolution and secondary precipitation reactions as the pH is neutralized, immobilizing contaminants within coatings and co-precipitates in the subsurface (Szecsody et al., 2012).

Due to its recent proposal for vadose zone remediation, there is limited information quantifying the effects of NH₃-induced alkaline conditions on clay mineral alterations (Emerson et al., 2018; Katsenovich et al., 2016, 2018; Szecsody et al., 2012, 2020). Emerson *et al.*, noted that NH₃ gas treatment increased uranium (U) removal more than aqueous [sodium hydroxide (NaOH) and ammonium hydroxide (NH₄OH)] alkaline treatments and concluded that precipitation of secondary mineral phases in clay minerals occurred due to incongruent dissolution. Similarly, Katsenovich et al. (2016) and Szecsody et al. (2012) conducted different NH₃-gas treatment experiments to evaluate uranium (U) removal from solution over time. While Szecsody's team

used Hanford Site sediments for a one-year treatment, Katsenovich's batch solutions were U-spiked during a two-day contact time. Both researchers found that hydrous U-silicates (e.g., sodium boltwoodite) should predominantly precipitate. These results were confirmed via geochemical speciation modeling. Katsenovich and team also reported that uranyl carbonate phases formed following NH_3 gas injection via X-ray diffraction (XRD) analysis.

Select studies have analyzed clay alterations post-alkaline treatment using complementary analytical techniques. For example, Chen *et al.* synthesized Zeolite Socony Mobil-5 (ZSM-5), a widely used aluminosilicate catalyst in the petroleum industry, from illite mineral in 5.6 M NaOH solutions at 473 K (Chen *et al.*, 2019). After $\text{Na}_2\text{O}/\text{SiO}_2$ molar ratio quantification, XRD, Fourier-transform infrared spectroscopy (FTIR), ^{27}Al NMR (nuclear magnetic resonance), scanning electron microscope-energy dispersive spectroscopy (SEM-EDS)] analysis, the team concluded that the high alkalinity ($\text{pH} > 11$) led to condensation of Si–O–Si bonds for the ZSM-5 formation after 24 h (Chen *et al.*, 2019). Although the high temperature conditions of Chen and team's experiments is not relevant to environmental remediation conditions, these experiments can inform on potential reactions. Moreover, Marsh *et al.* noted illite and montmorillonite alterations after 24 h of exposure to NaOH solutions at 40 °C. For high Na:Al solution ratios, illite clay morphology was altered, while montmorillonite formed a new geopolymer (eco-friendly binder) hydrosodalite $\{\text{Na}_8[\text{AlSiO}_4]_6(\text{OH})_2\}$ phase identified via ^{27}Al and ^{27}Si NMR, SEM-EDS, FTIR, and XRD analysis (Marsh *et al.*, 2018). Additional studies confirmed zeolite formation from montmorillonite and illite following NaOH exposure (1 - 14 M) at different temperatures (30–100 °C) via SEM-EDS, FTIR, and XRD analysis (Belviso *et al.*, 2017; El Hafid & Hajjaji, 2015; Kang & Egashira, 1997). Additional researchers have also identified formation of secondary aluminosilicates in Hanford Site sediments interacted with simulated tank waste at $\text{pH} > 13.5$ in NaOH solution, such as cancrinite, zeolite, and sodalite. These had formed upon dissolution and were characterized via SEM-EDS, FTIR, and XRD analysis (Barnes *et al.*, 1999; Qafoku *et al.*, 2004; Zhao *et al.*, 2004), including Raman spectroscopic analysis (Buck & McNamara, 2004).

However, unlike the aforementioned research, our study proposes a gaseous alkaline treatment with NH_3 under environmental conditions. After NH_3 mass loss due to gas diffusion and reaction with porewaters, the pH is expected to return to natural soil conditions within nine months of 10% NH_3 gas addition at 1.0% porewater content (Szecsody *et al.*, 2020). As a consequence, we expect to observe changes in the solid phase due to both the dissolution and precipitation of secondary minerals. However, few works have investigated these conditions and most research was conducted previously with simulated tank waste (STW) solutions as opposed to gas treatments. Mashal and team noted that XRD diffraction patterns of aluminosilicates were altered due to dissolution upon interaction with STW solutions (Mashal *et al.*, 2004). With various analytical techniques (i.e., SEM-EDS, FTIR, and XRD) and saturation index calculations, the team concluded that dissolved Si and Al precipitated to form secondary minerals including cancrinite and sodalite (Mashal *et al.*, 2004). Similarly, Wan *et al.*, tested Hanford Site sediments with STW solutions over a broad pH range (7 - 14) at room temperature (Wan *et al.*, 2004). X-ray diffraction and SEM analysis confirmed cancrinite-zeolite precipitation and sodalite formation. The team suggested that the secondary mineral formation was the result of hydroxide neutralization. Indeed, both batch-STW studies reported newly formed precipitation of secondary silicates minerals in Hanford sediments after base was neutralized.

Although previous research demonstrates evidence of clay alteration under alkaline conditions, there is a need to systematically measure alteration during NH_3 gas injection under environmental

conditions as previous research has not been found that adequately addresses clay alteration under alkaline conditions relevant for environmental remediation of the subsurface. Indeed, pH manipulation needs to be understood in order to (1) describe mineral alteration, (2) develop a conceptual model for contaminant interaction, and (3) predict the fate and transport of contaminants.

Subtask 1.1: Objectives

The objective of this research was to identify the major physicochemical changes of aluminosilicate minerals, illite and montmorillonite, following NH₃ gas and subsequent aeration treatments. This research conducted batch experiments to compare mineral solids at different stages of interaction with NH₃ gas with complementary characterization techniques. In this report, results are presented for batch experiments conducted with exposure to 5% NH₃/95% N₂ gas followed by aeration with ultrapure air for illite and montmorillonite minerals. These experiments provide a systematic investigation using X-ray Diffraction (XRD), scanning electron microscope with energy dispersive X-ray spectroscopy (SEM-EDS), Transmission Electron Microscope (TEM) analysis and Fourier-transform infrared (FTIR).

Subtask 1.1: Methodology

Experiments were conducted using two minerals: illite (Clay Minerals Society, Cambrian Hole, Silver Hill Mount) and montmorillonite (Clay Mineral Society, Crook County, Wyoming). The minerals were washed prior to experiments following the procedure described in Di Pietro *et al.*, 2020 based on previous research (Baeyens & Bradbury, 2004; Boggs *et al.*, 2015). Briefly, suspensions (100 g/L) were mixed with 1.0 M NaCl prepared with ultrapure H₂O (resistivity greater than 18 MΩ·cm, DIW), allowed to flocculate overnight, and centrifuged at 4500 rpm (18,100 rcf) in a benchtop centrifuge with a swing bucket rotor attachment (Thermo Scientific, Corvall ST 16R). Supernatant was then decanted and replaced with DIW. This process was repeated until the conductivity was less than 20 μS/cm to show that most ions had been removed. Montmorillonite (6.0 g), however, was first mixed with 60 mL of 0.001 M HCl and 0.5 mL of H₂O₂ to remove salts and limit redox active species (Boggs *et al.*, 2015) followed by a DIW wash. After each step, the samples were centrifuged at 4500 rpm for 6 hrs for montmorillonite and 30 minutes for illite, after which the liquid was decanted. The longer centrifugation time was used for montmorillonite to aide in dewatering the expanding layers. Subsequently, minerals were dried for 6 days in an oven at 30°C prior to use in experiments (LabNet International Inc.).

The batch protocol consisted of previously washed minerals. Minerals were suspended (70 g/L) in synthetic groundwater solution (SGW, Table 1, 7.2 mM total ionic strength). The simplified SGW in Table 1 is based on previous work (Emerson *et al.*, 2017, 2018; Szecsody *et al.*, 1998; Truex *et al.*, 2017). Duplicate suspensions were exposed to 5% NH₃ (anhydrous UN1007RQ, Airgas)/95% N₂ (UHP300, Airgas) inside a plastic glovebag (GlasCol, 27 x 27 x 15 inch). Samples inside were uncapped for 12-16 hours to equilibrate with the gas phase. Then, samples were re-capped, covered with parafilm, and set to equilibrate on an end-over-end tube revolver at 40 rpm (Thermo Scientific) for approximately one month. Because there is a need to investigate secondary precipitation under circumneutral pH conditions reached after re-equilibration of minerals and solutions with air, a second set of suspensions underwent aeration treatment after the one-month equilibration with NH₃. The aeration step consisted of a 10 psi flow rate (5.68 mL/min) of ultrapure air split into three tubing lines to allow for simultaneous treatment of three samples per tank. pH

measurements (Thermo Scientific Orion VersaStar, 8175BNWP) were taken prior to and following the aforementioned steps to confirm alkaline and aeration treatments, respectively, with a three-point calibration (pH 4.01, 7.00, and 10.01 Buffers, Thermo Scientific). Table 2 lists the recorded pH measurements taken 30 days post 5% NH₃/95% N₂ injection and 24 h of aeration treatment.

Various characterization techniques were used to identify solid phase minerals prior to and post treatment. Techniques included X-Ray Diffraction (XRD), Brunauer-Emmet-Teller (BET) surface area analysis, scanning electron microscope with energy dispersive X-ray spectroscopy (SEM-EDS), transmission electron microscope (TEM) analysis, and Fourier transform infrared spectroscopy (FTIR). This approach combined complementary techniques to determine mineral alterations upon pH manipulation based on comparison with control minerals.

Table 1. Synthetic groundwater (SGW) composition for batch protocol (7.2 mM total ionic strength).

Element	(mmol/L)
Na ⁺	1.1
K ⁺	0.22
Ca ²⁺	1.4
Mg ²⁺	0.6
HCO ₃ ⁻	1.32
Cl ⁻	3.9

Table 2. PH readings post 5% NH₃/95% N₂ injection (~30 d) and post aeration step (24 h)

Mineral	pH initial	pH aeration
Illite	11.24 ± 0.06	8.58 ± 0.08
Montmorillonite	11.22 ± 0.05	8.51 ± 0.22

Subtask 1.1: Results and Discussion

The focus of this study was to identify major physicochemical changes of aluminosilicate minerals, illite and montmorillonite, following NH₃ gas and subsequent aeration treatments. As Figure 1 shows below, illite and montmorillonite underwent crystallographic alternations upon transmission electron microscopy analysis (TEM). The selected area electron diffraction (SAED) patterns and TEM images at 100 and 200 nm resolution chosen demonstrate a difference between untreated (Figure 1a and Figure 1d) versus ammonia and aerated treated samples (Figure 1b-c and Figure 1e-f). The features observed for untreated minerals are similar to images presented in the literature, showing multiple rings representative of polymorphism for the SAED patterns and layer-stacking sequences for the TEM micrographs characteristic of phyllosilicate minerals (Bauluz et al., 2002; Dağ et al., 2019; Nadeau, 1985; Nieto et al., 2010; Xiang et al., 2019). After the minerals were exposed to NH₃ treatment for 30 days, the SAED patterns have less pronounced polymorphic rings (Figure 1b and Figure 1e), indicative of less crystalline phases. While it is difficult to demonstrate NH₄⁺ ion intercalation within the patterns, TEM micrographs show some corrosion traces on the edges of the minerals. The long, parallel and undulated darker zones on the edge of the mineral could be frayed due to the alkaline-induced dissolution, potentially demonstrating the intercalation of the polyatomic cation NH₄⁺. These micrograph images correlate to Dağ *et al.*, studies, in which the team observed interlayer expansion of montmorillonite via

SEM, TEM, and XRD analysis after a polymerization (styrene monomer) alteration at 85°C for 2 h. It is important to note that the need to investigate the polyatomic cation is due to the alkalinity of the system. The increase in pH caused by treatment with NH₃ gas treatment is shown by Eq. 1.

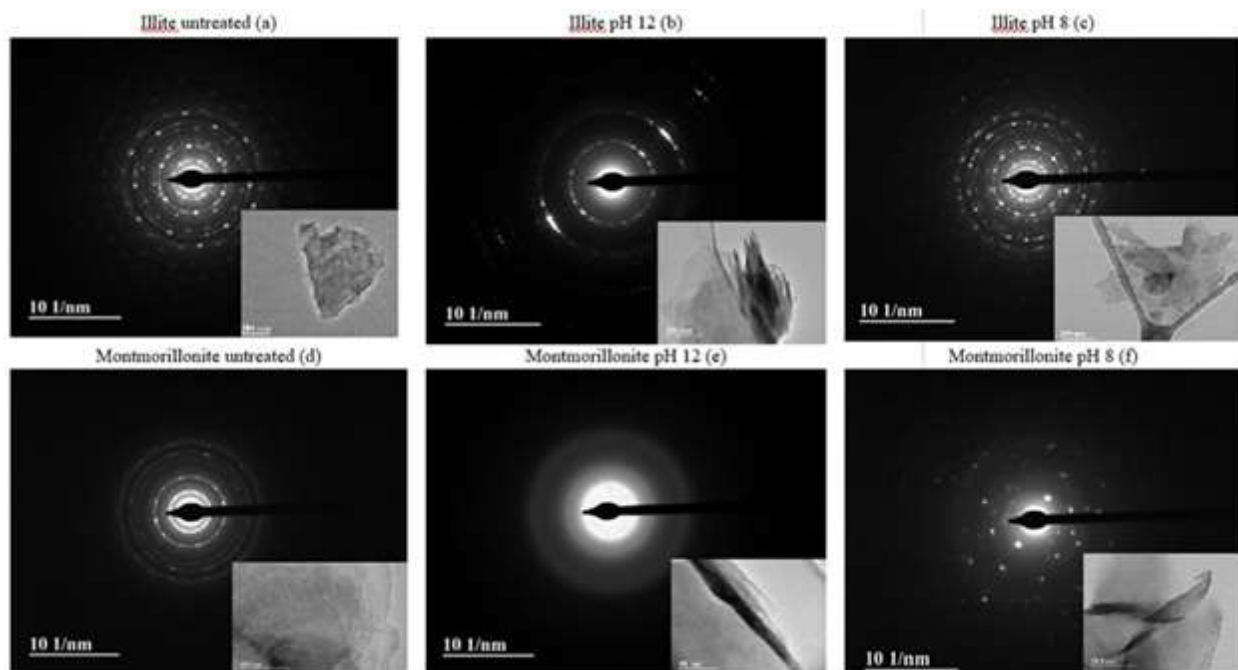
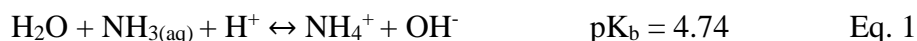


Figure 1. Selected area electron diffraction (SAED) image patterns of the crystalline aluminosilicate minerals (illite, top; montmorillonite, bottom) for untreated minerals (a and d), treated with 95% N₂/5% NH₃ gas for 30-day contact time in SGW solution (7.2 mM) at pH 12 (b and e) and aerated-treated at pH 8 (c and f). Bottom right show inset micrographs of Transmission Electron Microscope (TEM) images at 100 and 200 nm resolution.

To further investigate the intercalation of NH₄⁺ in the investigated phyllosilicate minerals, FTIR analysis was conducted. Figure 2a below compares the NH₄⁺ intercalation for untreated and alkaline treated aluminosilicate minerals. The montmorillonite-treated spectrum shows a broad and pronounced infrared absorption at ~3334 cm⁻¹, indicative of NH₄⁺ stretching in the stretching zone (3300-2840 cm⁻¹) (Kim et al., 1994; Petit et al., 1998). Although the NH₄⁺ deformation absorption band, or bending vibration of the N-H atoms, at 1385-1430 cm⁻¹ is observed for both minerals, it is significantly more pronounced for montmorillonite (Navratilova et al., 2007).

The intercalation of the NH₄⁺ cation suggests a disruption or collapse of the interlayer and, hence, the degree of cation fixation. Numerous reports studied the fixation in both expandable and non-expandable layers (Sawhney, 1972). Ultimately, it is the nature of the cation which dictates the selective sorption in the interlayer. Rajec *et al.*, explains that the preferential sorption of cations to clays is predominantly related to their low hydration level. This is the case of montmorillonite, for which the clay readily sorbs water and polar molecules, resulting in interlayer expansion (Barton, 2002; Chiou & Rutherford, 1997; Laird, 1987; Nadeau, 1985). Zhen *et al.*, on the contrary, explain that intercalation studies in illite are less common because the interlayer is collapsed and bound tightly (Zhen et al., 2017). Lastly, Pironon *et al.*, concluded that K⁺ and NH₄⁺ have similar radii

(K^+ , $r = 1.37 \text{ \AA}$; NH_4^+ , $r = 1.43 \text{ \AA}$) allowing the polyatomic ion to substitute for K^+ in minerals, explaining why there is a broader adsorption band for treated illite in Figure 2b (Lumen Learning, 2019; Pironon et al., 2003).

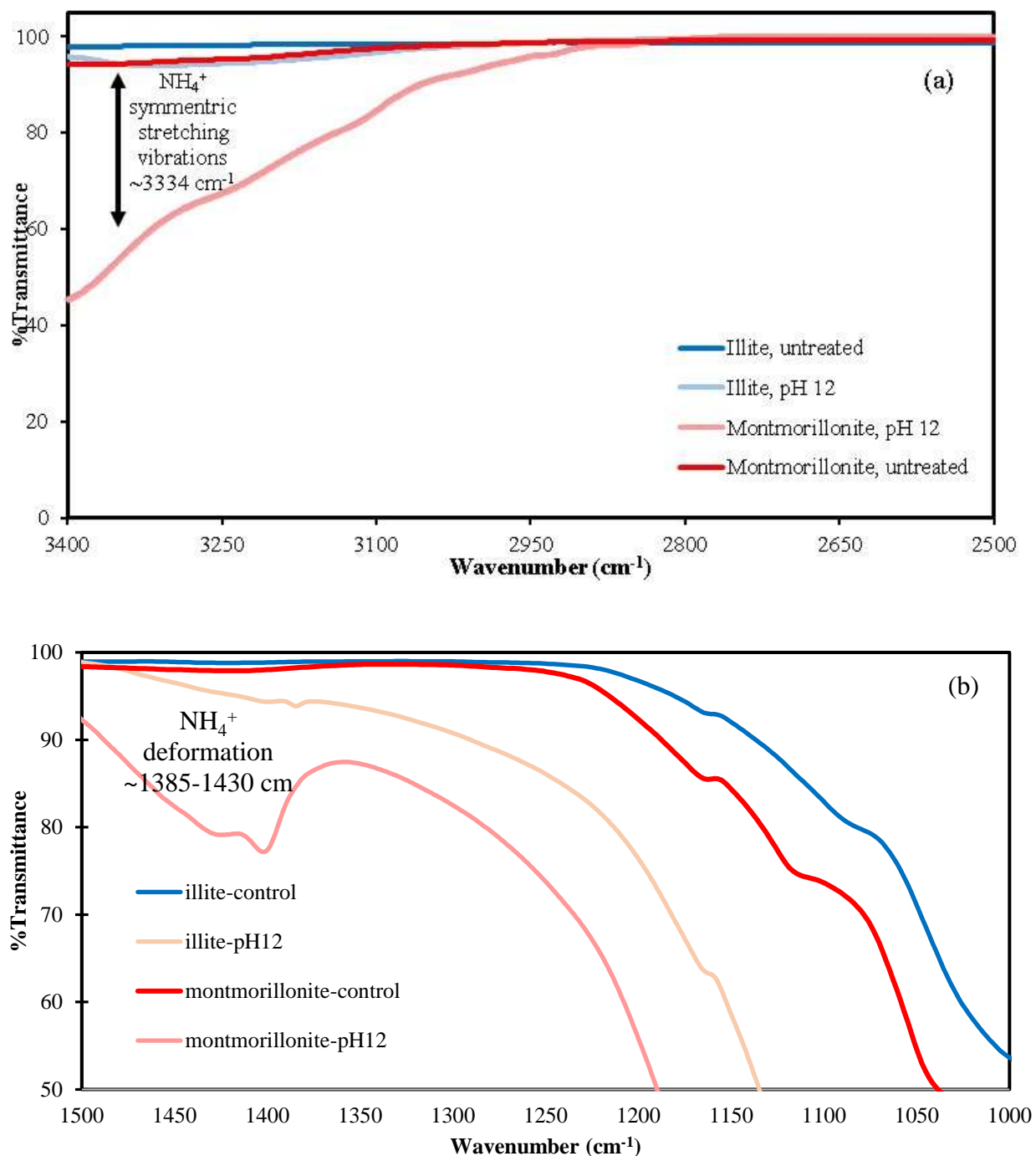


Figure 2. (a) Infrared spectra of aluminosilicate minerals (illite-blue and montmorillonite-red) showing the effect of ammonia intercalation at $\sim 3334 \text{ cm}^{-1}$ symmetric stretching vibration of N-H groups at $\sim 3334 \text{ cm}^{-1}$; (b) Infrared spectra of aluminosilicate minerals (illite-blue and montmorillonite-red) showing the bending vibration of N-H groups at $\sim 1440 \text{ cm}^{-1}$ prior to 95% N_2 /5% NH_3 gas treatment (control, darker) and post treatment (lighter) for 30-day contact time in SGW solution (7.2 mM) at pH 12.

Lastly, insight into micro-structural alterations can also be supported with particle size and surface area analysis. Figure 3 includes micrographs which depict morphology changes of the measured particles by SEM following NH₃ gas and aeration treatments at zoom magnification 1000x. For the untreated illite, SEM micrographs (Figure 3a) appear as mostly plate-like (i.e., common feature of phyllosilicate minerals), irregular particles with sizes ranging from approximately 0.5 to 15 μm. After ammonia treatment (Figure 3b), SEM micrographs reflect agglomeration of smaller particles. For the aerated samples (Figure 3c), SEM micrographs show particles occur mostly in clusters slightly larger than following only ammonia treatment. The particle range for ammonia (pH 12) and aerated (pH 8) treatments ranges from 9.1 – 21.9 μm and 15.1 – 24.9 μm, respectively. In order to corroborate that the particle size is different between both treatments, two-factor replication statistical analysis was conducted for particle sizes estimated at 1000x magnification. Table 3 below shows the calculated average particle size (in μm) for 33 data points and *p*-value for the *Between-Subjects-Effects* test. Because the *p*-value is ≤ 0.05 (*p*=0.0003), it was concluded that there is a statistically significant difference between ammonia (pH 12) and aerated (pH 8) treatments.

For all investigated phyllosilicate minerals, montmorillonite shows a significant effect upon NH₃ gas injection in its interlayer as demonstrated by FTIR analysis. However, illite shows a physical alternation given by its decreased particle size and morphology upon aeration treatment.

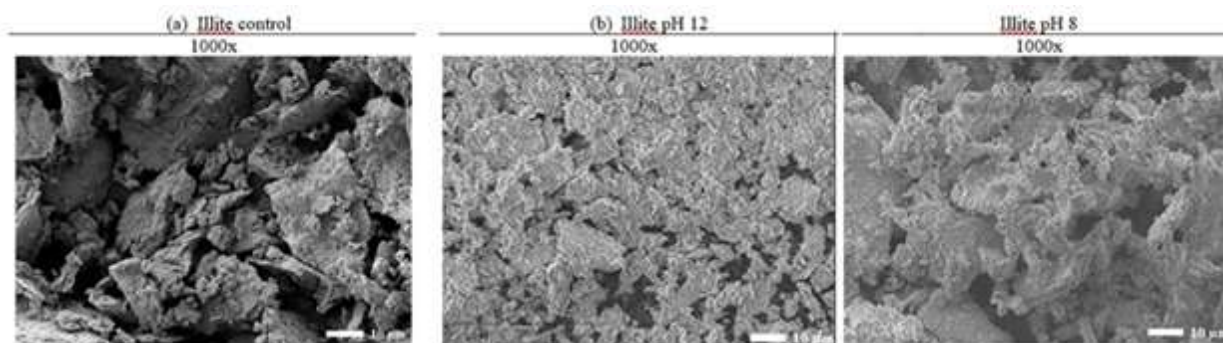


Figure 3. SEM images of (a) untreated illite mineral taken in backscatter mode, (b) illite treated with 95% N₂/5% NH₃ gas treatment at pH 12, and (c) post treatment in secondary mode for 30-day contact time in SGW solution (7.2 mM).

Table 3. Descriptive Statistics (ANOVA: two-factor with replication) and particle size measurements of illite ammonia- and aerated- treated samples taken from magnification 1000x SEM images

pH - Treatment	Average Particle Size (μm)	Data Points	Significance <i>p</i> value ^a (≤ 0.05)
12 - Ammonia	15.0 ± 4.9	n = 33	0.0003
8 - Aerated	18.4 ± 3.0	n = 33	

^a ‘Tests of Between-Subjects Effects’ with significant *p* ≤ 0.05

Subtask 1.1: Conclusions

This unique study considered series of phyllosilicate clay minerals treated with ammonia gas during a one-month contact time period with subsequent aeration treatment for the first time.

Results showed significant dissolution and physicochemical alternation occur upon exposure to highly alkaline (pH > 11) gas treatment. It is important to note that significant incongruent dissolution phenomena was evidenced as solid phase characterization data presents. Currently the experimental work presented in this report is part of a larger draft manuscript effort to be published in the journal of *Geochimica et Cosmochimica Acta*. Future work should focus on identification of secondary minerals by using thermodynamic predictions and determination of their ability to incorporate contaminants.

Subtask 1.1: References

- Baeyens, B., & Bradbury, M. H. (2004). Cation exchange capacity measurements on illite using the sodium and cesium isotope dilution technique: effects of the index cation, electrolyte concentration and competition: modeling. *Clays and Clay Minerals*, 52(4), 421–431.
- Barnes, M. C., Addai-Mensah, J., & Gerson, A. R. (1999). The solubility of sodalite and cancrinite in synthetic spent Bayer liquor. *Colloids and Surfaces A: Physicochemical and Engineering Aspects*, 157(1–3), 101–116.
- Barton, C. D. (2002). Clay minerals. In: *Rattan Lal, Comp., Ed. Encyclopedia of Soil Science*. New York, New York: Marcel Dekker: 187-192.
- Bauluz, B., Peacor, D. R., & Ylagan, R. F. (2002). Transmission electron microscopy study of smectite illitization during hydrothermal alteration of a rhyolitic hyaloclastite from Ponza, Italy. *Clays and Clay Minerals*, 50(2), 157–173.
- Belviso, C., Cavalcante, F., Niceforo, G., & Lettino, A. (2017). Sodalite, faujasite and A-type zeolite from 2: 1 dioctahedral and 2: 1: 1 trioctahedral clay minerals. A singular review of synthesis methods through laboratory trials at a low incubation temperature. *Powder Technology*, 320, 483–497.
- Boggs, M. A., Dai, Z., Kersting, A. B., & Zavarin, M. (2015). Plutonium (IV) sorption to montmorillonite in the presence of organic matter. *Journal of Environmental Radioactivity*, 141, 90–96.
- Buck, E. C., & McNamara, B. K. (2004). Precipitation of Nitrate– Cancrinite in Hanford Tank Sludge. *Environmental Science & Technology*, 38(16), 4432–4438.
- Chen, S., Guan, D., Zhang, Y., Wang, Z., & Jiang, N. (2019). Composition and kinetic study on template- and solvent-free synthesis of ZSM-5 using leached illite clay. *Microporous and Mesoporous Materials*, 285, 170–177.
- Chiou, C. T., & Rutherford, D. W. (1997). Effects of exchanged cation and layer charge on the sorption of water and EGME vapors on montmorillonite clays. *Clays and Clay Minerals*, 45(6), 867–880.
- Dağ, S. E., Bozkurt, P. A., Eroğlu, F., & Çelik, M. (2019). Preparation, characterization, and properties of polystyrene/Na-montmorillonite composites. *Journal of Thermoplastic Composite Materials*, 32(8), 1078–1091.
- Doye, I., & Duchesne, J. (2003). Neutralisation of acid mine drainage with alkaline industrial residues: laboratory investigation using batch-leaching tests. *Applied Geochemistry*, 18(8), 1197–1213.

- El Hafid, K., & Hajjaji, M. (2015). Effects of the experimental factors on the microstructure and the properties of cured alkali-activated heated clay. *Applied Clay Science*, *116*, 202–210.
- Emerson, H. P., Di Pietro, S., Katsenovich, Y., & Szecsody, J. (2017). Effects of ammonium on uranium partitioning and kaolinite mineral dissolution. *Journal of Environmental Radioactivity*, *167*.
- Emerson, H. P., Di Pietro, S., Katsenovich, Y., & Szecsody, J. (2018). Potential for U sequestration with select minerals and sediments via base treatment. *Journal of Environmental Management*, *223*.
- Fernández, R., Ruiz, A. I., & Cuevas, J. (2014). The role of smectite composition on the hyperalkaline alteration of bentonite. *Applied Clay Science*, *95*, 83–94.
- Kang, S.-J., & Egashira, K. (1997). Modification of different grades of Korean natural zeolites for increasing cation exchange capacity. *Applied Clay Science*, *12*(1–2), 131–144.
- Katsenovich, Y. P., Cardona, C., Lapierre, R., Szecsody, J., & Lagos, L. E. (2016). The effect of Si and Al concentrations on the removal of U(VI) in the alkaline conditions created by NH₃ gas. *Applied Geochemistry*, *73*, 109–117.
- Katsenovich, Y. P., Cardona, C., Szecsody, J., Lagos, L. E., & Tang, W. (2018). Assessment of calcium addition on the removal of U(VI) in the alkaline conditions created by NH₃ gas. *Applied Geochemistry*, *92*, 94–103.
- Kim, S. H., Kim, H. S., Hwang, J. S., Choi, J. G., & Chong, P. J. (1994). In situ FTIR analysis for the thermal decompositions of trimethylgallium and trimethylgallium-ammonia adduct. *Chemistry of Materials*, *6*(3), 278–281.
- Laird, D. A. (1987). *Layer charge and crystalline swelling of expanding 2: 1 phyllosilicates*. University Microfilms International.
- Lumen Learning. (2019). *Silicate Minerals*.
<https://courses.lumenlearning.com/physicalgeology/chapter/2-4-silicate-minerals/>
- Marsh, A., Heath, A., Patureau, P., Evernden, M., & Walker, P. (2018). Alkali activation behaviour of un-calcined montmorillonite and illite clay minerals. In *Applied Clay Science* (Vol. 166, pp. 250–261).
- Mashal, K., Harsh, J. B., Flury, M., Felmy, A. R., & Zhao, H. (2004). Colloid formation in Hanford sediments reacted with simulated tank waste. *Environmental Science & Technology*, *38*(21), 5750–5756.
- Mason, C. F. V., Turney, W. R. J. R., Thomson, B. M., Lu, N., Longmire, P. A., & Chisholm-Brause, C. J. (1997). Carbonate Leaching of Uranium from Contaminated Soils. *Environmental Science & Technology*, *31*(10), 2707–2711.
- Nadeau, P. H. (1985). The physical dimensions of fundamental clay particles. *Clay Minerals*, *20*(4), 499–514.
- Navratilova, Z., Wojtowicz, P., Vaculikova, L., & Sugarkova, V. (2007). Sorption of alkylammonium cations on montmorillonite. *Acta Geodynamica et Geomaterialia*, *4*(3), 59.
- Nieto, Mellini, M., & Abad, I. (2010). The role of H₃O⁺ in the crystal structure of illite. *Clays and Clay Minerals*, *58*(2), 238–246.

- Petit, S., Righi, D., Madejová, J., & Decarreau, A. (1998). Layer charge estimation of smectites using infrared spectroscopy. *Clay Minerals*, 33(4), 579–591.
- Pironon, J., Pelletier, M., De Donato, P., & Mosser-Ruck, R. (2003). Characterization of smectite and illite by FTIR spectroscopy of interlayer NH₄⁺ cations. *Clay Minerals*, 38(2), 201–211.
- Qafoku, N. P., Ainsworth, C. C., Szecsody, J. E., & Qafoku, O. S. (2004). Transport-controlled kinetics of dissolution and precipitation in the sediments under alkaline and saline conditions. *Geochimica et Cosmochimica Acta*, 68(14), 2981–2995.
- Sawhney, B. L. (1972). Selective Sorption and Fixation of Cations by Clay Minerals: A Review. In *Clays and Clay Minerals* (Vol. 20). Pergamon Press.
- Szecsody, Bagwell, C., Mackley, R., & Hoyle, S. (2020). *Evaluation of Ammonia Discharge into PUREX Crib 216-A-37-1 and Nitrogen Species Fate in the Subsurface*.
- Szecsody, J. E., Krupka, K. M., Williams, M. D., Cantrell, K. J., Resch, C. T., & Fruchter, J. S. (1998). *Uranium mobility during in situ redox manipulation of the 100 areas of the hanford site*. Pacific Northwest National Lab.(PNNL), Richland, WA (United States).
- Szecsody, Truex, M. J., Zhong, L., Johnson, T. C., Qafoku, N. P., Williams, M. D., Greenwood, W. J., Wallin, E. L., Bargar, J. D., & Faurie, D. K. (2012). Geochemical and Geophysical Changes during Ammonia Gas Treatment of Vadose Zone Sediments for Uranium Remediation. *Vadose Zone Journal*, 11(4).
- Tro, N. J., Fridgen, T. D., Shaw, L., & Boikess, R. S. (2017). *Chemistry: A molecular approach*. Pearson Boston, MA.
- Truex, M. J., Demirkanli, D. I., Szecsody, J. E., Snyder, M. M., Moran, J. J., Nims, M. K., Lawter, A. R., Resch, C. T., Saunders, D. L., & Qafoku, N. P. (2017). *Contaminant Attenuation and Transport Characterization of 200-DV-1 Operable Unit Sediment Samples from Boreholes C9497, C9498, C9603, C9488, and C9513*. Pacific Northwest National Lab.(PNNL), Richland, WA (United States).
- Wan, J., Larsen, J. T., Tokunaga, T. K., & Zheng, Z. (2004). pH neutralization and zonation in alkaline-saline tank waste plumes. *Environmental Science & Technology*, 38(5), 1321–1329.
- Xiang, G., Ye, W., Yu, F., Wang, Y., & Fang, Y. (2019). Surface fractal dimension of bentonite affected by long-term corrosion in alkaline solution. *Applied Clay Science*, 175, 94–101. <http://www.sciencedirect.com/science/article/pii/S0169131719301358>
- Zhao, H., Deng, Y., Harsh, J. B., Flury, M., & Boyle, J. S. (2004). Alteration of kaolinite to cancrinite and sodalite by simulated Hanford tank waste and its impact on cesium retention. *Clays and Clay Minerals*, 52(1), 1–13.
- Zhen, R., Jiang, Y. S., Li, F. F., & Xue, B. (2017). A study on the intercalation and exfoliation of illite. *Research on Chemical Intermediates*, 43(2), 679–692. <https://doi.org/10.1007/s11164-016-2645-1>
- Zhong, L., Szecsody, J. E., Truex, M. J., Williams, M. D., & Liu, Y. (2015). Ammonia gas transport and reactions in unsaturated sediments: Implications for use as an amendment to immobilize inorganic contaminants. *Journal of Hazardous Materials*, 289, 118–129.

Subtask 1.2: Re-oxidation of Redox Sensitive Contaminants Immobilized by Strong Reductants (NEW)

Subtask 1.2: Introduction

Technetium-99 (^{99}Tc) management is a high-priority activity for the EM complex due to its high aqueous solubility, toxicity and environmental mobility. Approximately 700 Ci of ^{99}Tc have been released to the Hanford subsurface and its remediation is challenging due to the variability of waste chemistries and heterogeneity of the deep vadose zone. For example, a perched water zone located beneath 200-DV-1 Operable Unit at Hanford contains ^{99}Tc as pertechnetate ($\text{Tc}^{\text{VII}}\text{O}_4^-$) that can potentially migrate to the underlying aquifer. Reducing conditions without or with sulfides may temporarily immobilize ^{99}Tc as one or more Tc^{IV} precipitates. However, previous research has shown that ^{99}Tc as pertechnetate that has been reduced to $\text{Tc}^{\text{IV}}\text{O}_2$ will quickly re-oxidize (remobilize) and TcS_x precipitates will slowly reoxidize (Lukens, Bucher et al. 2005). Previous research has also shown that reduced Tc precipitates that have been coated with other low solubility precipitates can be effective for preventing Tc remobilization, so may be useful for remediation (Pearce, Serne et al. 2018). Finally, Tc can be incorporated into low solubility precipitates such as iron oxides (Boglaenko, Soltis et al. 2020) or tin oxides (Luksic, Riley et al. 2015), which may have application for ex-situ treatment. For this reason, there is a need for additional research under the specific conditions of subsurface remediation for the Hanford Site as other Tc species may form.

Recent bench scale evaluations provided insights on the pertechnetate process using strong reductants (Lawter, Garcia et al. 2018); however, this process was not evaluated for the remobilization of ^{99}Tc under aerobic conditions. Hence, this study investigated re-oxidation of ^{99}Tc to mimic field conditions where the groundwater and perched water zone will be slowly re-oxidized to naturally occurring conditions. Laboratory experiments evaluated re-oxidation behavior of ^{99}Tc initially reduced by strong reductants such as zero valent iron (ZVI, Hepure Technologies), sulfur modified iron (SMI-PS Inc), and calcium polysulfide (CPS) in batch scale experiments under sequential anaerobic conditions followed by aerobic conditions.

Sediment samples obtained from the Hanford Site Ringold Formation were sieved and the < 2 mm size fraction used in the batch experiments conducted in two phases: (phase 1) reduction of ^{99}Tc in the presence of strong reductants under anaerobic conditions; and (phase 2) re-oxidation of reduced ^{99}Tc under aerobic conditions. Two contacting solutions were used in these experiments: (1) a synthetic perched water solution amended with $10 \mu\text{g/L}$ (34 pCi/L) of ^{99}Tc and (2) a synthetic groundwater solution amended with $420 \mu\text{g/L}$ (122.3 pCi/L) of ^{99}Tc .

Subtask 1.2: Objectives

The objective of this subtask is to study re-oxidation kinetics of perched and groundwater contaminants, such as $^{99}\text{Tc(VII)}$ that have been initially reduced by strong reductants such as ZVI, SMI and CPS in batch-scale experiments under anaerobic initial conditions followed by aerobic conditions. Two types of samples will be evaluated in these experiments: a) ^{99}Tc only and b) ^{99}Tc comingled with uranium and nitrate. This report presents results on Tc reoxidation behavior when ^{99}Tc is present in the perched and groundwater solutions.

Subtask 1.2: Methodology

Sediment Sieving

Two clean 5-gallon sediment samples from Richland, WA, were collected by PNNL collaborators and sent to FIU ARC laboratory. Sediments were sieved to separate sediment fractions into sand, silt, and clay. Before sieving, sediments were air dried in an oven at 30°C for 48 hours. This was done to prevent clumping in the soil caused by moisture, which could affect the size distribution analysis. The whole soil was sieved through a 2mm sieve, in order to remove large sediment fractions. 100 g of the remaining sediment was subsequently hand sieved and each fraction weighed for the size distribution analysis. Three sieves (500, 63, 20 μ m) were used to separate the soil into four total fractions (sand, silt, and clay), and it was found that more than 75% of the soil was sand (<2 mm, >500 μ m).

After separation of the dried soil into three fractions, sand, silt and clay, each fraction was separately analyzed in duplicate using an X-ray powder diffraction (XRD) instrument. Possible species within the soil were determined by matching with the crystallography database (PDF). In preparation for batch experiments, the rest of the soil sample was sieved through a 2mm sieve to remove larger constituents.

Synthetic Simulant Preparation

A groundwater and perched water simulant were made to mimic various conditions for technetium re-oxidation experiments. 2.5 L of two simulants were prepared as artificial groundwater and synthetic perched water solutions. The simulants were prepared using different salt concentrations listed in Table 4, and diluted using nanopure water $\geq 18\text{m}\Omega$ purged with N₂ for 30 min. The solutions were then pH adjusted by hydrochloric acid (2 M and 1 M) to a pH of 8.2 and 7.8 to ± 0.1 for the artificial groundwater and synthetic perched water solutions, respectively. The pH electrode was calibrated before measuring using select buffers (pH: 4.01, 7.00, 10.01) with a 95% linear fit.

Table 4. Recipes for Prepared Simulants

Synthetic Perched Water Recipe (~pH 8.2)		
Chemical	mmol/L	g/L
NaHCO ₃	10.708	0.900
KHCO ₃	0.310	0.031
MgSO ₄	2.703	0.325
CaSO ₄ •2H ₂ O	0.561	0.097
Na ₂ SO ₄	1.744	0.248
NaCl	3.301	0.193
Artificial Ground Water Recipe (~pH 7.8)		
Chemical	mmol/L	g/L
NaHCO ₃	1.586	0.133

KHCO ₃	0.123	0.012
MgSO ₄	0.366	0.090
MgCl ₂ •6H ₂ O	0.247	0.050
CaCl ₂ •2H ₂ O	1.071	0.157
NaHCO ₃	1.586	0.133

A fresh Tc stock was prepared and independently checked for accuracy using a Liquid Scintillation Counter (LSC). The stock had a calculated concentration of 4.217 mM of ⁹⁹Tc, and 59.9μL and 2.515mL of the stock was added to the 2.5L of synthetic perched water and ground water, respectively. The resulting concentration of ⁹⁹Tc in the synthetic simulants was also checked using LSC and confirmed as 10.2 μg/L for the perched water and 427.5 μg/L for groundwater. The solutions were placed in anaerobic conditions in a glovebox for 72 hours to prepare for contact with the reductants and sieved sediment.

Sample Preparation

10g of soil was weighed for each sample with a ±0.01g to achieve a 1:10 solid to liquid (100mL) ratio to be used in the experiment. Each of the tested reductants was weighed to prepare for batch experiments, within ±0.001 (Hepure zero valant iron(ZVI) (0.1%, 1%), Calcium polysulfide (0.5%, 5%), and Sulfide modified zero valent iron (0.1%, 1%)). Each sample for the specific reductant evaluated at a high and low concentration was prepared in triplicate. Bottles with weighed soil and separate reductants were kept in an anaerobic glovebox for 48 hours before contacting with the synthetic groundwater and perched water solutions amended with ⁹⁹Tc.

After batches amended with the reductants were contacted with the synthetic groundwater and perched water solutions amended with ⁹⁹Tc, at each sampling point 1mL of sample was taken and filtered through a 0.2μm syringe filter (PTFE, Fisher Scientific). Filtered samples were stored in a refrigerator in a tightly capped tube at 5 °C, until later elemental analysis via UV-vis, ICP-MS and ICP-OES), cognizant of minimizing the total amount of volume removed from the solutions (<10%). Samples were kept inside the glovebox and sampled after 1 day, 2 days and 5 days (Phase 1). At each time point, the pH, dissolved oxygen concentration, and oxidation-reduction potential (ORP) were tracked. An ORP electrode was calibrated outside of the glovebox to maintain accuracy. Before the batches were taken out of anaerobic conditions, the dissolved oxygen (DO) was measured in each of the bottles. Solutions were then taken outside the glovebox into aerobic conditions, commencing Phase 2 of the experiment. In order to track possible re-oxidation reactions in the solution, specifically of ⁹⁹Tc, sampling was done after 1 day, 7 days, 14 days, and 30 days. After the samples were exposed to aerobic conditions, the same sampling procedure as before continued, including DO measurements. Samples were opened every day to introduce atmospheric oxygen to the experimental bottles.

After the concentration of ⁹⁹Tc was measured, the data was normalized by dividing over the average concentration of the respective control batches (containing soil but no reductant). Re-oxidation rates were approximated using a linear regression model with the following equation:

$$k_{reoxidation} = \ln\left(\frac{C_t}{C_0}\right) \quad (1)$$

Liquid Analysis (ICP-OES, ICP-MS, LSC)

A fresh batch of ^{99}Tc standards was created through serial dilution for ICP-MS ranging from 0.005 $\mu\text{g/L}$ to 25 $\mu\text{g/L}$ and measured to an R^2 of 1.00. Fe standards were also prepared through a 100 mg/L Fe stock solution to measure aqueous iron in the samples (0.5-500 $\mu\text{g/L}$). Filtered samples drawn throughout the experiment were used to prepare samples for ICP-MS analysis to quantify Tc removal and iron dissolution in samples containing ZVI. Each sample was diluted with fresh 2% nitric acid (HNO_3) solution at a 10x dilution and stored in a fridge until time of assay.

It was noted that in the samples of the batches containing 5% calcium polysulfide (CPS), there was a formation of precipitates when contacted to the HNO_3 ; while in the samples from the zero valent iron (ZVI), and sulfur modified iron (SMI), no precipitate was observed. Due to the precipitate formation, alternate methods analysis via a liquid scintillation counter (LSC) were considered to quantify Tc (VII) in the 5% CPS-amended samples. Sample preparation for LSC involved mixing of 200 μL of CPS-filtered sample with 10mL of ultima gold cocktail. Samples were analyzed for 30 minutes for GW (420 $\mu\text{g/L}$ ^{99}Tc) and for 6 hours for PW (10 $\mu\text{g/L}$ ^{99}Tc) in the LSC, and results will be compared with ones obtained from the ICP-MS where one of the polysulfide batches was measured (0.5% CPS in the ground water solution). It was noted that low weight percentages (0.5%) of CPS added to the perched water and groundwater samples did not exhibit the formation of precipitates when mixing with nitric acid and could be run via ICP-MS.

Solid analysis (XRD)

Dried sediment used in the fraction analysis, as well as the whole soil was characterized using XRD. Sediment was packed flat on to a sample holder and run for an hour via Bruker D2 PHASER, analyzing from a 2θ value of 10-90° with a 0.05° step size. Obtained X-ray diffraction patterns were compared to the International Centre for Diffraction Data's power diffraction file database (PDF).

One bottle from each batch was sacrificed to analyze the solids in the system at equilibrium (>30 days aerobic). Solids were allowed to settle, and supernatant was removed through decanting, and stored for possible later use. The remaining soil was moved to a 50mL vial and rinsed using nanopure water $\geq 18\text{m}\Omega$ and centrifuged at 4500 RPM for 15 minutes. After centrifuging, the supernatant was removed using a transfer pipette, and the remaining solids were dried in vacuum (25in mmHg) for 96 hours at 35°C. The dried solids were crushed and mixed using a pestle and mortar to attain a more homogeneous distribution of solids and minimize noise. Pristine Hepure ZVI and sulfur modified ZVI were also run for comparison. Each type of solid was run in triplicate to assure replicability and consistency.

Subtask 1.2: Results and Discussion

Sediment Sieving and Fraction Analysis

Most of the sediment in the Hanford soil was classified as sand. Table 5 depicts the results from the fraction analysis done. A coarser soil particle size seen in the Hanford soil, is expected to lead to less sediment suspension in the batch experiments. The clay fraction was the smallest fraction measured by a significant margin.

Table 5. Fraction Analysis of Hanford Soil

Fraction	Soil Weight (g)	Weight Percentage
2000µm-500µm (Sand)	7.52	7.5
500µm-63µm (Sand)	87.15	87.2
63µm-20µm (Silt)	4.06	4.1
<20µm (Clay)	1.22	1.2

Aqueous Removal of ⁹⁹Tc by different reductants

Under anaerobic conditions, reduction of ⁹⁹Tc occurred very quickly (Figure 4 and Figure 5). Before entering the aerobic phase of the experiments, all batches had less than 5% of technetium remaining as pertechnetate in the aqueous phase. This was expected, as there was a high reductant loading versus initial concentration of technetium. In the aerobic phase, different reductants led to varying reoxidation behavior of technetium.

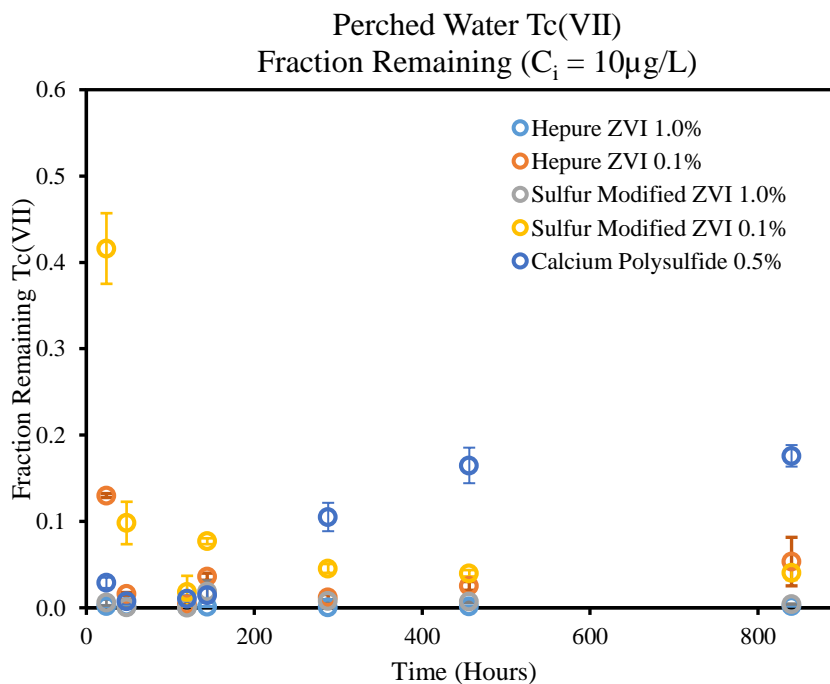


Figure 4. Reductive removal of technetium over time in aerobic and anaerobic conditions via different reductants.

Ground Water Tc(VII)
 Fraction Remaining ($C_i = 420 \mu\text{g/L}$)

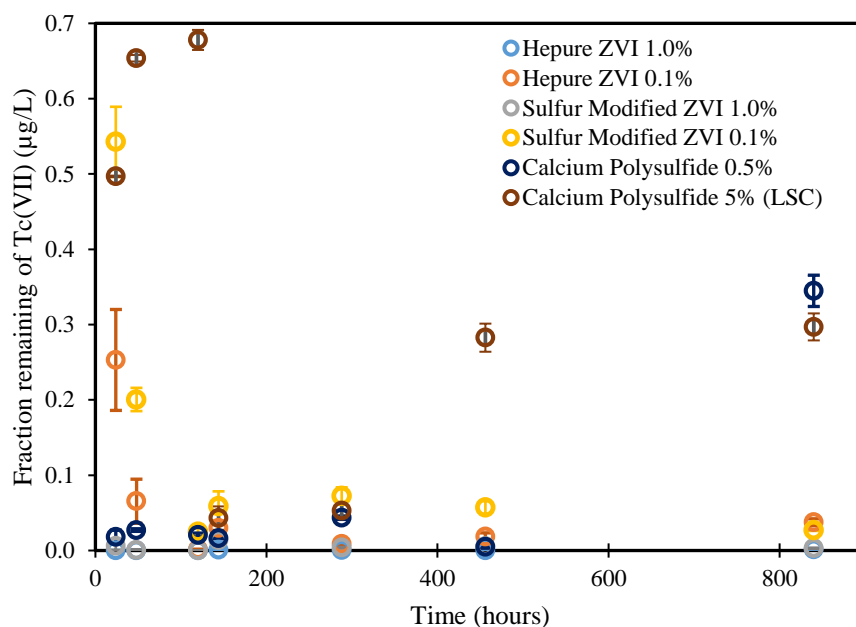


Figure 5. Reductive removal of technetium over time in aerobic and anaerobic conditions via different reductants.

The highest reoxidation was observed for 0.5% and 5% CPS for both perched and groundwater samples.

Analysis Via Liquid Scintillation Counter

Analysis was done via a liquid scintillation counter to avoid possible effects on measurements caused by precipitate formation in calcium polysulfide samples. Figure 6 shows the change over time of technetium reduction in samples containing polysulfide. Samples containing groundwater in 0.5% CPS gave consistent results between ICP-MS and LSC, validating results obtained with ICP-MS for low CPS concentrations. Comparing results between the two instruments gives confidence to the results measured using ICP-MS. Samples of the perched water simulant were close to the limit of detection of the instrument and were not used for this comparison.

LSC Measurements for CPS samples
Tc(VII) Fraction Remaining

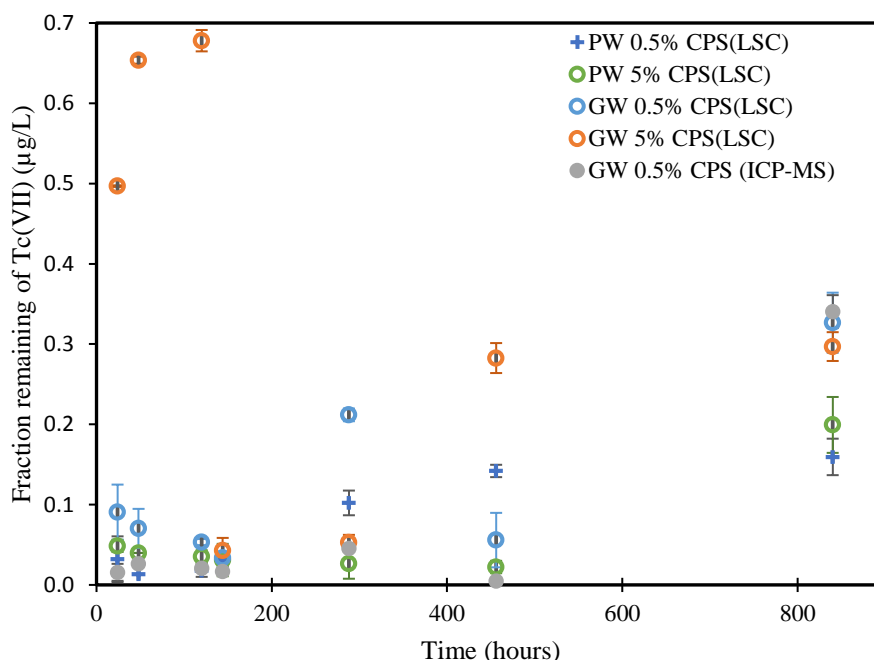


Figure 6. Technetium reduction and reoxidation behavior in calcium polysulfide samples using LSC. The results present data for 0.5% calcium polysulfide samples in the ground water simulant measured via ICP-MS.

Analysis of Dissolved Iron in Batch Experiments

In batches containing iron-based reductants, tracking the dissolved total iron over the span of the experiment provides insight into the effect that aqueous Fe(II) and Fe(III) have on the rates of reductions of ⁹⁹Tc in the prepared simulants. Results in Figure 7 and Figure 8 show higher aqueous iron concentrations in the anaerobic phase of the experiment. After entering the aerobic phase of the batch experiments, the aqueous iron concentration consistently decreases in all batches until it almost reaches zero µg/L by Day 30. Initially, the surface of the iron particles can easily oxidize and this oxide layer can passivate the surface of iron particles. Over time there is less metallic Fe⁰ that has not been oxidized, leading to a lower concentration of aqueous iron in the simulant solution.

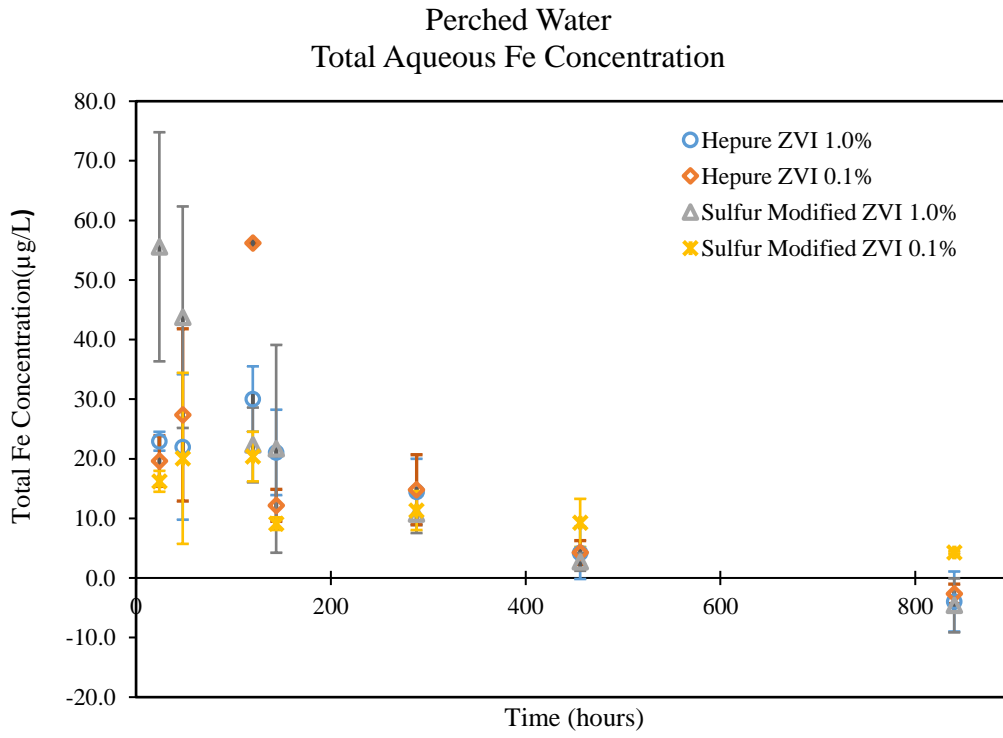


Figure 7. Measured total iron via ICP-MS for samples in perched water simulant.

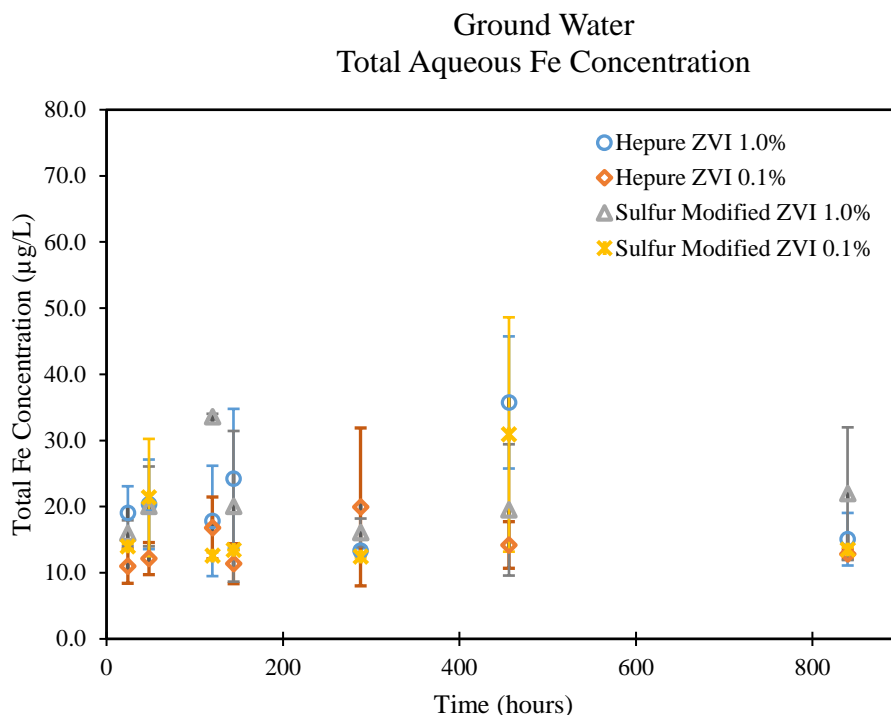


Figure 8. Measured total iron via ICP-MS for samples in ground water simulant.

Oxidation Reduction Potential

Measuring the oxidation-reduction potential (ORP) can provide information into the reductive/oxidative behavior of species in the system. As the amount of available aqueous iron decreases, the ORP in the samples increases leading to reoxidation of technetium from Tc(IV) to Tc(VII). Measurements in Figure 9 and Figure 10 show that 1% Hepure ZVI had the lowest ORP after being in aerobic conditions for 30 days, this is consistent with the lower ⁹⁹Tc reoxidation seen via ICP-MS measurements. On the other hand, ⁹⁹Tc in calcium polysulfide samples exhibited the highest reoxidation, which is consistent with the higher ORP measurements compared to other reductants.

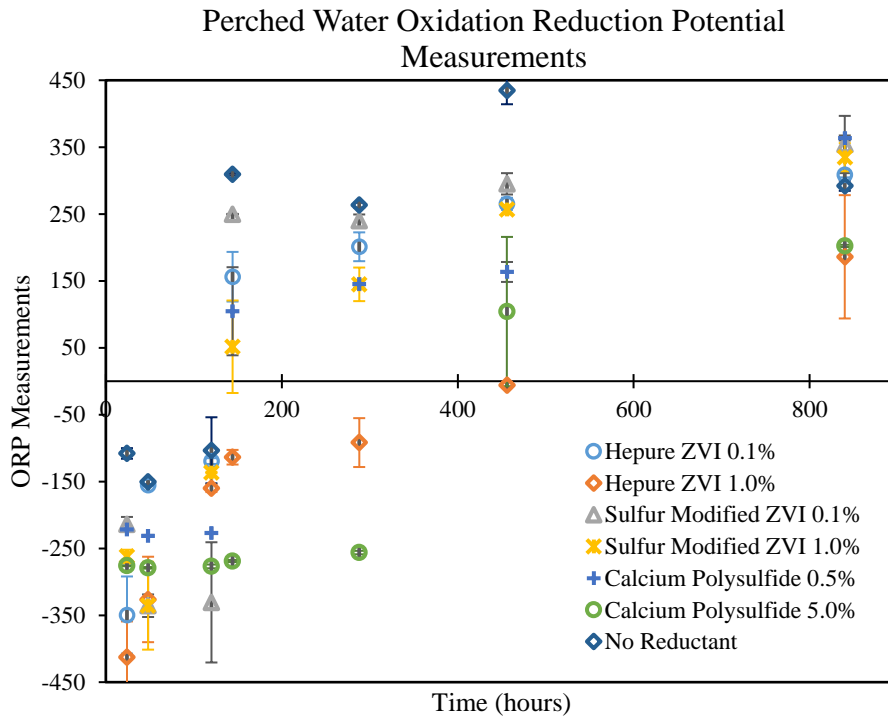


Figure 9. Measured oxidation reduction potential for batches containing perched water simulant.

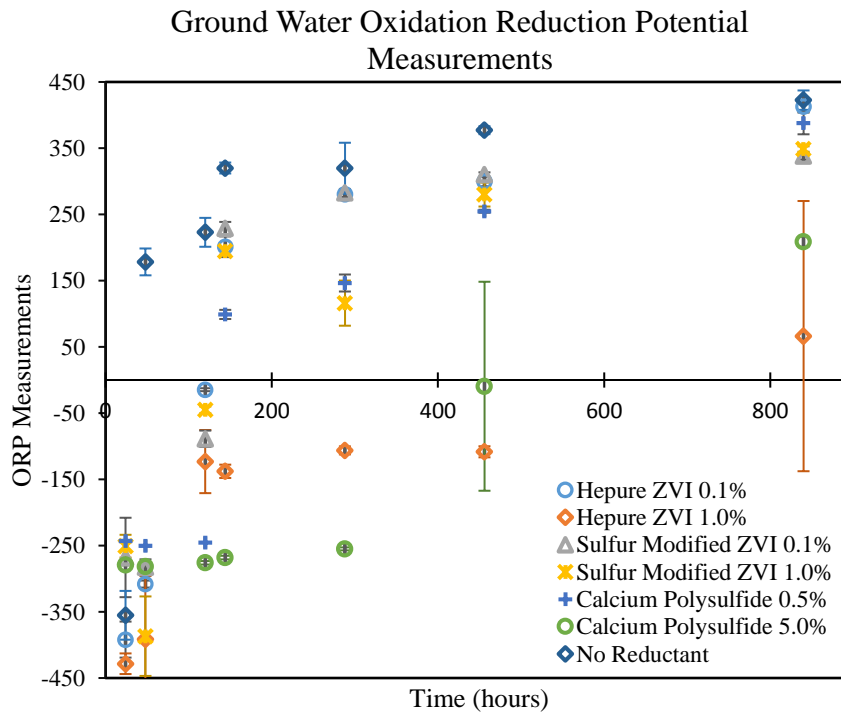


Figure 10. Measured oxidation reduction potential for batches containing ground water simulant.

Table 6 - Table 9 present changes in pH and ORP measurements over time.

Table 6. Phase 1 Perched Water Averages in the Anaerobic Conditions (~10ppb Tc, ~pH8.2)

		pH	ORP
Day 1	Control	8.139 ± 0.029	-108.0 ± 7.9
	0.1% Hepure ZVI	7.802 ± 0.027	-349.6 ± 57.7
	1.0% Hepure ZVI	8.041 ± 0.078	-412.7 ± 53.5
	0.1% SMI	7.915 ± 0.018	-213.9 ± 11.0
	1.0% SMI	7.701 ± 0.023	-261.9 ± 9.9
	0.5% CPS	8.186 ± 0.028	-221.5 ± 1.3
	5.0% CPS	9.501 ± 0.018	-276.0 ± 0.7
Day 2	Control	8.203 ± 0.022	-150.5 ± 4.3
	0.1% Hepure ZVI	7.971 ± 0.027	-155.3 ± 1.2
	1.0% Hepure ZVI	8.149 ± 0.021	-326.3 ± 63.9
	0.1% SMI	7.982 ± 0.023	-335.7 ± 16.9
	1.0% SMI	7.869 ± 0.017	-335.7 ± 65.7
	0.5% CPS	8.316 ± 0.013	-231.0 ± 1.2
	5.0% CPS	9.486 ± 0.014	-279.1 ± 1.2
Day 5	Control	8.165 ± 0.007	-103.3 ± 49.4
	0.1% Hepure ZVI	7.995 ± 0.011	-119.4 ± 4.3
	1.0% Hepure ZVI	8.241 ± 0.032	-159.9 ± 5.8
	0.1% SMI	7.951 ± 0.006	-330.7 ± 89.9
	1.0% SMI	8.003 ± 0.016	-136.6 ± 1.1
	0.5% CPS	8.336 ± 0.008	-227.0 ± 1.5
	5.0% CPS	9.480 ± 0.013	-276.9 ± 2.8

Table 7. Phase 2 Perched Water Averages in Aerobic Conditions (~10ppb Tc, ~pH8.2)

		pH	ORP
Day 1	Control	8.096 ± 0.005	309.6 ± 1.6
	0.1% Hepure ZVI	8.060 ± 0.024	156.2 ± 37.1
	1.0% Hepure ZVI	8.229 ± 0.063	-113.7 ± 10.9
	0.1% SMI	7.879 ± 0.006	249.8 ± 0.4
	1.0% SMI	7.870 ± 0.049	51.5 ± 69.2
	0.5% CPS	8.982 ± 0.155	104.6 ± 65.8
	5.0% CPS	9.974 ± 0.342	-268.8 ± 1.6
Day 7	Control	8.060 ± 0.013	263.3 ± 3.6
	0.1% Hepure ZVI	7.946 ± 0.041	201.0 ± 21.6
	1.0% Hepure ZVI	8.240 ± 0.122	-91.8 ± 36.6
	0.1% SMI	7.957 ± 0.034	239.9 ± 9.5
	1.0% SMI	7.568 ± 0.052	144.8 ± 25.1
	0.5% CPS	9.068 ± 0.026	145.4 ± 5.5
	5.0% CPS	10.207 ± 0.076	-256.2 ± 2.6
Day 14	Control	8.122 ± 0.012	434.8 ± 20.6
	0.1% Hepure ZVI	8.064 ± 0.021	265.3 ± 9.0
	1.0% Hepure ZVI	8.061 ± 0.100	-5.9 ± 4.3
	0.1% SMI	7.950 ± 0.011	295.1 ± 16.0
	1.0% SMI	7.453 ± 0.036	256.6 ± 7.0

Day 30	0.5% CPS	8.296	± 0.416	163.4	± 14.9
	5.0% CPS	9.909	± 0.167	104.1	± 111.6
	Control	8.231	± 0.019	292.3	± 7.6
	0.1% Hepure ZVI	8.143	± 0.022	308.9	± 4.1
	1.0% Hepure ZVI	8.058	± 0.046	186.0	± 92.2
	0.1% SMI	8.037	± 0.031	353.9	± 42.8
	1.0% SMI	7.476	± 0.013	334.9	± 21.1
	0.5% CPS	7.098	± 0.319	363.7	± 3.8
	5.0% CPS	9.602	± 0.086	202.3	± 1.7

Table 8. Phase 1 Ground Water Averages in Anaerobic Conditions (~420 ppb Tc, ~pH 7.8)

		pH		ORP	
Day 1	Control	8.156	± 0.060	-355.3	± 36.8
	0.1% Hepure ZVI	7.920	± 0.049	-392.0	± 27.2
	1.0% Hepure ZVI	7.945	± 0.036	-428.4	± 15.6
	0.1% SMI	8.002	± 0.008	-268.0	± 60.0
	1.0% SMI	7.591	± 0.033	-250.9	± 17.2
	0.5% CPS	9.460	± 0.035	-243.2	± 1.9
	5.0% CPS	10.016	± 0.021	-279.3	± 0.6
Day 2	Control	8.201	± 0.041	178.3	± 20.3
	0.1% Hepure ZVI	7.980	± 0.030	-308.1	± 5.3
	1.0% Hepure ZVI	8.186	± 0.037	-391.1	± 95.4
	0.1% SMI	8.046	± 0.029	-282.8	± 12.0
	1.0% SMI	7.699	± 0.068	-386.8	± 60.0
	0.5% CPS	9.439	± 0.016	-250.4	± 0.9
	5.0% CPS	10.004	± 0.012	-281.5	± 1.1
Day 5	Control	8.284	± 0.069	223.0	± 21.8
	0.1% Hepure ZVI	7.915	± 0.003	-14.7	± 2.2
	1.0% Hepure ZVI	8.437	± 0.005	-123.2	± 47.7
	0.1% SMI	8.082	± 0.012	-88.8	± 12.4
	1.0% SMI	7.852	± 0.004	-45.2	± 5.1
	0.5% CPS	9.369	± 0.013	-245.5	± 0.2
	5.0% CPS	10.000	± 0.007	-276.0	± 2.6

Table 9. Phase 2 Ground Water Averages in Aerobic Conditions (~420 ppb Tc, ~pH 7.8)

		pH		ORP	
Day 1	Control	8.161	± 0.051	320.1	± 8.3
	0.1% Hepure ZVI	8.422	± 0.044	201.2	± 15.6
	1.0% Hepure ZVI	8.472	± 0.010	-137.9	± 10.0
	0.1% SMI	8.028	± 0.047	229.1	± 9.5
	1.0% SMI	7.790	± 0.035	194.8	± 5.6
	0.5% CPS	9.412	± 0.027	99.0	± 6.9

Day 7	5.0% CPS	10.485 ± 0.013	-268.1 ± 2.7
	Control	7.740 ± 0.057	319.7 ± 38.6
	0.1% Hepure ZVI	8.036 ± 0.031	280.6 ± 5.1
	1.0% Hepure ZVI	8.137 ± 0.063	-106.3 ± 6.1
	0.1% SMI	7.755 ± 0.060	282.5 ± 5.9
	1.0% SMI	7.288 ± 0.026	116.0 ± 34.1
Day 14	0.5% CPS	9.452 ± 0.078	146.5 ± 12.8
	5.0% CPS	10.234 ± 0.019	-255.0 ± 2.3
	Control	7.745 ± 0.044	377.2 ± 6.0
	0.1% Hepure ZVI	8.039 ± 0.024	299.7 ± 7.2
	1.0% Hepure ZVI	8.008 ± 0.045	-108.4 ± 8.4
	0.1% SMI	7.682 ± 0.058	310.2 ± 3.3
Day 30	1.0% SMI	7.154 ± 0.033	280.0 ± 18.1
	0.5% CPS	8.980 ± 0.096	254.8 ± 2.2
	5.0% CPS	9.342 ± 0.214	-9.4 ± 157.8
	Control	7.793 ± 0.049	422.6 ± 14.6
	0.1% Hepure ZVI	7.855 ± 0.038	413.0 ± 9.3
	1.0% Hepure ZVI	7.823 ± 0.052	66.3 ± 204.0
	0.1% SMI	7.732 ± 0.021	338.0 ± 5.2
	1.0% SMI	7.235 ± 0.029	348.8 ± 4.1
	0.5% CPS	5.786 ± 0.299	388.2 ± 17.2
	5.0% CPS	9.428 ± 0.066	208.8 ± 7.5

Scanning Electron Microscope

Measurements from the scanning electron microscope (SEM) were used to evaluate the elemental composition in each of the dried solid samples. SEM provides an accurate assessment, which helps with mineralogical analysis using other methods like X-ray diffraction. The elemental composition showed an increase in iron content in samples amended with 0.1% and 1% ZVI and SMI compared to initial content on the level of 10-13 wt%, which might lead to the formation of iron oxide phases within sediment (Table 10). Low concentrations of TcO_4^- used in this study did not allow for Tc identification via EDS analysis.

Table 10. SEM-EDS Results for Artificial Ground Water Batches

Element	Calcium	Hepure ZVI		Sulfur Modified ZVI	
	Polysulfide 0.5%	0.1%	1.0%	0.1%	1.0%
B	11.78±5.3	10.94±5.0	6.91±6.3	8.50±7.72	5.22±4.19
Na	0.09±0.06	1.31±4.58	0.04±0.04	0.88±2.86	0.15±0.30
O	39.69±1.5	33.24±7.38	30.53±3.91	35.44±6.47	29.48±5.75
Mg	2.35±1.13	1.43±1.16	0.97±0.85	1.48±1.52	0.64±0.60
Al	4.11±1.15	2.37±1.58	2.02±1.39	2.90±1.76	2.20±1.93

Si	24.19±2.3	16.14±10.0	12.54±5.02	18.24±9.26	9.60±8.42
S	1.14±1.84	1.08±3.97	0.14±0.15	0.69±2.49	0.51±0.47
K	0.21±0.14	0.17±0.17	0.19±0.21	0.27±0.21	0.45±0.94
Ca	2.77±2.66	1.07±0.58	1.06±0.86	5.01±11.93	1.19±1.02
Ti	0.28±0.16	0.16±0.14	0.13±0.07	0.26±0.16	1.33±3.56
Cr	0.02±0.02	0.06±0.17	0.08±0.20	0.03±0.05	0.02±0.02
Fe	13.21±4.4	31.61±20.4	45.11±13.5	26.07±22.6	48.08±21.0
Mn	0.12±0.08	0.22±0.30	0.19±0.09	0.12±0.16	0.24±0.21
Ni	0.04±0.04	0.08±0.12	0.05±0.04	0.05±0.08	0.04±0.06

SEM-EDS images

SEM images of post-treated sediment samples are presented in Figure 11- Figure 13. SEM has not identified typical magnetite octahedral crystals in samples amended with ZVI and SMI. In Hepure ZVI treated samples, SEM spotted rounded crystals that could be associated with the formation of magnetite (Figure 11). SEM also spotted small crystals similar to goethite but smaller in size. The replacement of some Fe atoms in the crystal by other metals present in sediment including Al and Si can affect the formation of iron oxidation products and their structures (Cornell and Schwertmann, 2003).

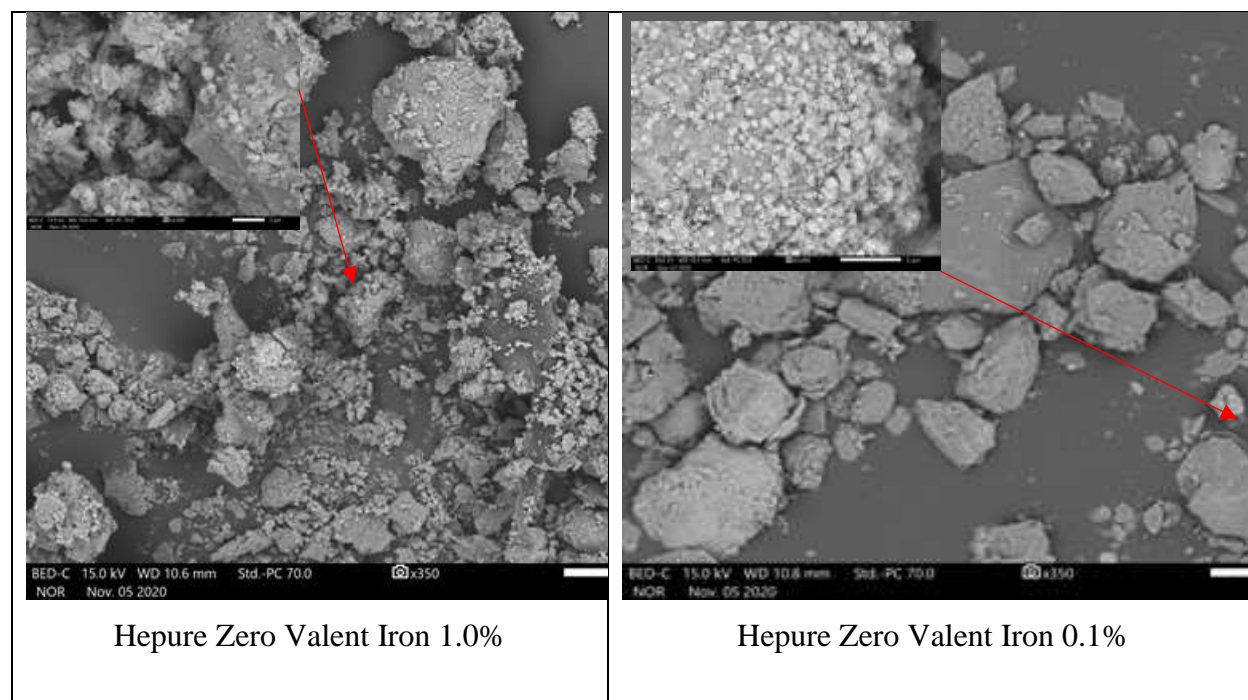


Figure 11. SEM-EDS images of Hepure ZVI treated sediment samples.

SEM spotted rounded crystals in sediment samples treated with SMI (Figure 12). These rounded crystals might be magnetite or globular goethite on quartz grains produced in the presence of sediment and synthetic GW solution (Cornell and Schwertmann, 2003).

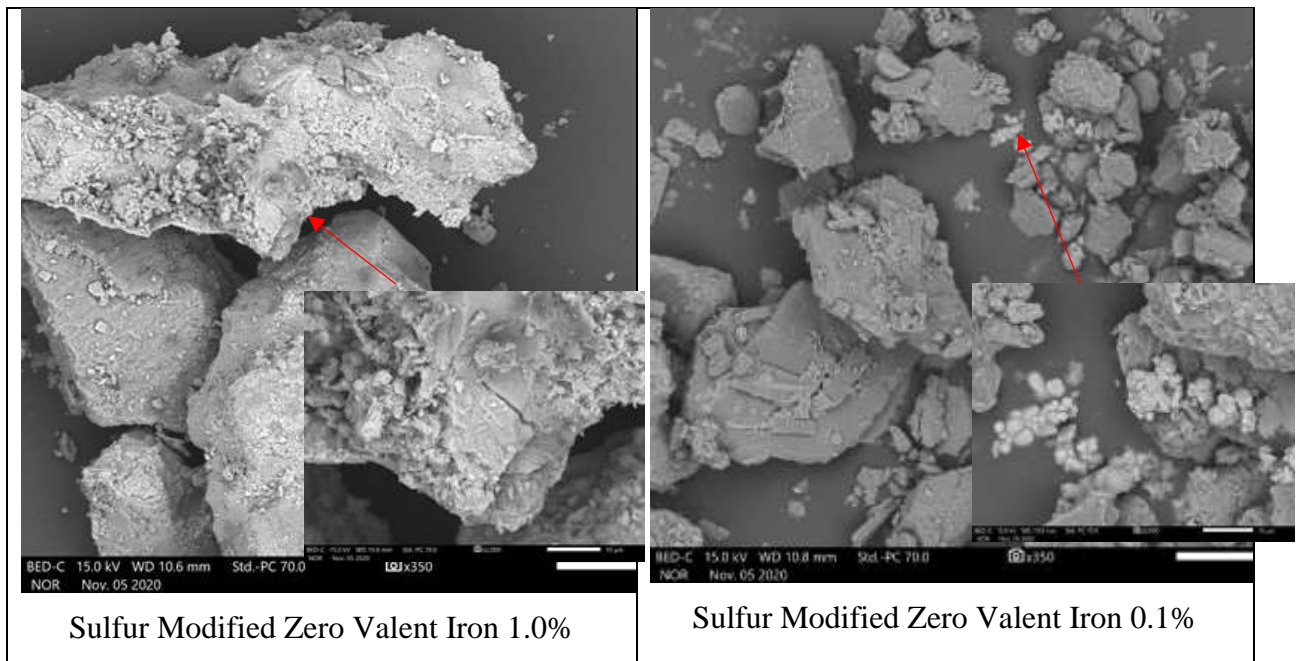


Figure 12. SEM-EDS images of sulfur modified ZVI treated sediment samples.

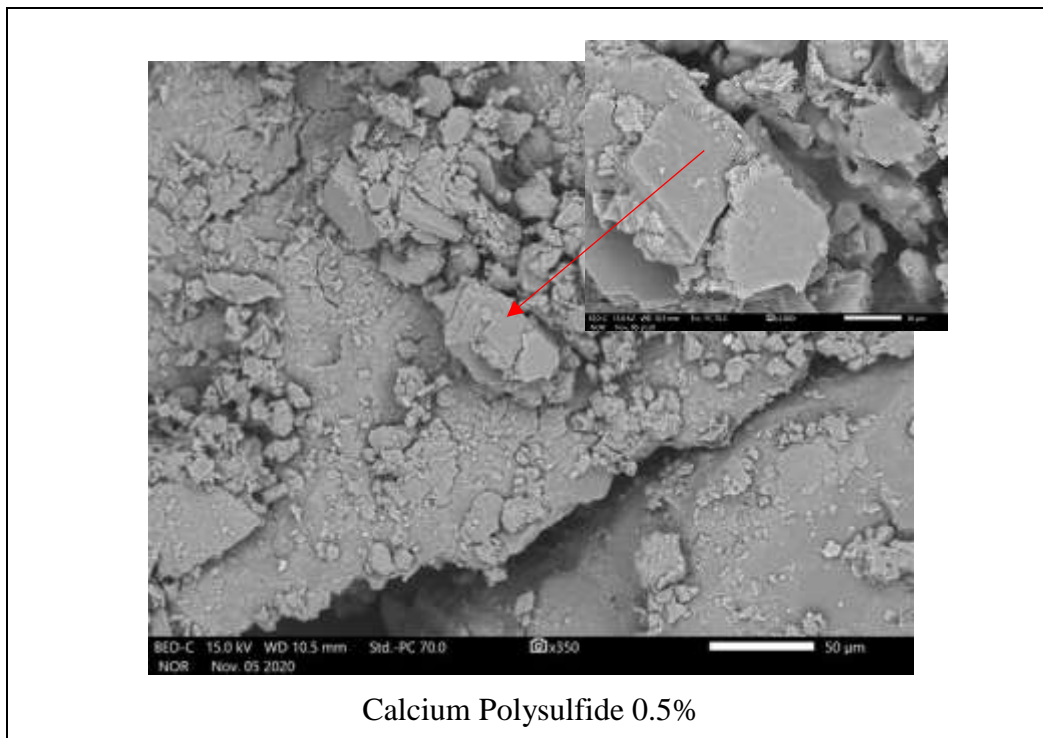


Figure 13. SEM-EDS images of calcium polysulfide treated sediment samples.

X-Ray Crystallography Analysis

Each of the solids samples was run in triplicate to assure replicability. Lack of homogeneity in the sieved sediment samples with size fraction < 2 mm caused inconsistent matches for the mineralogy of the obtained X-ray patterns (Figure 14). ZVI and SMI treated sediment samples didn't show presence of iron oxides phases like magnetite or goethite might be due relatively low weight percentage of ZVI and SMI in the sediment or potential incorporation of iron oxides to sediment's aluminosilicate minerals structures (

Table 11).

Artificial Ground Water Samples

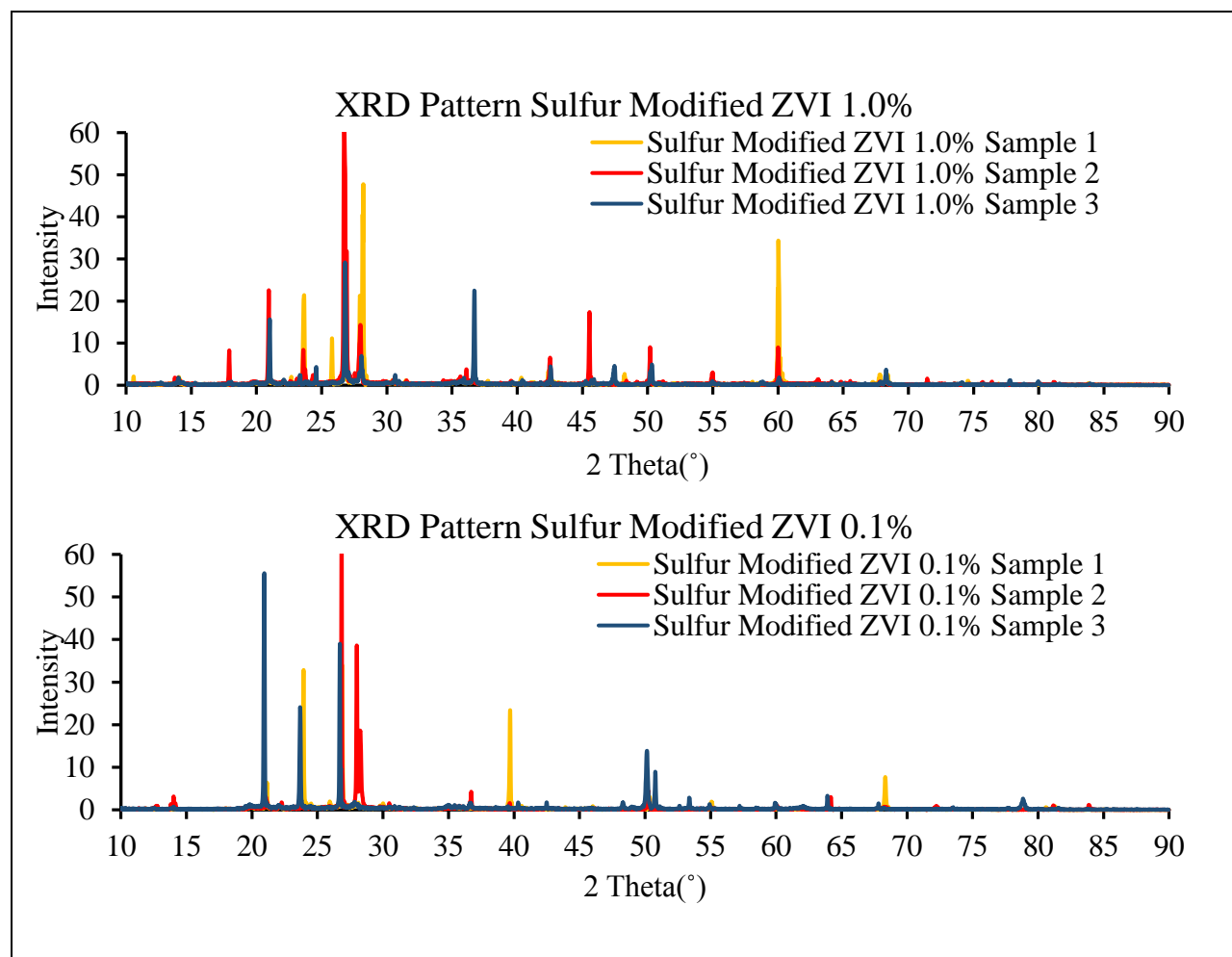


Figure 14. Sulfur modified ZVI, XRD patterns from triplicate samples in artificial ground water.

Table 11. Solid Phases Matched in 1% Sulfur Modified ZVI Treated Sediment in Artificial Ground Water

	Name	ID	Formula	Percentage
GW SMI 1% S1	Quartz, low	PDF 00-005-0490	SiO ₂	8.6
	Vermiculite	PDF 04-017-7292	Ca _{0.465} Mg _{2.810} Fe _{0.065} Al 1.190Si _{2.895} O ₁₀ (OH) ₂ (H ₂ O) ₄	1.6
	Anorthite, sodian	PDF 01-083-1371	Ca _{0.64} Na _{0.35} (Al _{1.63} Si _{2.37} O ₈)	89.8
GW SMI 1% S2	Quartz, syn	PDF 00-046-1045	SiO ₂	29.1

	Albite, ordered	PDF 00-009-0466	NaAlSi ₃ O ₈	28.7
	Polythionite-1M, ferroan	PDF 00-042-1399	K(AlFeLi)(Si ₃ Al)O ₁₀ (OH)F	9.4
	Albite, disordered	PDF 00-010-0393	Na(Si ₃ Al)O ₈	32.8
GW SMI 1% S3	Vermiculite	PDF 04-017-7292	Ca _{0.465} Mg _{2.810} Fe _{0.065} Al 1.190Si _{2.895} O ₁₀ (OH) ₂ (H ₂ O) ₄	2.8
	Quartz, syn	PDF 00-046-1045	SiO ₂	5.3
	Albite, calcian, ordered	PDF 00-041-1480	(Na,Ca)Al(Si,Al) ₃ O ₈	48.6
	Tooeleite	PDF 04-014-4569	Fe ₃ (AsO ₃) ₂ (SO ₄) _{0.5} (OH) ₂ (H ₂ O) ₂	10.4
	1,2-Ethandiolmethylether Silicon Oxide	PDF 00-044-0704	C ₃ H ₆ O ₂ ·6SiO ₂	32.9
GW SMI 0.1% S1	Tooeleite	PDF 04-014-4569	Fe ₃ (AsO ₃) ₂ (SO ₄) _{0.5} (OH) ₂ (H ₂ O) ₂	9.2
	Nontronite	PDF 00-058-2026	(Na,Ca) _{0.3} Fe ₂ (Si,Al) ₄ O ₁₀ (OH) ₂ ·xH ₂ O	84.7
	Vermiculite	PDF 04-013-2154	Mg _{2.68} Fe _{0.48} Al _{1.44} Si _{2.72} O ₁₀ (OH) ₂ (H ₂ O) _{4.32}	6.1
GW SMI 0.1% S2	Quartz, syn	PDF 00-046-1045	SiO ₂	10.8
	Albite, calcian, ordered	PDF 00-041-1480	(Na,Ca)Al(Si,Al) ₃ O ₈	65.1
	barium aluminosilicate Barium Aluminum Silicate	PDF 01-079-9793	Ba ₃₆ (Si ₁₂ Al ₇ O ₃₈₄)	1.4
	Sanidine	PDF 01-087-0680	(K _{0.86} Na _{0.14})(AlSi ₃ O ₈)	17.5
	Petalite	PDF 00-014-0090	LiAlSi ₄ O ₁₀	5.2
GW SMI 0.1% S3	Albite, calcian, ordered	PDF 00-041-1480	(Na,Ca)Al(Si,Al) ₃ O ₈	41.1
	Silver tecto-aluminosilicate hydrate Silver Aluminum Silicate Hydrate	PDF 01-079-1884	Ag _{74.24} Si ₉₆ Al ₉₆ O ₃₈₄ (H ₂ O) _{78.72}	2.6
	Nontronite	PDF 00-058-2026	(Na,Ca) _{0.3} Fe ₂ (Si,Al) ₄ O ₁₀ (OH) ₂ ·xH ₂ O	53.4
	potassium tecto-aluminosilicate Potassium Aluminum Silicate	PDF 01-088-0193	K _{9.38} (Al ₉ Si ₂₇ O ₇₂)	3.0

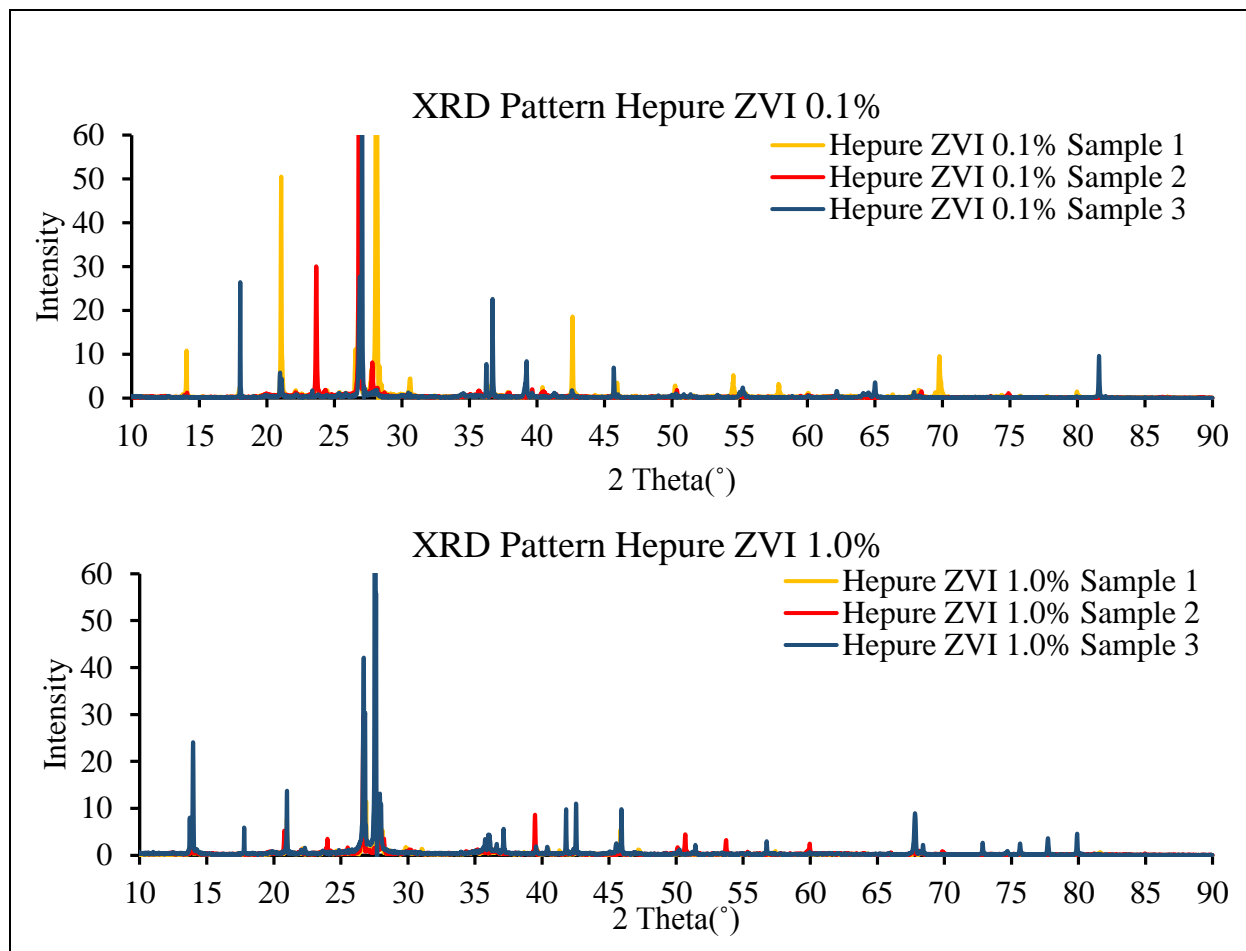


Figure 15. Hepure ZVI XRD patterns from triplicate samples in artificial ground water.

Table 12. Matched Solid Phases for 1% Hepure ZVI Treated Sediment in Artificial Ground Water

	Name	ID	Formula	Percentage
GW ZVI 1% S1	Quartz, syn	PDF 00-046-1045	SiO ₂	43.2
	Silver Aluminum Silicon Oxide	PDF 04-009-5238	Ag _{25.25} Al _{25.25} Si _{22.75} O ₉₆	1.2
	Tavagnascoite	PDF 04-023-2382	Bi ₄ (SO ₄)O ₄ (OH) ₂	8.8
	melilite, syn Barium Cobalt Magnesium Silicate	PDF 04-021-1001	Ba ₂ Mg _{0.7} Co _{0.3} Si ₂ O ₇	23.2
	Keatite, syn (NR)	PDF 01-077-3514	SiO ₂	23.6
GW ZVI 1% S2	Quartz, syn	PDF 00-046-1045	SiO ₂	36.7
	Traskite	PDF 04-012-1641	Ba ₂₄ CaTi ₁₂ Fe ₄ Si ₁₂ (Si ₂ O ₇) ₆ Cl ₆ O ₄₂ (OH) ₂₄ (H ₂ O) ₁₄	1.1
	Anorthite, ordered	PDF 00-041-1486	CaAl ₂ Si ₂ O ₈	43.6
	faujasite-K, syn Potassium Aluminum Silicate	PDF 00-026-0894	K _{48.2} Al _{148.2} Si _{143.8} O ₃₈₄	9.0
	Nosean	PDF 00-067-0038	Na ₈ Al ₆ Si ₆ O ₂₄ (SO ₄)	9.6
GW ZVI 1% S3	Quartz, syn	PDF 00-046-1045	SiO ₂	16.1

	Anorthoclase, disordered	PDF 00-009-0478	(Na,K)(Si ₃ Al)O ₈	37.9
	Illite-2M2, glycolated (NR)	PDF 00-058-2016	(K,H ₃ O)Al ₂ (Si ₃ Al)O ₁₀ (OH) ₂ ·xH ₂ O	46.0
GW ZVI 0.1% S1	Albite, calcian, ordered	PDF 00-041-1480	(Na,Ca)Al(Si,Al) ₃ O ₈	95.8
	Quartz, syn	PDF 00-046-1045	SiO ₂	4.2
GW ZVI 0.1% S2	Sodium Silver Aluminum Silicon Oxide	PDF 04-009-5237	NaAg _{20.5} Al _{21.5} Si _{26.5} O ₉₆	1.0
	Pretulite	PDF 00-051-1454	ScPO ₄	42.3
	potassium tecto- alumosilicate hydrate Potassium Aluminum Silicate	PDF 01-071-6200	K _{9.3} (Al _{9.3} Si _{26.7} O ₇₂)	2.1
	Albite, disordered	PDF 00-010-0393	Na(Si ₃ Al)O ₈	54.6
GW ZVI 0.1% S3	Lithium Magnesium Aluminum Iron Silicate Hydroxide	PDF 04-015-8489	Li _{0.31} Mg _{0.27} Fe _{0.23} Al _{11.6} Si _{3.9} O ₁₀ (OH) ₂	18.7
	Silver Aluminum Silicon Oxide	PDF 04-009-1982	Ag ₂₃ Al ₂₃ Si ₂₅ O ₉₆	0.4
	Masutomilite-1M, ferroan	PDF 00-064-0693	K(Li,Al,Mn,Fe) ₃ (Si,Al) ₄ O ₁₀ F ₂	80.0
	Traskite	PDF 04-012-1641	Ba ₂₄ CaTi ₁₂ Fe ₄ Si ₁₂ (Si ₂ O ₇) 6Cl ₆ O ₄₂ (OH) ₂₄ (H ₂ O) ₁₄	0.9

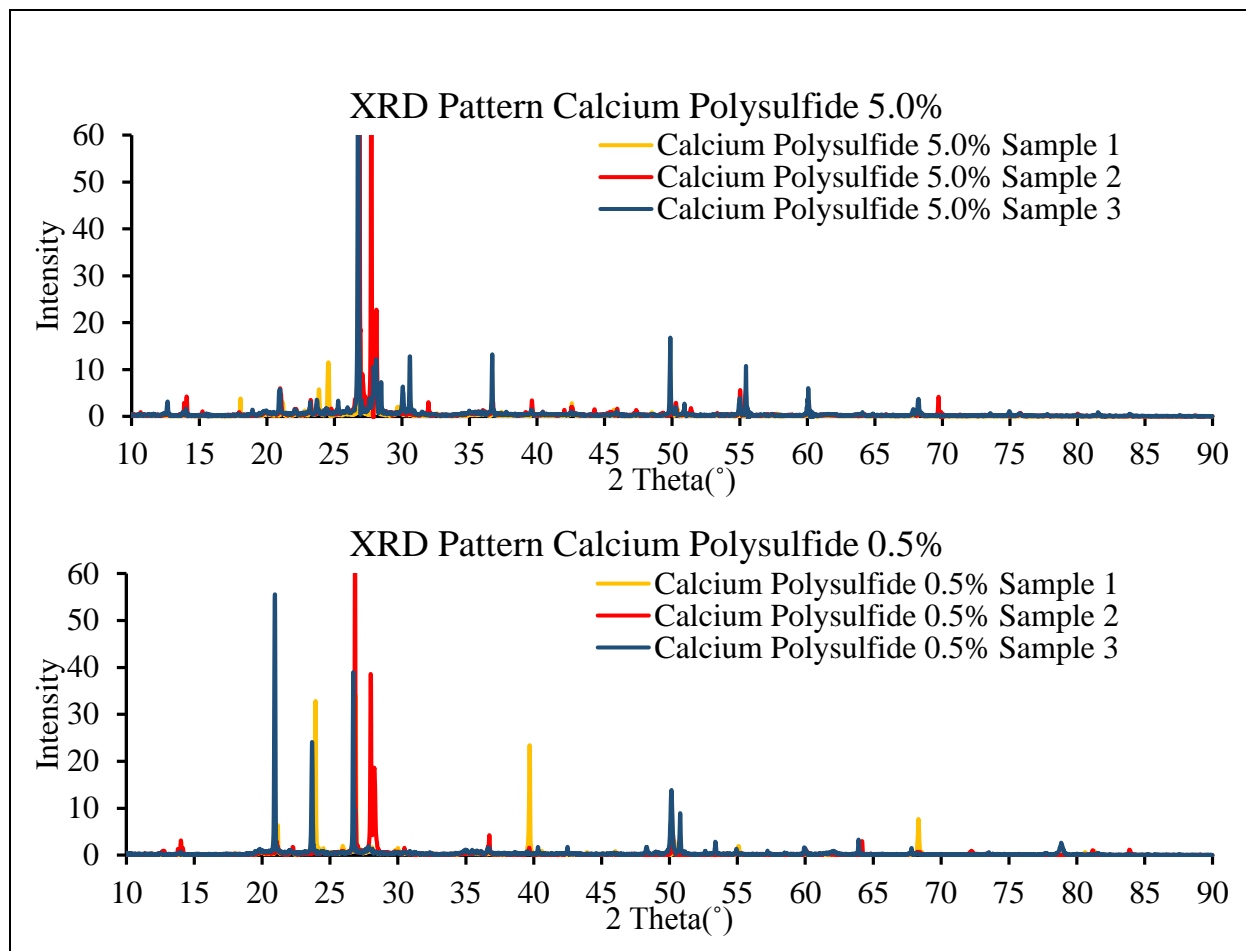


Figure 16. Calcium polysulfide XRD patterns from triplicate samples in artificial ground water.

Table 13. Solid Phases Identified in Sediment Treated with 5% Calcium Polysulfide in Artificial Groundwater

	Name	ID	Formula	Percentage
GW CPS 5% S1	silver tecto-alumosilicate hydrate Silver Aluminum Silicate Hydrate	PDF 01-079-1884	Ag _{74.24} Si ₉₆ Al ₁₉₆ O ₃₈₄ (H ₂ O) _{78.72}	3.7
	Lithium Magnesium Aluminum Iron Silicate Hydroxide	PDF 04-015-8489	Li _{0.31} Mg _{0.27} Fe _{0.23} Al _{11.6} Si _{3.9} O ₁₀ (OH) ₂	9.2
	Plombierite	PDF 04-012-0539	Ca _{2.5} Si ₃ O ₈ (OH)(H ₂ O) _{3.5}	9.7
	Kolskyite	PDF 04-020-1987	NaCa _{0.5} Ti ₂ (Si ₂ O ₇)O ₂ (H ₂ O) _{3.5}	5.0
	potassium tecto-alumosilicate hydrate Potassium Aluminum Silicate	PDF 01-071-6200	K _{9.3} (Al _{9.3} Si _{26.7} O ₇₂)	2.2
	Boulangerite	PDF 00-018-0688	Pb ₅ Sb ₄ S ₁₁	52.2
	Albite, calcian, ordered	PDF 00-041-1480	(Na,Ca)Al(Si,Al) ₃ O ₈	18.0
GW CPS 5% S2	Silver Aluminum Silicon Oxide	PDF 04-009-1982	Ag ₂₃ Al ₂₃ Si ₂₅ O ₉₆	0.8

	Albite, disordered	PDF 00-010-0393	Na(Si3Al)O8	88.2
	Quartz, syn	PDF 00-046-1045	SiO2	3.9
	Mitryaevaite	PDF 01-074-2741	(Al5(PO4)2((P0.74S0.26)O3(O0.76(OH)0.24)) 2F2(OH)2(H2O)8)(H2O)6.48	7.1
GW CPS 5% S3	Quartz, syn	PDF 00-046-1045	SiO2	12.6
	Albite, calcian, ordered	PDF 00-041-1480	(Na,Ca)Al(Si,Al)3O8	50.0
	Zaherite-16A	PDF 00-029-0088	Al12(SO4)5(OH)26	26.1
	calcium mica Calcium Aluminum Silicate	PDF 00-046-0744	Al3Ca0.5Si3O11	11.3
GW CPS 0.5% S1	Sodium Silver Aluminum Silicon Oxide	PDF 04-009-5237	NaAg20.5Al21.5Si26.5O96	2.1
	Albite, disordered	PDF 00-010-0393	Na(Si3Al)O8	80.7
	α-Si O2, quartz-alpha Fe-doped brown, syn Silicon Oxide	PDF 04-007-0522	SiO2	11.0
	Silicon Oxide	PDF 04-011-0544	SiO2	6.1
GW CPS 0.5% S2	Petalite	PDF 00-014-0090	LiAlSi4O10	56.4
	Silver Aluminum Silicon Oxide	PDF 04-009-1982	Ag23Al23Si25O96	1.8
	Sampleite	PDF 04-014-6019	NaCaCu5(PO4)4Cl(H2O)4.5	7.5
	leucite, syn Rubidium Aluminum Silicate	PDF 04-013-2100	RbAlSi2O6	34.3
GW CPS 0.5% S3	Quartz, syn	PDF 00-046-1045	SiO2	11.1
	Vermiculite	PDF 04-017-7291	Na0.930Mg2.810Fe0.065Al 1.185Si2.895O10(OH)2(H2O)3	1.4
	Ye`elimitite, syn	PDF 00-033-0256	Ca4Al6O12SO4	71.2
	Albite	PDF 04-007-5466	NaAlSi3O8	16.4

Synthetic Perched Water Samples

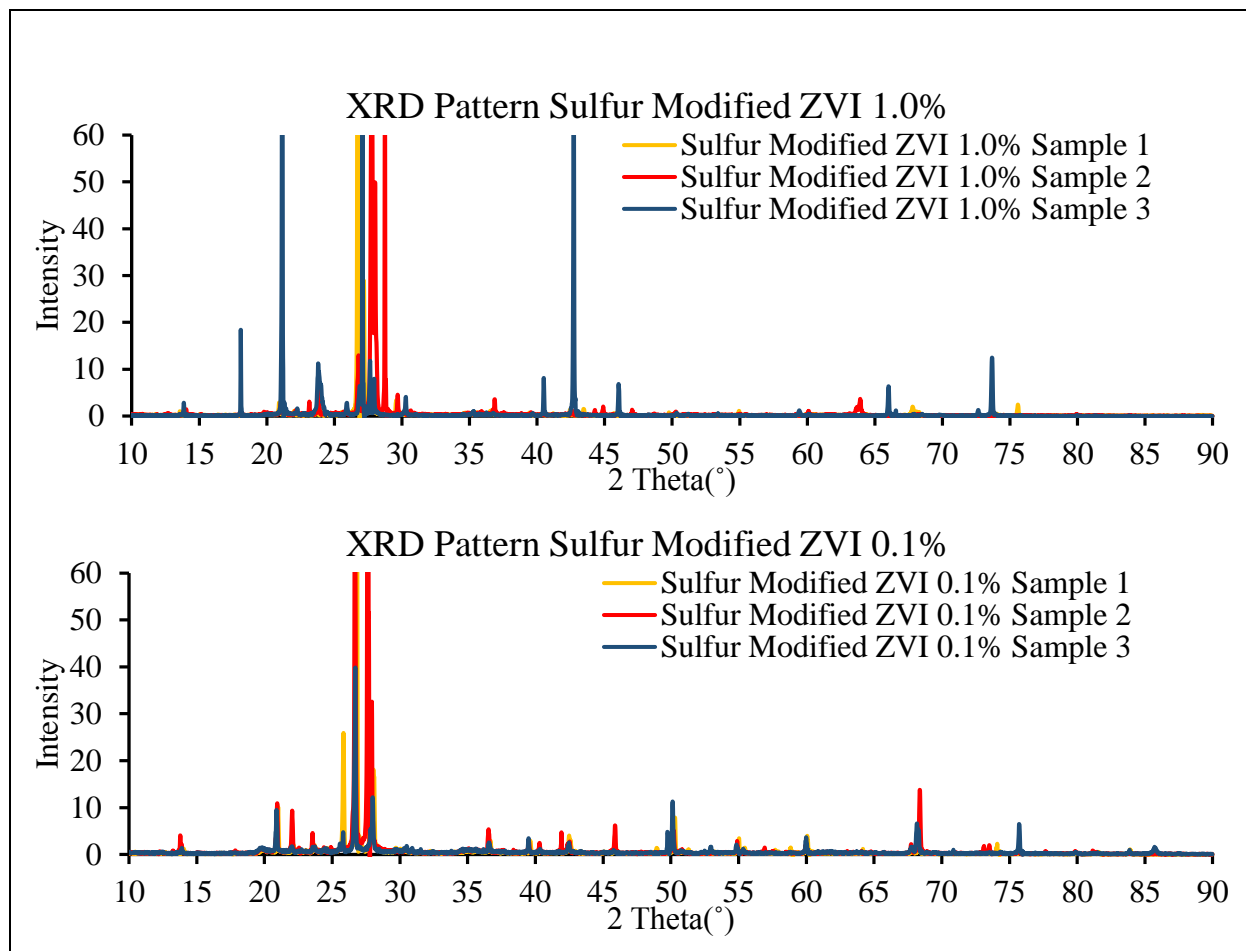


Figure 17. Sulfur modified ZVI XRD patterns from triplicate samples in synthetic perched water.

Table 14. Solid Phases for Identified in Sulfur Modified ZVI Treated sediment Samples prepared with Synthetic Perched Water

	Name	ID	Formula	Percentage
PW SMI 1% S1	Quartz, syn	PDF 00-046-1045	SiO ₂	41.6
	Vermiculite	PDF 04-017-7291	Na _{0.930} Mg _{2.810} Fe _{0.065} Al _{1.185} Si _{2.895} O ₁₀ (OH) ₂ (H ₂ O) ₃	1.6
	Albite	PDF 04-017-1022	Na _{0.98} Ca _{0.02} Al _{1.02} Si _{2.98} O ₈	56.8
PW SMI 1% S2	Vermiculite	PDF 04-013-2154	Mg _{2.68} Fe _{0.48} Al _{1.44} Si _{2.72} O ₁₀ (OH) ₂ (H ₂ O) _{4.32}	0.8
	Albite, disordered	PDF 00-010-0393	Na(Si ₃ Al)O ₈	77.4
	faujasite nickel m-dichlorobenzene Nickel Aluminum Silicate Hydrate	PDF 01-085-1352	Ni _{28.9} Si ₁₃₃ Al ₅₉ O ₃₈₄ (H ₂ O) ₂₄	0.7
	Bavenite	PDF 01-074-2068	Ca ₄ (Be _{2.5} Al _{1.5})(Si ₉ O _{25.5} (OH) _{0.5})(OH) ₂	21.1
PW SMI 1% S3	Petalite	PDF 00-014-0090	LiAlSi ₄ O ₁₀	17.1
	Pretulite	PDF 00-051-1454	ScPO ₄	71.9
	Anorthite, ordered	PDF 00-041-1486	CaAl ₂ Si ₂ O ₈	10.1

	Lithium Magnesium Aluminum Iron Silicate Hydroxide	PDF 04-015-8489	$\text{Li}_{0.31}\text{Mg}_{0.27}\text{Fe}_{0.23}\text{Al}_{1.6}\text{Si}_{3.9}\text{O}_{10}(\text{OH})_2$	0.9
PW SMI 0.1% S1	Quartz, syn	PDF 00-046-1045	SiO_2	7.4
	Albite, calcian, ordered	PDF 00-041-1480	$(\text{Na,Ca})\text{Al}(\text{Si,Al})_3\text{O}_8$	6.3
	Sodium Thallium Vanadium Uranium Oxide	PDF 00-059-0359	$\text{Na}_{0.25}\text{Tl}_{10.75}\text{VUO}_6$	54.0
	Nontronite	PDF 00-058-2026	$(\text{Na,Ca})_0.3\text{Fe}_2(\text{Si,Al})_4\text{O}_{10}(\text{OH})_2 \cdot x\text{H}_2\text{O}$	32.3
PW SMI 0.1% S2	Nontronite	PDF 00-058-2026	$(\text{Na,Ca})_0.3\text{Fe}_2(\text{Si,Al})_4\text{O}_{10}(\text{OH})_2 \cdot x\text{H}_2\text{O}$	36.8
	Vermiculite	PDF 04-017-7292	$\text{Ca}_{0.465}\text{Mg}_{2.810}\text{Fe}_{0.065}\text{Al}_{1.190}\text{Si}_{2.895}\text{O}_{10}(\text{OH})_2(\text{H}_2\text{O})_4$	2.6
	Albite, calcian, ordered	PDF 00-041-1480	$(\text{Na,Ca})\text{Al}(\text{Si,Al})_3\text{O}_8$	60.7
PW SMI 0.1% S3	Quartz, low	PDF 00-005-0490	SiO_2	30.0
	Albite, calcian	PDF 01-083-1939	$\text{Na}_{0.685}\text{Ca}_{0.347}\text{Al}_{1.46}\text{Si}_{2.54}\text{O}_8$	42.7
	Hotsonite	PDF 00-038-0366	$\text{Al}_{11}(\text{PO}_4)_2(\text{SO}_4)_3(\text{OH})_{21} \cdot 16\text{H}_2\text{O}$	7.5
	Zaherite-16A	PDF 00-029-0088	$\text{Al}_{12}(\text{SO}_4)_5(\text{OH})_{26}$	19.9

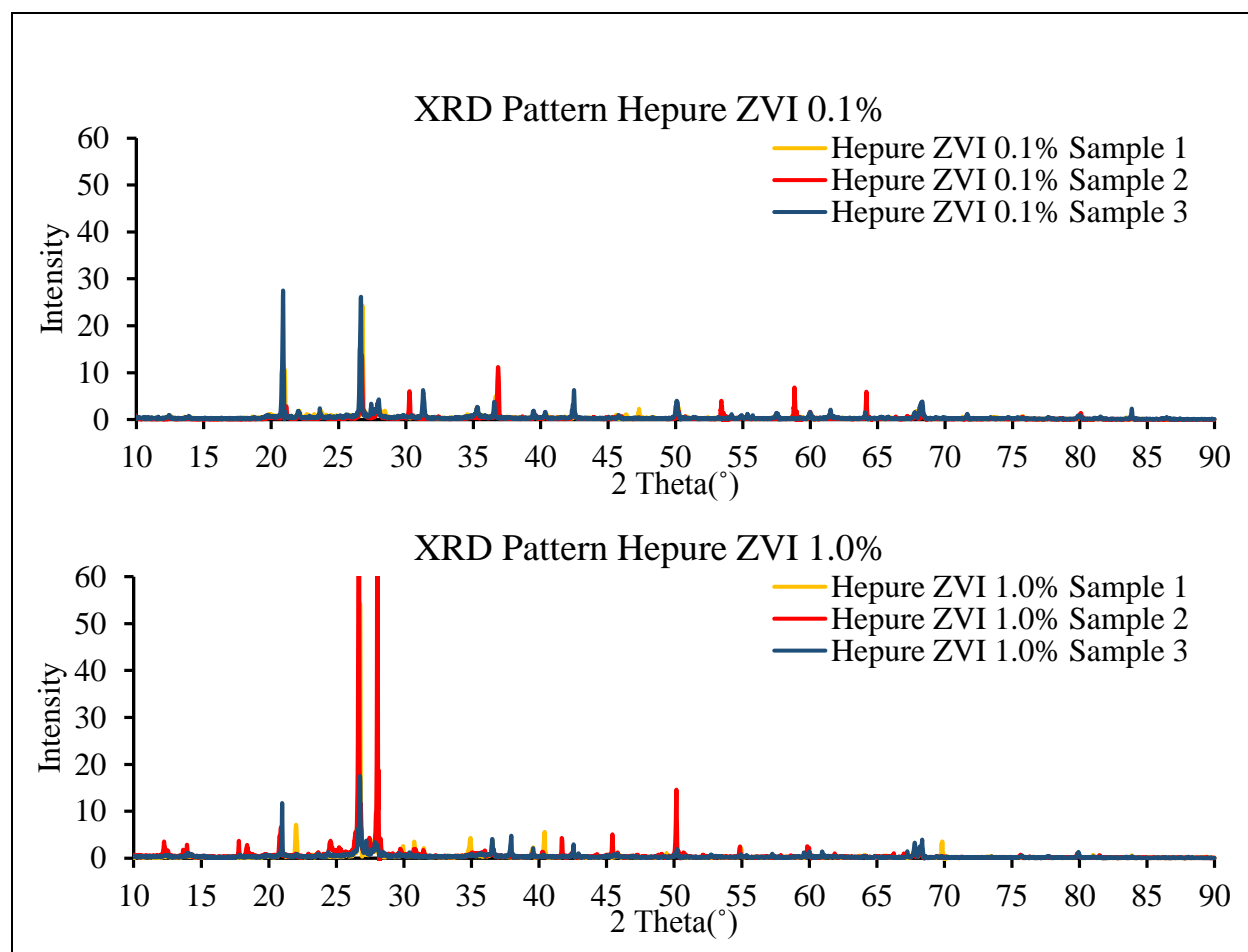


Figure 18. Hepure ZVI XRD patterns from triplicate samples in synthetic perchd water.

Table 15. Solid Phases for 1% Hepure ZVI Treated Sediment in Synthetic Perched Water

	Name	ID	Formula	Percentage
PW ZVI 1% S1	Quartz, syn	PDF 00-046-1045	SiO ₂	40.7
	Albite, high	PDF 01-083-2215	K _{0.2} Na _{0.8} AlSi ₃ O ₈	50.3
	Schorl, aluminian, magnesian	PDF 04-020-1421	Na _{0.7} Mg _{0.52} Mn _{0.05} Fe _{1.82} Al _{6.71} Si _{5.9} (BO ₃) ₃ O _{18.32} (OH) _{3.5} F _{0.18}	8.4
	Polythionite-1M, ferroan	PDF 00-042-1399	K(AlFeLi)(Si ₃ Al)O ₁₀ (OH)F	0.6
PW ZVI 1% S2	α-Si O ₂ , quartz-alpha Fe-doped brown, syn Silicon Oxide	PDF 04-007-0522	SiO ₂	47.8
	Muscovite-2M1	PDF 00-058-2035	KAl ₂ (Si,Al) ₄ O ₁₀ (OH) ₂	9.2
	Albite, calcian, ordered	PDF 00-041-1480	(Na,Ca)Al(Si,Al) ₃ O ₈	43.0
PW ZVI 1% S3	Quartz, syn	PDF 00-046-1045	SiO ₂	36.9
	Polythionite-1M, ferroan	PDF 00-042-1399	K(AlFeLi)(Si ₃ Al)O ₁₀ (OH)F	5.5
	Albite, calcian, ordered	PDF 00-020-0548	(Na,Ca)(Si,Al) ₄ O ₈	28.1
	calcium mica Calcium Aluminum Silicate	PDF 00-046-0744	Al ₃ Ca _{0.5} Si ₃ O ₁₁	29.4
PW ZVI 0.1% S1	Nontronite	PDF 00-058-2026	(Na,Ca) _{0.3} Fe ₂ (Si,Al) ₄ O ₁₀ (OH) ₂ ·xH ₂ O	37.1
	Anorthite, sodian	PDF 04-015-4238	Na _{0.5} Ca _{0.5} Al _{1.5} Si _{2.5} O ₈	23.8
	Silicon oxide hydroxide - tetramethylammonium hydroxide - water	PDF 01-076-7505	(Si ₁₆ O ₃₂ (OH) ₄)(((CH ₃) ₄ N)(OH)) _{3.8} (H ₂ O) _{10.88}	4.3
	Clinocllore, chromian	PDF 01-083-1381	Mg _{5.0} Al _{0.75} Cr _{0.25} Al _{1.00} Si _{3.00} O ₁₀ (OH) ₈	34.8
PW ZVI 0.1% S2	Quartz, syn	PDF 00-046-1045	SiO ₂	46.5
	Albite, calcian, ordered	PDF 00-041-1480	(Na,Ca)Al(Si,Al) ₃ O ₈	43.8
	Tschörtnerite	PDF 01-088-1228	Ca ₄ (Sr _{1.03} K _{0.65} Ba _{1.32})Cu ₃ (Si ₁₂ Al ₁₂ O ₄₈)(OH) ₈ (H ₂ O) _{20.465} Cl _{0.056}	8.6
	Strontium Aluminum Silicon Oxide	PDF 04-010-2037	Sr _{1.5} Al ₂₃ Si ₂₅ O ₉₆	1.1
PW ZVI 0.1% S3	Quartz, low	PDF 00-005-0490	SiO ₂	20.4
	Anorthite, sodian	PDF 04-015-4238	Na _{0.5} Ca _{0.5} Al _{1.5} Si _{2.5} O ₈	9.5
	Nontronite	PDF 00-058-2026	(Na,Ca) _{0.3} Fe ₂ (Si,Al) ₄ O ₁₀ (OH) ₂ ·xH ₂ O	67.4
	Biotite-1M, titanian	PDF 01-088-1906	K(Mg _{1.46} Fe _{1.34} Ti _{0.20})(Al _{1.24} Si _{2.76} O ₁₀)(OH) _{1.84} O _{0.16}	2.8

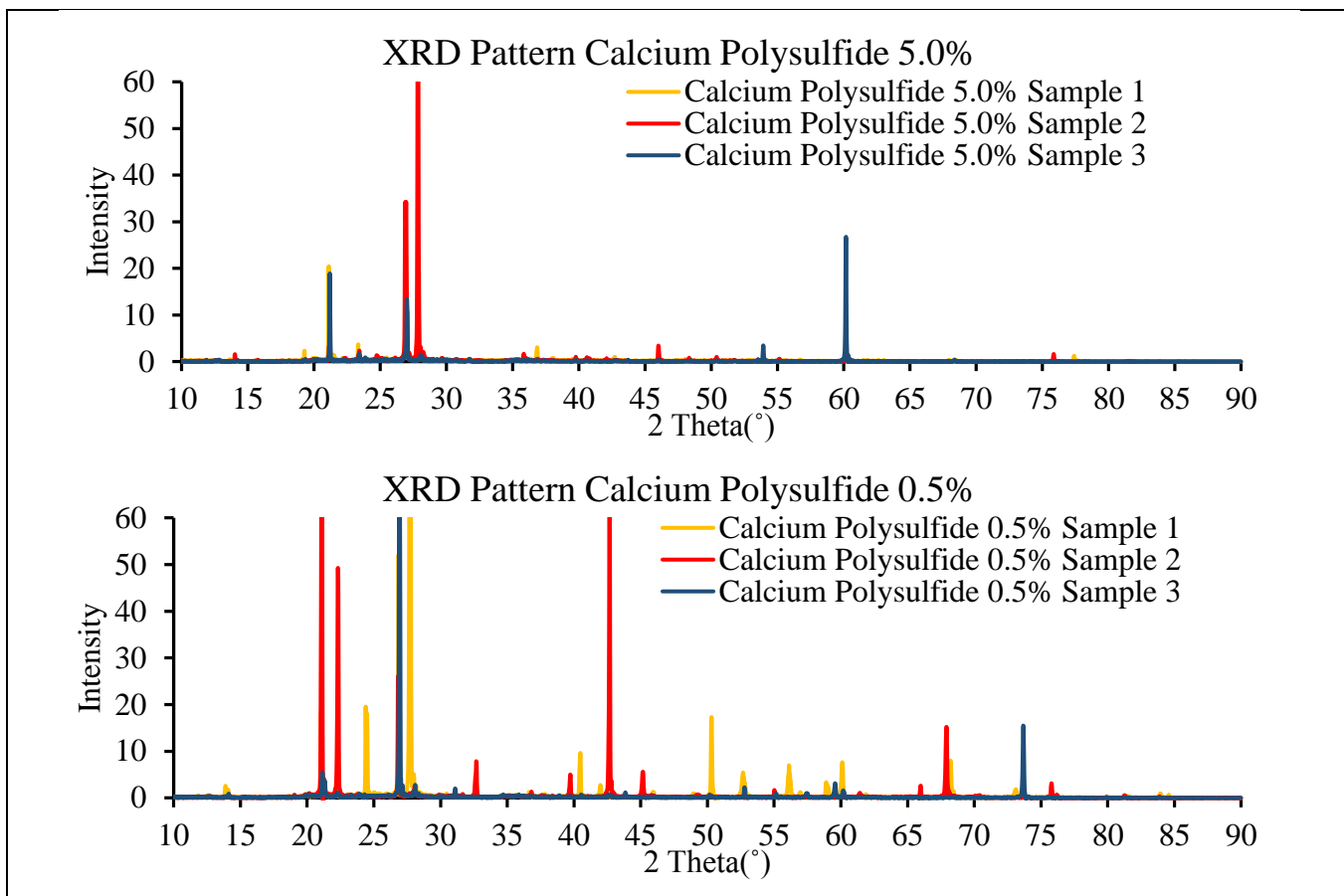


Figure 19. Calcium polysulfide XRD patterns from triplicate samples in synthetic perched water.

Table 16. Solid Phases Identified in 5% Calcium Polysulfide Treated Sediment iSamples Prepared with Synthetic Perched Water

	Name	ID	Formula	Percentage
PW CPS 5% S1	Thallium Barium Aluminum Silicate	PDF 04-016-3043	Ba _{7.5} Tl ₈ Al ₂₃ Si ₂₅ O ₉₆	5.1
	Jouravskite	PDF 04-018-4944	Ca ₃ Mn(CO ₃)(SO ₄)(OH) ₆ (H ₂ O) ₁₂	31.4
	Barium Calcium Aluminum Silicate	PDF 00-044-0048	Ca _{0.32} Ba _{3.32} (Al _{8.6} Si _{39.9})O ₉₆	10.6
	Zircon, metamict	PDF 00-012-0251	ZrSiO ₄	53.0
PW CPS 5% S2	Silver Aluminum Silicon Oxide	PDF 04-009-1982	Ag ₂₃ Al ₂₃ Si ₂₅ O ₉₆	0.3
	quartz low Silicon Oxide	PDF 01-070-2536	SiO ₂	4.8
	Lithium Magnesium Aluminum Iron Silicate Hydroxide	PDF 04-015-8489	Li _{0.31} Mg _{0.27} Fe _{0.23} Al _{1.6} Si _{3.9} O ₁₀ (OH) ₂	1.2
	Sulfur, syn	PDF 00-064-0585	S	2.6
	Anorthite, ordered	PDF 00-041-1486	CaAl ₂ Si ₂ O ₈	91.0
PW CPS 5% S3	Vermiculite	PDF 04-011-6576	Mg _{3.5} AlSi ₃ O ₁₀ (OH) ₂ (H ₂ O) ₄	22.8
	Silicon Oxide	PDF 04-011-0544	SiO ₂	27.1
	Gottardiite	PDF 00-049-1831	Na ₃ Mg ₃ Ca ₅ Al ₁₉ Si ₁₁₇ O ₂₇₂	50.0
PW CPS 0.5% S1	silver tecto-alumosilicate hydrate Silver Aluminum Silicate Hydrate	PDF 01-079-1886	Ag _{73.92} Si ₉₆ Al ₉₆ O ₃₈₄ (H ₂ O) _{114.24}	0.6

	Sodium Aluminum Bromide Chloride Silicate	PDF 04-011-4698	$\text{Na}_8\text{Al}_6(\text{SiO}_4)_6\text{Br}_{1.74}\text{Cl}_{0.26}$	10.9
	vermiculite ((CH ₃) ₃ SO)-exchanged Trimethylsulfoxonium magnesium titanium manganese iron(III) aluminium silicon oxide hydroxide (1.7/5.05/0.03/0.01/0.58/2.80/5.48/20/4)	PDF 01-083-5035	$((\text{CH}_3)_3\text{SO})_{1.7}(\text{Mg}_{5.05}\text{Ti}_{0.03}\text{Mn}_{0.01}\text{Fe}_{0.58}\text{Al}_{0.28})(\text{Si}_{5.48}\text{Al}_{2.52})\text{O}_{20}(\text{OH})_4$	0.5
	Caminite, syn	PDF 04-011-5317	$\text{Mg}_{1.33}(\text{SO}_4)(\text{OH})_{0.66}(\text{H}_2\text{O})_{0.33}$	88.0
PW CPS 0.5% S2	Kihlmanite-(Ce)	PDF 01-083-6462	$\text{Ca}_{0.31}\text{Ce}_2(\text{Ti}_{0.76}\text{Nb}_{0.24})\text{O}_2(\text{SiO}_4)(\text{HCO}_3)_{1.06}(\text{CO}_3)_{0.94}(\text{H}_2\text{O})_{0.68}$	2.7
	Vermiculite	PDF 04-017-7292	$\text{Ca}_{0.465}\text{Mg}_{2.810}\text{Fe}_{0.065}\text{Al}_{1.190}\text{Si}_{2.895}\text{O}_{10}(\text{OH})_2(\text{H}_2\text{O})_4$	2.4
	cristobalite beta Silicon Oxide	PDF 01-077-8628	SiO_2	32.0
	Khademite	PDF 04-014-1868	$\text{Al}(\text{SO}_4)\text{F}(\text{H}_2\text{O})_5$	14.6
	Calciolangbeinite	PDF 04-019-1366	$\text{K}_2\text{Ca}_{1.24}\text{Mg}_{0.76}(\text{SO}_4)_3$	5.0
	Elbaite	PDF 01-075-1170	$(\text{Na}_{0.875}\text{Ca}_{0.125})(\text{LiAl}_2)(\text{Al}_{5.8}\text{Fe}_{0.1}\text{Mn}_{0.1})(\text{BO}_3)_3(\text{Si}_6\text{O}_{18})\text{O}(\text{OH})_3$	39.0
	Villiaumite, syn	PDF 04-005-4663	NaF	4.3
PW CPS 0.5% S3	Sodium cobalt Aluminum silicon oxide hydrate Sodium Cobalt Aluminum Silicate Hydrate	PDF 01-076-8154	$\text{Na}_{9.6}\text{Co}_{32}(\text{Al}_{192}\text{Si}_{1000}\text{O}_{384})(\text{H}_2\text{O})_{46.4}$	4.6
	Cristobalite beta, syn Silicon Oxide	PDF 01-077-8630	SiO_2	13.9
	Nontronite	PDF 00-058-2027	$(\text{Na,Ca})_{0.3}\text{Fe}_2(\text{Si,Al})_4\text{O}_{10}(\text{OH})_2 \cdot x\text{H}_2\text{O}$	74.1
	Sodium Aluminum Cyanide Silicate Hydrate	PDF 00-037-0196	$\text{Na}_8\text{Al}_6\text{Si}_6\text{O}_{24}(\text{CN})_2 \cdot x\text{H}_2\text{O}$	7.5

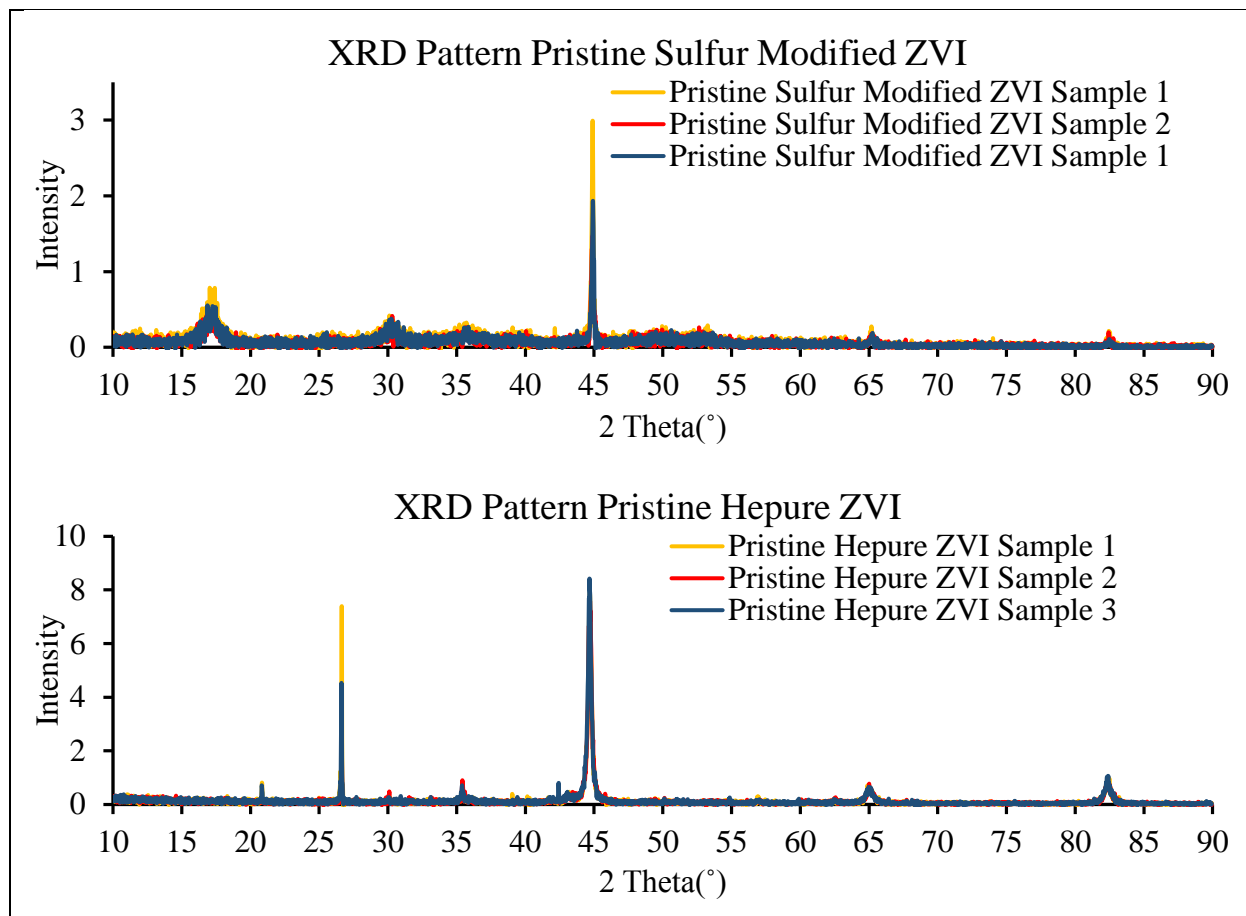


Figure 20. Pristine Hepure ZVI and sulfur modified ZVI.

Table 17. Solid Phases Identified in Pristine Iron

	Name	ID	Formula	Average Percentage
Pristine SMI	Iron, syn	PDF 04-007-9753	Fe	68.9±4.7
	Magnetite	PDF 01-086-1344	Fe ₂ .946O ₄	8.0±2.5
	Mackinawite, syn	PDF 04-003-5937	FeS	23.2±2.7
Pristine ZVI	Iron, syn	PDF 04-007-9753	Fe	55.9±18.2
	Magnetite	PDF 01-086-1344	Fe ₂ .946O ₄	27.3±26.2
	Quartz, syn	PDF 00-046-1045	SiO ₂	14.9±17.9

Subtask 1.2: Conclusions

These experiments provided insights on the reoxidation behavior of immobilized ⁹⁹Tc after sequestration with Hepure ZVI, SMI, and CPS. Experimental data showed that technetium reduction occurs in the presence of all reductants under anaerobic conditions. Results showed that the oxidation-reduction potential (ORP, mV, SHE) in the presence of each ZVI material significantly increased after 30 days, but samples amended by 1% Hepure ZVI exhibited the lowest ORP values compared to other tested conditions. ORP readings correlated with lower Tc

reoxidation behavior in sediment samples treated with Hepure ZVI. Calcium polysulfide samples were found to have the highest likelihood of reoxidation compared to ZVI and SMI when exposed to similar oxidation conditions. Hanford sediment, its different soil fractions, and post-treatment solids were characterized via x-ray diffraction (XRD), surface morphology, and elemental composition via SEM-EDS before and after treatment, documenting expected changes. Fraction analysis of the soil also showed the composition of sand, silt and clay. Future work will investigate the effect of reductants when Tc is comingled with other contaminants, such as uranyl and nitrate.

Subtask 1.2: References

- Cornell, RM and U. Schertmann (2003). *The iron Oxides. Structure, Properties, Reactions, Occurrences and Uses*. Wiley-VCH GmbH & Co. KGaA, Weinheim.
- Boglaienko, D., J. A. Soltis, R. K. Kukkadapu, Y. Du, L. E. Sweet, V. E. Holfeltz, G. B. Hall, E. C. Buck, C. U. Segre and H. P. Emerson (2020). "Spontaneous redox continuum reveals sequestered technetium clusters and retarded mineral transformation of iron." *Communications Chemistry* **3**(1): 1-11.
- Lawter, A. R., W. L. Garcia, R. K. Kukkadapu, O. Qafoku, M. E. Bowden, S. A. Saslow and N. P. Qafoku (2018). "Technetium and iodine aqueous species immobilization and transformations in the presence of strong reductants and calcite-forming solutions: remedial action implications." *Science of the Total Environment* **636**: 588-595.
- Lukens, W. W., J. J. Bucher, D. K. Shuh and N. M. Edelstein (2005). "Evolution of technetium speciation in reducing grout." *Environmental science & technology* **39**(20): 8064-8070.
- Luksic, S. A., B. J. Riley, M. Schweiger and P. Hrma (2015). "Incorporating technetium in minerals and other solids: A review." *Journal of Nuclear Materials* **466**: 526-538.
- Pearce, C. I., R. J. Serne, S. A. Saslow, W. Um, R. M. Asmussen, M. D. Miller, O. Qafoku, M. M. Snyder, C. T. Resch and K. C. Johnson (2018). "Characterizing technetium in subsurface sediments for contaminant remediation." *ACS Earth and Space Chemistry* **2**(11): 1145-1160.

Subtask 1.3: Evaluation of Competing Attenuation Processes for Mobile Contaminants in Hanford Sediments

Subtask 1.3: Introduction

Contaminants, including U, ^{99}Tc , I, Cr, ^{129}I , and NO_3^- , migrated to the vadose zone creating subsurface plumes at the Hanford 200 Area located in the Central Plateau. These mobile contaminants persist in the subsurface and have potential to enter the groundwater via downward migration through the vadose zone. U is in the form of hexavalent uranium [U(VI)] primarily existing as neutral and anionic carbonates ($\text{Ca}_2\text{UO}_2(\text{CO}_3)_3$ aq, $\text{CaUO}_2(\text{CO}_3)_3^{2-}$ in the natural oxic vadose zone environment at solution pH of ~ 8 .¹ Many technologies have been explored to decrease U mobility in the Hanford Site vadose zone including using a reactive gas, a gas-advected liquid, or a foam-advected liquid.² Tc is primarily in the form of anionic pertechnetate (TcO_4^-).³ When pertechnetate is exposed to reducing conditions, Tc changes from +7 to +4 valence state and normally precipitates to the solid TcO_2 , immobilizing and effectively removing Tc from the groundwater. Reduced Tc (IV) readily returns to the mobile pertechnetate ion under oxidizing conditions.⁴ Unfortunately, ^{99}Tc has been reported above the drinking water standard of 900 pCi/L

in groundwater and is currently treated using a Purolite A530E ion exchange resin within a large pump-and-treat (P&T) system.⁵ Chromium is typically present in the hexavalent form (the most mobile form of chromium) [Cr(VI)] as chromate (CrO_4^{2-}).⁶ Once chromium (VI) is converted to chromium (III), it will typically rapidly precipitate as a highly insoluble phase such as $\text{Cr}(\text{OH})_3$ and is effectively immobilized upon treatment.⁴ Remediation efforts are in progress to ensure that the groundwater is restored to meet the drinking water standard (48 $\mu\text{g/L}$) and to protect the Columbia River by ensuring that discharge of groundwater to the river is below the surface-water quality standard (10 $\mu\text{g/L}$). Current remedies include application of Pump-and-Treat (P&T) and Monitored Natural Attenuation (MNA).⁷ At Hanford, major aqueous species of I have been distributed as 76% IO_3^- , 22% organo-iodine, and 2% I^- . ^{8129}I is present at the Hanford Site Central Plateau in contaminated groundwater plumes at concentrations above the primary drinking water standard of 1 pCi/L (this is the lowest standard on the federal register for a radioactive contaminant); there is currently no treatment method.⁵ Nitrate is stable and mobile in oxygenated environments, and the amount not taken up by plants is leached into the local aquifer.⁴ Although many wells at the Hanford Site exceed the Maximum Contaminant Level (MCL) for nitrate, there is currently no remediation method.

Once active remediation is completed, a transition to more passive approaches, such as monitored natural attenuation (MNA), is needed. Effective MNA requires a thorough understanding of the contaminant immobilization processes that keep the contaminants stable and resistant to remobilization during any changes in environmental conditions or groundwater chemistry. Quantifying contaminant attenuation processes via competitive adsorption mechanisms on vadose zone sediment will assess competitive attenuation processes. This assessment will support the development of site conceptual models with co-located contaminants and identify relevant contaminant fate and transport parameters. Understanding of contaminant sorption behavior is also important for assessing the viability of long-term MNA.

Subtask 1.3: Objectives

This research is focused on competitive adsorption between contaminants of concern onto the Hanford Formation vadose zone sediment as an assessment of their mobility and fate.

Subtask 1.3: Methodology

Uncontaminated sediment samples were sent from the Pacific Northwest National Laboratory (PNNL); the Hanford formation samples were collected from Pasco, WA, from the Tristate Asphalt gravel pit. These sediments were then separated into different sized fractions using 2 mm, 0.5 mm, 0.063 mm, and 0.02 mm sieves. Fractions of sediment that were obtained included sand, silt and clay which were then analyzed using solid characterization techniques. Surface and materials characterization that require instrumentation not available on campus will be conducted through a variety of collaborations or visitations to national lab facilities as part of the DOE Fellows student summer internship. The following are methods that have been implemented for specific instruments currently used in this study. BET surface area analysis was conducted by Amin Rabiei from the FIU Department of Mechanical and Materials Engineering. SEM/EDS was conducted at the Florida Center for Analytical Electron Microscopy with aid from Thomas H.

Beasley (Program Coordinator) in order to determine the elemental composition of each sediment fraction. Specimens for microscopy were prepared by attaching double sided adhesive carbon tape (12 mm, Electron Microscopy Sciences) to aluminum studs and then sprinkling the dried sediment on the carbon tape. The specimen mounts were loaded into a seven-stud holder to prepare for SEM-EDS analysis. Surface characterization was conducted via a JEOL IT500HR Field Emission Microscope equipped with the Bruker XFlash 6160 mm window SDD detector. EDS operating conditions were set at 15 kV accelerating voltage. Specific mineralogy was determined using XRD analysis. XRD patterns were collected by the Bruker D2 PHASER instrument equipped with the LYNXEYEXET detector operated at 30 kV and 10 mA using $\text{CuK}\alpha$ radiation ($\lambda=1.54060 \text{ \AA}$) in the 2θ range from 10° to 90° with a step size of 0.02° , 1s per step. Samples were loaded into a zero diffraction plate $\varnothing 24.6 \text{ mm} \times 1.0 \text{ mm}$ thickness with cavity $\varnothing 10 \text{ mm} \times 0.2 \text{ mm}$ depth (MTI Corporation). Crystalline phase identification was performed via DIFRAC.EVA.V5.1 XRD pattern processing software by matching the powder patterns with those retrieved from the crystallography open database. After completion of solid characterization, it was decided to conduct competitive adsorption experiments with the $\leq 2 \text{ mm}$ bulk size fraction. This was done in order to have the greatest amount of elements that will participate in adsorption interactions. This was also due to the small amount of clay fraction available after sieving which is not enough to conduct batch sorption experiments.

Physical analysis of the bulk size fraction including dry bulk density, particle density, and porosity was conducted. The bulk density (ρ_b) of a solid is defined as the ratio of the dry mass of the solid to its bulk volume. The bulk volume includes both the solid and void volume. The volume of the soil had to be measured without compaction, as it was taken from the field/as used in the lab studies. The mass of the solid was determined after drying the known volume in a laboratory oven.¹⁰ The bulk weight of the solid mixtures was determined gravimetrically by using the following procedure with triplicate samples. A beaker (100 mL) was filled with soil mixture and the volume was noted. The mixture was then dried for one day at 105°C until the weight was stabilized. After cooling in a desiccator, the mass of the soil was determined. The bulk density (ρ_b) was calculated using the following equation:

$$\text{Bulk Density} = \frac{\text{Oven dry soil weight}}{\text{Volume of soil } \left(\frac{\text{g}}{\text{cm}^3}\right)}$$

Particle density is the average density of the soil. Experimental procedures were followed as given in the Methods of Soil Analysis for the Pycnometer Method¹⁰ to determine the particle density of soil with triplicate samples. Air-dried soil samples (12.5 g) were weighed and introduced to oven-dried and pre-weighed 25 mL volumetric flasks. Deionized water (DIW) was added to the flasks until about one-half full. The flasks were then gently boiled with the solid slurry for a few minutes to eliminate air bubbles among the particles. After flasks were allowed to cool down, they were filled to the 25 mL mark by adding from previously boiled and cooled DIW. Temperatures of all the samples were observed (to ensure that all samples had the same temperature) and their final combined weights were determined. The soil/DIW mixture was discarded, and the flasks were filled with cooled-boiled DIW and were weighed. The particle density of the soil was then determined using the following equation:

$$\rho_p = \frac{\rho_w(W_s - W_a)}{[(W_s - W_a) - (W_{sw} - W_w)]}$$

Where ρ_p : particle density, ρ_w : density of water in grams per cubic centimeter at the temperature observed (25 °C), W_s : weight of the pycnometer (flask) plus soil, corrected to oven-dry water content, W_a : weight of pycnometer filled with air, W_{sw} : weight of pycnometer filled with soil and water slurry, W_w : weight of pycnometer filled with water at temperature observed.

The measurement of porosity is described in Methods of Soil Analysis¹⁰ as the ratio of void volume of the soil to its total volume. The total porosity of the samples was determined using the following equation: $Pt = 1 - \frac{p_b}{p_p}$

Where: p_p : particle density, p_b : dry bulk density. Porosity is a dimensionless quantity and is reported as a percentage or a decimal fraction.

Batch sorption experiments were initiated with chromate using the following methodology. Artificial groundwater (AGW, 2L) used in the experiment was created using the formulation found in Table 18. AGW was placed in 5 different 100 mL bottles and were then spiked with the concentration of chromium listed in Table 19. These five bottles were stored in the refrigerator.

Table 18. AGW formulation

Constituent	Formula weight (g/mol)	Conc. (mmol/L)	Mass (g/L)
NaHCO ₃	84.006	1.586	0.1333
KHCO ₃	100.114	0.1231	0.0123
MgSO ₄ •7H ₂ O	246.466	0.3660	0.0902
MgCl ₂ •6H ₂ O	203.351	0.2468	0.0502
CaCl ₂ •2H ₂ O	147.036	1.0708	0.1574

1M HCl add 0.150 mL for pH 7.8

Table 19. Concentrations of each contaminant used in experiments^{11,12}

Contaminant	I-129, µg/L	Tc-99, µg/L	Cr(VI) µg/L	NO ₃ ⁻ µg/L	U(VI)mg/L *	U(VI) µg/L
1	100	2.6	530	1990	99	9000
2	80	2.6	400	1600	80	6500
3	60	2.6	250	1200	60	4000

4	40	2.6	100	800	40	1500
5	20	2.6	50	400	20	100

* *These concentrations may not be studied due to precipitation occurring with the AGW. This will be further investigated with speciation studies using Geochemist Workbench software.*

Oven dried sediment (32.3 ± 0.8 g, 20 ± 0.01 mL), was placed in 50 mL centrifuge tubes in triplicate for each concentration. Spiked AGW (20 ± 0.01 mL) was then added to the sediments. A control without any sediment was also done for each concentration in order to measure the amount of chromium absorbed on the tube and the cap. Centrifuge tubes were then placed on an end-over-end tube revolver at 30 rpm as shown in Figure 21. For preliminary sorption equilibrium experiments, samples were taken at the following times in order to establish equilibrium time: 1 hour, 3 hours, 1 day, 3 days, 5 days, and 7 days after the addition of the spiked AGW to sediment. During these sampling times, the sediment was allowed to settle for 10 min before 0.5mL of supernatant was taken and filtered through a 0.2 μ m syringe filter into a 1.5mL centrifuged vial. To ensure a constant solid:solution ratio, the total amount of solution withdrawn from samples was less than 10%. Samples were stored in the refrigerator for chemical analyses.



Figure 21. Sediment samples in an end-over-end tube revolver at 30 rpm

Due to previous incorrect formulation of 2% HNO_3^- which gave a higher concentration than intended, a further dilution was required giving a dilution factor of around 70 for each sample. After replacing sample cones and filter on the ThermoFisher Scientific iCAP RQ inductively coupled plasma-mass spectrometer (ICP-MS) and running diagnostic testing with tuning solution, the instrument was ready to use for analysis of Cr. Analytical geochemical techniques will be done for metals, Ca, Al, Si, K, Na, Mg, via Perkin Elmer OPTIMA 7300DV inductively coupled plasma optical emission spectroscopy (ICP-OES) and ICP-MS for U, Tc, Fe, Cr, and iodine. Anions, Cl⁻,

NO_3^- , NO_2^- , and SO_4^{2-} will be measured by Integrion Dionex ion chromatography (IC). All contaminants will be subjected to the same batch adsorption experiment method separately and then together at each respective concentration.

Subtask 1.3: Results and Discussion

Sediments are multi-phase systems that consist of numerous minerals. The composition of sediment pore fluid and mobility of contaminants in a sediment are limited through adsorption/desorption and precipitation/dissolution reactions between these minerals and the pore fluid. Therefore, it is important to identify the various minerals and their abundance in sediments used for estimating contaminant-pore water-solid interactions.¹³ The Hanford formation is composed of Pleistocene age flood deposits from Ice-Age floods and is the upper-most layer (30 to 70 m) at the Hanford Site. This sedimentary deposit is a major component of the vadose zone at the Hanford Site Central Plateau.¹⁴ The bulk samples (<2-mm size fraction) of Hanford Formation sediments are largely dominated by quartz (SiO_2), plagioclase feldspar [general formula $(\text{Na,Ca})\text{Al}(\text{Al,Si})\text{Si}_2\text{O}_8$], and alkali (potassium) feldspar (KAlSi_3O_8) with quartz usually being the dominant of these three minerals and plagioclase usually being more abundant than alkali feldspar. The clay-size fractions (<2 μm) of Hanford Formation sediments are dominated by four clay minerals illite {general formula $(\text{K,H}_3\text{O})(\text{Al,Mg,Fe})_2(\text{Si,Al})_4\text{O}_{10}[(\text{OH})_2,\text{H}_2\text{O}]$ }, smectite, chlorite, and kaolinite [$\text{Al}_2\text{Si}_2\text{O}_5(\text{OH})_4$].¹³ BET results illustrated in Figure 22 showed that the smallest size fraction had the greatest surface area compared to the largest sized fraction which had the least surface area; this was expected.

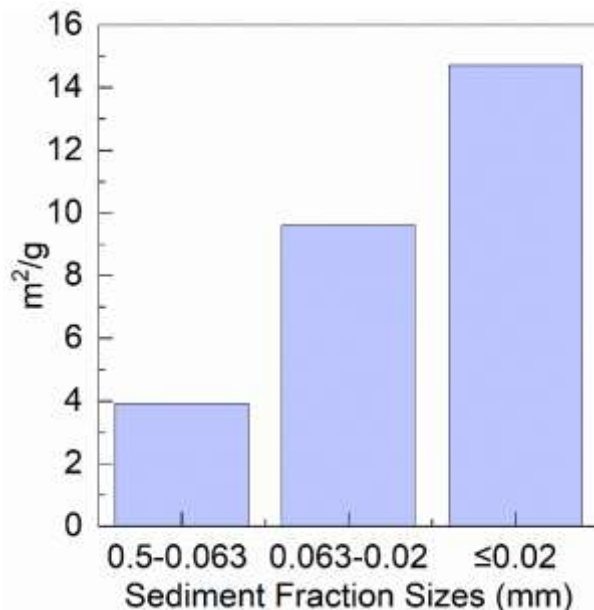


Figure 22. BET surface areas for Hanford formation sediment fractions (0.5-0.063 mm, 0.063-0.02 mm, and ≤ 0.02 mm)

The different sediment fractions were each analyzed for specific mineralogy via XRD, and the results are illustrated in

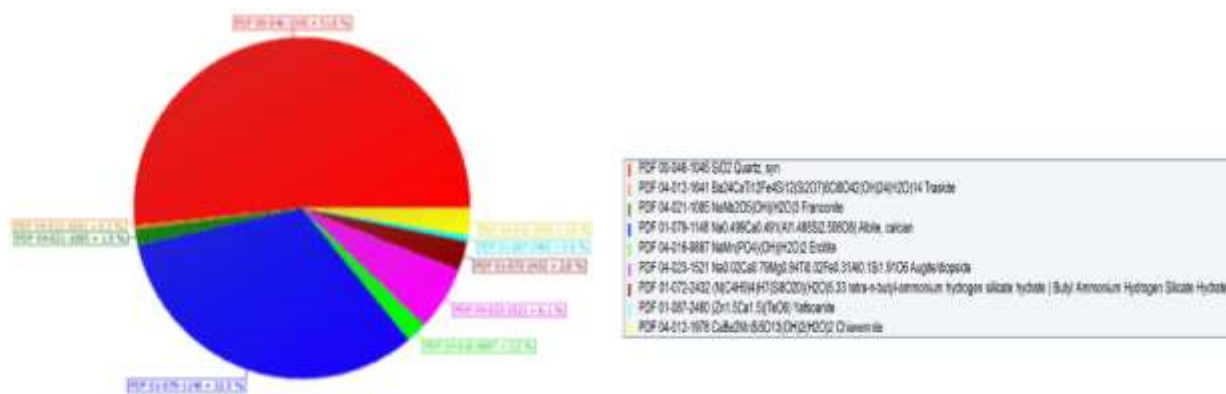
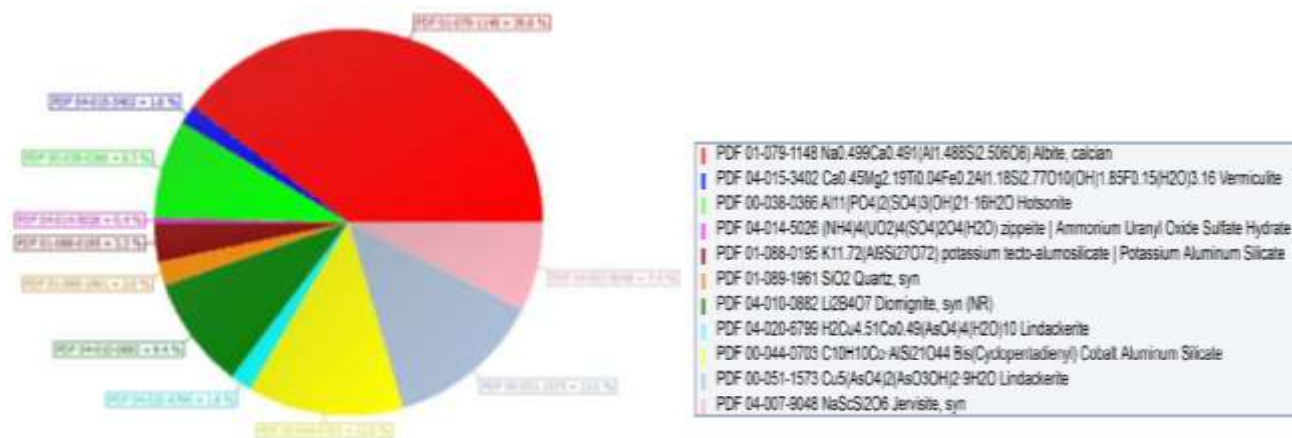


Figure 24. Results for XRD measurements on 63 μm -20 μm Hanford Formation sediments.



,and Figure 25. Based on the results, semi-quantitative elemental data was achieved and the geological make-up of sediments was estimated. The dominating mineral in the larger size fractions was found to be quartz, and the smaller size fractions were made up primarily of albite. These results are important for the design of competitive adsorption experiments, as some sediment fractions possess more redox sensitive elements than others. The major element in this study is Fe(II). These fractions will more actively participate in the transport mechanisms of contaminants of concern at the Hanford site.

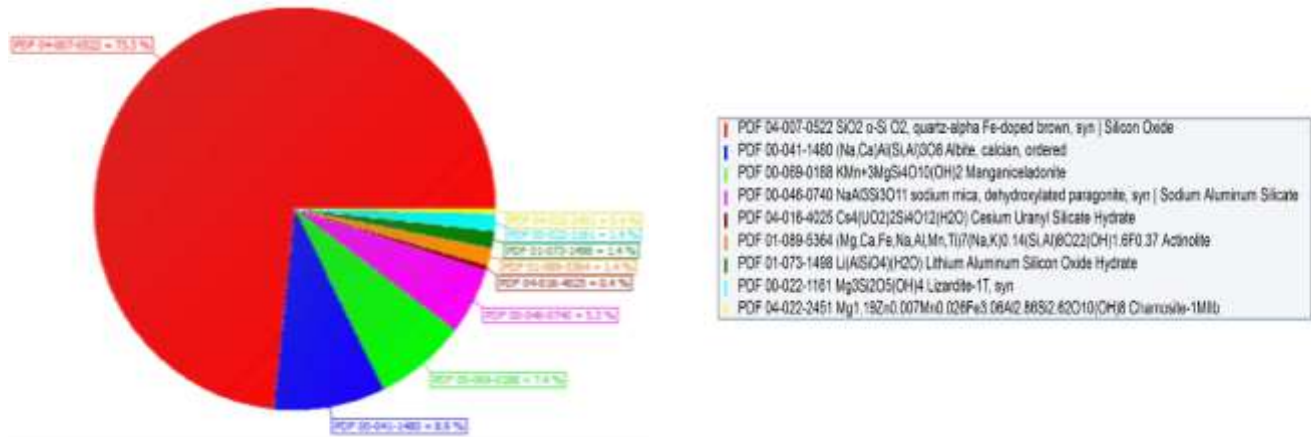


Figure 23. Results for XRD measurements on 0.5 mm-0.063 mm Hanford Formation sediments.

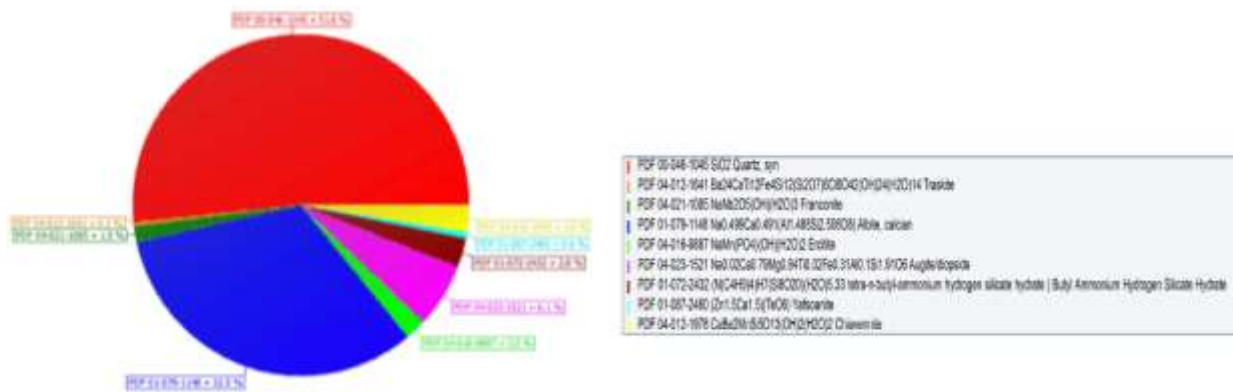


Figure 24. Results for XRD measurements on 63 μm -20 μm Hanford Formation sediments.

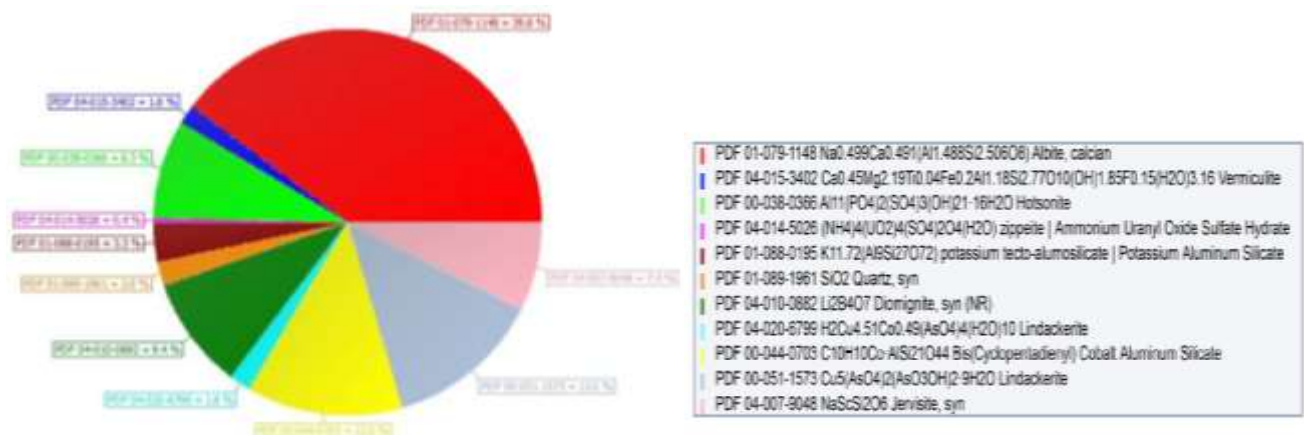


Figure 25. Results for XRD measurements on less than 20 μm Hanford Formation sediments.

The elemental composition of each sediment fraction was found using SEM/EDS and XRF. The results from this analysis are shown in Figure 26. There are a variety of elements present in each

sediment size fraction. Notably, Si makes up the majority of all fractions along with the presence of Fe, Ca, and Al. The last three elements mentioned will be important components in future adsorption experiments.

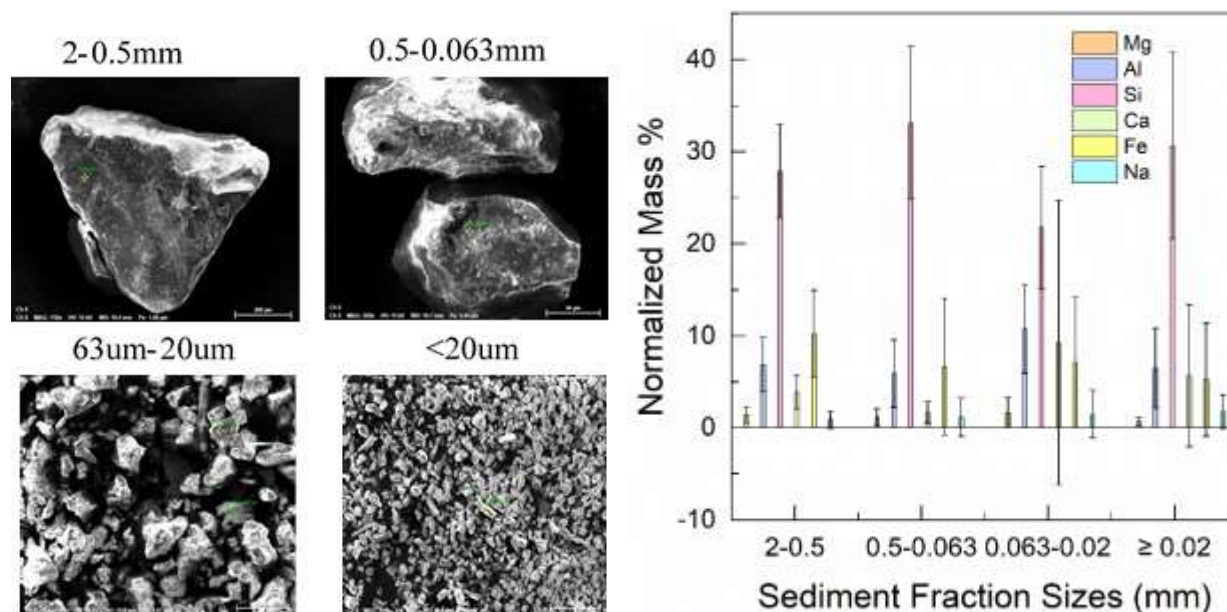


Figure 26. A: SEM-EDS analysis of Hanford sediment. B: EDS elemental distribution for Hanford sediment.

Figure 27 illustrates the concentration of Cr over a 7-day period. Negative values are observed after 3 days of sampling, indicating the dilution factor was too high. Because of these results, the batch adsorption experiment will be conducted again. Substantial sorption was still observed despite the high dilution factor. Therefore, additional sampling periods will be placed during the 7 days (1 hour, 3 hour, 8 hours, 1 day, 2 days, 4 days, and 7 days) in order to more accurately determine the time it takes to acquire equilibrium. After this is established, data will be fitted to an adsorption isotherm such as Langmuir or Freundlich to understand the occurring adsorption mechanisms. From Figure 28, it appears that the adsorption isotherm may fit best with a Langmuir model. It appears that the last two data points appear to be reaching possible saturation in the system. This will be further investigated.

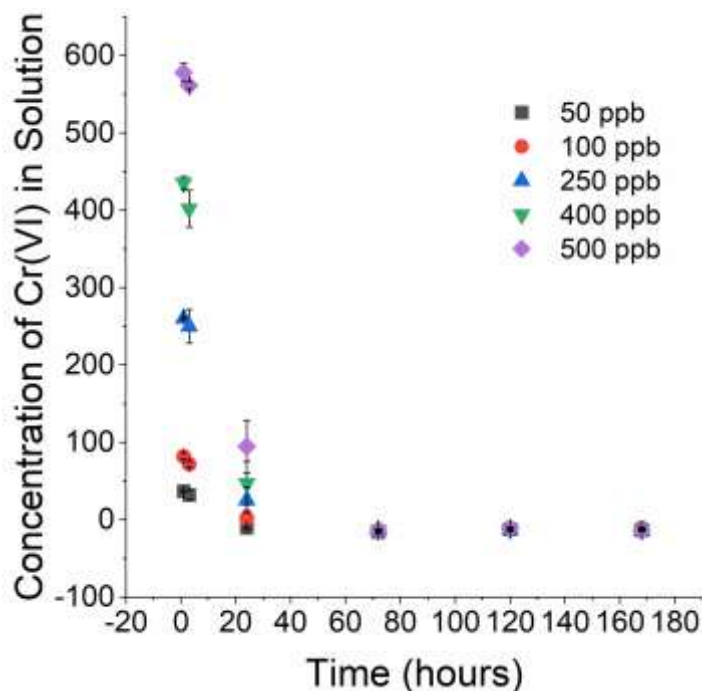


Figure 27. Cr batch adsorption experiment: Concentration of Cr(VI) in solution vs Time (hours).

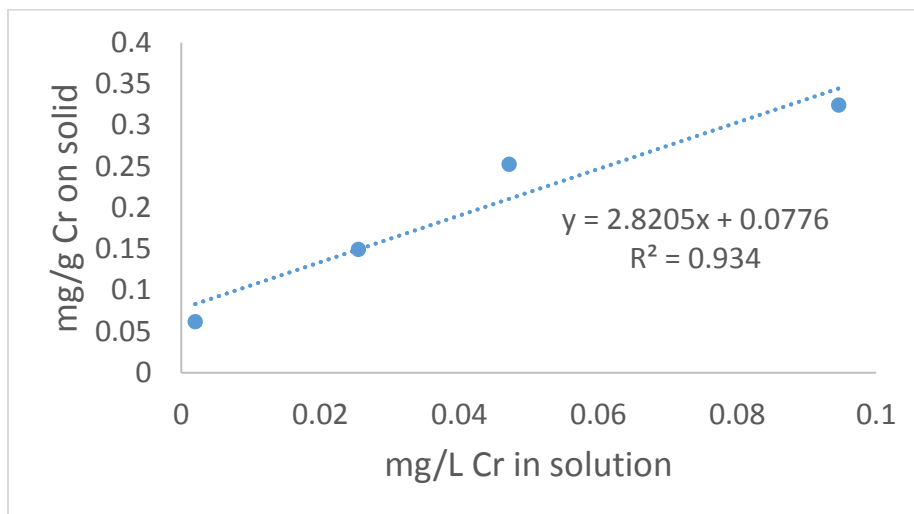


Figure 28. mg/g of Cr on solid vs mg/L Cr in solution.

Subtask 1.3: Conclusions

Once active remediation is completed at the Hanford Site, a transition to more passive approaches, such as MNA, is needed. A thorough understanding of the contaminant immobilization processes that keep the contaminants stable and resistant to remobilization during any changes in environmental conditions or groundwater chemistry is crucial for effective MNA. Conducting competitive adsorption experiments along with flow through column experiments, sequential extraction experiments and solid characterization with the following contaminants: U(VI), ⁹⁹Tc,

Cr(VI), ^{129}I , and NO_3^- will assess competitive attenuation processes. This assessment will support the development of site conceptual models with co-located contaminants and identify relevant contaminant fate and transport parameters. Overall, these studies will assess the viability of long-term MNA in supporting Hanford Site's cleanup efforts.

Subtask 1.3: References

- (1) Gorman-Lewis, D.; Shvareva, T.; Kubatko, K.-A.; Burns, P. C.; Wellman, D. M.; Mcnamara, B.; Szymanowski, J. E. S.; Navrotsky, A.; Fein, J. B. Thermodynamic Properties of Autunite, Uranyl Hydrogen Phosphate, and Uranyl Orthophosphate from Solubility and Calorimetric Measurements. *Environ. Sci. Technol.* **2009**, *43* (19), 7416–7422. <https://doi.org/10.1021/es9012933>.
- (2) Szecsody, J.; Truex, M.; Zhong, L.; Williams, M. *Remediation of Uranium in the Hanford Vadose Zone Using Gas-Transported Reactants: Laboratory-Scale Experiments*; 2010.
- (3) Peretyazhko, T. S.; Zachara, J. M.; Kukkadapu, R. K.; Heald, S. M.; Kutnyakov, I. V.; Resch, C. T.; Arey, B. W.; Wang, C. M.; Kovarik, L.; Phillips, J. L.; et al. Pertechnetate (TcO_4^-) Reduction by Reactive Ferrous Iron Forms in Naturally Anoxic, Redox Transition Zone Sediments from the Hanford Site, USA. *Geochim. Cosmochim. Acta* **2012**, *92*, 48–66. <https://doi.org/10.1016/j.gca.2012.05.041>.
- (4) Martin, C. J. *Overview of Hanford Hydrogeology and Geochemistry*; 2011.
- (5) Pearce, C. I.; Cordova, E. A.; Garcia, W. L.; Saslow, S. A.; Cantrell, K. J.; Morad, J. W.; Qafoku, O.; Matyá, J.; Plymale, A. E.; Chatterjee, S.; et al. Evaluation of Materials for Iodine and Technetium Immobilization through Sorption and Redox-Driven Processes. *Sci. Total Environ.* **2020**, *716*, 1–12. <https://doi.org/10.1016/j.scitotenv.2019.136167>.
- (6) Zachara, J.; Ainsworth, C.; Brown, G.; Catalano, J.; McKinley, J.; Qafoku, O.; Smith, S.; Szecsody, J.; Traina, S.; Warner, J. Chromium Speciation and Mobility in a High Level Nuclear Waste Vadose Zone Plume. *Geochim. Cosmochim. Acta* **2004**, *68* (1), 13–30. [https://doi.org/10.1016/S0016-7037\(03\)00417-4](https://doi.org/10.1016/S0016-7037(03)00417-4).
- (7) Truex, M.; Szecsody, J.; Qafoku, N.; Sahajpal, R.; Zhong, L.; Lawter, A.; Lee, B. *Assessment of Hexavalent Chromium Natural Attenuation for the Hanford Site 100 Area*; Richland, Washington, 2015.
- (8) Xu, C.; Kaplan, D. I.; Zhang, S.; Athon, M.; Ho, Y. F.; Li, H. P.; Yeager, C. M.; Schwehr, K. A.; Grandbois, R.; Wellman, D.; et al. Radioiodine Sorption/Desorption and Speciation Transformation by Subsurface Sediments from the Hanford Site. *J. Environ. Radioact.* **2015**, *139*, 43–55. <https://doi.org/10.1016/j.jenvrad.2014.09.012>.
- (9) Zachara, J. M. Hanford Site Vadose Zone Studies: An Overview. *Vadose Zo. J.* **2007**, *6* (4), 899–905. <https://doi.org/10.2136/vzj2006.0179>.
- (10) Blake, G. R.; Hartge, K. H. Bulk Density. In *Methods of Soil Analysis: Part 1 Physical and*

- Mineralogical Methods*; Klute, A., Ed.; 1986.
- (11) *Hanford Site Groundwater Monitoring Report for 2018*; Richland, Washington, 2019.
- (12) *Hanford Site 2018 Pump and Treat Report*; Richland, Washington, 2019.
- (13) Mackley, R.; Last, G.; PNNL. *Hanford Site Vadose Zone Sediment Mineralogy ---Emphasis on Central Plateau*; 2007.
- (14) Szecsody, J. E.; Truex, M. J.; Qafoku, N. P.; Wellman, D. M.; Resch, T.; Zhong, L. Influence of Acidic and Alkaline Waste Solution Properties on Uranium Migration in Subsurface Sediments. *J. Contam. Hydrol.* **2013**, *151*, 155–175. <https://doi.org/10.1016/j.jconhyd.2013.05.009>.

Subtask 1.4: Experimental Support of Lysimeter Testing

Subtask 1.4: Introduction

The vitrification of radioactive waste in the form of glass is one of the established treatment technologies for long term nuclear waste management (Pierce et al., 2008b). At the Hanford Site both the low activity waste (LAW) and high-level waste (HLW) fractions of the legacy waste stored on site will be vitrified to produce glass waste forms. The resulting HLW glass will be disposed of at a yet-to-be determined federal repository while the LAW glass will be disposed of on-site at the Hanford IDF. As a result of vitrification of LAW secondary wastes, both liquid and solid, will be generated. These secondary wastes will be immobilized as a grout waste form and are also planned for disposal at the IDF. The most recent iteration of the IDF PA projected 278,797 m³ of immobilized LAW (ILAW) glass and 18,900 m³ of grouted liquid secondary waste and 41,447 m³ of grouted solid secondary waste to be disposed of in the IDF (Lee, 2018)

The release of contaminants and radionuclides from glass and grout waste forms can be influenced by several environmental factors, such as pH, temperature, and concentration of dissolved components in the solution (Strachan et al., 1994; Vienna et al., 2013). The performance of candidate waste forms under these variables is assessed in the laboratory and the data collected is used to parameterize simulation models to assess the long-term release from the IDF. The Hanford Field Lysimeter Test Facility (FLTF), located in the 600 area of the Hanford Site, is being utilized by Pacific Northwest National Laboratory (PNNL) and Washington River Protection Solutions (WRPS) for field testing of the various waste forms expected, or possible candidates, to be produced during treatment and LAW at Hanford. The FLTF test will be used to validate model predictions of long-term waste form behavior upon disposal in the Hanford IDF (Neeway et al., 2018).

One of the planned configurations of the lysimeter units described in the FLTF Implementation Plan (Bacon et al., 2018) is to place cementitious waste forms (also termed grout waste forms) above glass waste forms with IDF sediment between the waste forms. This waste form arrangement was modeled; however, limited laboratory data is available regarding the dissolution of glass in the presence of groundwater which has contacted a cementitious material and then been buffered through sediment.

In this work, single-pass flow-through (SPFT) experiments (McGrail et al., 2001; Pierce et al., 2008a) were conducted to investigate the impact of grout-contacted solution on the dissolution behavior of a borosilicate glass (ORLEC28) designed for the immobilization of Low Activity Waste (LAW), at a varied temperature (25 °C, 40 °C, 70 °C, and 90 °C). The addition of grout to the system above the glass waste forms has the potential to alter the glass dissolution behavior (Muller et al., 2017) through either the increased concentration of dissolved species (e.g. Si, Al) or alteration of the pH environment. Baseline control experiments were conducted in a (LiOH/LiCl) buffer solution at pH 12. The results of these experiments provide information on the long-term dissolution behavior of glass waste forms in the FLTF experiment.

Subtask 1.4: Objectives

The objective of this study is to determine the effect of temperature, pH and dissolved components on the glass dissolution rate in the presence of grout contacted solution. This would help to evaluate if the dissolution behavior of the glass is controlled by a pH-mediated effect by the sediment or by the chemical makeup of the grout-contacted groundwater. The results of these experiments will provide information to support the design of future FTLF units to investigate the dissolution of waste forms at the Hanford Site Integrated Disposal Facility (IDF).

Subtask 1.4: Methodology

Materials

The glass used in the study is named ORLEC28 and is one of the two glasses emplaced in the FLTF experiment and its fabrication is reported elsewhere (Neeway et al., 2018). The composition of ORLEC28 is shown in Table 20. The grout used to generate the grout-contacted solutions was Cast Stone (47 wt% ground granulated blast furnace slag, 45 wt% class F fly ash and 8 wt % ordinary portland cement) used to immobilize simulated LAW and its fabrication is covered elsewhere (Asmussen et al., 2018). The waste form samples were provided by PNNL. LiCl, LiOH, and ACS grade HNO₃ (aq) (67-70%) for solution preparation and analytical measurements were purchased from Fischer Chemicals.

Table 20. Measured percent mass composition of ORLEC28 glass (Neeway et al., 2018)

Oxides	% composition
SiO ₂	39.23
Na ₂ O	21.58
B ₂ O ₃	10.07
Al ₂ O ₃	9.15
ZrO ₂	5.49
ZnO	3.27
K ₂ O	2.83
SnO ₂	2.17
CaO	2.04
MgO	1.07

Fe ₂ O ₃	0.57
TiO ₂	0.57
Cr ₂ O ₃	0.47
SO ₃	0.40
Cl	0.20
P ₂ O ₅	0.14
Re ₂ O ₇	0.10
F	0.08
NiO	0.01
PbO	0.01
V ₂ O ₅	0.01

Preparation of glass and grout

Powdered glass samples were prepared in the manner described in ASTM Method C1285-14 *Determining Chemical Durability of Nuclear, Hazardous and Mixed Waste Glasses and Multiphase Glass Ceramics: The Product Consistency Test*. The bulk glass was crushed with an agate mortar and pestle then sieved to the desired size fraction (149 - 74 μm). The samples were washed with alternating DI water (>18 M Ω) and ethanol to remove fine particulate material formed during the previous step. The glass particles were then dried in an oven overnight.

The ground-contacted DIW was prepared by first crushing the bulk grout sample with a hammer and sieving to < 2 mm. 1000g DI water was contacted with the 25g of the powdered grout for 7 days. The filtrate was used as a grout contacted solution and had a pH of 12.40 ± 0.08 .

Collection and analysis of samples

Corrosion of the glass was monitored using ASTM Method C1662-18, *Standard Practice for Measurement of the Glass Dissolution Rate Using the Single Pass Flow Through (SPFT) Test Method*. The SPFT samplings were performed using an IS-95 Interval sampler with a 4-column adapter (Fischer Scientific). An Isometric Peristaltic Pump (IPC Series) was employed for pumping solution into the reactors (TeflonTM, ID: 40.8 mm, h = 63.6 mm) at a controlled flow rate. All reactors and influent bottles were set up inside an oven to control temperature at each experiment.

Four experiments at 25 °C, 40 °C, 70 °C, and 90 °C were conducted under identical conditions. Each experiment included a control reactor using a pH 12 adjusted buffer (using LiOH/LiCl) and two reactors with grout-contacted solutions as leachate. The pH 12 test provided data on glass dissolution at approximately the same pH as the grout-contacted solution (pH 12.40). Six blanks before the addition of glass were collected from each reactor using a flow rate of 216 mL/day. Reactor 1 was connected to the buffer (LiCl/LiOH solution, pH 12) and Reactors 2 and 3 were connected to the grout solution (25 g in 1000 mL DI water). After the collection of blanks was complete, all reactors were emptied and cleaned, and then 0.1g of glass powder (size fraction of 74 - 149 μm) was added to each reactor. The ratio of surface area of glass to solution volume was calculated as 34.17 m^{-1} . Mesh (spectrum) (Spectrum Labs, PEEK mesh, 35 μm opening, 47 mm

diameter) was placed to all reactors for in-line effluent filtration. Then Reactor 1 was connected to the buffer and Reactors 2 and 3 to the grout solution to collect duplicate samples under identical conditions. The pump peristaltic cartridges were carefully calibrated before starting samples collection to have a flow rate of 40 mL/day. About 40 - 50 samples were collected from each glass reactor between 1.69 days and 6 days. The pH of the collected blanks and samples was measured with a pH meter, Orion Star A215 meter equipped with Orion 8156BNUWP Ross Ultra electrode.

The concentrations of B and Re, which is a chemical surrogate of Tc, in the samples and blanks were measured by the inductively coupled plasma mass spectroscopy (Thermo Fisher Scientific, iCAP RQ ICP-MS). The concentration of Si was measured by the inductively coupled plasma optical emission spectroscopy (ICP-OES, Perkin Elmer, Optima 7300 DV). The ICP-MS estimated limits of quantification (LOQ) for B and Re as 9.2 $\mu\text{g/L}$ and 0.13 $\mu\text{g/L}$, respectively. The LOQ for Si by the ICP-OES was determined as 50 $\mu\text{g/L}$. Solutions were diluted with 2% HNO_3 before analysis. Micrographs and elemental analysis of used glass and precipitated grout on the surface of glass from each experiment were taken from a JEOL JSM-5900LV scanning electron microscopy/energy-dispersive X-ray spectroscopy (SEM/EDS) at 25.0 kV and a takeoff angle of 35.0°. Glass powder was placed on a carbon tape attached to an aluminum sample holder and coated with gold.

Subtask 1.4: Results and Discussion

The B and Re dissolution rates of the grout-contacted experiments are given in Figure 29 and Figure 30, respectively. The samples labeled R1 designates Reactor 1 where the leachate was a pH 12 LiOH/LiCl-adjusted buffer, whereas R2 and R3 designate Reactors 2 and 3, respectively, where the leachate was a grout-contacted solution. The concentrations of B and Re in the solutions increased with increasing temperature as expected. For example, average concentration of Re from the duplicate experiments was measured as $0.43 \pm 0.09 \mu\text{g/L}$ at 25 °C, $0.94 \pm 0.02 \mu\text{g/L}$ at 40 °C and $1.04 \pm 0.05 \mu\text{g/L}$ at 70 °C. The concentrations of B and Re for grout contacted solutions at 90 °C, however, was found to decrease. The concentrations of B and Re, measured in the collected samples (R2 and R3) using grout-contacted solutions at all four experiments (25 °C, 40 °C, 70 °C, and 90 °C), were significantly lower compared to their corresponding controls using pH 12-adjusted buffer. The concentrations of B and Re collected from duplicate reactors R2 and R3 were similar with standard deviations between the two reactors on the level of $\leq 22\%$. An average Si concentration in an influent grout-contacted solution from 14 different samples was measured as $5,345.28 \pm 254.42 \mu\text{g/L}$. The presence of the dissolved species from the grout appears to lower the dissolution of the glass.

Observed drop in dissolution rate for the glass in the grout-contacted solution compared with the pH 12 buffer may result from a common ion effect. For example, glass matrix dissolution is driven by hydrolysis of the glass network, primarily made up of Si-O linkages. Through the hydrolysis, species from the glass are released into solution in an aqueous soluble ionic form: e.g., SiO_2 in the glass would form H_4SiO_4^- (aq) in solution. With increased glass dissolution (e.g. Si-O hydrolysis), the potential release of the glass components (B) or contaminant analogues (Re) is also increased. This dissolution process is a chemical pseudo-equilibrium. As the concentration of dissolved species increased in solution the dissolution rate of the glass is suppressed. (Abraitis et al., 2000; Pierce et al., 2008b). This common ion effect may be occurring in the grout-contacted solution as the grout provides dissolved species such as Si into the leachate solution prior to contacting the glass. The rate of B and Re release at 90 °C was found lower, compared to experiments conducted

at 25-70 °C temperatures. This effect may be due to the potential co-precipitation of these elements with Ca and Si-containing solids, which is evident from higher Re content in the elemental composition of precipitate detected by the EDS analysis (Table 21). EDS analysis of the precipitate also confirmed the precipitation of Al as aluminum oxide. Incorporation and co-precipitation of Re and Tc with Al containing minerals has been reported in previous studies (Harsh et al., 2015; Luo et al., 2009). A study by N. Mayordomo showed that Tc retention by γ -Al₂O₃ increased with increase in pH(Mayordomo et al., 2020). Further studies on the detailed composition of precipitates are in progress.

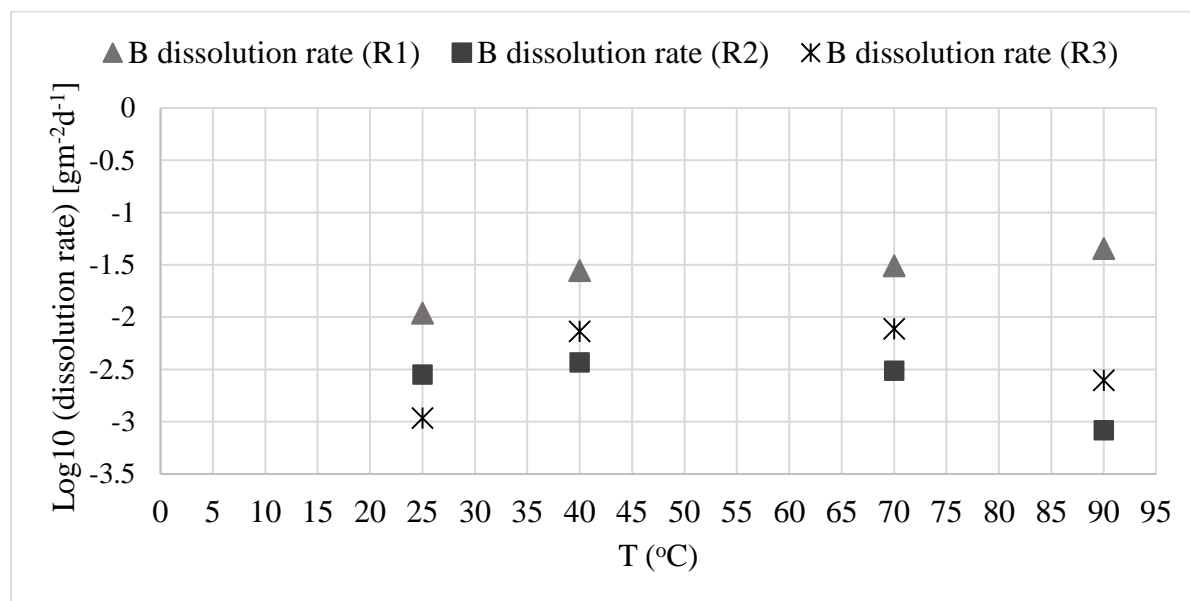


Figure 29. The release rates for B from ORLEC28 glass at 25 °C, 40 °C, 70 °C and 90 °C, utilizing pH 12 buffer (control) as a leachate in R1 and grout-contacted solution as the leachate (R2 and R3). The x-axis represents temperature (°C) and the y-axis represents the normalized release rate (g m⁻² d⁻¹).

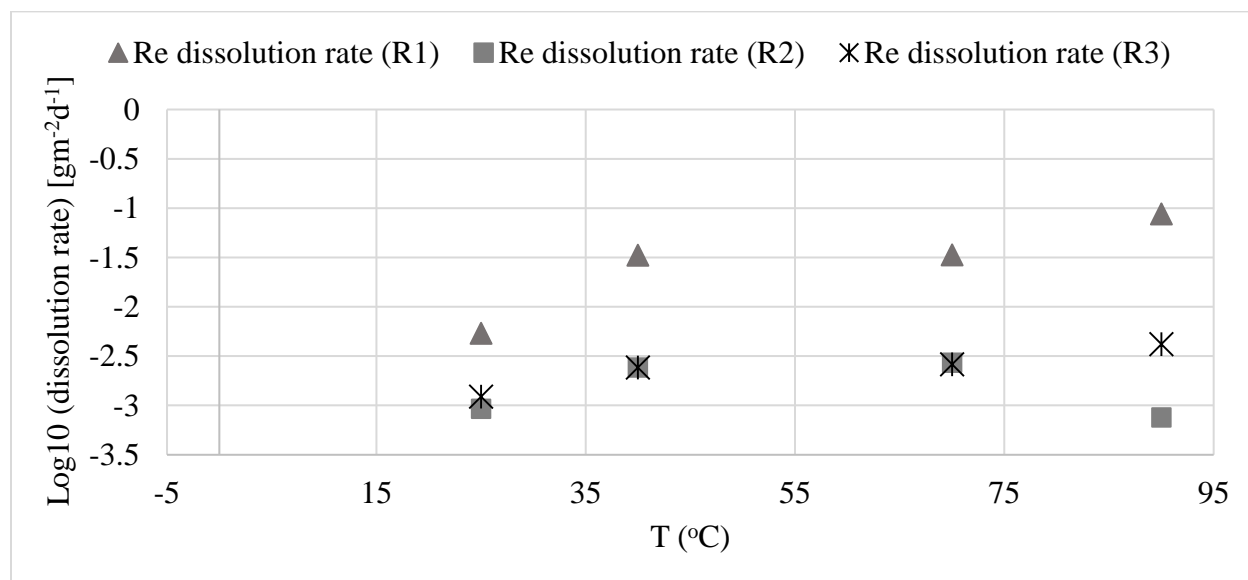


Figure 30. The release rates for Re from ORLEC28 glass at 25 °C, 40 °C, 70 °C, and 90 °C, utilizing pH 12 buffer (control) as a leachate in R1 and grout-contacted solution as the leachate (R2 and R3). The x-axis represents temperature (°C) and the y-axis represents the normalized release rate (g m⁻² d⁻¹).

Table 21. Measured percent elemental composition of grout-treated glass and precipitated grout solution. Only major constituents are reported. (Note: Averages and standard deviations from reactors R2 and R3)

Elements	% Normalized mass in composition	
	Grout-contacted glass	Precipitate formed on the glass surface
Oxygen	58.71 ± 0.67	50.52 ± 0.06
Sodium	10.12 ± 1.48	1.26 ± 1.41
Calcium	1.27 ± 0.08	45.76 ± 2.27
Potassium	1.48 ± 0.06	0.00 ± 0.00
Silicon	19.34 ± 0.64	1.50 ± 0.62
Re	0.007 ± 0.007	0.04 ± 0.03
Al	5.38 ± 0.03	0.20 ± 0.27

The surface of the glass was observed by SEM/EDS before and after corrosion shown in

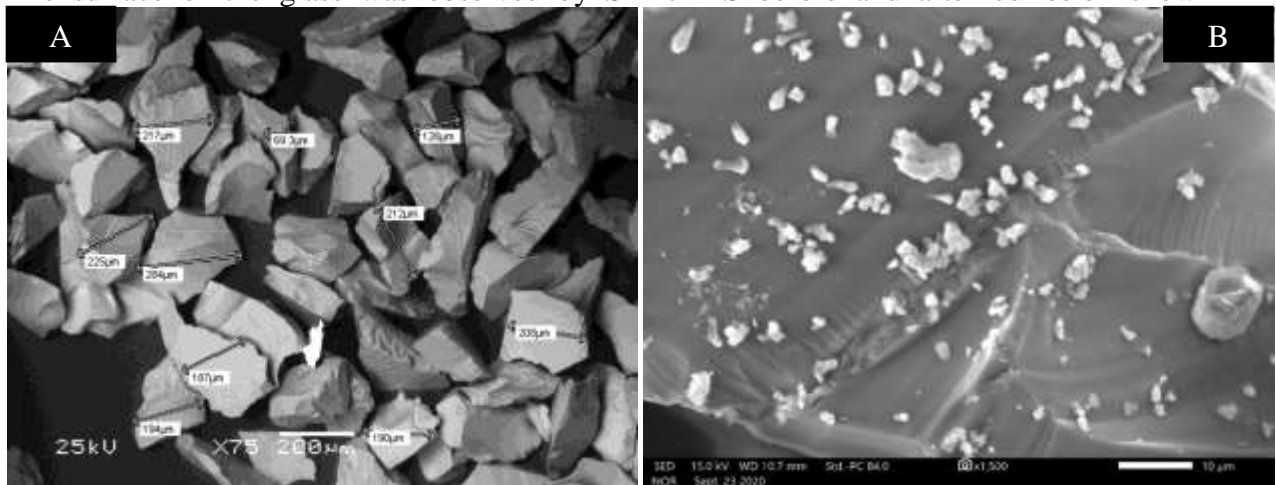


Figure 31. The glass surface has no fines prior to corrosion (

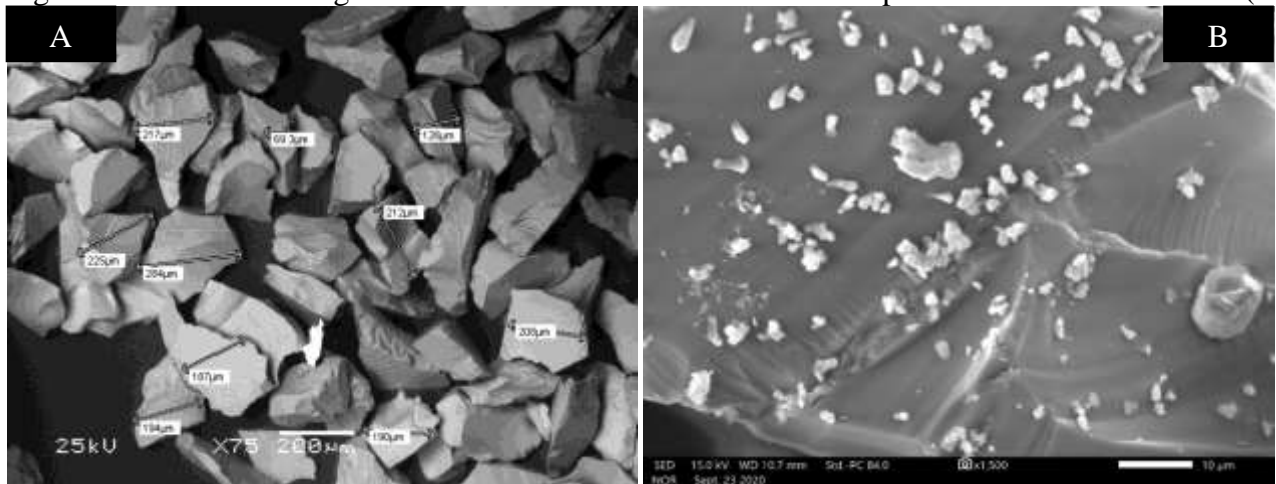


Figure 31A) yet after corrosion some particulates have appeared on the glass surface (

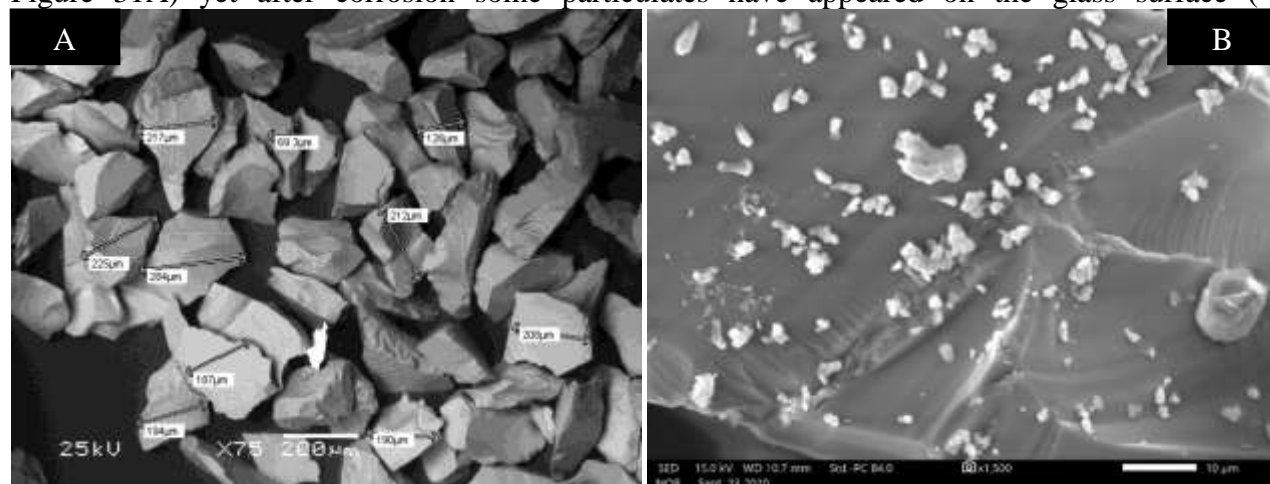


Figure 31B). A preliminary chemical assessment of the surface using EDS showed Na measured in the corroded glass samples was less than 70% compared to a pristine glass sample in all experiments. The loss of Na may be driven by an ion exchange process that occurs faster than the dissolution rate of the glass.

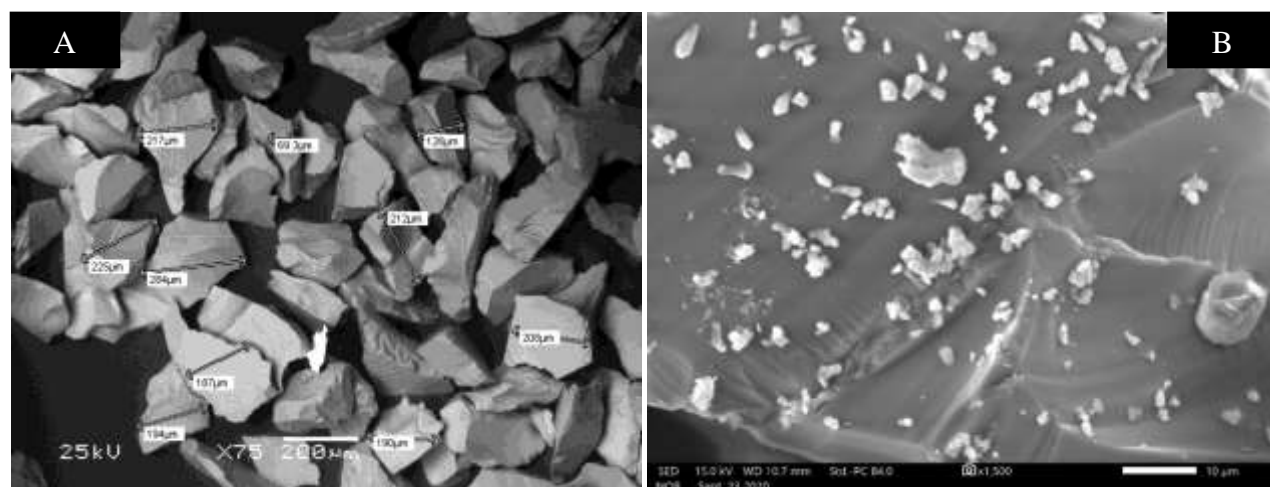


Figure 31. SEM micrograph of pristine glass (ORLEC28) (A) and a magnified crystal of a used glass sample at 25 oC in the presence of grout contacted solution (B).

SEM images of used glass and precipitate from grout solution in 90 °C experiment is given in Figure 32A and Figure 32B respectively. A glass sample from Reactor 1, in which the influent buffer solution was pH adjusted, did not show presence of any precipitates. A glass sample from Reactors 2 and 3, in which the influent was a grout contacted solution, contained some precipitates on the surface of glass. The elemental analysis of the precipitate showed that calcium and oxygen are the main elements with the weight percent (wt%) in composition of $45.78 \pm 2.27\%$ of Ca and $50.52 \pm 0.05\%$ of O. The wt% of Na and K measured in the surface composition was significantly less compared to the pristine grout sample (Asmussen et al., 2019). This might be due to high solubility of Na and K salts in aqueous solution. The surface elemental composition of precipitate contained about $0.04 \pm 0.04\%$ of Rerwich, which was lower than Re concentration in the glass composition after dissolution at 90 °C. The high standard deviation obtained was because Re is

localized in some areas. Elemental composition of major elements from used glass and precipitate is given in Table 21.

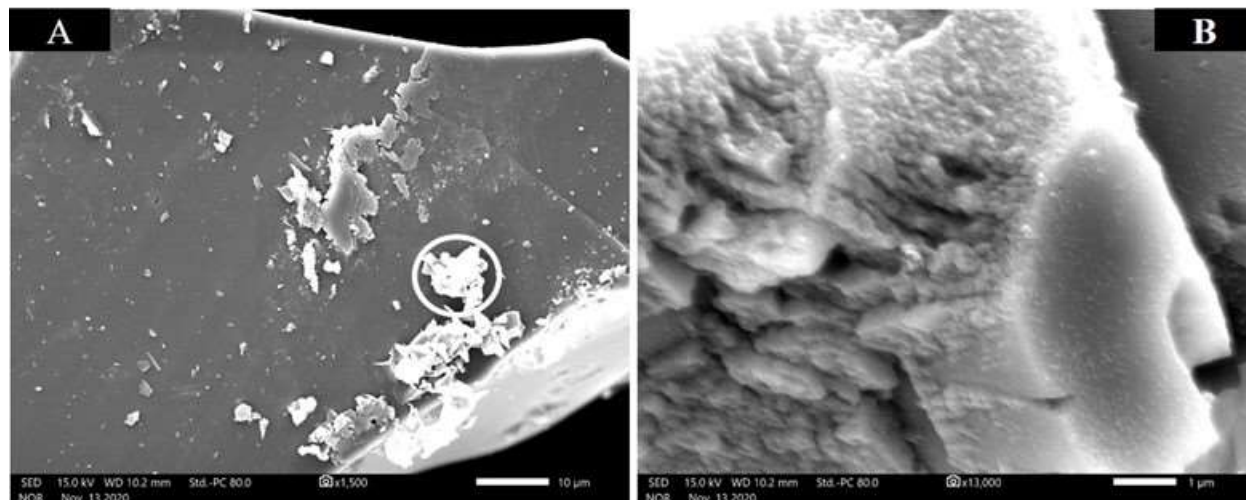


Figure 32. SEM micrographs of glass residue at 90 °C experiment from reactor 2 (x1500) (A) and a magnified image (x13,000) of white precipitate (inside a white circle) (B).

Subtask 1.4: Conclusions

A single-pass flow-through (SPFT) experiment was conducted in support of the Hanford Lysimeter Test Facility (FLTF). The effect of the grout-contacted solution on the glass dissolution was performed at varying temperatures (25 °C, 40 °C, 70 °C, 90 °C). The dissolution rate of the glass was lower in experiments using a grout-contacted solution as the leachate, when compared to a buffer solution with the same pH. The lowered dissolution rate may be due to a common ion effect occurring due to the presence of dissolved species from the grout in the leachate, however further work is ongoing to interpret and understand the controlling mechanisms. In addition, further work is planned to observe glass dissolution rates in grout contacted solution that has also contacted IDF sediment, to garner representative data to be used in the design of a co-located FLTF experiment.

Subtask 1.4: References

- Abraitis, P., Livens, F., Monteith, J., Small, J., Trivedi, D., Vaughan, D., and Wogelius, R., 2000, The kinetics and mechanisms of simulated British Magnox waste glass dissolution as a function of pH, silicic acid activity and time in low temperature aqueous systems: Applied geochemistry, v. 15, no. 9, p. 1399-1416.
- Asmussen, R. M., Pearce, C. I., Miller, B. W., Lawter, A. R., Neeway, J. J., Lukens, W. W., Bowden, M. E., Miller, M. A., Buck, E. C., and Serne, R. J., 2018, Getters for improved technetium containment in cementitious waste forms: Journal of hazardous materials, v. 341, p. 238-247.
- Asmussen, R. M., Saslow, S. A., Neeway, J. J., Westsik, J. H., Rod, K. A., Lonergan, C. E., and Johnson, B., 2019, Development and Characterization of Cementitious Waste Forms for Immobilization of Granular Activated Carbon, Silver Mordenite, and HEPA Filter Media Solid Secondary Waste: Pacific Northwest National Lab.(PNNL), Richland, WA (United States).

- Bacon, D. H., Meyer, P. D., Neeway, J. J., Fang, Y., Asmussen, R. M., and Strickland, C. E., 2018, Field-Scale Lysimeter Studies of Low-Activity Waste Form Degradation: Pacific Northwest National Lab.(PNNL), Richland, WA (United States).
- Harsh, J. B., Dickson, J. O., Pierce, E. M., and Bargar, J., 2015, Technetium (VII) Co-precipitation with Framework Aluminosilicates: Washington State Univ., Pullman, WA (United States).
- Lee, K. P., 2018, Results for Hanford's Integrated Disposal Facility Performance Assessment, RPP-RPT-59958 Rev 1.
- Luo, W., Kelly, S. D., Kemner, K. M., Watson, D., Zhou, J., Jardine, P. M., and Gu, B., 2009, Sequestering uranium and technetium through co-precipitation with aluminum in a contaminated acidic environment: *Environmental science & technology*, v. 43, no. 19, p. 7516-7522.
- Mayordomo, N., Rodríguez, D. M., Schild, D., Molodtsov, K., Johnstone, E. V., Hübner, R., Azzam, S. S. A., Brendler, V., and Müller, K., 2020, Technetium retention by gamma alumina nanoparticles and the effect of sorbed Fe²⁺: *Journal of Hazardous Materials*, v. 388, p. 122066.
- McGrail, B. P., Bacon, D. H., Icenhower, J. P., Mann, F. M., Puigh, R. J., Schaefer, H. T., and Mattigod, S. V., 2001, Near-field performance assessment for a low-activity waste glass disposal system: laboratory testing to modeling results: *Journal of nuclear materials*, v. 298, no. 1-2, p. 95-111.
- Muller, I. S., Matlack, K. S., Pegg, I. L., and Joseph, I., 2017, Enhanced LAW Glass Correlation-Phase 3, VSL-17R4230-1, Rev 0: Hanford Site (HNF), Richland, WA (United States).
- Neeway, J. J., Asmussen, R. M., Cordova, E. A., Lonergan, C. E., Williams, B. D., Leavy, I. I., and Mcelroy, E. M., 2018, FY2017 ILAW Glass Corrosion Testing with the Single-Pass Flow-Through Method: Pacific Northwest National Lab.(PNNL), Richland, WA (United States).
- Pierce, E. M., Richards, E. L., Davis, A. M., Reed, L. R., and Rodriguez, E., 2008a, Aluminoborosilicate waste glass dissolution under alkaline conditions at 40° C: implications for a chemical affinity-based rate equation: *Environmental Chemistry*, v. 5, no. 1, p. 73-85.
- Pierce, E. M., Rodriguez, E. A., Calligan, L. J., Shaw, W. J., and McGrail, B. P., 2008b, An experimental study of the dissolution rates of simulated aluminoborosilicate waste glasses as a function of pH and temperature under dilute conditions: *Applied Geochemistry*, v. 23, no. 9, p. 2559-2573.
- Strachan, D., McGrail, B., and Bourcier, W., 1994, Toward a consistent model for glass dissolution: *Radioactive Waste Management and Environmental Restoration*, v. 19, no. 1-3, p. 129-145.
- Vienna, J. D., Ryan, J. V., Gin, S., and Inagaki, Y., 2013, Current understanding and remaining challenges in modeling long-term degradation of borosilicate nuclear waste glasses: *International Journal of Applied Glass Science*, v. 4, no. 4, p. 283-294.

TASK 2: REMEDIATION RESEARCH AND TECHNICAL SUPPORT FOR SAVANNAH RIVER SITE

Task 2: Executive Summary

Iodine-129 and uranium represent the major radiological risk drivers from contaminants released at the Savannah River Site. Radionuclides previously disposed of through unlined seepage basins as a constituent of acidic, aqueous waste are moving towards Four Mile Branch and Tims Branch wetland with natural groundwater flow, where they may subsequently be interacting with natural organic materials present in the wetland or with humic materials injected for remediation purposes. The fate and transport of uranium, technetium, and iodine in the subsurface are controlled by various environmental factors such as pH, temperature, ORP, etc. A better understanding of the environmental conditions that affect these processes is critical to a more realistic risk assessment.

During FIU Performance Year 10, FIU initiated a research task to investigate the factors controlling the attenuation of iodine in wetland as well as continued research to investigate the impact of humic acid on U mobility at the Savannah River Site. The following subtasks were developed during FIU Performance Year 10.

Subtask 2.1: Environmental Factors Controlling the Attenuation and Release of Contaminants in the Wetland Sediments at Savannah River Site (NEW)

Subtask 2.1: Introduction

The Savannah River Site (SRS) F-Area covers about 6.5 acres and consists of three unlined basins. Approximately 7 billion liters of low-level acidic radioactive waste was discharged into the unlined seepage area basins between 1955-1988. The acidic nature of the liquid waste eventually resulted in groundwater contamination below the basins. Through time, contaminants such as iodine-129 (^{129}I) and other radionuclides have passed through the vadose zone and migrated in the groundwater to exposure points at springs within the wetlands at SRS. In 1986, the Resource Conservation and Recovery Act (RCRA) began regulating the F-Area basins and closure activities began. Low-permeability clay caps were installed over the seepage basins in 1990 to minimize water infiltration (Wan et al. 2012), however, contaminants continued to emerge throughout the F-Area.

From 1997 to 2003, a pump-and-treat system was used to remove groundwater contaminants and reduce the migration of these contaminants. This system removed most radionuclides, apart from tritium, and then reinjected the treated water upgradient of the basins. Due to the high cost of the system (~ \$1.3 million a month), the remediation system had to be replaced. In 2004, a funnel-and-gate with base injection was installed. Barriers were constructed out of grout which consisted of a low swelling clay, fly ash, and sodium hydroxide. This combination of materials created a pozzolan material with low permeability and extended to 20 meters into the Tan clay. To neutralize the acidic groundwater and influence the adsorption/precipitation of metals, a base solution is injected at the gate. To this day, the system continues to be in use. The contaminant of concern, ^{129}I , began to be treated in 2009 through a pilot study, which injected ultra-fine silver chloride (AgCl) particles into the groundwater plume. This study demonstrated that while effective at sequestering ^{129}I , the travel distance of the AgCl particles from the injection wells was less than predicted (Denham et al. 2010a, b). In 2011, 2015, and 2019, AgCl was injected into various

locations around the SRS. Effects of the AgCl particle injections continue to be monitored today. Despite remediation efforts, groundwater concentrations of ^{129}I at SRS wetlands have been reported to be as high as 1618 pCi/L, far surpassing the Environmental Protection Agency's (EPA) maximum contaminant limit of 1 pCi/L (EPA 2002). Iodine poses a significant human health risk due to its tendency to accumulate in the thyroid and its 16-million-year half-life.

Denham et al (2019) proposes to create a system of both the traditional point measurements and new spatially integrative methods to track contaminant mobility. These methods include the use of UAV imaging, spectral analysis, LiDAR, and high-resolution gamma detectors. In order to properly calibrate these instruments, parameters need to be set up that will determine which conditions would cause contaminants to mobilize. By knowing the conditions ahead of time, preventative measures can be taken to limit the remobilization of contaminants. Zones of vulnerability within the F-Area system are those locations which contamination is expected to exist for long periods of time (Denham et al. 2019). The three zones are currently (1) the basin soils & vadose zone, (2) the treatment zones in the gates, and (3) the SRS wetlands. In the SRS wetlands, ^{129}I has been identified as a vulnerable contaminant because of its complex chemical behavior. ^{129}I can be found as iodide (I^-) in acidic groundwater, and as iodate (IO_3^-) in neutral groundwater (Kaplan et al. 2011). Sorption of both species occurs at lower pH values, but iodide sorption is significantly stronger than iodate (Emerson et al. 2014). Iodine has also been found to strongly sorb onto organic-rich sediments of the F-Area wetlands (Zhang et al. 2011), particularly to water-extractable colloids (Xu et al. 2011), which are more susceptible to being released into groundwater.

The SRS wetlands is a complex and dynamic environment. While pH appears to be the primary factor affecting adsorption of contaminants, other factors may play a role as well. There are various short and long-term processes that affect the mobilization and attenuation of contaminants at the SRS wetlands. Intense rainstorms can cause erosion of wetland surface soils. In one case, particulate-bound uranium was released from flood plain sediments at much higher masses during intense rainstorms than at baseflow conditions (Batson et al., 1996).

Longer-term processes include seasonal changes, such as the fluctuation from wet and dry conditions, and have a profound influence on the redox conditions of the soil and contaminant behavior. Soils can also change from aerobic to anaerobic conditions as a result of flooding, causing less oxygen diffusion into soils. The rapid consumption of oxygen by roots, microorganisms, and soil reductants (Howeler and Bouldin, 1971) causes anaerobic microorganisms to use alternative electron acceptors for respiration (Ponnamperuma et al., 1967). The presence of abundant organic matter and vegetation mixing with rain and groundwater can also have an effect on the mobilization of contaminants.

Subtask 2.1: Objectives

The reason for seasonal variation between ^{129}I concentrations is still unknown. It has been predicted that this oscillating nature is the result of increased microbial degradation during warmer periods, but this theory has yet to be tested. Therefore, this research has 3 objectives: (I) Understand the reaction rates of ^{129}I and the sorption capacity of SRS sediment, (II) Understand the effects of successive aerobic and anaerobic conditions on ^{129}I attenuation and mobility, and (III) Understand how different temperatures affect ^{129}I attenuation and mobility.

Subtask 2.1: Methodology

Soil Preparation and Particle Classification

950 grams of SRS wetland soil was dried in an oven (Figure 33) at 30°C until the weight of the soil was constant, after which it was stored in a desiccator to be used in the experiments. 50 grams of dried soil was then sieved using U.S. Standard Testing Sieves according to USDA classifications (USDA 2012). Sediment that passed through a #10 sieve but not #230 sieve was classified as sand; sediment that passed through the #230 sieve but not #1000 sieve was classified as silt; and finally, sediment that passed through the #1000 sieve was classified as clay. This analysis was conducted in triplicate to get an average value and standard deviation for each fraction.



Figure 33. SRS soil samples being dried in the oven.

Soil pH

The procedure outlined by the USDA (2014) was recreated to measure the natural pH of the soil as follows: A soil paste was created, consisting of a 1:2 0.01 M CaCl₂ mixture. When deionized water is used, it is possible that the pH may be lower than it really is because of the soluble salt content of soil. By using CaCl₂, the soluble salt content of the soil can be overcome. 20 grams of soil were mixed with 40mL 0.01 M CaCl₂ solution. The pH electrode was calibrated and washed with DI water prior to use. The pH electrode was then gently lowered into the soil paste and the pH was recorded after the reading stabilized.

X-Ray Diffraction

Mineralogy of the SRS wetland soil was determined using X-Ray Diffraction (XRD) via a Bruker AXS D2 Phaser. Three scans were run on each of the bulk ($\leq 2\text{mm}$), sand (2mm - 63 μm), and silt fraction (63 μm - 2 μm) of the soil. The measurement conditions of the scans are shown in Table 22.

Table 22. Measurement Conditions of XRD scans

Parameter	Value/Condition
Scan Type	<i>Coupled TwoTheta/Theta</i>
Scan Mode	<i>Continuous PSD fast</i>
Start	<i>5.002</i>

End	84.993
Step Size	0.020
Time/Step	0.5 s

Finally, the triplicate scans were consolidated into one average scan for each particle fraction, in which the peaks were fitted according to the ICDD database.

Brunauer-Emmett-Teller Surface Area Analysis

The specific surface area and the pore volume of the bulk fraction of the SRS wetland sediment was determined by the nitrogen adsorption Brunauer-Emmett-Teller (BET) method at FIU’s Department of Mechanical Engineering using a Micrometrics TriStar II 3020 instrument. Three samples were analyzed with BET to calculate average value. Only the bulk fraction was analyzed since future experiments will only be using this fraction of the soil.

X-Ray Fluorescence in Scanning Electron Microscopy

X-Ray Fluorescence in Scanning Electron Microscopy (SEM-XRF) was performed using a JEOL JSM 5900LV coupled with a Bruker XTrace on the bulk ($\leq 2\text{mm}$), sand ($2\text{mm} - 63\mu\text{m}$) and silt ($63\mu\text{m} - 2\mu\text{m}$) fraction of the soil. Three different particles were selected from each fraction. For each particle, three different points were selected to perform XRF analysis.

Subtask 2.1: Results and Discussion

Particle Classification

Particle size classification results are presented in Table 23. Sand was found to be the primary component of the SRS soil, accounting for up to 98.55% of the total mass. Approximately 1% of silt is present in the soil while only 0.05% of clay was found in the soil. According to the USDA textural classification (1951), this sediment can be classified as a sand. One fact to consider is that only 50 grams of soil were used in this experiment. If a larger mass of soil had been used, a larger fraction of silt and clay could likely have been accounted for.

Table 23. Average and Standard Deviation of Soil Fractions. Mass of each fraction was divided by total mass of the sample. The values were then combined into one average value.

Soil fraction	Average (%)
Sand	98.55% \pm 0.81
Silt	0.97% \pm 0.62
Clay	0.05% \pm 0.02

Soil pH

A soil pH experiment was conducted by following the procedure described in the methodology section. Following the calibration of the pH electrode and the creation of the soil paste, the pH electrode was lowered into the paste. Once the meter had stabilized, the pH recorded was found to be 5.67.

X-Ray Diffraction

The mineralogical composition of the bulk, sand, silt, and silt + clay fractions are shown in Figure 34 - Figure 37. A summary of the results may also be found in Table 24. The mineralogical composition of the SRS wetland soil used in this study is mostly agreeable with previous studies. More recent findings have stated that SRS wetland soil is primarily composed of quartz and kaolinite (Dong *et al.*, 2012). An earlier report by Denham (1999) also found that kaolinite was the dominant clay present in SRS wetland soil. Unlike the results from this study, however, Denham found illite and smectite in the soil, although in much smaller quantities than kaolinite. Gibbsite is thought to have been found primarily in modified soils (Serkiz *et al.* 1995), but metal oxyhydroxides, such as gibbsite, have been naturally found in the SRS aquifer (Serkiz & Thibault, 1999). It cannot be concluded whether the gibbsite found in this sample of SRS wetland sediment is modified or natural, but both options should still be considered for future experiments.

Table 24. Summary of XRD Results (percentage of each mineral found in each fraction of soil)

Particle fraction	Mineral	Percent (%)
Bulk	<i>Quartz</i>	95.8
	<i>Kaolinite</i>	3.0
	<i>Goethite</i>	1.2
Sand	<i>Quartz</i>	94.9
	<i>Kaolinite</i>	5.1
Silt	<i>Quartz</i>	79.3
	<i>Kaolinite</i>	20.7
Silt + Clay	<i>Quartz</i>	89.2
	<i>Kaolinite</i>	8.2
	<i>Gibbsite</i>	2.6

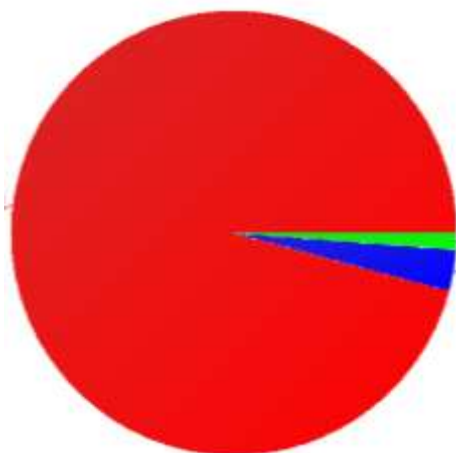


Figure 34. Bulk fraction mineralogy. Red - Quartz; Blue- Kaolinite; Green - Goethite

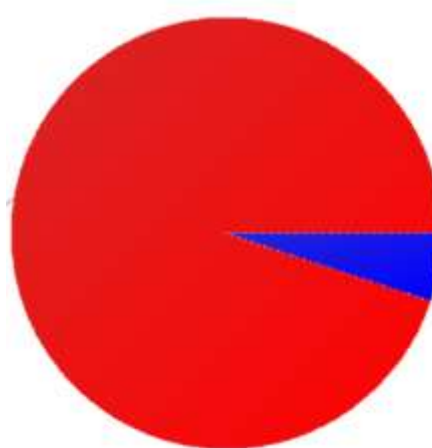


Figure 35. Sand fraction mineralogy. Red - Quartz, Blue - Kaolinite

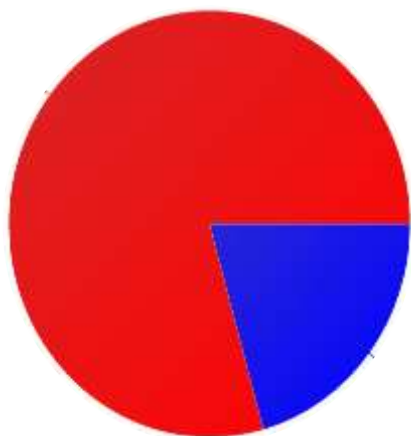


Figure 36. Silt fraction mineralogy. Red - Quartz; Blue - Kaolinite

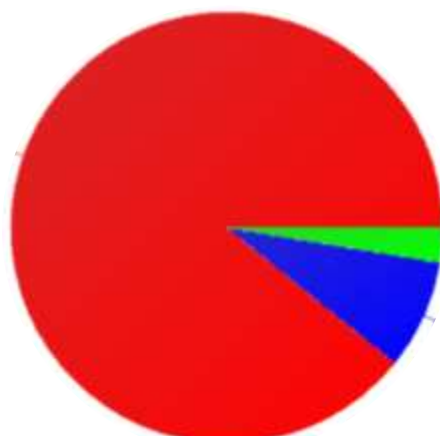


Figure 37. Silt + clay mineralogy. Red - Quartz; Blue - Kaolinite, Green - Gibbsite

Brunauer-Emmett-Teller Surface Area Analysis

The BET Surface Area Analysis in this study found an average specific surface area (SSA) of $7.49 \pm 0.37 \text{ m}^2/\text{g}$ (Table 25). This information will be particularly useful when considering the sorption capacity of the wetland sediment.

Table 25. BET Surface Area Analysis results of triplicate samples of bulk fraction sediment

	#1	#2	#3	Average
<i>Sample Mass (g)</i>	1.3836	2.0282	2.0831	1.83 ± 0.39
<i>Surface Area (m²/g)</i>	7.117	7.8628	7.5048	7.49 ± 0.37
<i>Pore Volume (cm³/g)</i>	0.025711	0.02843	0.027292	0.027 ± 0.001
<i>Pore Size (Å)</i>	144.5066	144.6311	145.4633	144.86 ± 0.52

X-Ray Fluorescence in Scanning Electron Microscopy

The results of the SEM-XRF analysis for the bulk ($\leq 2\text{mm}$) of the sediment are shown in Table 26. The SEM images of bulk, sand and silt fractions are shown in Figure 38, Figure 39 and Figure 40 respectively. These results are highly agreeable with the XRD results. Given that quartz (SiO_2) and kaolinite ($\text{Al}_2 \text{Si}_2 \text{O}_5 (\text{OH})_4$) are found in the greatest quantities, it makes sense that SEM-XRF would have oxygen, silicon, and aluminum taking up the largest percentage of the mass.

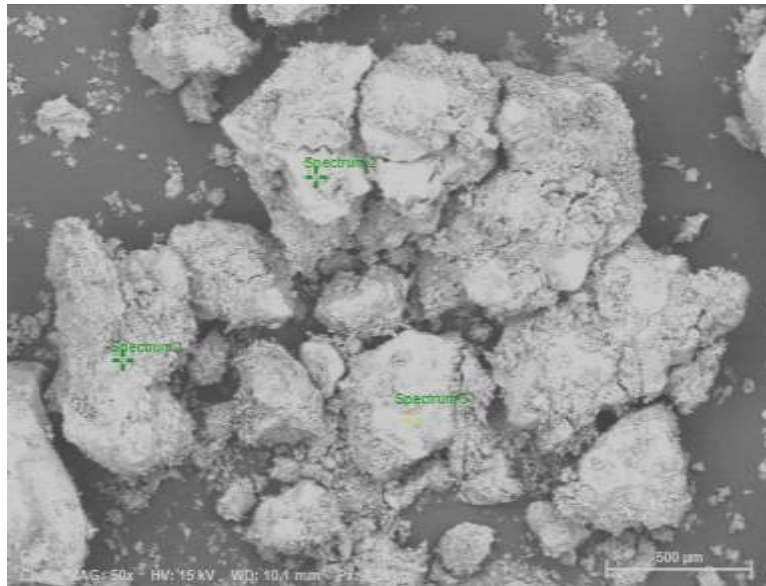


Figure 38. Scanning Electron Microscope image from particle from the bulk fraction of the SRS soil, with three separate points selected for XRF analysis.

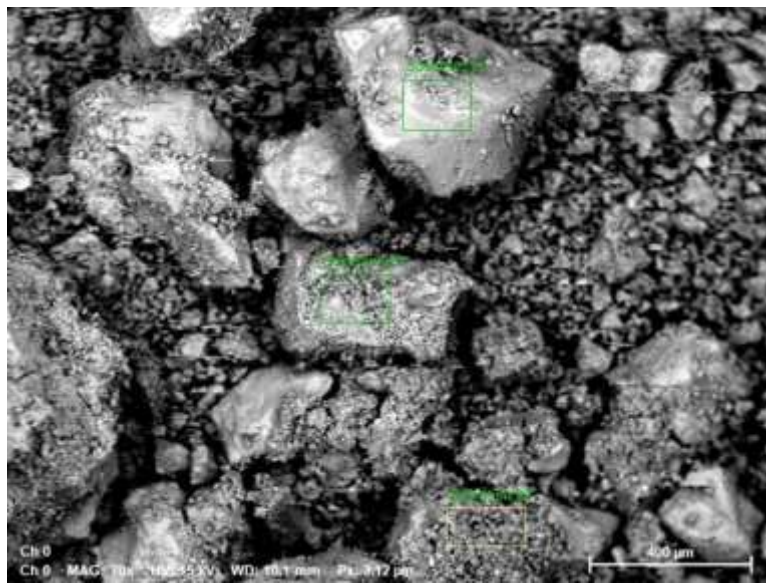


Figure 39. Scanning Electron Microscope image from particle from sand fraction of the SRS soil, with three separate points selected for XRF analysis.

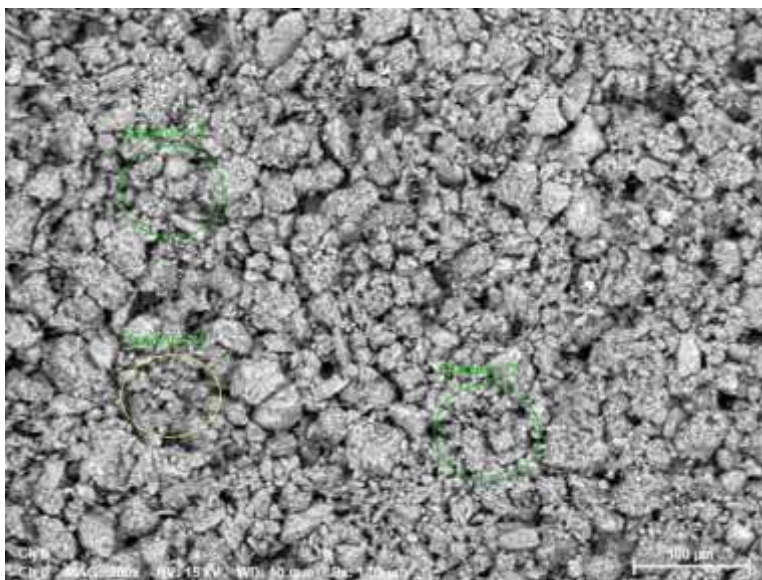


Figure 40. Scanning Electron Microscope image from particle from silt fraction of the SRS soil, with three separate points selected for XRF analysis.

Table 26. Summary of Results from SEM-XRF Analysis (Results of each spectra, average of the three spectra and the standard deviation are shown)

<i>Element</i>	<i>Bulk Mass %</i>	<i>Sand Mass %</i>	<i>Silt Mass %</i>
<i>O</i>	48.07 ± 1.66	45.03 ± 1.37	48.73 ± 5.45
<i>Si</i>	25.85 ± 6.98	24.89 ± 2.65	29.27 ± 0.00
<i>Al</i>	16.65 ± 6.06	16.31 ± 1.13	13.98 ± 0.08
<i>Fe</i>	6.22 ± 2.48	9.01 ± 2.99	6.16 ± 1.75
<i>Ti</i>	1.29 ± 1.41	1.29 ± 0.41	0.80 ± 0.13
<i>K</i>	0.58 ± 0.44	0.56 ± 0.14	0.38 ± 0.12
<i>Ca</i>	0.43 ± 0.33	0.29 ± 0.06	0.10 ± 0.08
<i>P</i>	0.35 ± 0.26	0.31 ± 0.06	0.19 ± 1.27
<i>Mg</i>	0.36 ± 0.24	0.24 ± 0.04	0.23 ± 0.12
<i>Na</i>	0.09 ± 0.14	0.06 ± 0.05	0.09 ± 0.04
<i>S</i>	0.10 ± 0.06	0.05 ± 0.03	0.06 ± 5.67

Subtask 2.1: Conclusions & Future Studies

The characterization of the SRS wetland soil will greatly assist future batch and reactor experiments by providing data that will allow better interpretation of future results. Batch experiments will be conducted to further understand the kinetics of iodine in SRS soil, as well the sorption capacity of the soil. The effect of pH on iodine desorption will also be investigated. Finally, the effect of successive aerobic and anaerobic conditions will be studied through the use of a biogeochemical microcosm.

Subtask 2.1: References

- Batson, V. L., P. M. Bertsch, and B. E. Herbert. 1996. Transport of Anthropogenic Uranium from Sediments to Surface Waters during Episodic Storm Events. *J. Environ. Qual.* 25:1129-1137. doi:10.2134/jeq1996.00472425002500050028x
- Denham M.E., Eddy-Dilek C.A., Wainwright H.M., Thibault J., Boerstler K. A New Paradigm for Long Term Monitoring at the F-Area Seepage Basins, Savannah River Site. 2019. No.SRNL-ST-2019-00019. Savannah River Laboratory, Aiken, S.C.
- Denham, M., R. Nichols, M. Bach, and M. Millings. 2010a. Laboratory Tests of an Injectable Silver Chloride Amendment for Treatment of I-129 in Groundwater. SRNL-STI-2010-00179, Savannah River National Laboratory, Aiken, SC.
- Denham, M., M. Millings, and J. Noonkester, 2010b. Post-Injection Assessment of the Silver Chloride Field Demonstration for Treatment of I-129 in Groundwater at the F-Area Seepage Basins. SRNL-TR 2010-00367.
- Emerson, H.P., C. Xu, Y.F. Ho, S. Zhang, K.A. Schwehr, M.Lilley, D.I. Kaplan, P.H. Santschi, and B.A. Powell. 2014. Geochemical controls on iodine uptake and transport in Savannah River Site subsurface soils. *Applied Geochemistry*, 45, 105-113.
- Howeler, R.H., Bouldin, D.R., 1971. The diffusion and consumption of oxygen in submerged soils. *Soil Science Society of America Journal* 35, 202-208.
- Kaplan D.I., Roberts K.A., Schwehr K.A., Lilley M.S., Brinkmeyer R., Denham M.R., DiPrete D., Li H., Powell B.A., Xu C., Yeager C.M., Zhang S., and Santschi P.H. 2011. Evaluation of a Radioiodine Plume Increasing in Concentration at the Savannah River Site. *Environmental Science & Technology*. 45, 489-495.
- Killian, T.H., Kolb, N.L., Corbo, P., Marine, I.W., 1985. F-Area Seepage Basins, Rep. No.SPST 85-704, E.I. du Pont de Nemours & Co., Savannah River Laboratory, Aiken, SC.
- Köhler, F., Riebe, B., Scheinost, A.C., König, C., Hölzer, A., Walther, C., 2019. Sorption of iodine in soils: insight from selective sequential extractions and X-ray absorption spectroscopy. *Environmental Science and Pollution Research* 26, 23850-23860.
- Otasaka S., Schwer K.A., Kaplan D.O., Roberts K.A., Zhang S., Xu C., Li H., Ho Y., Brinkmeyer R., Yeager C.M., and Santschi P.H. 2011. Factors controlling mobility of 127I and 129I species in an acidic groundwater plume at the Savannah River Site. *Science of the Total Environment*, 19, 3857-3865.
- Ponnamperuma, F.N., Tianco, E.M., Loy, T., 1967. Redox equilibria in flooded soils: I. The iron hydroxide systems. *Soil Science* 103, 374-382.
- Sams A.C. 2017. Geochemical Controls of Iodine Sorption to Wetland Sediments. All Theses. 2771. https://tigerprints.clemson.edu/all_theses/2771
- U.S. Environ. Prot. Agency, [Report] EPA. 2002. Cancer Risk Coefficients for Environmental Exposure to Radionuclides, Fed. Guid. Rep. 13, CD Supplement, Revised. EPA 402-R-99 001. <http://www.epa.gov/radiation/federal/techdocs.html>
- United States Department of Agriculture, Natural Resources Conservation Service. 2014. Soil survey laboratory methods manual. Ver. No. 5.0. Soil Survey Investigations Report No. 42.

- Watts, M. J., & Mitchell, C. J. 2008. A pilot study on iodine in soils of Greater Kabul and Nangarhar provinces of Afghanistan. *Environmental Geochemistry and Health*, 503-509.
- Wan J., Tounaga T.K., Dong E., Denham M.E., Hubbard S.S. 2012. Persistent Source Influences on the Trailing Edge of a Groundwater Plume, and Natural Attenuation Timeframes: The F-Area Savannah River Site. *Environ. Sci. Technol.*, 46, 8, 4490-4497.
- Yu K., Rinklebe J. 2011. Advancement in Soil Microcosm Apparatus for Biogeochemical Research. *Ecological Engineering*, 12, 2071-2075.
- Zhang S., Schwer K.A., Ho Y.F., Xu C., Roberts K.A., Kaplan D.I., Brinkmeyer R., Yeager C.M., Santschi P.H. 2010. A Novel Approach for the Simultaneous Determination of Iodide, Iodate, and Organo-Iodide for 127I and 129I in Environmental Samples Using Gas Chromatography-Mass Spectrometry. *Environ. Scie Technol.*, 44, 9042-9048.

Subtask 2.2: Humic Acid Batch Sorption Experiments with SRS Soil

Subtask 2.2: Introduction

In the 1950s, Savannah River Site (SRS) in Aiken, South Carolina became a nuclear defense production facility during the Cold War. SRS produced plutonium and irradiated fuel, which then contributed to the production of radioactive and acidic hazardous waste (Evans, et. al., 1992). Approximately 1.8 billion gallons of acidic waste containing low-level radionuclides and dissolved heavy metals were disposed of in SRS F/H Area seepage basins. This led to the unintentional creation of highly contaminated groundwater plumes consisting of radionuclides and chemicals with an acidic pH range of 3 to 5.5, which contributed to the mobility of several constituents of concern (COC) such as Tritium, Uranium-238, Iodine-129, and Strontium-90 in the F-Area plume. The groundwater remains acidic with uranium concentrations surpassing the Environmental Protection Agency (EPA) maximum contaminant levels (Dong et. al., 2012). Previously, SRS implemented a few processes to assist in the removal of contaminants from the groundwater like the pump-and-treat and re-inject system. Implemented in 1997, this system pumped downgrade groundwater to a water treatment facility and then re-injected upgrade within the aquifer. However, the pump and treat system proved to be ineffective and was swapped out in 2004 for a funnel-and-gate process that injected sodium hydroxide into the groundwater, creating a treatment zone with a higher pH to reverse the acidic nature of the contaminated sediments while producing a negative net charge on the sediment particles. This amplified the adsorption of cationic contaminants on the sediment and resulted in the decrease of Sr-90 and U-238 concentrations but had no effect on the treatment of iodine. To maintain the pH neutral within the treatment zone, systemic injections were required. Carbonate forms strong complexes with uranium and could remobilize uranium that was already adsorbed within the treatment zone (Gudavalli et. al., 2013).

Humic substances (HS) are major components of soil organic matter, which are polyfunctional organic macromolecules that are formed from the decomposition of biomass or dead organic matter (Trevisan, et. al., 2010). Humic substances can be divided into three main fractions: humin, which is insoluble at all pHs, humic acid (HA), soluble at pHs greater than 3.5, and fulvic acids, which are soluble at all pHs (Choppin et. al., 1992). Humic acid is an important ion exchange and metal complexing ligand with a high complexation capacity, allowing it to chemically bind to metals and influence their migration behavior (Davis et. al., 2002). Previous studies suggest that the sorption of U(VI) in the presence of humic acid is a complex process (Perminova et. al., 2002).

Ivanov et al (2012) studied U(VI) sorption onto bentonite with and without humic acid and proved enhanced uranium sorption at pHs lower than 3.8, while it was reduced at pHs above 3.8. In another study, U(VI) sorption proved to be influenced by pH, the U(VI) concentration, humic acid, and inorganic carbon species (Krepelova et al., 2007).

A chemically modified humate, commercially known as KW-15 referred here as modified humic acid (mod-HA), is being tested for its use in remediation techniques to reduce the mobility of uranium in the subsurface at SRS. This project focuses on studying the characterization of mod-HA and the sorption of uranium in the presence of humate onto SRS sediments, with parameters set to evaluate the effect of pH, time, and concentrations of U and HA. This study determines if humic substances containing humic/fulvic acids of different molecular weights can be used to control uranium mobility and understands the different interactions and mechanisms occurring in the presence of the modified humic acid. These interactions affect the adsorption of uranium onto the sediments that impacts U(VI) mobility in SRS groundwater. This study evaluates if humic substances could be used for in-situ remediation of uranium in acidic environment and determine optimal conditions for U(VI) removal from the aqueous phase.

This research also suggests if modified humic substances can be used as potential amendments at other DOE sites, where soil and groundwater conditions are less acidic compared to SRS.

Subtask 2.2: Objectives

The objective of this research is to investigate, via batch experiments, the sorption behavior of modified humic substances and evaluate the effect of sorbed humic substances on uranium sorption to support groundwater remediation strategies. The outcome of these studies will help to determine approaches to deploy humate technology under varying site-specific conditions.

Subtask 2.2: Methodology

Materials:

This study utilized sediment samples that were collected from the F-Area at SRS (FAW1 70-90 ft) and sieved. A fraction ≤ 2 mm was used in the experiments. This sediment was chosen due to its comparability to the soil composition in the uranium contaminated aquifer layer. For U(VI), a commercial 1000 ppm uranyl stock solution in 2% nitric acid was used. A humate stock solution consisting of 1000 mg of mod-HA in 1000 mL of deionized water (DIW) was prepared for use in the experiments.

Experimental Procedures:

Characterization of Mod-HA

The attenuated total reflectance Fourier transform infrared spectroscopy (ATR-FTIR) spectra of the mod-HA and Huma-K were obtained using an Agilent FTIR (Santa Clara, CA, USA) in the spectral range of 400 - 4000 cm^{-1} with 16 scans per spectrum. The zeta potentials and hydrodynamic sizes of mod-HA and Huma-K were determined using a Malvern Zetasizer Nano Z (Malvern, Worcestershire, United Kingdom). The surface area of humic substances were measured by the Brunauer-Emmett-Teller (BET). The differential potentiometric titrations (DPT) provide useful information on the protonation/deprotonation properties of functional groups, which can be involved in the sorption process.

Humate Sorption Experiments on SRS Sediment

Batch humate sorption experiments were conducted in triplicates, with 200 mg of SRS sediments spiked with 50 ppm of mod-HA with a total volume of 20 mL in 50 mL polypropylene centrifuge tubes. Samples were pH adjusted to pH 4 daily using 0.1 M HCl or 0.1 M NaOH and placed on a platform shaker at 100 rpm to equilibrate. After 5 days, samples were centrifuged at 2700 rpm for 30 minutes and the supernatant was analyzed via a UV-Vis spectrophotometer.

To study the effect of pH (4-8) on mod-HA, two sets of triplicate samples were prepared with 50 ppm of mod-HA (i) in the presence of 200 mg SRS sediment, and (ii) with the absence of sediment. The samples without sediment provide information on humate precipitation occurring at each pH, while the samples with sediment provide the total humate removal due to sorption and precipitation.

For kinetic studies, 20 mL of 50 ppm mod-HA samples were prepared with 200 mg of SRS sediments and were equilibrated at different time intervals, ranging from 30 minutes to 10 days. Samples were pH adjusted to pH 4 daily and placed on the platform shaker for the allocated time. Afterwards, the samples were centrifuged and the supernatant was analyzed via UV-Vis.

For equilibrium studies, triplicate samples were prepared with mod-HA concentrations ranging from 10 - 700 ppm with a total volume of 20 mL. The samples were pH adjusted daily to pH 4 and placed on a platform shaker for 5 days and then centrifuged and analyzed on a UV-Vis. Another set was prepared without sediments to distinguish precipitation from sorption.

To study desorption, 20 mL triplicate samples were prepared with 200 mg SRS sediments and 50 ppm of mod-HA, which were left on the platform shaker for 5 days, and then centrifuged for 30 minutes at 2700 rpm. The supernatant was removed and analyzed on the UV-Vis, while 20 ml of fresh DIW was added to mod-HA amended sediment. These samples were pH adjusted daily to pH 4 and placed on a platform shaker for 5 days. They were then centrifuged at 2700 rpm for 30 minutes and the supernatant removed for analysis on the UV-Vis. The desorption experiment was repeated three time by removing supernatant and adding fresh DIW to study the effect of multiple desorption cycles on humate sorption.

U(VI) Sorption Onto SRS Sediment

Uranium sorption studies were conducted by preparing a set of 20 mL samples in triplicates with 50 ppm of mod-HA, and with 200 mg of SRS sediment. The samples were pH adjusted daily to pH 4 and left on the platform shaker at 100 rpm for 7 days. The samples were centrifuged, and the supernatant removed (analyzed on the UV-Vis) and spiked with 20 ml of 0.5 ppm U(VI) solution. Samples were pH adjusted daily to pH 4-8 and placed on a platform shaker at 100 rpm for 7 days. Samples were centrifuged for 30 minutes at 2700 rpm and the supernatant removed and analyzed on the ICP-MS for remaining uranium in the supernatant solution.

For kinetic studies, 20 mL triplicate samples were prepared with 0.5 ppm of U(VI) and 200 mg of SRS sediments coated with mod-HA and placed on the platform shaker for different intervals ranging from 30 minutes to 10 days. After the designated time, the sample was centrifuged for 30 minutes at 2700 rpm, and the supernatant analyzed on the ICP-MS.

Uranium equilibrium studies were conducted by preparing 20 mL triplicate samples with 200 mg of SRS sediment coated with mod-HA and U(VI) ranging from 0.025 ppm to 1 ppm. The samples were pH adjusted to pH 4 daily for 7 days and left on the platform shaker at 100 rpm. They were then centrifuged, and the supernatant analyzed on the ICP-MS.

Desorption uranium studies called for preparing 20 mL triplicate samples with 50 ppm of mod-HA and 200 mg of SRS sediment that were pH adjusted daily to pH 4 and left on the platform shaker at 100 rpm for 5 days. They were then centrifuged for 30 minutes at 2700 rpm and the supernatant removed for analysis and replaced with 20 ml of 0.5 ppm of U(VI). These were then pH adjusted daily to pH 4 and left on the platform shaker at 100 rpm for 7 days. They were then centrifuged for 30 mins at 2700 rpm and the supernatant removed for analysis and replaced with 20 mL of DIW to record the uranium desorption process. The samples were pH adjusted daily to pH 4-8 and left on the platform shaker at 100 rpm for 7 days. After the 7 days, the samples were centrifuged at 2700 rpm for 30 minutes and the supernatant removed and analyzed on the ICP-MS.

Subtask 2.2: Results and Discussion

Characterization of mod-HA

In ATR-FTIR spectra (Figure 41), the broad peak at 3000-3600 cm^{-1} denotes to the O-H stretching of the phenols, alcohols, and carboxylic acids for mod-HA and Huma-K. The sharp bands at 2916 and 2848 cm^{-1} can be attributed to the aliphatic sp^3 C-H stretching. The band at 1559 cm^{-1} in mod HA corresponds to the asymmetric C=O stretching of carboxylate anion (COO^-) and the N-H of HA (Jiang, Cai et al. 2014). The energies of the COO^- absorption band depend on several factors such as the electron density, intra- and inter-molecular H bonding, interactions with metal ions, and coupling with other vibrational modes in the molecule. The study reported by Hay and Myneni (Hay and Myneni 2007) showed that the structural environment of the carboxyl group affects the energies of the asymmetric stretching vibrations of the COO^- in natural organic molecules. Due to a lower COO^- vibrational energy, 1559 cm^{-1} , we conclude that the dominant fraction of carboxyl groups in our mod HA and Huma-K are substituted aromatics. The COO^- symmetric stretching frequency and N-H of our HAs is 1379 cm^{-1} , which is within the range of 1368 and 1382 cm^{-1} for the reported natural organic molecules (Hay and Myneni 2007). The strong peak at 1100 cm^{-1} denotes the C-O stretching vibration of the humic substances. The peaks at 1100–925 cm^{-1} can also be assigned for the Si-O-Si and Si-O-C moieties (Zhou, Huang et al. 2018).

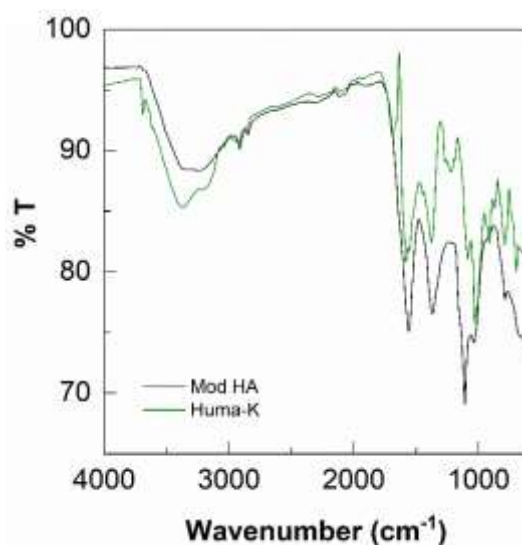


Figure 41. FTIR Spectra of mod-HA and Huma-K.

The zeta potentials of both humate materials is shown in Figure 42. The zeta potential of Huma-K and mod-HA shows the same trend: at higher pH range, HA is more negatively charged compared

to the lower pH range indicating higher stability than the lower pH range. Figure 43 shows the averaged hydrodynamic size of Huma-K in water is 330.1 nm with a little amount of aggregate at 5305 nm, while approximately 65% of modified-HA hydrodynamic size in water is 428.3 nm, 29% of mod-HA is 122.3 nm, and a small amount of aggregate at 5285 nm. The BET analysis shows the surface area of mod-HA is significantly larger than Huma-K, 1.1507 m²/g and 0.0277 m²/g, respectively. The low surface area of Huma-K could be attributed to the impurities leached from leonardite during the alkaline extraction of humic substances (Gonzalez-Raymat et al. 2018).

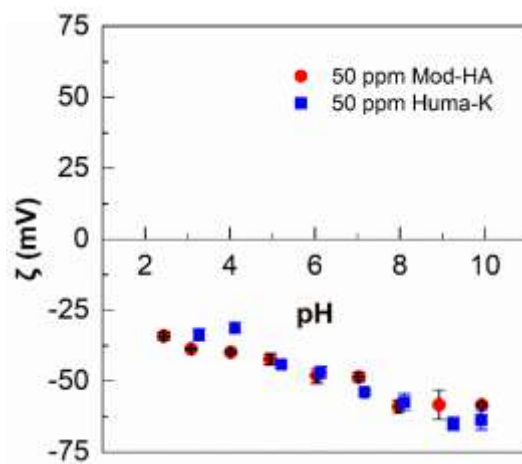


Figure 42. Zeta potential of mod-HA (●) and Huma-K (■).

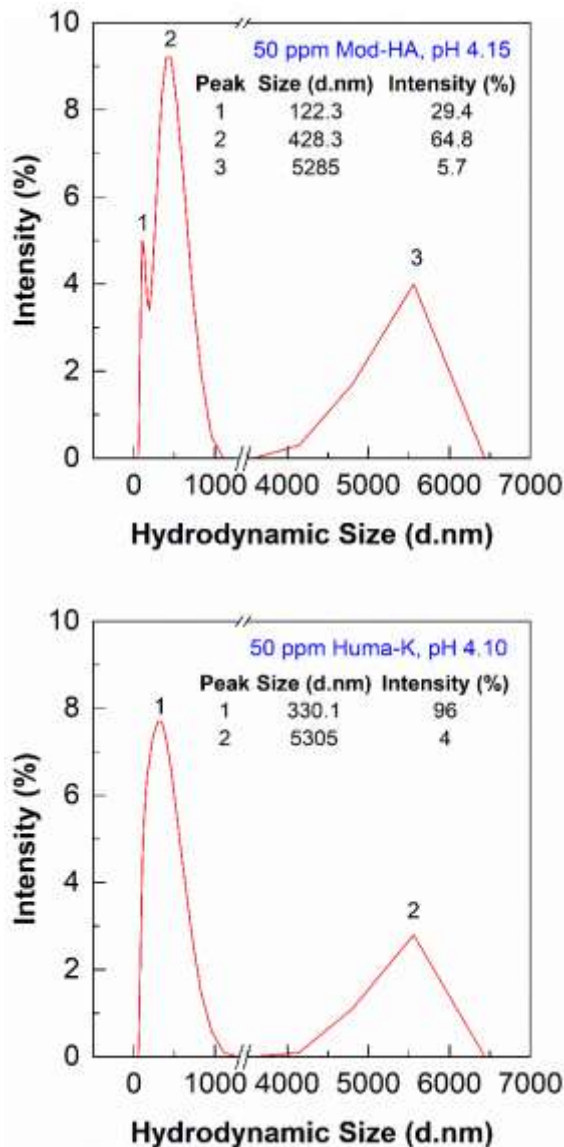


Figure 43. Hydrodynamic sizes of mod-HA (top) and Huma-K (bottom).

Figure 44 shows the differential potentiometric titration (DPT) of mod-HA and the electrolyte. In the DPT curve, the band at pH ~ 9.5 to 10.2 in mod-HA corresponds to hydroxyl/phenolic functionality of HA. The DPT curve of mod-HA reveals a broad peak at pH ~ 3 to 6.8 and is denoted to the carboxylic groups arranged in different configurations within mod-HA. The peaks at 7.1 and 10.5 can be assigned as the pKa values of carbonic acid (H₂CO₃). The mod-HA could have been extracted from leonardite using highly alkaline solution. The HCO₃⁻ could have formed because of highly alkaline solutions where the CO₂ in the atmosphere reacted with OH⁻ and then precipitated in the mod-HA. The peak at pH ~ 6.8 can correspond to the silanol group of the mod-HA (Gonzalez-Raymat et al. 2018).

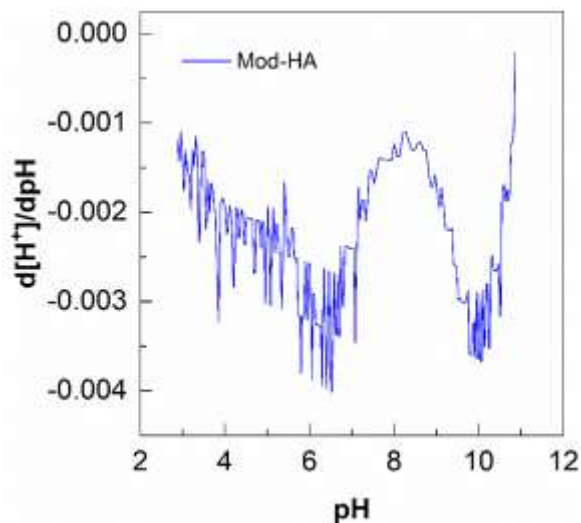


Figure 44. Potentiometric titration of mod-HA.

Humate Experiments

Effect of pH:

To study the effect of pH on humic acid sorption on to SRS sediment, samples with and without sediment were prepared to determine the precipitation and sorption. The samples with sediment provided total removal percentage (sorption + precipitation) of humate while the samples without sediment determined the precipitation occurring. Data presented in Figure 45a shows that the total humate removal and precipitation decreases with a pH increase. We can take the difference of the precipitation data from the total removal to calculate how much of the mod-HA is sorbing onto the sediment. Most removal occurred at pH 4 with 75% of humate removal, where 50% is attributed to precipitation, resulting in 25% removal due to sorption. At pH 8, 40% total removal and 39.4% of that removal due to precipitation was observed resulting in only 0.6% removal due to sorption. This is because at higher pH values, humic substances tend to be more soluble. In Figure 45b the mod-HA sorption data is compared to the Huma-K sorption which displayed a slightly higher sorption at pH 4, but then mod-HA from pH 5 to 8 shows more sorption than Huma-K. The percent difference is very small, the sorption is similar across both humate substances. This data is essential to determine which humic substance is most effective to our objectives.

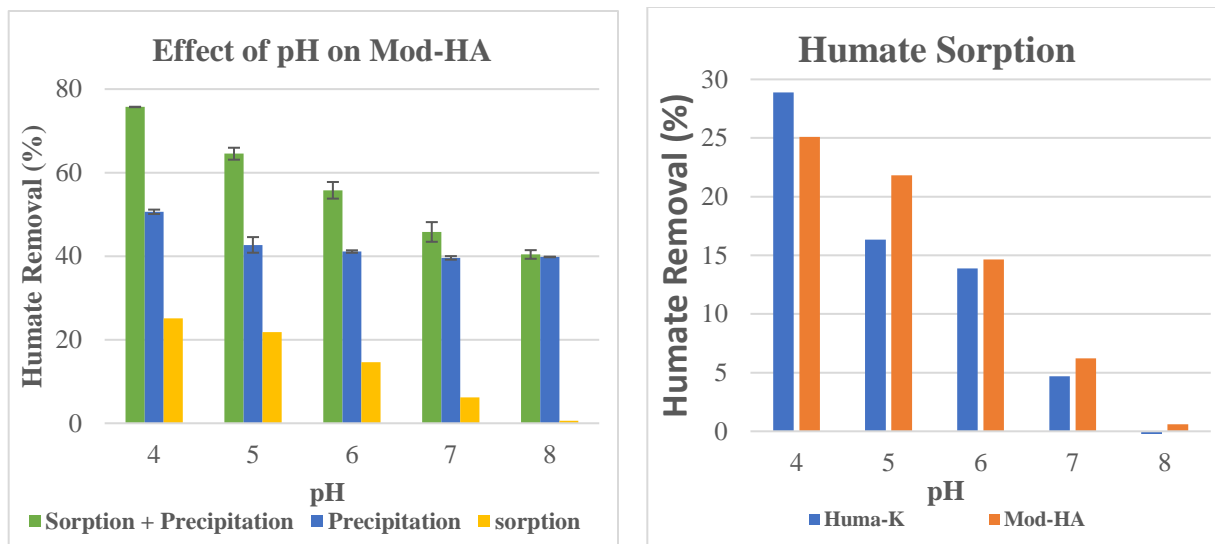


Figure 45. Effect of pH for humate substances (a) mod-HA (b) Huma-K and Mod-HA comparison.

Kinetics:

A kinetic model can determine if sorption is the rate-limiting step in the sorption process (Largitte and Pasquier 2016). The sorption can be calculated using the following equation:

$$q_t = (C_i - C_t) \frac{V}{w}$$

Where:

qt = amount of humate adsorbed to the sediments at time t

Ci = initial concentration of Humate

Ct = concentration of Humate at any time

V = total volume of solution used in the sample

w = weight of SRS sediment in the sample

After conducting kinetic experiments, as described before, the results displayed in Figure 46a indicate that mod-HA had a rapid initial sorption and reached equilibrium in 24 hours. In Figure 46b, the mod-HA and Huma-K kinetic sorption studies are compared and shows equilibrium being reached quicker by mod-HA, while Huma-K took about 5 days to reach equilibrium.

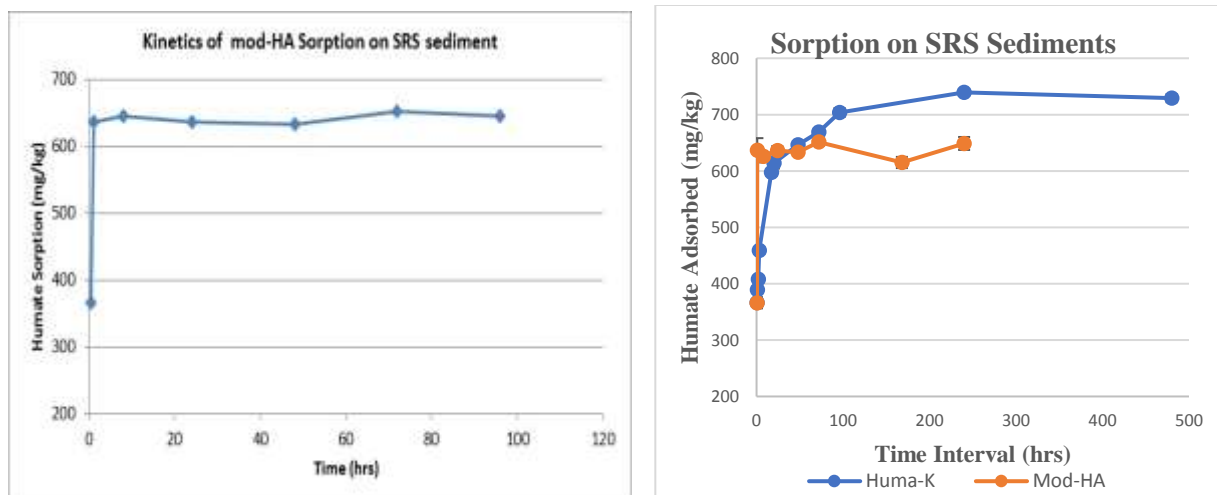


Figure 46. Kinetic Studies for Humate Substances (a) mod-HA (b) Huma-K.

Isotherms:

Figure 47 shows the isotherm data of adsorbed mod-HA on 200 mg SRS sediment (particle size: < 2mm) at pH 4. It showed that removal of mod-HA from solution with increasing initial mod-HA concentration. An initial plateau seems to be formed above the equilibrium concentration of ~ 200 mg/L because of saturation of all the binding sites in SRS sediment by mod-HA.

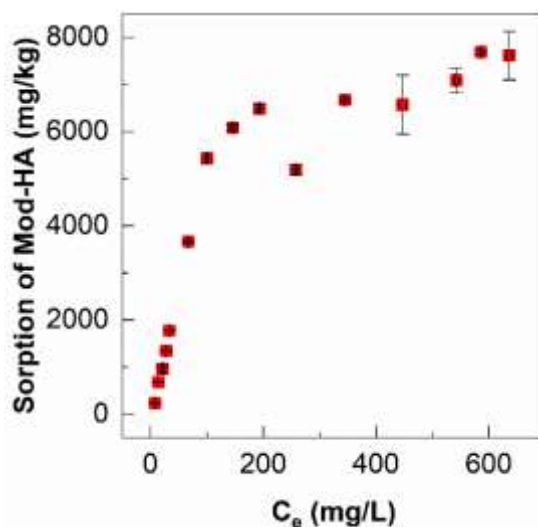


Figure 47. Isotherm of mod-HA with 200 mg SRS sediment.

Desorption:

To study desorption, fresh DIW was introduced at the end of the sorption procedure to previously prepared sorption samples. The sorption of mod-HA at pH 4 for the beginning of the desorption process shows a constant trend of 4,000 mg/kg removal. In Figure 48 the first desorption iteration is displayed with a similar desorption percentage of about 9% from pH 4 to 6, and then an increase from pH 6 to 8 which is expected because at higher pHs the presence of hydroxyl ions increase the

net negative charges for mod-HA, therefore enhancing its desorption (Avena and Koopal, 1998). Figure 49 displays the results of multiple desorption cycles at pH 4 between mod-HA and Huma-K, showing similar trends of decrease with each cycle. The sorbed mod-HA decreased slowly from 4000 mg/kg to 3000 mg/kg.)

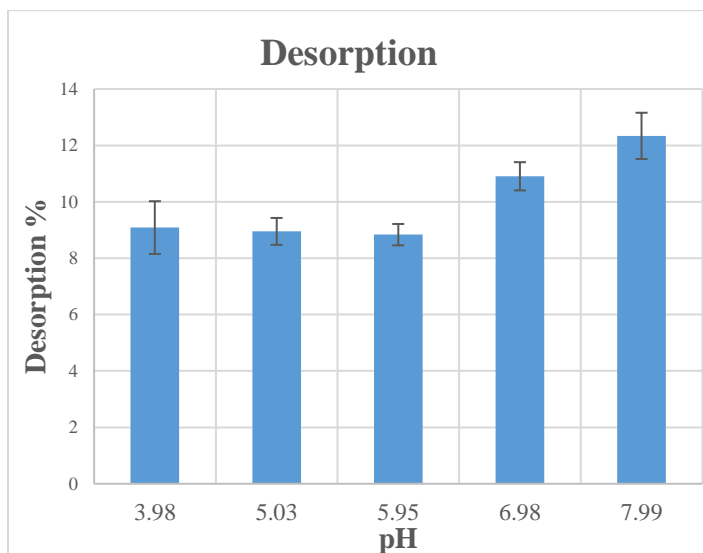


Figure 48. Desorption of Mod-HA with pH.

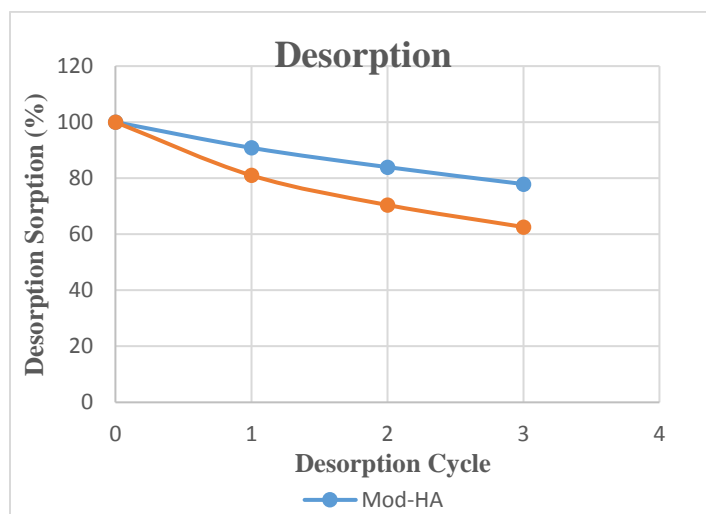


Figure 49. Effect of desorption cycles on Mod-HA and Huma-K (mg/kg).

Sorption of U(VI):

Uranium sorption experiments study the effect of pH on the sorption of uranium onto mod-HA amended sediments. In Figure 50a, the precipitation of the uranium was analyzed and displayed an increase as the pH increased with the highest removal at pH 7 with around 200 ppb of uranium removal through precipitation. In Figure 50b, the sorption of uranium onto the sediment displayed

a trend that increased as the pH reached pH 5 and then decreased from pH 5 to 8. The unfiltered and filtered samples both showed similar removal.

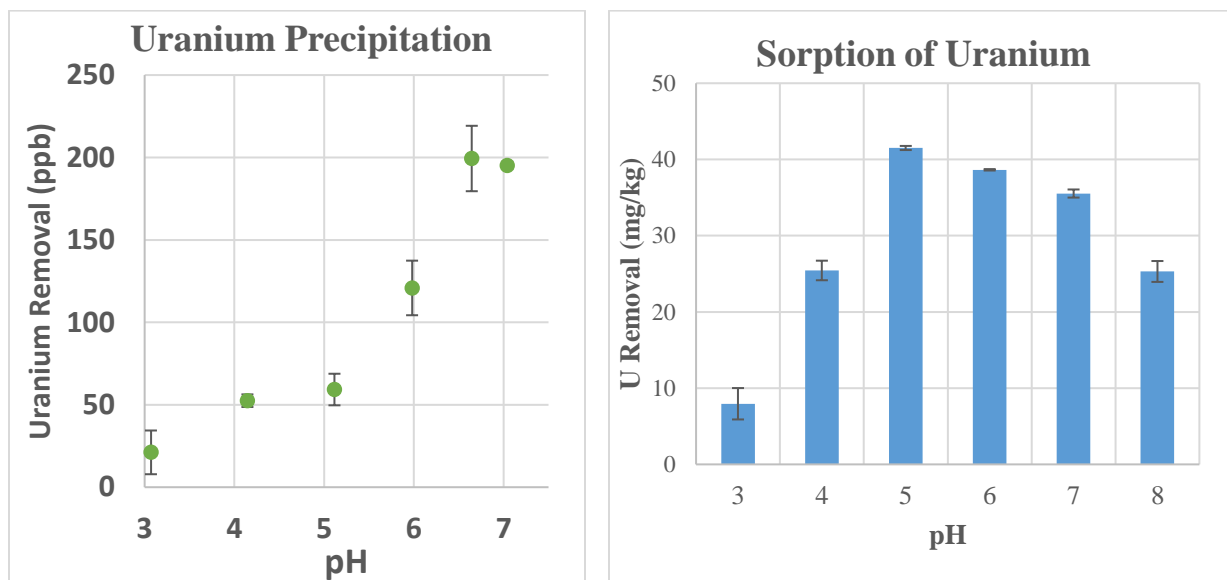


Figure 50. (a) Uranium Precipitation (b) Effect of pH on Uranium Sorption.

Kinetics:

Uranium sorption kinetics with mod-HA amended SRS sediment is shown in Figure 51 where in 30 minutes there is 20 mg/kg of U sorption and then quickly reached equilibrium after 2 days with 30 mg/kg of U sorption. This behavior is attributed to the metal-mineral systems in which rapid sorption is related to reaction-controlled sorption (Gonzalez-Raymat et al., 2018). Following this, the sorption begins to slowly increase until 4 days and then decreases slightly until reaching 10 days. Huma-K has a slower increase in uranium sorption with time, reaching equilibrium after 7 days at 30 mg/kg of uranium sorption.

Isotherms:

Equilibrium studies of U(VI) sorption on mod-HA amended SRS sediment shows a steady increase in sorption of U(VI) until the U(VI) concentrations reached 0.3 mg/L. After this, the removal decreases slightly and then rapidly increases again (Figure 52). Carboxyl and phenolic OH groups highly contribute to the increased sorption of uranium onto mod-HA amended sediments (Kremleva et al., 2009; Pompe et al., 2000). When comparing mod-HA to Huma-K data we see a similar amount of uranium sorption across each uranium concentration.

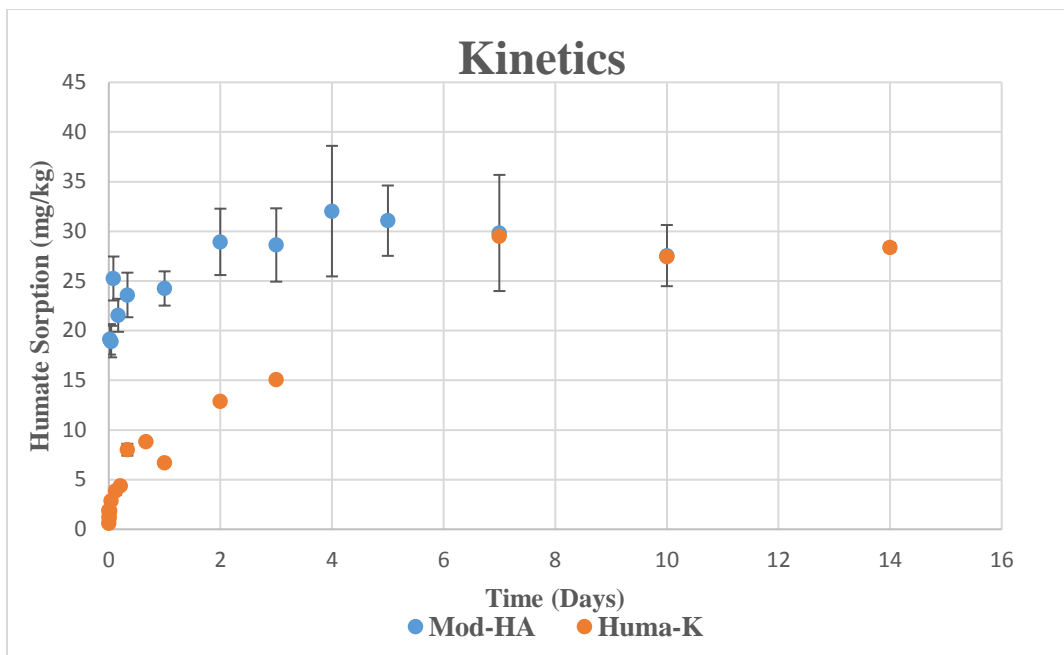


Figure 51. Uranium Sorption Kinetic Studies mod-HA vs Huma-K.

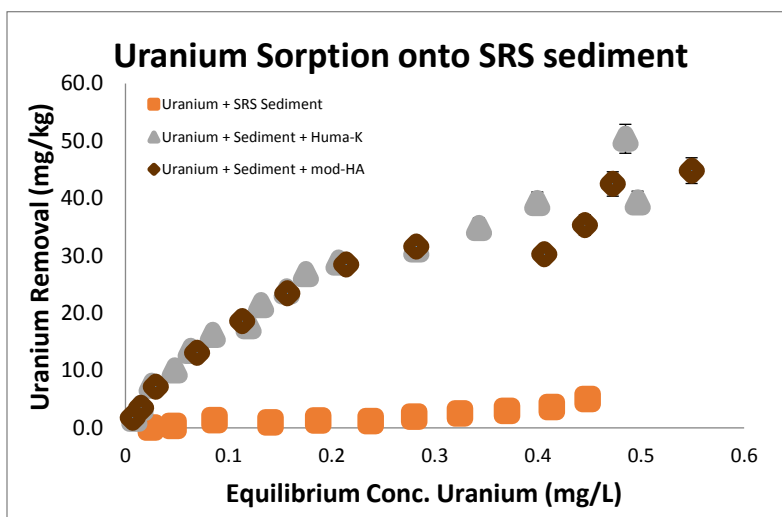


Figure 52. Uranium Sorption Equilibrium Studies.

Desorption:

Desorption studies of uranium on mod-HA amended sediments displayed in Figure 53a shows a trend of increase in uranium desorption until reaching pH 5 and then slowly decreasing as the pH reaches 8. In Figure 53b, Huma-K desorption results were presented which shows a similar trend to mod-HA with the exception at pH 7.5 where the desorption of Huma-K starts to increase, while for mod-HA it continues to decrease from pH 7 to 8. Mod-HA had a higher desorption of the humate compared to Huma-K.

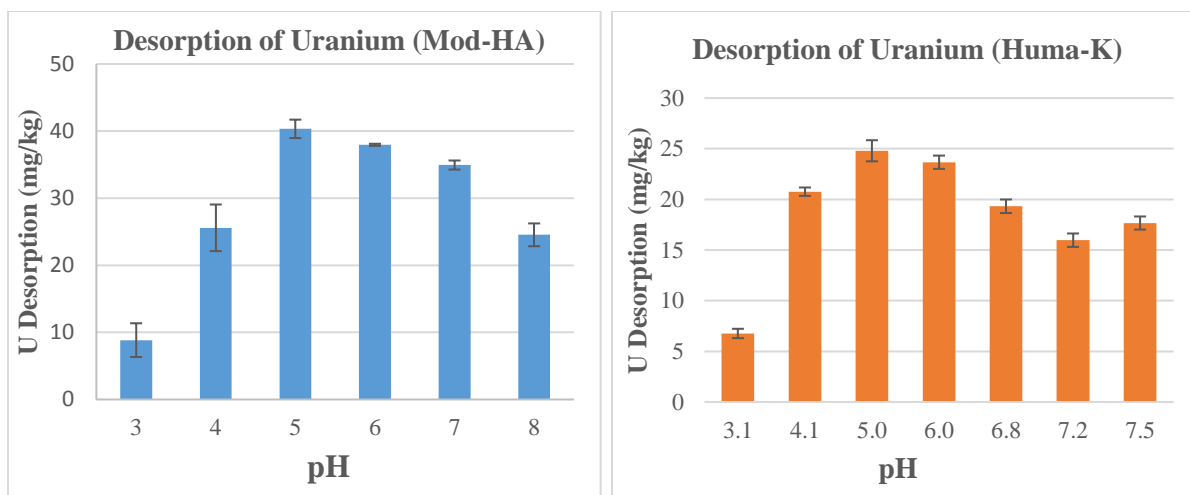


Figure 53. Desorption of Uranium (mg/kg) (a) mod-HA (b) Huma-K

Subtask 2.2: Conclusions

While the sorption of Huma-K was higher compared to mod-HA, the desorption of Hum-K was also increased compared to mod-HA material resulting in similar percentage of humate coating on SRS sediments. Both mod-HA and Huma-K improved the uranium removal by seven times compared to the plain SRS sediment. Future studies will include new humate material provided by SRNL.

Subtask 2.2: References

- Avena, M., Koopal, L.K., 1998. Desorption of humic acids from an iron oxide surface. *Environ. Sci. Technol.* 32, 2572-2577.
- Choppin, G.R., 1992. The role of natural organics in radionuclide migration in natural aquifer systems. *Radiochim. Acta* 58/59, 113.
- Dong, W., Tokunga, T. K., Davis, J. A., Wan, J., (2012). Uranium(VI) Adsorption and Surface Complexation Modeling onto Background Sediments from the F-Area Savannah River Site. *Environ. Sci. Technol.* 46, 1565-1571.
- Evans, A.G., Bauer, L.R., Haselow, J.S., Hayes, D.W., Martin, H.L., McDowell, W.L., Pickett, J.B., 1992. Uranium in the Savannah River Site environment. Westinghouse Savannah River Co., Aiken, SC (United States), p. 95.
- Gonzalez-Raymat, H., V. Anagnostopoulos, M. Denham, Y. Cai and Y. P. Katsenovich (2018). "Unrefined humic substances as a potential low-cost amendment for the management of acidic groundwater contamination." *Journal of Environmental Management* 212: 210-218.
- Gudavalli, R., Katsenovich, Y., Wellman, D., Idarraga, M., Lagos, L., Tansel, B., 2013. Comparison of the kinetic rate law parameters for the dissolution of natural and synthetic autunite in the presence of aqueous bicarbonate ions
- Hay, M. B. and S. C. B. Myneni (2007). "Structural environments of carboxyl groups in natural organic molecules from terrestrial systems. Part 1: Infrared spectroscopy." *Geochimica et Cosmochimica Acta* 71(14): 3518-3532.

- Ivanov, P., Griffiths, T., Bryan, N.D., Bozhikov, G. and S. Dmitriev, 2012. The effect of humic acid on uranyl sorption onto bentonite at trace uranium levels. *J. Environ. Monit.*, 14, 2968 - 2975.
- J.A. Davis. Adsorption of natural dissolved organic matter at the oxide/water interface, 1982, 2002. *Geochim. Cosmochim. Acta* 46, 2381-2393.
- Jiang, W., Q. Cai, W. Xu, M. Yang, Y. Cai, D. D. Dionysiou and K. E. O'Shea (2014). "Cr (VI) adsorption and reduction by humic acid coated on magnetite." *Environmental science & technology* 48(14): 8078-8085.
- Kremleva, A., Krüger, S., Rösch, N., 2009. Role of aliphatic and phenolic hydroxyl groups in uranyl complexation by humic substances. *Inorg. Chim. Acta.* 362, 2542-2550.
- Krepelova. A., 2007. Influence of Humic Acid on the Sorption of Uranium(VI) and Americium(III) onto Kaolinite (Dissertation).
- Largitte, L. and R. Pasquier (2016). "A review of the kinetics adsorption models and their application to the adsorption of lead by an activated carbon." *Chemical Engineering Research and Design* 109: 495-504.
- Perminova, I.V, Hatfield, K., Hertkorn, N., 2002. Use of humic substances to remediate polluted environments: from theory to practice. In the proceedings of the NATO Advance Research Workshop, Springer, P.O Box 17, 3300 AA Dordrech, The Netherland.
- Pompe, S., Schmeide, K., Bubner, M., Geipel, G., Heise, K.H., Bernhard, G., Nitsche, H., 2000. Investigation of humic acid complexation behavior with uranyl ions using modified synthetic and natural humic acids. *Radiochim. Acta.* 88, 553.
- Raymat, Hansell Gonzalez. "Unrefined Humic Substances as a Potential Low-Cost Remediation Method for Groundwater Contaminated with Uranium in Acidic Conditions." 2018, doi:10.25148/etd.fidc007039.
- Trevisan, Sara, et al. "Humic Substances Biological Activity at the Plant-Soil Interface." *Plant Signaling & Behavior*, vol. 5, no. 6, 2010, pp. 635–643., doi:10.4161/psb.5.6.11211.
- Zhou, T., S. Huang, D. Niu, L. Su, G. Zhen and Y. Zhao (2018). "Efficient Separation of Water-Soluble Humic Acid Using (3-Aminopropyl)triethoxysilane (APTES) for Carbon Resource Recovery from Wastewater." *ACS Sustainable Chemistry & Engineering* 6(5): 5981-5989.

TASK 3: CONTAMINANT FATE AND TRANSPORT MODELING IN THE TIMS BRANCH WATERSHED

Task 3: Executive Summary

This task involves the development and application of an integrated hydrology and contaminant transport model to be used as a tool for studying the fate of priority pollutants with emphasis on interactions with sediment transport processes in the Tims Branch ecosystem at SRS. The aim is to examine the response of Tims Branch to historical discharges and environmental management remediation actions and to provide a means of assessment, evaluation and post-closure long-term monitoring of water quality and environmental conditions following remedial activities. The Tims Branch ecosystem represents an important applied science opportunity as a result of significant past research by SRNL and SREL. Recent innovative cleanup technologies developed by DOE EM have eliminated anthropogenic mercury sources from Tims Branch watershed; however, a known quantity of relatively inert tin oxide tracer was introduced to the ecosystem. DOE EM has highlighted the need to track the tin and to understand the impact of frequent or extreme atmospheric events on its behavior in the Tims Branch system. FIU has utilized the data available from the tin-based remediation technology to develop a model that can not only be extended to investigate other contaminants of concern (e.g., mercury, uranium, nickel, aluminum and other metals and radionuclides), but can also be applicable to other nearby watersheds. Results from this study will be key to evaluating the effectiveness of tin (II)-based mercury treatment of a wetland system at the SRS site, and are also relevant to evaluating the potential application of this novel remediation technology in other mercury-contaminated streams.

Task 3: Introduction

A MIKE SHE/MIKE 11 hydrology model of the Tims Branch watershed has been developed by FIU and over the past year FIU has focused on the calibration and optimization of this model as well as development of the sediment and contaminant transport components. Coupling of the hydrology and contaminant transport components will, in future, provide SRS and DOE EM's Office of Soil and Groundwater Remediation with a tool to monitor the fate and transport of sediment and major contaminants of concern (e.g., mercury, uranium, nickel) in Tims Branch, particularly during extreme hydrological events. This will assist DOE-EM in examining the response of the Tims Branch ecosystem to innovative EM-developed remediation treatment technologies that have eliminated anthropogenic mercury sources from this watershed, and determine the potential applicability of these technologies in other contaminated stream systems at SRS and possibly other DOE sites.

Task 3: Objectives

The principal objective is to develop and test a comprehensive transport model using available hydrology software and geographical information systems (GIS) tools to examine the response of Tims Branch to historical discharges and environmental management remediation actions. In FIU Performance Year 9, the integrated MIKE SHE/MIKE 11 hydrological model of the Tims Branch watershed was revised and improved by FIU. The development of the contaminant transport component was completed and successfully coupled with the integrated hydrological model. The calibration and validation of the hydrological model was also initialized and will continue as more

streamflow data becomes available. During FIU Performance Year 10, contaminant transport templates for the heavy metals and radionuclides of interest such as mercury, nickel and uranium, will be further refined with site- and contaminant-specific data based on transport parameters retrieved from literature review or acquired from experimental studies. Sensitivity analysis and calibration will also be performed based on historical water quality data to verify the performance of the fully coupled contaminant transport model. FIU will use the calibrated model to study transport scenarios of heavy metals under extreme hydrological conditions that provide information related to inter-compartmental transfers and the environmental conditions that result in mobilization of adsorbed heavy metals in sediment, and accumulation of priority contaminants of concern due to sedimentation.

Task 3: Methodology

Research in the past year has focused on improving the Tims Branch model performance and expanding its capability to event-based modeling for predicting flow and sediment transport processes under a range of extreme design storm events. The work included (1) recalibration of the MIKE SHE/MIKE11 hydrodynamic model; (2) simulation of time-dependent flow and bed shear stress associated with design precipitation events for Average Recurrence Intervals (ARIs) ranging from 5 years to 500 years; (3) development and verification of a Cohesive Sediment Transport (CST) model using the MIKE 11 AD (advection-dispersion) module to integrate with the calibrated MIKE SHE/MIKE 11 hydrodynamic model; and (4) simulation of suspended sediment concentration and sediment loads associated with design storm events for ARIs ranging from 1 year to 500 years. Apart from modeling activities, FIU ARC's hydrology modeling team visited Savannah River Site (SRS) to re-install a HOBO remote monitoring station near the Tims Branch watershed outlet and perform routine maintenance on two other stations in the main branch.

In March 2020, Dr. Muhammad Alam joined the ARC hydrology modeling team as a Senior Research Scientist. Dr. Alam has been working as the technical lead. He has reviewed the model development and recalibrated it introducing some major changes in parameterizations for both surface water and groundwater components. He has developed the sediment transport model and verified its performance against field measurements. He has developed codes in PYTHON to automate a series of model runs for simulating flow and sediment transport processes associated with design storm events from 1-year to 500-year ARIs. Postdoctoral Associate, Dr. Yan Zhou, supported the modeling effort by carrying out a model parameter optimization study using the auto calibration tool (available in MIKE ZERO software package) and providing consistent feedback (derived from auto calibration outcomes) on probable convergence criteria for model calibration. He also developed a spreadsheet algorithm to fit design precipitation depths to temporal patterns obtained from NOAA's Precipitation Frequency Data Server. He has analyzed the hydraulic component of the model results at key locations in the main branch. DOE Fellows Amanda Yancoskie, Juan Morales and Stevens Charles have been trained on hydrological modeling concepts, tools and software. They have worked on developing precipitation time series for design storm events and interpreting model results under supervised conditions. Ms. Angelique Lawrence has provided regular GIS support based on the model input requirements, served as the task point of contact and led the overall task management, coordination and reporting prior to Dr. Alam's arrival. Dr. Alam and Dr. Zhou have developed two different manuscripts as lead authors which

were submitted to the WM2021 conference for both oral presentations and publication in the conference proceedings. DOE Fellow Stevens Charles also submitted an abstract as a lead author for a poster presentation in the student poster competition at the WM2021 conference. The following provides a summary of the research area as well as model development, calibration, verification, and simulation results from the hydrodynamic and sediment transport components of the model.

Research Area

Tims Branch watershed is located in the northwestern side of the U.S. Department of Energy's Savannah River Site (SRS), Aiken, South Carolina (Fig. 1). Steed Pond, which is located around two miles upstream from the watershed outlet, received approximately 44,000 kg of depleted uranium from 1954 to 1985 (Pickett, 1990). Deposition of uranium occurred in several shallow beaver ponds located upstream of Steed Pond. However, most deposition occurred primarily in Steed Pond as it has longer residence time of water compared to other shallow beaver ponds (Evan et al., 1992). Tims Branch, which is the main branch of the Tims Branch watershed, is a braided and secondary stream that flows through Steed Pond. It originates from the north of SRS and passes through Beaver Ponds 1–5 and Steed Pond. It travels around 15 km to the south before it makes a confluence with Upper Three Runs Creek at the outlet of the watershed (Figure 54). It receives water from stormwater runoff, groundwater, and facility discharge from the SRS A/M areas. The upper segment of Tims Branch located upstream of the A-014 tributary is generally considered as a losing stream as it is permanently disconnected from the groundwater system. In contrast, the lower segment of Tims Branch (located downstream of the A-014 tributary) is very close to the groundwater table and receives discharge seasonally. The watershed features a humid subtropical climate with mean temperature of 18 °C and an average annual precipitation of 1,225 mm (Kilgo, 2005). The erosion mechanism in Tims Branch is responsible for resuspension and transport of sediment-bound contaminants within the study area.

Data Source

Topography of the Tims Branch watershed was represented by a 3-m resolution digital elevation model (DEM) of South Carolina derived from LiDAR data, obtained from the South Carolina Department of Natural Resources (SCDNR) with the elevation ranging from approximately 130 m to 460 m above mean sea level. The DEM was clipped to the model domain and resampled to 50 m resolution to represent the topography of the research area.

The climatic condition of Tims Branch watershed was assumed to be uniformly distributed and represented by time series of precipitation and reference evapotranspiration (ET_0). Precipitation data was obtained from a rain gauge (700-A station, Figure 54) located within SRS and managed by the Savannah River National Laboratory's (SRNL's) Atmospheric Technologies Group (ATG). Cumulative precipitation was measured in 15-minute increments, which is considered adequate to represent storm events. ET_0 was estimated from pan evaporation measurements taken adjacent to the SRS CLM station. Daily averaged ET_0 was calculated from daily pan evaporation based on a constant pan coefficient of 0.7, an averaged pan coefficient found for five major lakes in the Savannah River Basin (Phillips et al., 2016). To develop representative precipitation time series of designed storm events, rainfall depths for various average recurrence intervals (ARIs) were obtained from the National Oceanic and Atmospheric Administration (NOAA), as well as temporal

distribution of various rainfall durations (6-, 12-, 24-, and 96-hour), quartiles (1st, 2nd, 3rd and 4th) and load types (front-loaded and back-loaded), which were obtained from NOAA's Precipitation Frequency Data Server (PFDS).

Land cover and soil type were represented by spatially distributed categorical maps derived from federal databases, as their influence on the hydrological response of the watershed is critical in model uncertainties. Land cover was represented by vegetation/land use categories based on land use data of 2016 obtained from the Multi-Resolution Land Characteristics (MRLC) consortium National Land Cover Database (NLCD). The land cover map included 15 vegetation/land use categories where the most dominant land cover type is evergreen forest, covering approximately 62% of the Tims Branch watershed. The soil map was represented by soil types and associated soil physical properties, based on the soil map of 2016 and the associated soil metadata obtained from the Soil Survey Geographic Database (SSURGO) provided by the United States Department of Agriculture (USDA) Natural Resources Conservation Service (NRCS). The soil type map included 44 soil types and was summarized as 20 soil categories. Similar to the DEM, both land cover and soil type maps were clipped to the model domain and resampled to the grid of the model.

Groundwater elevation and discharge records were represented by time series at monitoring points and used in generating initial conditions and model calibration. Groundwater elevation time series were obtained from South Carolina Department of Natural Resources (SCDNR) at multiple locations within SRS (Figure 54). Streamflow records are scarce in this restricted watershed. Therefore, in order to collect a consistent and detailed timeseries dataset of flow rate, three HOBO RX3000 remote monitoring stations were installed onsite at SRS to collect water level data at strategic locations along the Tims Branch stream and the A-014 outfall tributary (Figure 54). The water depth is recorded every 15 minutes and downloadable every 4 hours from its cloud-based storage. The recorded water depth at the outlet was then used to calculate flow rate based on a rating curve developed from field measurements.

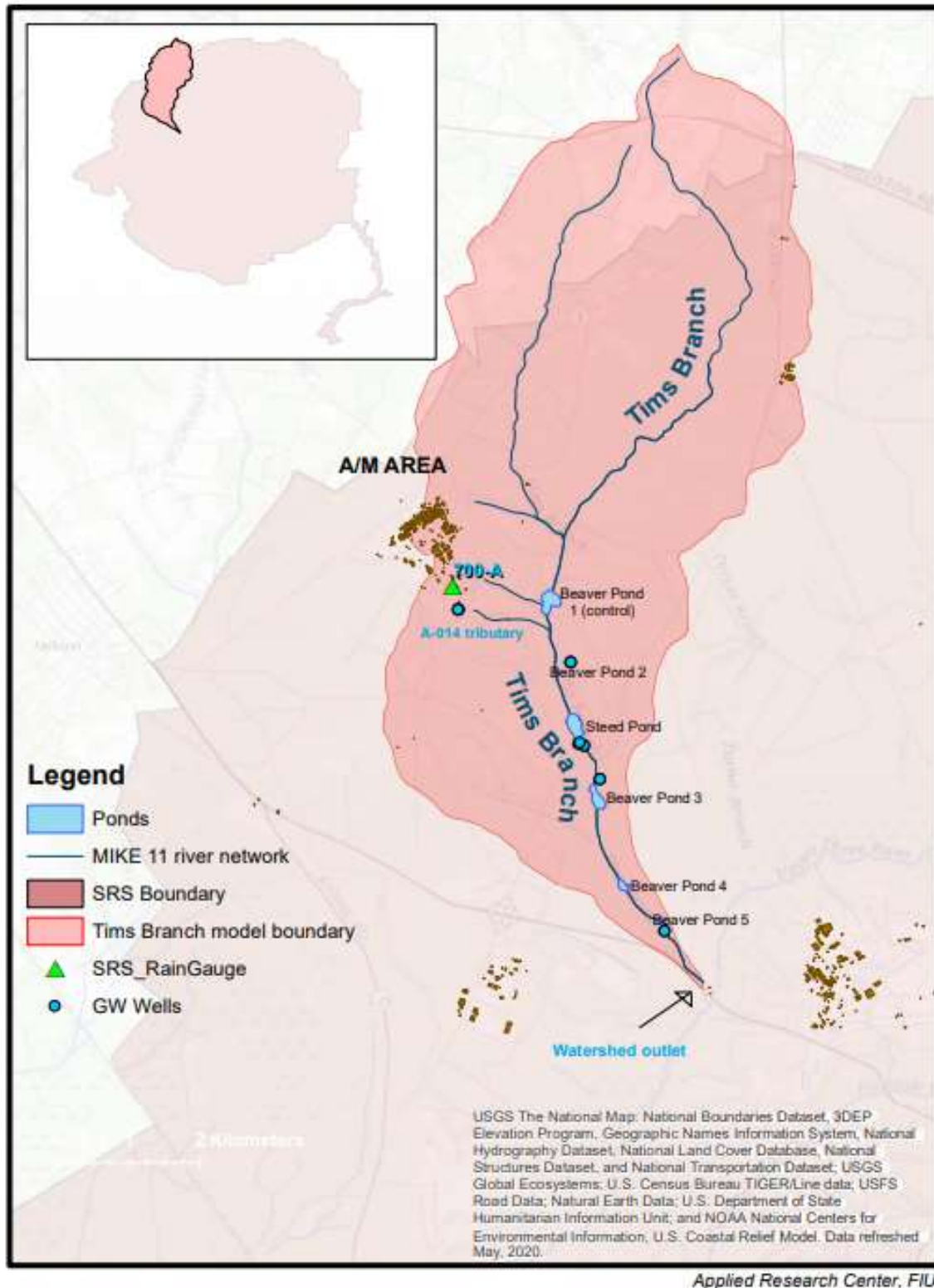


Figure 54. Tims Branch watershed study area within the Savannah River Site, showing significant features including: watershed boundary (model domain), ponded areas, A-014 tributary, A/M Area, precipitation gauge, groundwater wells and stream stages.

Site Visit

In December 2019, Dr. Yan Zhou and DOE Fellows Amanda Yancoskie and Juan Morales visited SRS between 12/16/2019 to 12/18/2019. The purpose of this trip was to:

- re-install the HOBO remote monitoring station furthest downstream in Tims Branch that was removed due to culvert repairs that took place over the summer of 2019;
- perform routine maintenance on the other two stations; and
- meet with SRNL and SREL collaborators and tour the SRS study areas (A/M Area and Tims Branch).

During the site visit, the device located furthest downstream in Tims Branch was successfully reinstalled and calibrated as the culvert repairs were completed. The images below show Drs. Brian Looney, Mike Paller and Hansell Gonzalez Raymat from SRNL assisting the FIU team with the reinstallation of the Lower Tims Branch HOBO unit.

In addition, the device located in the A-014 outfall tributary was cleaned and calibrated. In August of 2018, unusual flow oscillations were observed from the graphed cloud data recorded from this device. After field inspection of the unit, it was noted that the pressure transducer/sensor was covered by sediment. After several subsequent observations, it became apparent that during high flow periods the suspension of sediment in the stream was causing temporary fouling of the sensor. During the site visit by FIU in December 2019, measures were taken to counteract this issue by securing a wire mesh to the protective PVC pipe that houses the transducer cables. This mesh as seen in Figure 57 below will serve to protect the sensor from potential fouling by sediment or debris such as leaves or biofilm during high flow periods.

Lastly, during the December site visit, the station located downstream of Beaver Pond 5 was discovered to be malfunctioning and was unable to be repaired in the field. The station was therefore removed and brought back to FIU for troubleshooting. It was also determined that once the device is repaired, it should be relocated downstream of Steed Pond at the point where Tims Branch starts to receive groundwater discharge.

During FIU's visit to SRS, measurements were also taken of hydraulic parameters including flow velocity, cross-section geometry and water depth. The FIU team was also given a tour of the SRNL facilities and other areas of SRS, and held discussions regarding FIU's modeling work and other potential areas of research interest.



Figure 55. SRNL collaborators, Drs. Brian Looney, Mike Paller and Hansell Gonzalez-Raymat, assisting the FIU team with the reinstallation of the HOBO remote monitoring device for recording water level in Tims Branch.



Figure 56. FIU and SRNL collaborators positioning the sensor/probe at the end of the PVC piping prior to placement in the stream.



Figure 57. Protective wire mesh installed to prevent fouling of the water level sensor by sediment or debris.

Integrated Hydrologic Model

The integrated hydrologic watershed model for Tims Branch watershed was developed by coupling the MIKE SHE (MSHE) land model that simulates surface/subsurface hydrologic processes (such as overland flow, evapotranspiration, unsaturated and saturated flow) and the MIKE 11 stream hydrodynamic model that accounts for stream water hydraulics (such as cross-sections and stream network).

The MSHE land model is a deterministic, physically-based, fully distributed numerical model designed for simulating various processes of the hydrologic cycle on the land surface as well as the subsurface. These hydrologic processes include evapotranspiration (ET), overland flow (OL), and flow in both the unsaturated zone (UZ) and saturated zone (SZ). Based on governing partial differential equations of mass, momentum, and energy conservation, MSHE numerically solves for water movement among model grids using a finite difference scheme and provides an estimate for various water budget components (Figure 58).

The Tims Branch watershed boundary, defined by United States Geological Survey (USGS) as the 12-digit hydrologic unit code (HUC) 030601060504, was specified as the computational model domain. The Tims Branch watershed hydrologic model with a total area of 45 km² was represented in MIKE SHE by 18,105 grids with a size of 50 m by 50 m.

Evapotranspiration (ET) in MSHE is calculated based on the empirical Kristensen and Jensen methods with the primary assumption being that the actual evapotranspiration (ET_a) cannot exceed reference evapotranspiration (Kristensen et al., 1975). A proportion of the rainfall will be firstly intercepted by the vegetation canopy dependent on leaf area index (LAI), which evaporates at the rate of ET₀. Throughfall reaches land surface and part becomes surface water runoff while the rest infiltrates to the unsaturated zone. Dependent on root depth (RD), a fraction of the infiltrating

water will be lost through transpiration of plant roots or evaporation from the upper root zone, while the remainder recharges the groundwater in the saturated zone. Water in the saturated zone is available directly to root uptake or indirectly through capillary force to replenish the unsaturated zone. Both LAI and RD are acquired from literature review (Malek-Mohammadi et al., 2012).

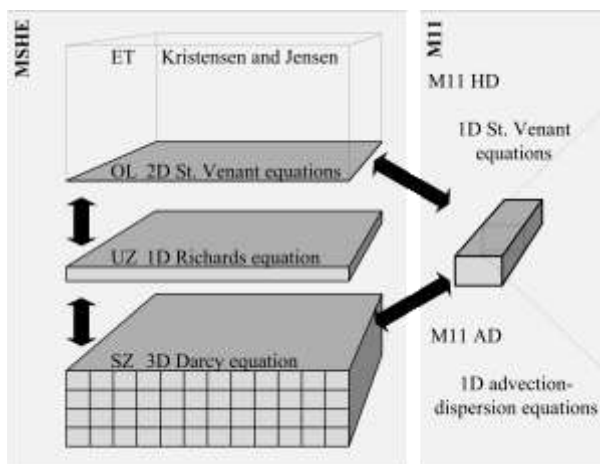


Figure 58. Diagram of an integrated hydrologic model showing the MIKE SHE land model including evapotranspiration (ET), overland flow (OL), and flow in the unsaturated zone (UZ) and saturated zone (SZ), MIKE 11 stream hydrodynamic model (M11 HD), and contaminant transport components including the MIKE 11 Advection Dispersion (M11 AD) module.

In the latest version of this model, the hydraulic parameters (horizontal hydraulic conductivity and vertical hydraulic conductivity) for aquifers of the groundwater module were modified based on the available literature for the Savannah River Site. The external boundary condition of the saturated zone module was modified at the outlet of the watershed. A fixed head water level boundary condition was assigned around the outlet of the watershed. The model cross sections were revised to improve the conveyance of watercourses for extreme events. The 1 m digital elevation model (DEM) for the study area was imported into the MIKE HYDRO module of the model and the cross sections were re-digitized at a regular interval using the DEM. The restructured model was finally calibrated to the discharge hydrograph estimated from the observed water levels at the outlet of the watershed in Tims Branch.

Model calibration was conducted using discharge time series observed at the outlet of the Tims Branch watershed, as well groundwater elevation data observed at multiple monitoring wells described in the Data Sources section. The nature of the coupled model requires calibration of parameters from both MSHE and M11 HD components covering evapotranspiration, overland flow, and the saturated zone module in MSHE and hydrodynamic components in M11. Model calibration was performed for the period of 04/01/2018 to 06/17/2018 using an auto-calibration tool based on the Population Simplex Evolution (PSE) method, a global optimization algorithm suited for simultaneous simulation in a parallel manner. Using the reflection and contraction operators included in the simplex method, PSE evolves a population of points until convergence criteria are met, during which a mutation component is included to avoid premature convergence. Calibration parameters, their initial values and boundaries are summarized in

Table 27.

Table 27. Summary of the calibration parameters from both the MIKE SHE land model (MSHE) and MIKE 11 stream hydrodynamic model (M11), including initial values and calibrated values.

		Unit	Initial	Calibrated
M11	Groundwater leakage coefficient	/s	5.00E-05	1.00E-05 to 1.50E-05
	Manning's M	m ^{1/3} /s	25.00	20
MSHE	Detention storage	mm	5.00	2
	Horizontal hydrological conductivity	m/s	5.00E-05	1.16E-07 to 1.16E-05
	Storage coefficient	/m	5.00E-05	2.45E-08 to 9.01E-08
	Specific yield		0.20	0.22 to 0.25

Rainfall Event Design and Scenario Tests

Flash flow resulted from rainfall events is anticipated as the primary driver that causes sediment remobilization in Tims Branch. To adequately simulate the flash flow, it is important to account for not only the total rainfall depth but also the timing and intensity of precipitation during a storm event. Therefore, four parameters were used to describe and derive a range of the rainfall time series for the scenario tests: i) average recurrence intervals (ARI) that describe the frequency of the event based on total rainfall depth; ii) rainfall durations that describe the temporal extent of the event; iii) quartiles that describe at which quartile of the duration rainfall concentrates; and iv) cumulative probability of occurrence for the temporal distribution. In this study, total rainfall depth for six ARIs were obtained from NOAA and distributed according to temporal distribution data obtained from NOAA’s PFDS. The generated time series of design rainfall events were then simulated with a consistent warming-up period to predict the flash flow after the event, and the resultant bed shear stress was analyzed to assess the implication for sediment transport.

Cohesive Sediment Transport Model

The sediment samples from previous studies [(Hayes,1986) and (Batson et al., 1996)] indicated that finer materials transported higher in the water column during baseflow or an episodic storm event. The nature of remobilized sediment materials factored in model selection and modeling approach adopted in this study. The advection-dispersion (AD) sediment transport model available in the MIKE 11 AD module was selected to simulate the cohesive sediment transport process within major watercourses in the research area. This model is integrated with the overland and subsurface flow module (MIKE SHE) and the river flow hydrodynamic module (MIKE 11 HD). The overall modeling framework is illustrated in Figure 59. The AD model is based on the one-dimensional equation of conservation of mass of dissolved or suspended sediment materials. The model takes the output from the MIKE 11 HD model, i.e., water level and discharge, cross-section area, and hydraulic radius. The governing equation of the MIKE 11 AD model is as follows:

$$\frac{\delta AC}{\delta t} + \frac{\delta QC}{\delta x} - \frac{\delta}{\delta x} \left(AD_L \frac{\delta C}{\delta x} \right) = -kCA + C_2q + Ew \quad (1)$$

where A cross-section area, C is the concentration, t the time coordinate, x the space coordinate, D_L the horizontal dispersion coefficient, k the linear decay coefficient, C_2 is source/sink concentration, q is the tributary inflow per unit length, E the net deposition/erosion, and w the river width. An implicit finite difference scheme is used to solve the above equation numerically. The AD model simulates both temporal and longitudinal spatial variations of sediment concentration, as well as accumulated sediment deposits over the simulation period (DHI, 2017).

The AD model considers a relatively simple description of the erosion and deposition as source/sink terms in the above-mentioned equation. In the case of deposition, the E term is solved by:

$$E = \frac{W_s C}{H^*} \left(1 - \frac{v^2}{v_{cd}^2} \right) \quad v < v_{cd} \text{ (deposition)} \quad (2)$$

where v is the flow velocity, v_{cd} the critical deposition velocity, W_s the fall velocity, and H^* is average depth through which the particle settled.

In the case of erosion, the E term is solved by:

$$E = \frac{M}{h} \left(1 - \frac{v^2}{v_{ce}^2} \right) \quad v \geq v_{ce} \text{ (erosion)} \quad (3)$$

where v_{ce} is the critical erosion velocity, M the erodibility coefficient, and h the flow depth.

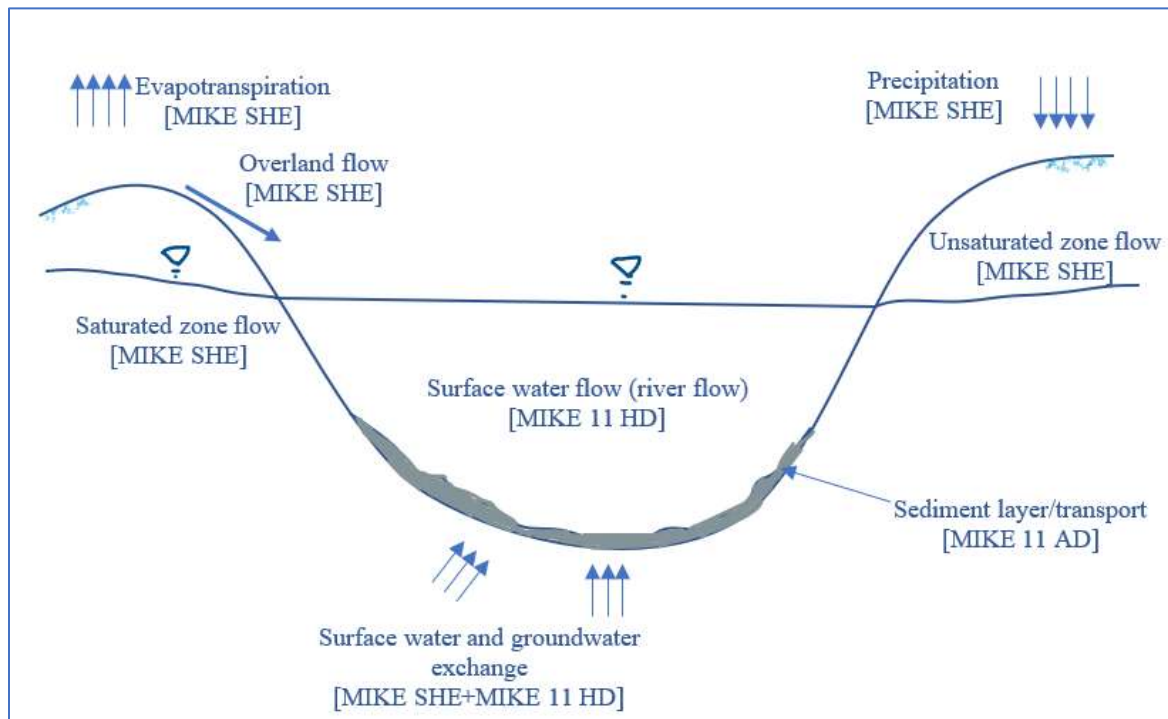


Figure 59. Flow and sediment transport modules/components included in the Tims Branch model.

Task 3: Results and Discussion

Hydrological Model

Model calibration achieved satisfactory results when compared to discharge records measured at the outlet of Tims Branch (Figure 60). The results from FITEVAL indicated an acceptable model performance with a root mean square error (RMSE) of 0.03 m³/s within the range of (0.018, 0.05) m³/s and a Nash–Sutcliffe efficiency (NSE) of 0.637 within the range of (0.211, 0.866) (Figure 61). According to FITEVAL, the probability of model performance within the category of very

good ($NSE > 0.9$) is 0.3%, 14.3% for good ($0.8 < NSE < 0.9$), 36.7% for acceptable ($0.65 < NSE < 0.8$) and 48.7% for unsatisfactory ($NSE < 0.65$).

Predictions of groundwater elevation in the calibration period are visualized in Figure 62. Due to lack of continuous monitored groundwater elevation time series, the groundwater elevation time series predicted for different wells were contrasted with the boxplot of observations at the same location. Figure 62 indicates that the predicted groundwater elevation fits the range of observations at the subsurface layer at the depth of 9.1 which dictates subsurface water interaction.

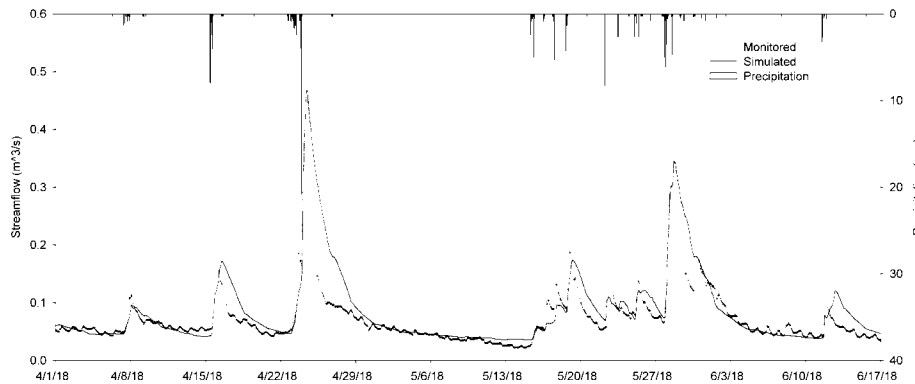


Figure 60. Model calibration result showing precipitation (bar from top), simulated (markers) and monitored discharge time series (solid line).

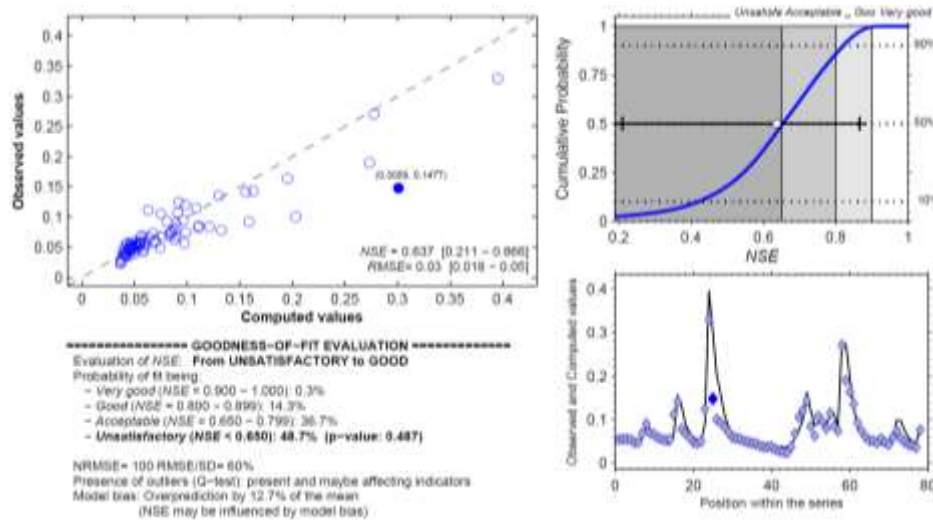


Figure 61. Model calibration evaluated using FITEVAL showing (a) regression of computed vs observed discharge, (b) FITEVAL plot of cumulative probability of NSE and its median, (c) FITEVAL goodness of fit evaluation including hypothesis test results, outliers, and the sensitivity of the indicators to model bias, and (d) scatter plot showing fit between computed vs observed discharge in order of the series.

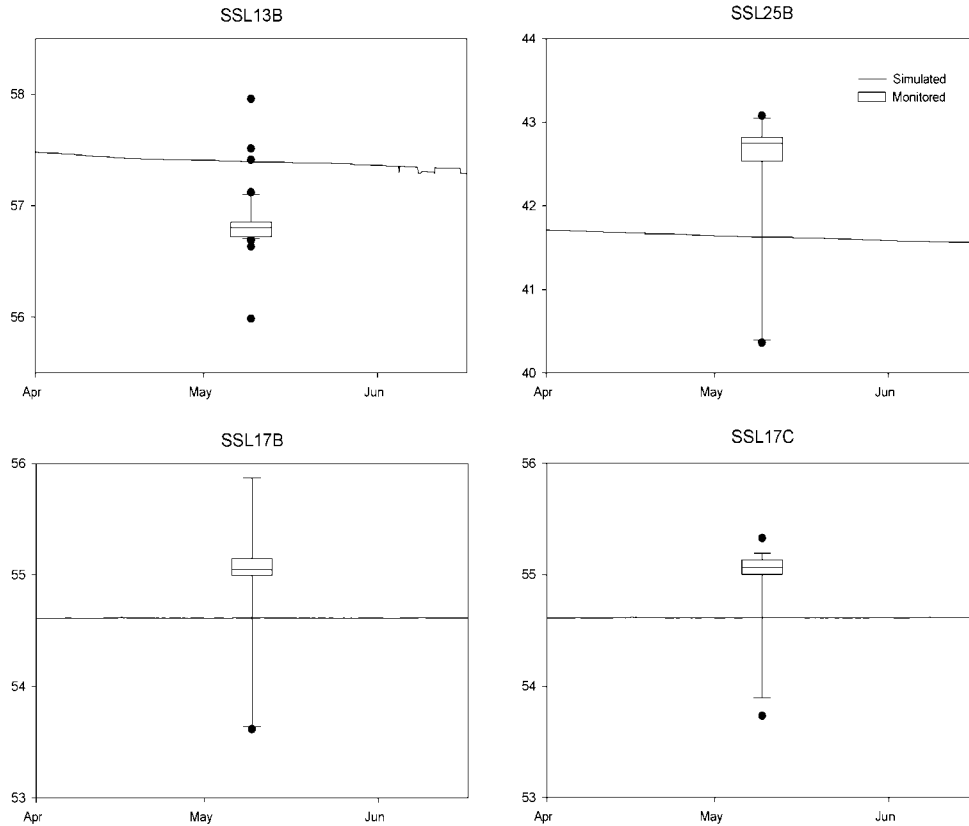


Figure 62. Predicted subsurface groundwater elevation time series represented by solid line contrasted against historical records represented as boxplots at the depth of 9.1 meters.

Rainfall Event Design and Scenario Tests

A total of 160 design events were generated with the combination of five ARIs (5, 10, 25, 100, and 500 years), four rainfall durations (6-, 12-, 24-, and 96-hour), four quartiles (1st, 2nd, 3rd and 4th) and two load types (front-loaded and back-loaded, representing 10% and 90% cumulative probability of occurrence). Based on four rainfall durations and four quartiles, the design events were visualized as four by four subplots with each subplot containing events with five different ARIs by two load types (Figure 63). Since the same temporal distribution was applied for events with the same duration, quartiles and load type, a higher ARI will result in a proportional upshifting of the curve compared to a lower ARI. Therefore, the curve of different ARIs in the same load type of the same subplot naturally falls on top of each other, with 5-year ARIs located at the bottom and 500-year ARIs at the top.

In the scenario test, the design events were inserted within the calibration period at the time 04/20/2018 using the foregoing simulation as a warming up period. The simulated stream hydraulic conditions after the start of the design event, shear stress in particular, were extracted and analyzed both spatially (Figure 64) and temporally at the most important location, Steed Pond (Figure 65). Figure 64 showed the spatial distribution of the maximum shear stress, with the x-axis representing the downstream distance after the confluence with A-014 tributary. The vertical reference lines in each subplot mark the location of ponds in Tims Branch, showing Beaver Pond 2 (BP2), Steed Pond, BP3, BP4 and BP5 from left to right, respectively. One can tell from Figure

64 that Steed Pond featured one of the lowest shear stresses, confirming it as the hotspot where the radionuclides concentrate. Figure 65 illustrated the temporal variation of shear stress of Steed Pond under various design rainfall events. Due to the stage shape of the cross-section, a shear stress of approximately 4 N/m^2 can be easily achieved for all events at the stream bottom, with only the duration varying from approximately 40 hours for flasher, smaller events to more than 180 hours for longer and larger events. Beyond the shear stress of approximately 4 N/m^2 , the peak value and duration increased less drastically by ARIs other than the sharp peaks presented in flasher events caused by adjacent flash runoff.

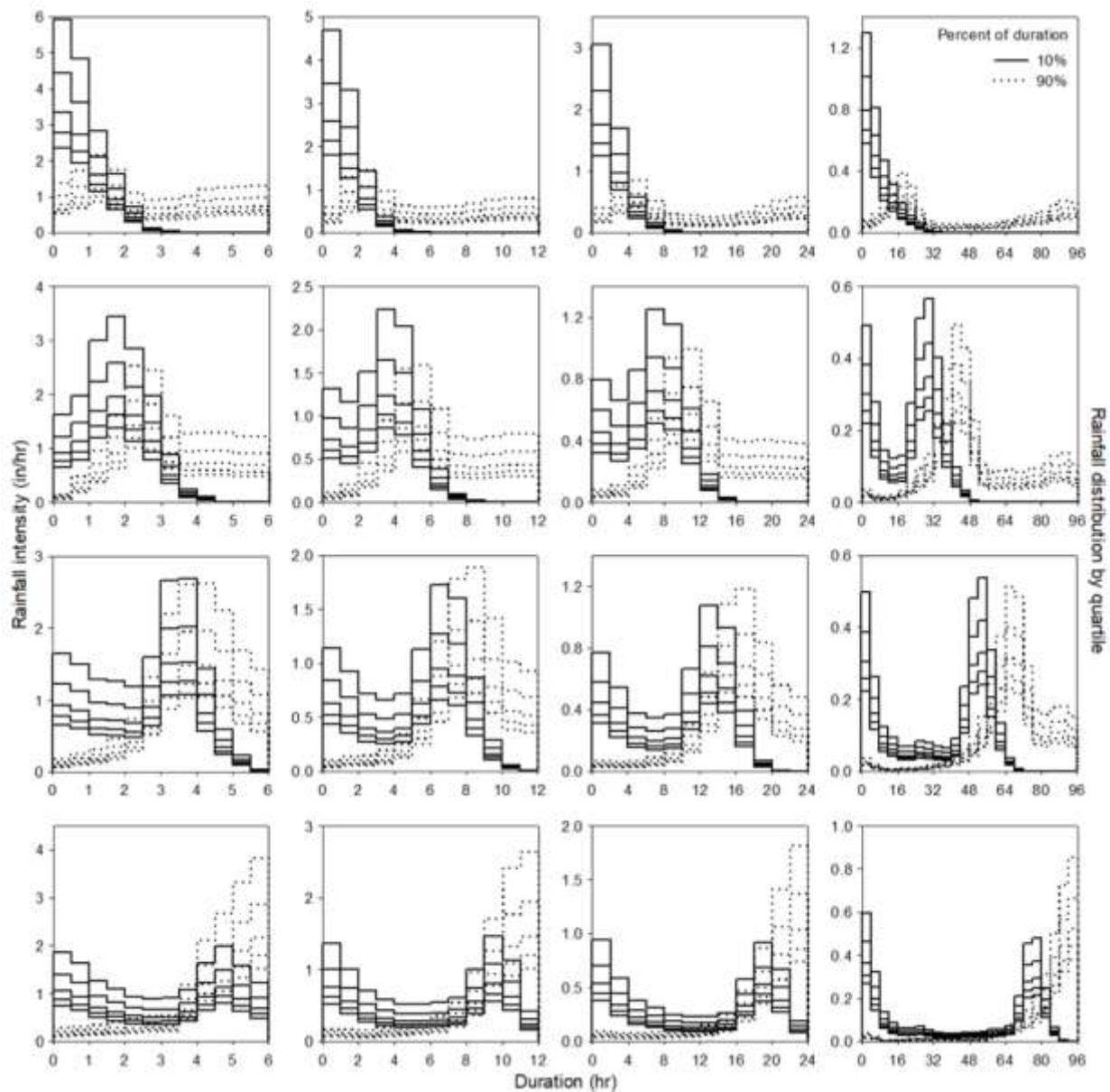


Figure 63. Design rainfall scenarios used in storm analysis. Note: 1) each column represents events with the same rainfall duration, 6h, 12h, 24h, and 96h, respectively from left to right; 2) each row represents events with the same rainfall temporal distribution out of four quartiles, 1st, 2nd, 3rd, and 4th, respectively from top to bottom; 3) each individual figure includes two groups of curves showing 10% and 90% percent of duration, while each group of curves represents design rainfall events with different ARIs, 5y, 10y, 25y, 100y and 500y, respectively from top to bottom.

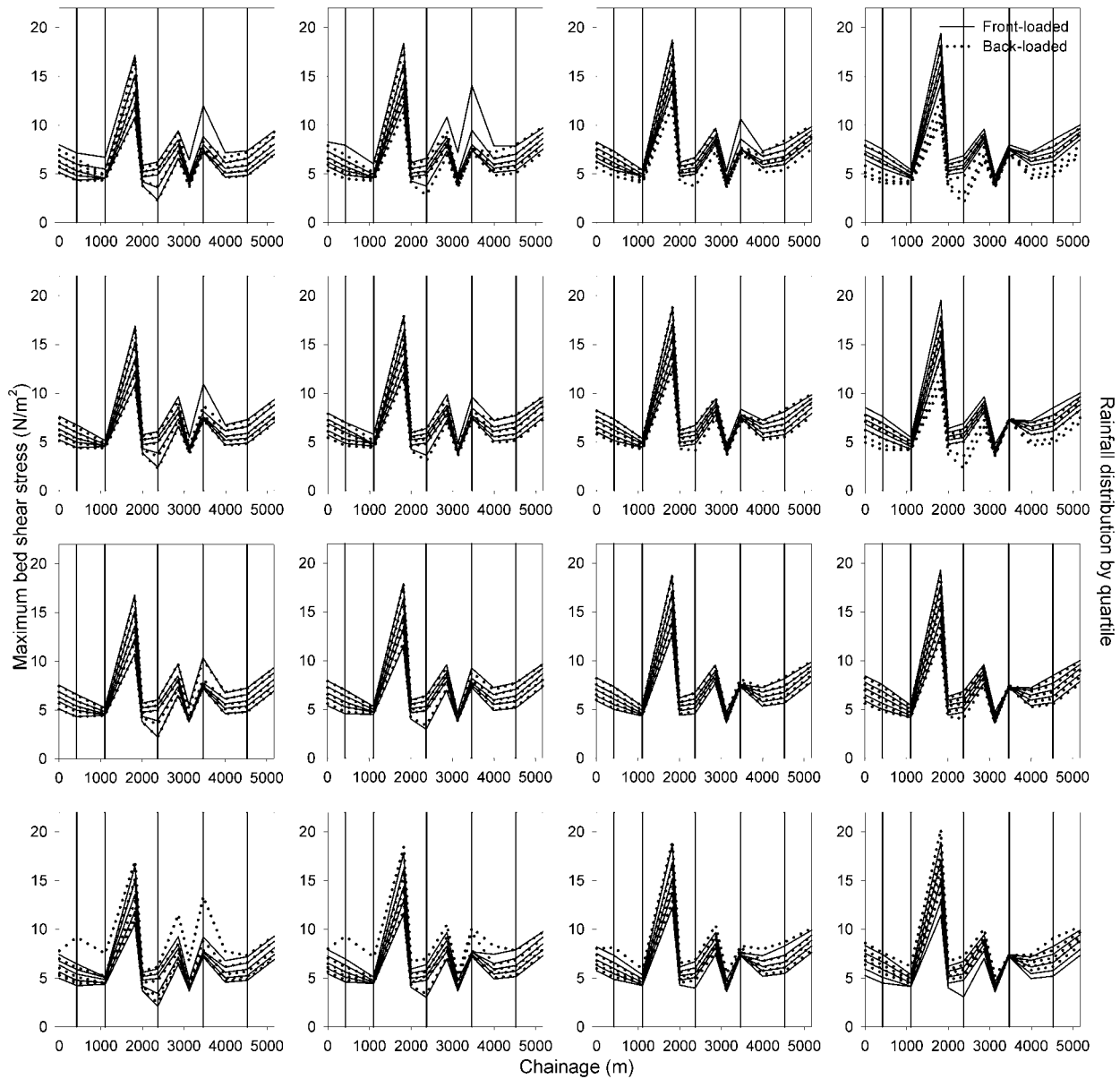


Figure 64. Spatial distribution of bed shear stress for locations downstream of the A014 confluence under various design rainfall scenarios. Note: 1) each column represents results under events with the same rainfall duration, 6h, 12h, 24h, and 96h, respectively from left to right; 2) each row represents results under events with the same rainfall temporal distribution out of four quartiles, 1st, 2nd, 3rd, and 4th, respectively from top to bottom; 3) each individual figure includes two groups of curves showing results under 10% and 90% percent of duration while each group of curves represents results under design rainfall events with different ARIs, 5y, 10y, 25y, 100y and 500y, respectively from top to bottom; 4) each vertical reference line represents pond downstream of the A014 confluence including Beaver Pond 2, Steed Pond, Beaver Pond 3, 4 and 5, left to right respectively.

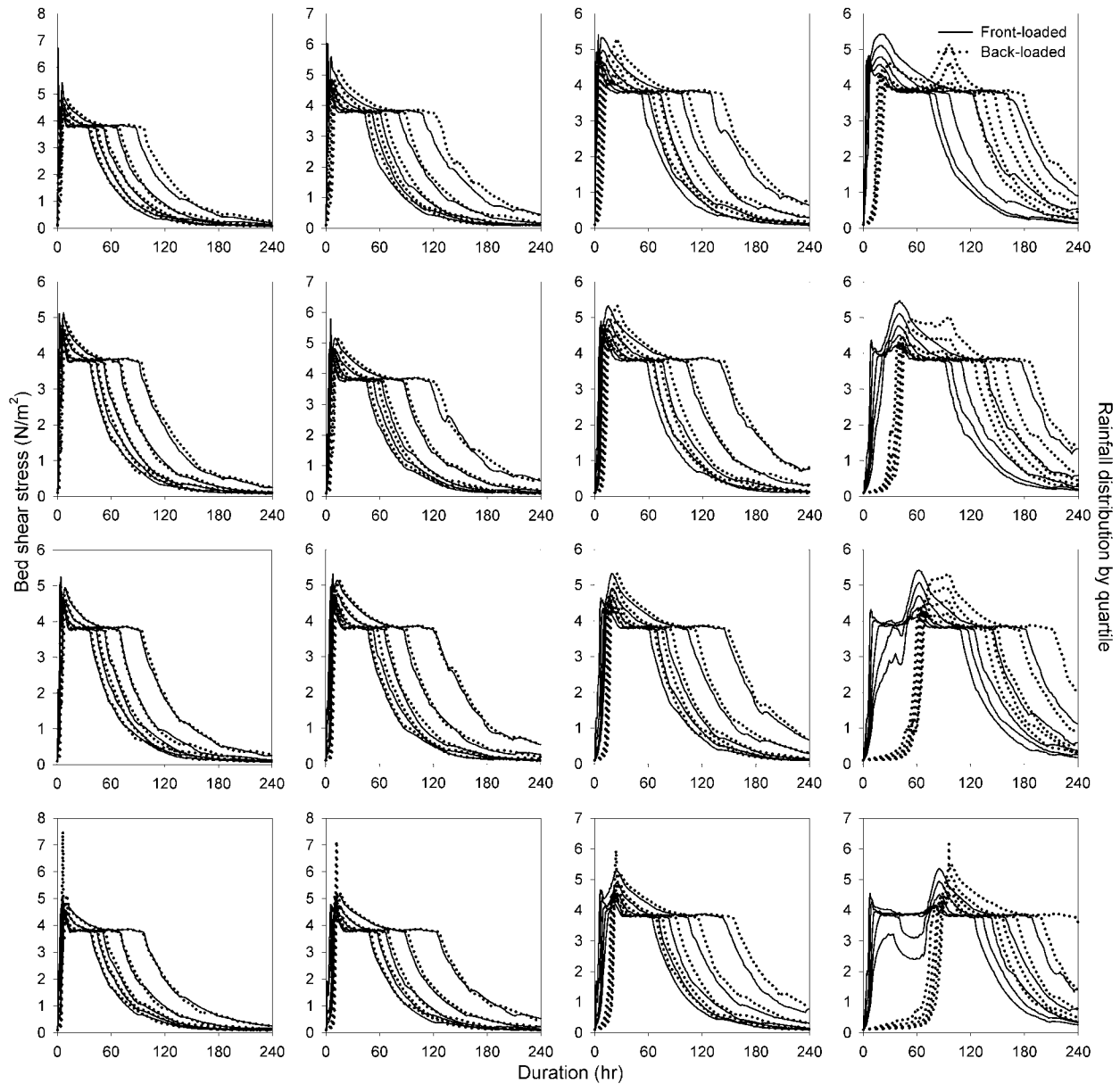


Figure 65. Bed shear stress at Steed Pond as a response to the design rainfall events. Note: 1) each column represents results under events with the same rainfall duration, 6h, 12h, 24h, and 96h, respectively from left to right; 2) each row represents results under events with the same rainfall temporal distribution out of four quartiles, 1st, 2nd, 3rd, and 4th, respectively from top to bottom; 3) each individual figure includes two groups of curves showing results under 10% and 90% percent of duration, while each group of curves represents results under events with different rainfall ARIs, 5y, 10y, 25y, 100y and 500y, respectively from top to bottom.

Cohesive Sediment Transport Model Verification and Scenario Modeling

The sediment transport model was verified using the measured amount of sediment transported to (Upper Three Runs Creek) UTRC near the outlet of the watershed, as reported in the sediment transport study (Hayes, 1986) regarding Tims Branch. There were only 5 out of the 134 reported

measurements with associated flows that had a 1-year return period or higher. As the main emphasis of this study is event-based modeling for design storm events with a return period ranging from 1-year to 500-year ARIs, those 5 measurements were considered qualified for model verification. Of the 5 measurements, one of them was treated as an outlier as the suspended sediment concentration (SSC) reported for that day resulted from no precipitation in the watershed for a 72-hour period. It was mentioned in that report that the measurement coincided with work that was being done to stabilize Steed Pond. The modeled SSCs are compared with the measured values in Table 28. The modeled SSCs displayed in the table are the resultant values from discharges within a range of 0.429–0.51 m³/s, and are compared with those measured from water samples collected near the outlet of the watershed. The model results fairly agree with the measured SSC. It should be mentioned that the team leading this research will be installing a turbidity sensor at the catchment outlet to collect additional timeseries measurements for model verification purposes. The model performance will be reassessed once sufficient field measurements have been attained. The model will be calibrated based on the field data recorded by the turbidity sensors. A decision was made to verify the model performance against the historical reported measurements until new field measurements are available. Interpretation of the modeling results reported in this article should take into consideration that the model performance is limited by data availability suitable for model calibration and verification. Although turbidity measurements were available from water samples collected in 2016 by the research team, they were not qualified for model verification as the measurements were not associated with an episodic precipitation event.

Table 28. Verification of Sediment Transport Model

Modeled		Measured	
Discharge [m ³ /s]	SSC [mg/L]	Discharge [m ³ /s]	SSC [mg/L]
0.429	29	0.425	39
0.433	35	0.425	21
0.439	14	0.453	38
0.459	36	0.510	27
0.463	43		
0.472	44		
0.51	47		
Average	35	Average	31

In order to assess the significance of extreme storm events on the transport of sediment within Tims Branch watershed, numerical simulations were performed for 1-, 5-, 10-, 25-, 100- and 500-year average recurrence interval (ARI) design storm events with 6-, 12-, 24- and 96-hour front-loaded (Q1), center-loaded (Q2 and Q3) and back-loaded (Q4) storm durations. The precipitation frequency estimates and associated information for the abovementioned design storm events were extracted from the National Oceanic and Atmospheric Administration’s (NOAA’s) Precipitation Frequency Data Server (PFDS). Ensembles of the 192 simulated design flow hydrographs are presented in Figure 66 for areas of significance downstream of Steed Pond and at the outlet of watershed for design storm events. Each subplot shows ensembles of the 16 simulated design flow hydrographs for storm events with a specific return period. The subplots on the left-hand side represent modeled flow hydrographs for the downstream end of Steed Pond, whereas the right-hand side subplots represent those for the outlet of the watershed. All subplots indicate a large spread of design flows depending on the storm durations. The simulation results show that the peak flow below Steed Pond should vary between 0.34 m³/s and 2.05 m³/s, whereas it should vary between 0.396 m³/s and 3.18 m³/s at the outlet.

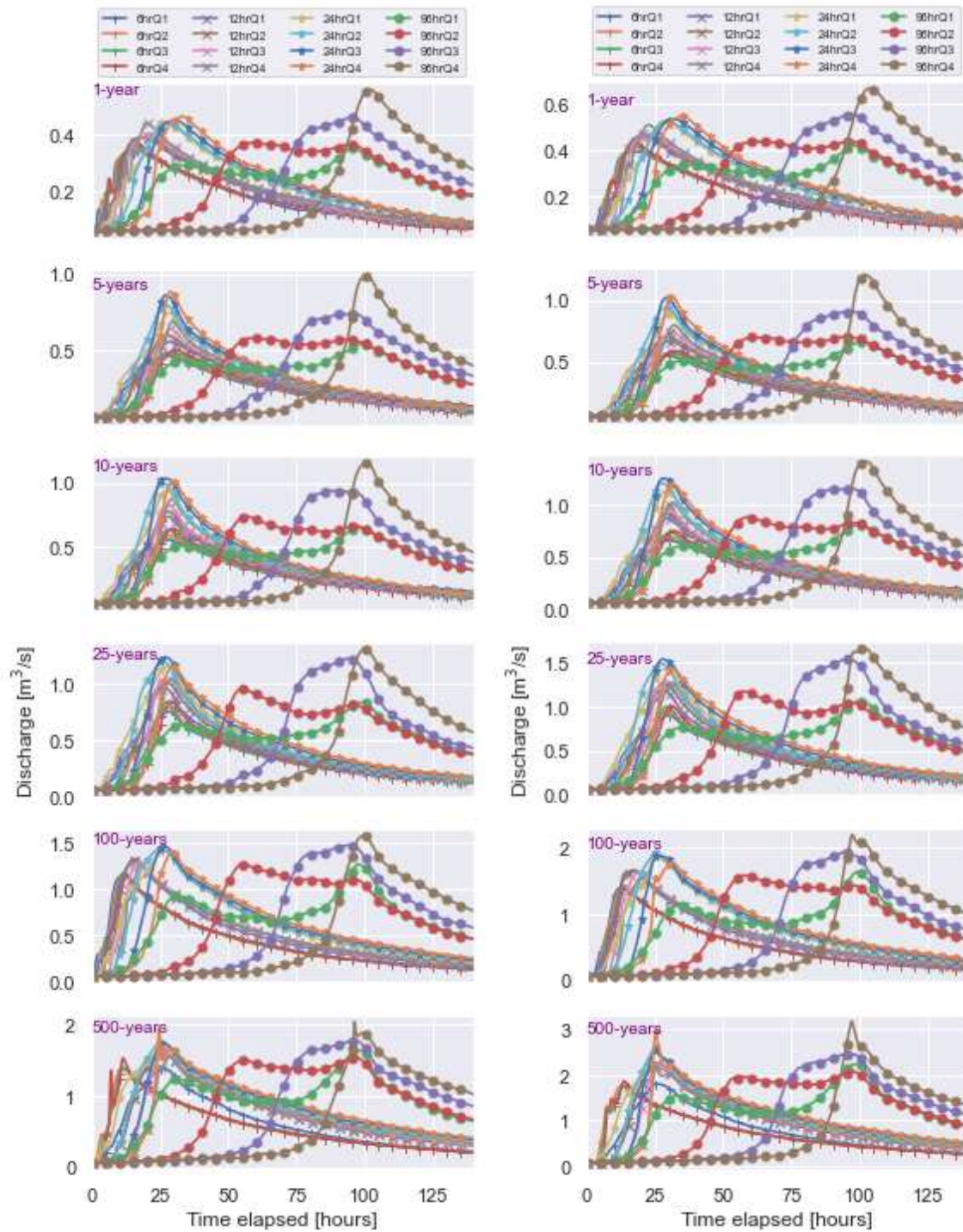


Figure 66. Simulated discharge hydrographs for the area below Steed Pond (left) and the outlet (right) of Tims Branch watershed.

The transport of suspended sediment through the cross-section at the downstream end of Steed Pond and the outlet of the watershed for all design storm events are presented in Figure 67. It is seen from Figure 66 and Figure 67 that the sediment concentration in the water column increases as flow increases. Figure 67 shows that the peak of suspended sediment concentration should vary

between 98 mg/L and 1,084 mg/L below Steed Pond, and between 14 mg/L and 1,139 mg/L at the outlet, under all hydrological conditions.

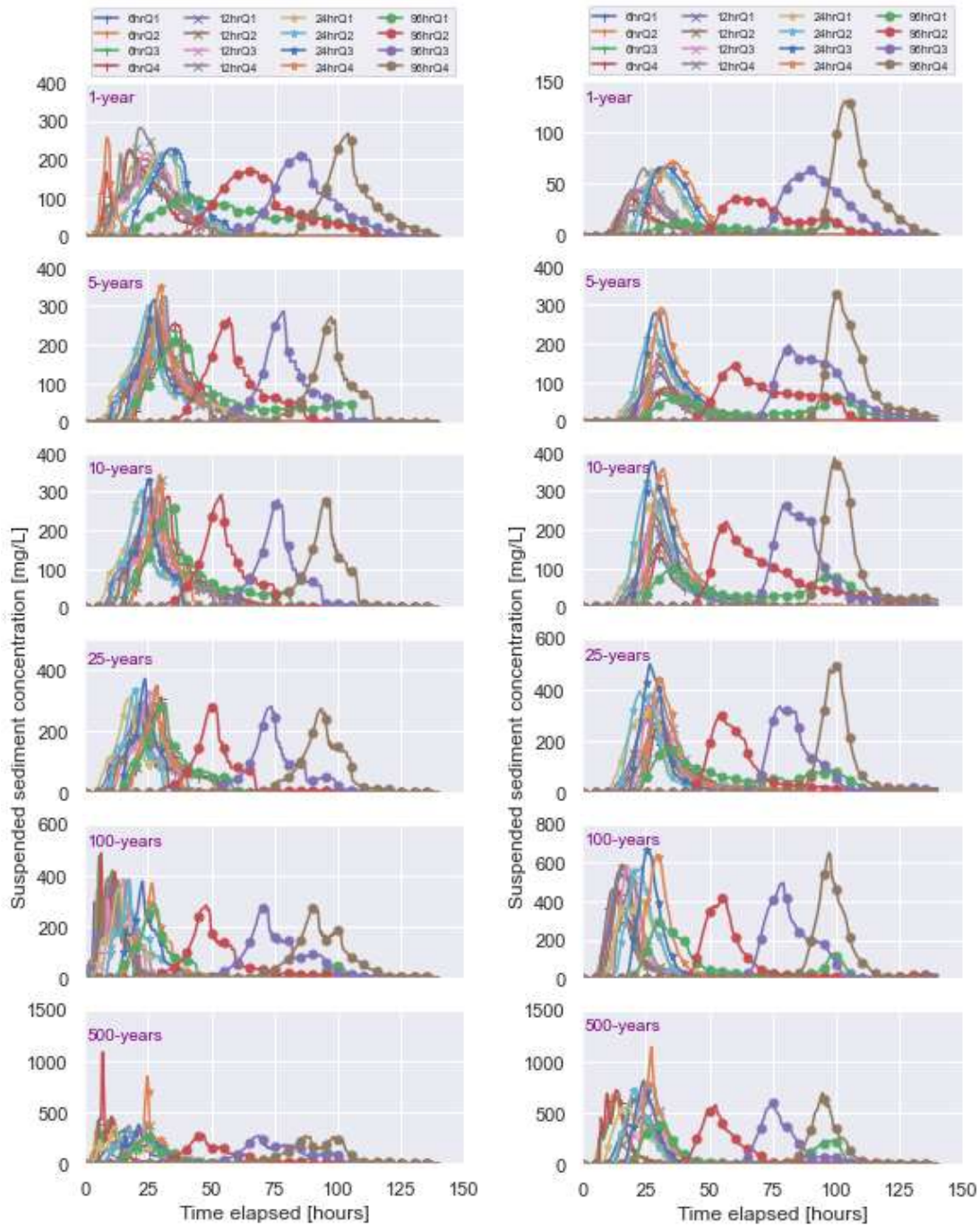


Figure 67. Simulated suspended sediment concentrations for the area below Steed Pond (left) and the outlet (right) of Tims Branch watershed.

Table 29. Suspended Sediment Concentrations and Sediment Loads at the Downstream End of Steed Pond and the Outlet of the Tims Branch Watershed for Various Design Storm Events

Design storm event	Steed Pond d/s Susp. Sedi. load (ton)	Outlet Susp. Sedi. load (ton)	Prevailing process	Design storm event	Steed Pond d/s Susp. Sedi. load (ton)	Outlet Susp. Sedi. load (ton)	Prevailing process
1yr6hrQ1	4.3	0.6	Deposition	25yr6hrQ1	10.0	10.6	Erosion
1yr6hrQ2	4.6	0.7	Deposition	25yr6hrQ2	10.0	11.8	Erosion
1yr6hrQ3	4.9	0.8	Deposition	25yr6hrQ3	10.0	11.7	Erosion
1yr6hrQ4	5.1	0.8	Deposition	25yr6hrQ4	10.1	12.1	Erosion
1yr12hrQ1	5.4	1.2	Deposition	25yr12hrQ1	10.3	17.9	Erosion
1yr12hrQ2	5.7	1.3	Deposition	25yr12hrQ2	10.5	20.2	Erosion
1yr12hrQ3	5.8	1.4	Deposition	25yr12hrQ3	10.8	21.1	Erosion
1yr12hrQ4	6.5	1.6	Deposition	25yr12hrQ4	10.7	19.8	Erosion
1yr24hrQ1	6.6	2.0	Deposition	25yr24hrQ1	11.4	24.1	Erosion
1yr24hrQ2	6.6	2.1	Deposition	25yr24hrQ2	11.9	25.9	Erosion
1yr24hrQ3	6.7	2.2	Deposition	25yr24hrQ3	12.5	28.0	Erosion
1yr24hrQ4	0.4	2.3	Erosion	25yr24hrQ4	11.5	25.2	Erosion
1yr96hrQ1	5.6	0.8	Deposition	25yr96hrQ1	10.4	18.4	Erosion
1yr96hrQ2	7.0	1.8	Deposition	25yr96hrQ2	11.0	22.7	Erosion
1yr96hrQ3	8.0	3.1	Deposition	25yr96hrQ3	13.7	30.2	Erosion
1yr96hrQ4	8.2	4.4	Deposition	25yr96hrQ4	13.4	33.5	Erosion
5yr6hrQ1	7.1	2.4	Deposition	100yr6hrQ1	11.6	24.6	Erosion
5yr6hrQ2	7.2	2.6	Deposition	100yr6hrQ2	11.7	24.3	Erosion
5yr6hrQ3	7.2	2.7	Deposition	100yr6hrQ3	12.0	24.1	Erosion
5yr6hrQ4	7.3	2.9	Deposition	100yr6hrQ4	12.1	23.6	Erosion
5yr12hrQ1	8.6	4.8	Deposition	100yr12hrQ1	13.8	33.9	Erosion
5yr12hrQ2	8.9	5.5	Deposition	100yr12hrQ2	14.0	34.3	Erosion
5yr12hrQ3	9.1	6.2	Deposition	100yr12hrQ3	13.5	32.3	Erosion
5yr12hrQ4	9.4	6.6	Deposition	100yr12hrQ4	13.0	29.9	Erosion
5yr24hrQ1	9.9	10.0	Erosion	100yr24hrQ1	16.0	39.7	Erosion
5yr24hrQ2	10.0	11.8	Erosion	100yr24hrQ2	17.1	44.5	Erosion
5yr24hrQ3	10.1	12.6	Erosion	100yr24hrQ3	16.2	43.0	Erosion
5yr24hrQ4	10.3	12.7	Erosion	100yr24hrQ4	15.1	40.1	Erosion
5yr96hrQ1	9.8	5.9	Deposition	100yr96hrQ1	13.0	29.0	Erosion
5yr96hrQ2	9.9	11.1	Erosion	100yr96hrQ2	16.2	34.9	Erosion
5yr96hrQ3	10.2	15.9	Erosion	100yr96hrQ3	20.0	52.7	Erosion
5yr96hrQ4	10.3	18.6	Erosion	100yr96hrQ4	19.3	52.5	Erosion
10yr6hrQ1	8.6	4.8	Deposition	500yr6hrQ1	15.3	38.2	Erosion
10yr6hrQ2	8.8	5.5	Deposition	500yr6hrQ2	14.8	38.2	Erosion
10yr6hrQ3	8.9	5.9	Deposition	500yr6hrQ3	14.8	36.6	Erosion
10yr6hrQ4	9.0	6.0	Deposition	500yr6hrQ4	18.7	39.2	Erosion
10yr12hrQ1	10.0	9.8	Deposition	500yr12hrQ1	20.8	56.5	Erosion
10yr12hrQ2	10.0	11.2	Erosion	500yr12hrQ2	20.8	56.5	Erosion
10yr12hrQ3	10.1	12.0	Erosion	500yr12hrQ3	20.2	57.0	Erosion
10yr12hrQ4	10.2	12.9	Erosion	500yr12hrQ4	19.2	55.1	Erosion
10yr24hrQ1	10.2	16.9	Erosion	500yr24hrQ1	22.7	59.0	Erosion
10yr24hrQ2	10.4	18.9	Erosion	500yr24hrQ2	23.3	62.5	Erosion
10yr24hrQ3	10.6	20.1	Erosion	500yr24hrQ3	22.8	64.1	Erosion
10yr24hrQ4	10.6	18.8	Erosion	500yr24hrQ4	25.8	66.7	Erosion
10yr96hrQ1	9.9	10.1	Erosion	500yr96hrQ1	21.2	53.2	Erosion
10yr96hrQ2	10.3	18.0	Erosion	500yr96hrQ2	21.3	55.5	Erosion
10yr96hrQ3	10.7	21.4	Erosion	500yr96hrQ3	28.3	65.5	Erosion
10yr96hrQ4	11.2	23.9	Erosion	500yr96hrQ4	26.0	67.8	Erosion

The suspended sediment loads (tons) at both locations were calculated for all design storm events

and are summarized in Table 29. The prevailing process for the reach between the area below Steed Pond and the outlet is also tabulated. In general, deposition is the prevailing process for design storm events with a return period from 1-year to 5-years. In contrast, the simulation results show that erosion should be the prevailing process for a storm rarer than a 5-year return period. The simulation results indicate that the erosion process is much stronger within the reach during such rare events (ranging from 10-year to 500-year return periods). Therefore, it is assumed that such storm events are able to transport materials from deeper layers of the riverbed.

Table 30 summarizes the estimated SSCs and sediment loads at the outlet for critical duration storm events for all return periods. The critical duration storm represents the event duration which produced the highest peak of suspended solid concentration or suspended solid load, and was generally 24 and 96 hours. Table 30 shows that the critical storm duration for SSC was 96 hours for events between 1-year and 10-year return periods, whereas it was 24 hours for larger events (25-year to 500-year return periods). The critical storm duration for suspended solid loads was found to be 96 hours for all return period events. The peak suspended solid loads and stream flows for the critical duration storms are displayed in Figure 68. The hydrographs for flow and cumulative suspended solid loads are presented in Figure 69. It can be seen from Table 30, Figure 68 and Figure 69 that the resuspension of fine particles can significantly increase the suspended sediment concentration up to 1,139 mg/L for an extreme event with a 500-year return period associated with a rainfall of 282 mm. A total of 68 tons of suspended solid can be transported through the outlet to Upper Three Runs in the case of a 333 mm rainfall event with a return period of 500-years, a storm duration of 96 hours and stream flow of 3.2 m³/s.

Table 30. Critical Duration Suspended Sediment Concentrations and Sediment Loads with Associated Precipitation Depths at the Outlet of the Tims Branch Watershed

ARI (1 in yr)	Critical suspended solid concentration				Critical suspended load			
	Duration	Peak flow (m ³ /s)	SSC (mg/L)	Rain (mm)	Duration	Peak flow (m ³ /s)	Load (ton)	Rain (mm)
1	96hrQ4	0.7	130	101	96hrQ4	0.7	4	101
5	96hrQ4	1.2	329	149	96hrQ4	1.2	19	149
10	96hrQ4	1.4	385	171	96hrQ4	1.4	24	171
25	24hrQ3	1.5	499	162	96hrQ4	1.7	33	204
100	24hrQ3	1.9	672	212	96hrQ3	1.9	53	259
500	24hrQ3	2.9	1139	282	96hrQ4	3.2	68	333

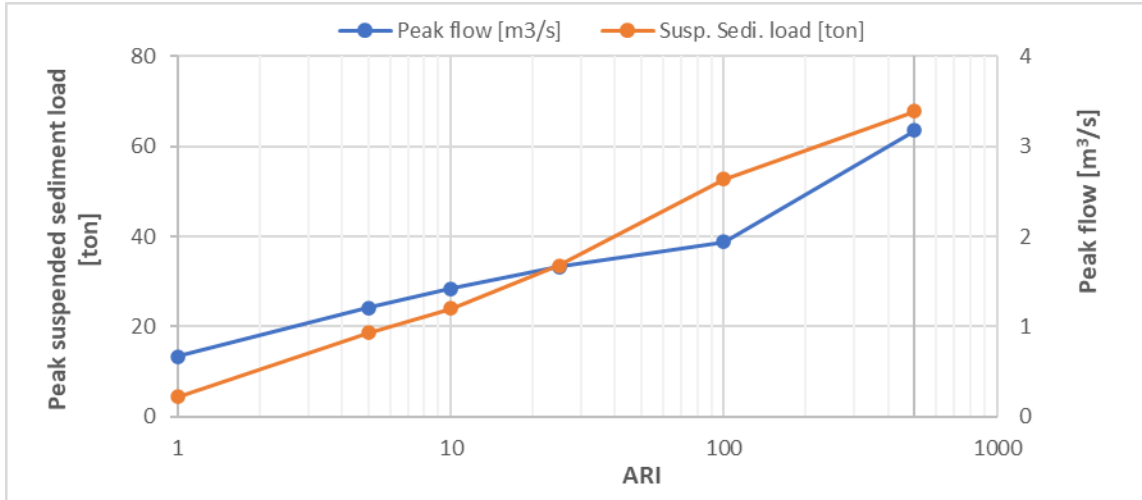


Figure 68. Critical duration peak flows and suspended sediment loads for all frequencies of design storm events at the outlet of the Tims Branch watershed.

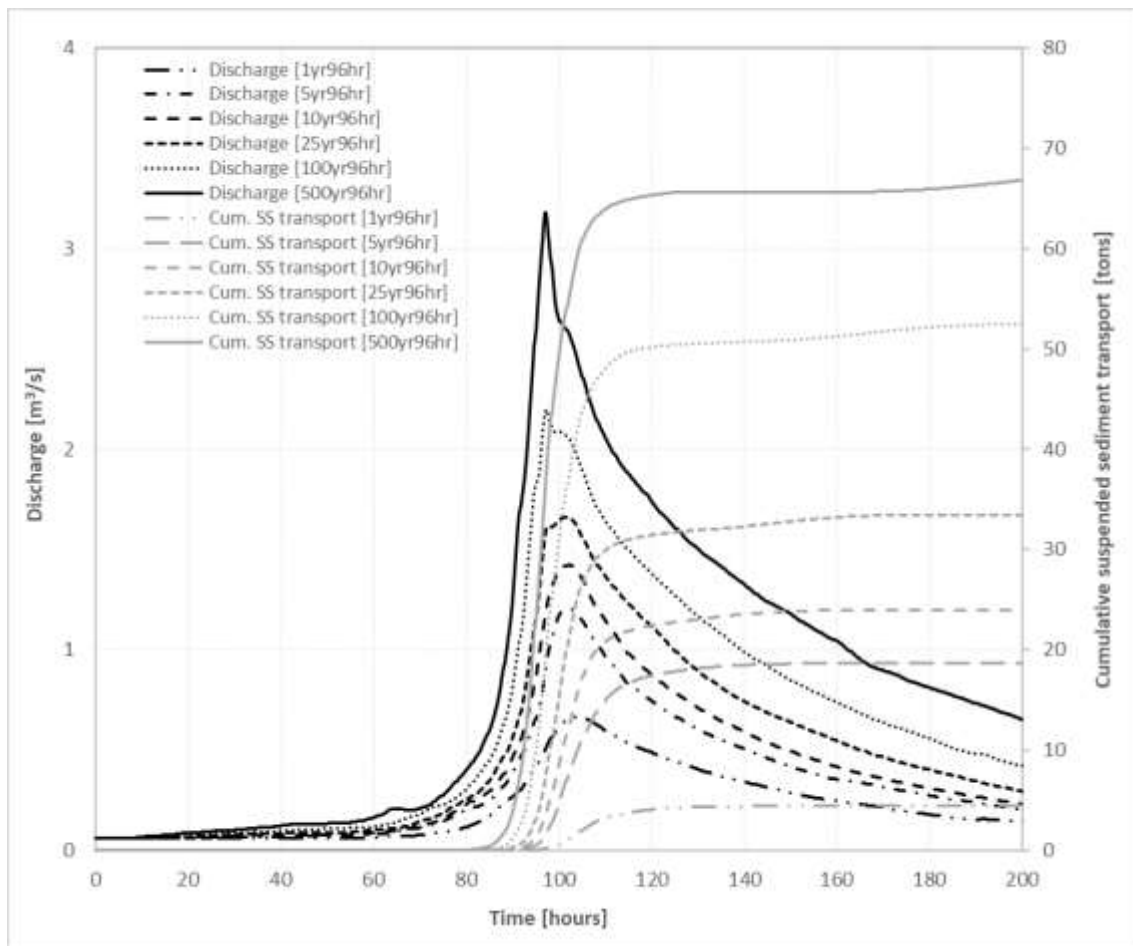


Figure 69. Critical duration peak flows and cumulative suspended sediment loads for all frequencies of design storm events at the outlet of the Tims Branch watershed.

Task 3: Conclusions

In order to provide forecasting capabilities for the flow and sediment transport within Tims Branch watershed, an integrated surface, subsurface and groundwater flow and sediment transport model was developed using the hydrodynamic and transport numerical package MIKE ZERO, developed by DHI. The model was calibrated for flows at the watershed outlet using historical field records. A fair correlation was found between modeled and measured flows, which implies an acceptable level of accuracy and reliability of the model for the hydrodynamic component. The model was then implemented to simulate flows and bed shear stress at key locations within the main branch. A total of 120 storm event scenarios were considered to address the knowledge gaps related to the potential remobilization of adsorbed contaminant in sediment associated with episodic storm events ranging from 1-year to 500-year ARIs. The results obtained from simulation runs confirmed that Steed Pond illustrated the lowest bed shear stress along the lower portion of Tims Branch, making it a hot spot for sedimentation and accumulation of contaminated sediment. The temporal analysis of scenario tests also showed all of the tested events can reach to a bed shear stress of 4 N/m^2 over an extensive period of time at Steed Pond. Therefore, mobilization of contaminated bed sediment at Steed Pond can be minimized by increasing critical shear stress of bed material to 4 N/m^2 or above with erosion control remediation techniques such as the application of geotextile fabric.

The performance of the sediment transport component of the integrated model was verified using reported historical field measurements, making it a very useful tool for predicting sediment transport for various extreme event conditions. However, this was only the first attempt to model transport for various hydrologic conditions, with limited field data that was dated and insufficient. Although several environmental and hydrological studies have been conducted in the Tims Branch watershed, the available field data was not satisfactory for an exact calibration of the model's sediment transport component. The modeling results for suspended sediment concentrations and sediment loads were therefore expected to be slightly overestimated due to insufficient data for the calibration of the sediment transport component of the model at the watershed outlet. For the purpose of improvement and additional calibration of the model, consistent sets of simultaneously measured suspended sediment concentrations and flows at the outlet of the watershed are needed. It is important for developing a suspended sediment rating curve for the watershed outlet. Also, measurements of suspended sediment concentrations at other locations within Tims Branch are necessary in order to improve the model calibration and subsequently the model performance.

Knowledge acquired from this research will assist in developing cost-effective remediation plans integrated into the SRS Area Completion Project (ACP) and accelerate progress of the DOE EM's environmental restoration mission. As an extension of the project, the results of scenario tests can support determining the possibility and timing of contaminated sediment mobilization when coupled with a sediment erodibility study. The model can also serve as a basis upon which additional components could be added in the future to account for the fate and transport of bed sediment and heavy metal and radionuclide contaminants of concern (U, Ni, and Hg). It also supports the interpretation of historical data on the trends of contaminant distribution in Tims Branch, particularly considering the effect of extreme hydrological events on the stream flow and consequent mobilization and redistribution of contaminants that have adsorbed onto the sediment.

FIU will continue execution of the final phase of the Tims Branch model development which involves model optimization to improve and verify the performance of the coupled hydrology and contaminant transport model. The optimization/calibration of the sediment transport model will be finalized using the Advection-Dispersion (AD) module and the ECO Lab module available in the MIKE 11 modeling framework developed for the surface water flow network. The Cohesive Sediment Transport (CST) model will be developed using the AD module of MIKE 11 to simulate the cohesive sediment transport process under different design storm events. The ECO Lab module will be added to the MIKE 11 modelling framework after that. The sediment transport process in ECO Lab will be optimized/calibrated based on the available field measurements for suspended sediment concentration. The ECO Lab module will be parameterized to simulate contaminant transport processes. The fully developed integrated surface water/groundwater MIKE SHE/MIKE 11 modeling framework with the newly added ECO Lab module will be implemented to simulate the resuspension, remobilization and transport of sediment particles under various extreme storm events. The in-situ field data will be gathered and documented to support the evaluation and optimization of the contaminant transport component.

Task 3: References

- Allison, J. D., & Allison, T. L. (2005). Partition Coefficients for Metals in Surface Water, Soil, and Waste. (July).
- Batson, V.L., Bertsch, P.M., Herbert, B.E. 1996. Transport of anthropogenic uranium from sediments to surface waters during episodic storm events. *Journal of Environmental Quality*. 25: 1129-1137 (1996).
- DHI: Danish Hydraulic Institute (DHI), MIKE 11 Environmental Hydraulics, Reference Manual, Horsholm, Denmark, 2007.
- Gibbs, R. J. (1987). "Sources of estuarine sediments and their coagulation." Sedimentation control to reduce maintenance dredging of navigational facilities in estuaries, National Academy Press.
- Hayes, D.W. (1986). "Sediment Transport studies in Tims Branch", Technical Division Savannah River Laboratory. Eddy, J. E., & Yeager, K. M. (2017). Effects of hydrologic connectivity and land use on floodplain sediment accumulation at the Savannah River Site, South Carolina (Unpublished master's thesis). University of Kentucky. Available at: <https://www.osti.gov/biblio/1415567>
- Kaplan, D. I., Buettner, S. W., Li, D., Huang, S., Koster van Groos, P. G., Jaffé, P. R., & Seaman, J. C. (2017). In situ porewater uranium concentrations in a contaminated wetland: Effect of seasons and sediment depth. *Applied Geochemistry*, 85, 128–136. <https://doi.org/10.1016/j.apgeochem.2016.11.017>
- Kristensen, K. J. and Jensen, S. E. (1975). "A model for estimating actual evapotranspiration from potential evapotranspiration," *Hydrol. Res.*, vol. 6, no. 3, pp. 170–188.
- Krone, R. B. (1987). "A method for simulating historic marsh elevations." *Proc., Spec. Conf. on Quantitative Approaches to Coastal Sediment Processes, Coast. Sediments '87*, 316–323.
- Malek-Mohammadi, S., Tachiev, G., Cabrejo, E. and Lawrence, A. (2012). "Simulation of flow and mercury transport in Upper East Fork Poplar Creek, Oak Ridge, Tennessee," *Remediat. J.*, vol. 22, no. 2, pp. 119–131.

- Mavis, F. T., and Laushey, L. M., "Formula for Velocity at Beginning of Bed-Load Movement is Reappraised," *Civil Engineering, ASCE*, Vol. 19, No. 1, Jan., 1949, pp. 38–39 and p. 72.
- McDonnald, T. E., and Cheng, R. T. (1997). "A numerical model of sediment transport applied to San Francisco Bay, California."
- Neary, V.S., Wright, S.A., and Bereciartua, P. "Case study: Sediment transport in proposed geomorphic channel for Napa River", *Journal of Hydraulic Engineering*, Vol. 127, No. 11 November, 2001, 901-910.
- Phillips, R. C., Saylor, J. R., Kaye, N. B. and Gibert, J. M. (2016). "A multi-lake study of seasonal variation in lake surface evaporation using MODIS satellite-derived surface temperature," *Limnology*, vol. 17, no. 3, pp. 273–289.
- van Rijn, L. C. (1989). "Sediment transport by currents and waves." *DelftHydr. Rep. No. 468*.

TASK 5: REMEDIATION RESEARCH AND TECHNICAL SUPPORT FOR THE WASTE ISOLATION PILOT PLANT

Task 5: Executive Summary

FIU in collaboration with research scientists at the Los Alamos National Laboratory's Actinide Chemistry and Repository Science (ACRSP) and DOE Carlsbad Field Office (DOE-CBFO) is conducting basic research to address and inform the WIPP performance assessment needs. Specifically, these experimental studies focused on the fate and transport of actinides and lanthanides in systems with high ionic strength to glean insights into radionuclide behavior in systems similar to that found at the WIPP site. These experiments are expected to reduce uncertainty in the behavior of actinides in the WIPP environment and may inform development of future performance assessment models that adequately address the interaction of actinides with mineral phases observed at the WIPP site.

During FIU Performance Year 10, FIU continued a research task investigating the impact of various salt solutions of varying ionic strength (0.1 – 5.0 M) on dolomite dissolution to understand the stability of actinides sorbed onto mineral phases. During Year 10, results from this research work were presented by students and staff in two conference posters at the Waste Management 2020 Symposium, Phoenix, Arizona. This work was supported by DOE Fellow Alexis Vento (MS ongoing, Environmental Engineering).

Subtask 5.2: Fate of actinides in the presence of ligands in high ionic strength systems

Subtask 5.2: Introduction

The nation's nuclear defense program in the 1940's resulted in the accumulation of a significant amount of radioactive waste streams. The Waste Isolation Pilot Plant (WIPP), the nation's only deep geologic waste repository opened in 1999 as a solution to the long-term disposal of the nation's legacy transuranic (TRU) wastes (Figure 70). Located near Carlsbad in New Mexico, the WIPP is sited ~655 m below the surface in a salt formation ~610-meter thick that was formed ~250 million years ago through evaporation cycles of the ancient Permian Sea. These salt beds are found in the Salado Formation which consists mainly of interbedded halite (NaCl) and anhydrite layers considered as an ideal repository due to the absence of free-flowing water, ease of mining, insignificant permeability, and geological stability (Figure 71). The Salado Formation overlying the Castile Formation is characterized by high ionic strength pore-waters (~ 7.4 M) and the unique regenerative ability to seal up due to their high plasticity (NAS-NRC, 1957).

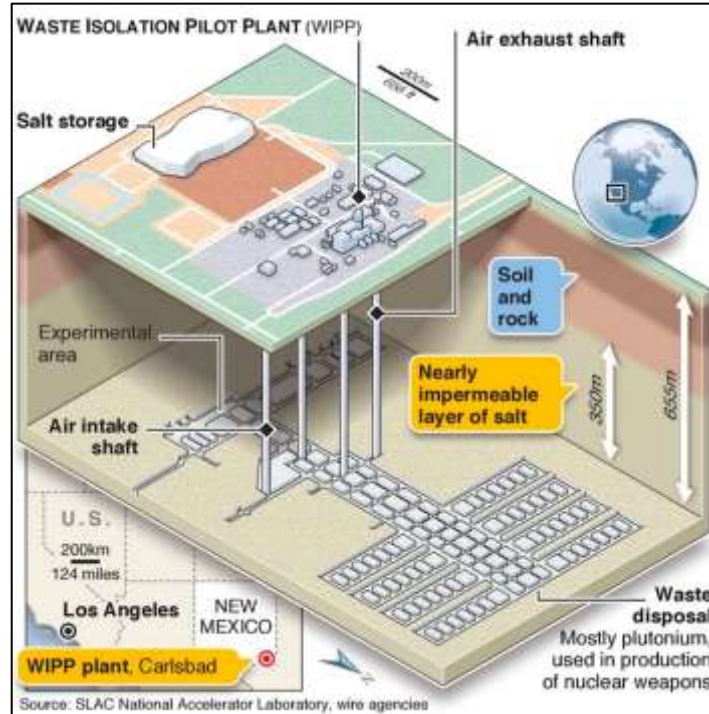


Figure 70. A rendered layout of the Waste Isolation Pilot Plant, near Carlsbad New Mexico (Tracy, 2019).

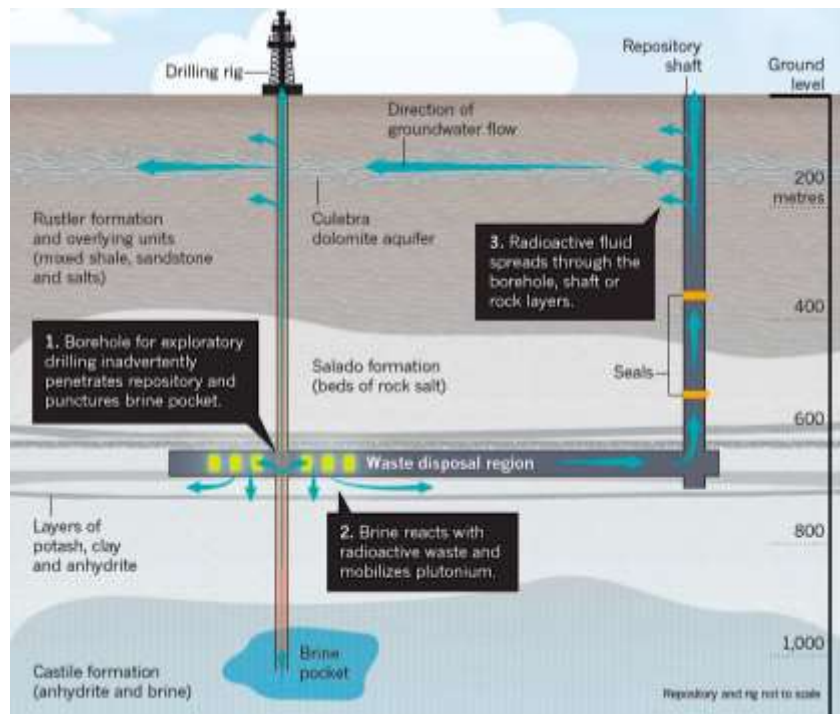


Figure 71. Drilling activities within the geologic formation of the WIPP site (Tracy, 2019).

The Permian Basin region is rich in geologic resources such as potash, salt, oil and gas, making it highly prone to intensive drilling of boreholes that could lead to the release of radionuclides from

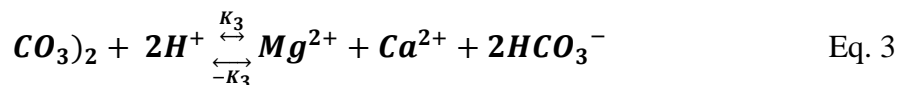
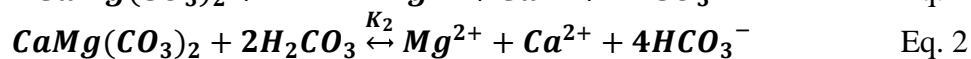
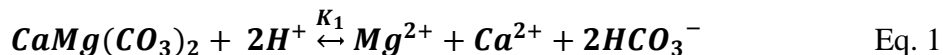
the WIPP environment due to drill intrusions. Drilling has been on the rise since the 1990's and continues to increase exponentially over the years. For example, the drill rate in 1996 was at about 46.8 boreholes/km² which increased to 67.3 boreholes/km² in 2014 (Tracy, 2019). This amounts to about a 40% increase with about 5 intrusion events over the projected 10,000-year post-closure period for the WIPP site (Tracy, 2019). With inadvertent or intentional intrusions, there is the potential for nuclear wastes to react with brine pockets and lead to an increase in mobility of radionuclides. Thus, there is a critical need to understand the mechanisms governing the behaviors of actinides in the environment and development of protective measures that could mitigate radioactive exposure risk to humans and the environment.

The Culebra Member within the Rustler Formation overlies the WIPP and is considered a top priority due to its relatively high transmissivity in most portions of the aquifer. The highly transmissive nature of the Culebra Member of the Rustler Formation may provide a pathway for migration of radionuclides in a low-probability groundwater intrusion, leading to dissolution of minerals and formation of soluble metal species (Brown et al., 1999; Brush & storz, 1996; Stein, 1985). The Culebra Member consists primarily of Dolomite (CaMgCO₃) and is characterized by heterogenous and complex geology due to the occurrence of many conduits, fissures, cracks and fractures that increase its hydraulic conductivity. Consequently, the free movement of water through this formation is expected to enhance mineral dissolution rate. Therefore, in the long-term this Culebra Member poses potential pathways for release of actinides to the environment and needs to be considered in development of a robust performance assessment model (PA) for the WIPP. Fracturing observed within the Culebra has been qualitatively shown to increase from east to west across the WIPP area (Holt et al., 2005). The relative high transmissivity of the Culebra varies over six orders of magnitude within a very small area of 1,000 km² (Beauheim & Holt, 1990).

It has been demonstrated that dolomite plays a significant role in the biogeochemical cycles of many environmentally relevant elements, but its reactivity and surface properties are not well understood in comparison to other important minerals such as carbonates, oxides, and silicates (Stumm, 1992). Few studies have shown that the fast dissolution rates and solubility make quantification of dolomite problematic. Using flow-through reactors and electro-kinetic measurements some studies successfully characterized the surface speciation of carbonates minerals such as rhodochrosite, siderite and magnesite which share similar geochemical properties with dolomite (Oleg S. Pokrovsky et al., 1999; Van Cappellen et al., 1993). Based on the results of these studies, a revised surface complexation model was developed that hypothesized the existence of three key hydration sites as follows: >CO₃H^o, >CaOH^o, and >MgOH^o. In most natural aquatic environments dolomite surface speciation is modeled as: >CO₃⁻, >CO₃Z⁺, >ZOH₂⁺, >ZHCO₃^o, and >ZCO₃⁻, where Z = Ca or Mg. This revised speciation model led to an improved understanding of key parameters governing dolomite dissolution/crystallization in aqueous systems. Furthermore, study results showed that dolomite dissolution is controlled by the protonation of >CO₃H^o surface complexes at pH<6 and by hydrolysis of >ZOH₂⁺ groups at pH>6 (Oleg S. Pokrovsky et al., 1999).

It has been postulated that dolomite exhibits a two-step reaction due its dependence on MgCO₃ dissolution. Compared to calcite and magnesite with four orders of magnitude difference in rate constants, dolomite dissolution is controlled by successive reactions, with the first CaCO₃ component reaching equilibrium because of the slow dissolution of MgCO₃ (Chou et al., 1989).

Dolomite dissolution can be described by the three parallel reactions given below (Oleg S Pokrovsky & Schott, 2001):



And an “overall dissolution rate” is modeled as:

$$R = k_1 \cdot a_{\text{H}^+}^n \cdot k_2 \cdot a_{\text{H}_2\text{CO}_3}^p + k_3 - (-k_3 \cdot a_{\text{Mg}^{2+}} \cdot a_{\text{Ca}^{2+}} \cdot a_{\text{CO}_3^{2-}}^2). \quad \text{Eq. 4}$$

where k_i refer to the rate constants for reactions 1 through 3; a_i represent the activity of aqueous species; exponent n varies from 0.5 to 0.75; p is equated to 1. The first term in the $R = k_1 \cdot a_{\text{H}^+}^n \cdot k_2 \cdot a_{\text{H}_2\text{CO}_3}^p + k_3 - (-k_3 \cdot a_{\text{Mg}^{2+}} \cdot a_{\text{Ca}^{2+}} \cdot a_{\text{CO}_3^{2-}}^2)$. Eq. 4 corresponds to protonation of dolomite surface, the second term represents carbonatation, the third term accounts for surface hydration, and the fourth term attributed to the precipitation reaction.

A potential release scenario envisioned in the WIPP performance assessment is groundwater intrusion through the highly transmissive Culebra Member overlying the WIPP that mobilizes nuclear wastes. In a low-probability TRU release scenario driven by dissolved brine and radionuclide mobility americium (Am), neptunium (Np) and plutonium (Pu) are considered the most important actinides species to be released from the WIPP environment. The waste streams reprocessing and degradation of repository components (e.g. cellulose degradation by calcium hydroxide present in cement, steel containers) resulted in formation of significant concentrations of ligands such as citrate, ethylenediaminetetraacetic acid (EDTA), oxalate, gluconate etc. in the WIPP that can form strong complexes with metals. The iron found in the steel waste containers and lead (Pb) in the shielded containers are expected to strongly react with sulfide and compete with actinides for complexation with organic ligands found in the WIPP brines. Along with low-probability groundwater intrusion, the presence of metal-chelating organic ligands, iron oxide minerals (magnetite), and intrinsic actinide colloids may provide a potential release pathway for migration of the actinides. Thus, a comprehensive understanding of the mobility of actinides and lanthanides in the presence of metal-chelating ligands in WIPP-relevant conditions is important to developing a robust risk assessment model.

The slurry-sludge mixture for TRU waste contains EDTA as high as 10^{-4} M which can form complexes with radionuclides (Nd, Th, U) in a low-probability groundwater intrusion release scenario (Leigh et al., 2005). EDTA complexation's affinity potential can promote dissolution of dolomite through precipitation or increased solubilization (Oviedo & Rodríguez, 2003). The complexation effect of strong chelating agents such as EDTA and oxalate has been accounted for in current performance assessment (PA) models, however the impact of EDTA on the stability of dolomite in varying ionic strength brines relevant to the WIPP environment is not well understood. Because previous studies did not fully cover conditions representative of the WIPP environment and to support the development of comprehensive PA models, FIU investigated the dissolution of dolomite in the presence of EDTA in varying ionic strength systems (Brady et al., 1999; Brown et al., 1999; Brush & storz, 1996).

This current work focused on the impact of EDTA on the sorption of radionuclides onto dolomite, a calcium magnesium carbonate mineral found within the Culebra Member of the Rustler Formation above the WIPP.

Subtask 5.2: Objectives

Risk assessment models have been extensively developed for the WIPP site, but the subsurface environment surrounding the WIPP have not been well studied. Moreover, the potential interaction between nuclear wastes and subsurface environment is not well understood. This current research focuses on dolomite dissolution and actinide transport for an improved understanding of the WIPP subsurface environment.

The overall objective of this task is to use updated experimental sorption data to elucidate the behavior of actinides and lanthanides in the presence of ligands relevant to the WIPP environment. The main objective of this current research is to (1) evaluate the effect of EDTA in varying ionic strength systems on the dolomite dissolution and (2) evaluate the sorption of tri- and tetravalent actinides onto dolomite in the presence and absence of EDTA in NaCl brines (0.1 - 5.0 M), GWB and ERDA-6 simulants. The Generic Weep Brine (GWB) simulates a high Mg environment, similar to the environment expected in the Salado brines. The U.S. Energy Research and Development Administration Well 6 brine (ERDA-6) simulates the environment of the Castile brine, which consists of high sodium concentrations. It is hypothesized that the dolomite dissolution rate will increase with increasing pH values and that addition of EDTA will promote loss of calcium and magnesium from dolomite, resulting in the release of U, Th, and Nd into solution.

Subtask 5.2: Methodology

Materials

Dolomite mineral samples were obtained from the Culebra bluff outcrop on the bank of the Pecos River near the WIPP. The dolomite rock samples were crushed in an impact mortar and pestle (Chemplex, catalogue no. 850), washed with Milli-Q H₂O (> 18 MΩ·cm), and sieved to 355–500 μm particle size fraction. Bulk surface area measured via the Brunauer-Emmett-Teller (BET) method (Micromeritics TriStar II 3020) was 1.70 m²/g (Emerson et al., 2018). Characterization via X-ray diffraction (XRD, Bruker D2000) and scanning electron microscope with energy dispersive x-ray spectroscopy (SEM-EDS, JEOL 5900LV) confirmed the samples to be >99% dolomite (Emerson et al., 2018).

All chemicals were ACS reagent grade or better in purity and used as received. Sodium chloride, sodium nitrate, sodium sulfate, potassium chloride, magnesium chloride (Fisher Scientific, Pittsburg, PA), calcium chloride, sodium bromide (Acros Organics, Geel, Belgium), sodium tetraborate (MPI Biomedicals, Santa Ana, CA) and ultrapure deionized water (>18 MΩ·cm) were used to prepare the brines and simulants. In addition to U(VI), Nd(III) and Th(IV) were used as stable analogues for Am(III) and Pu(IV), respectively, to represent the most common oxidation states of tri- and tetravalent actinides in the WIPP environment.

Batch experiments

Batch sorption experiments were used to evaluate the impact of ionic strength (0.1 - 5.0 M) and EDTA on dolomite dissolution and sorption of Nd(III), Th(IV), and U(VI) onto dolomite in NaCl brines, GWB and ERDA-6 simulants under ambient condition. Batch experiments were conducted

in triplicate by adding 50 mL of synthetic brine solutions to 0.20 g dolomite (5 g/L solid to liquid ratio) in 50 mL polypropylene centrifuge tubes (Corning CentriStar). Synthetic brine solutions of selected salts (NaCl, NaNO₃, CsCl, CaCl₂, Na₂B₄O₇ etc.) representing a range of ionic strengths (0.01–5 M) were prepared in deionized water (with resistivity of 18 MΩ). Approximately 3mM NaHCO₃ was added to all solutions to buffer the solution pH and equilibrate samples with atmospheric CO₂. The pH of the synthetic brine containing NaHCO₃ was then adjusted using either HCl or NaOH (0.1 M) to a constant pH $\sim 8.0 \pm 0.5$. Contaminant concentrations ($[M]_{\text{initial}} = 10$ and 1000 μg/L, where M= Nd, Th, U) representative of undersaturation and supersaturation limits were used to spike the brine. All contaminant spikes were from stock standard solutions made in 2% nitric acid (HNO₃) from High-Purity Standards (Charleston, SC). The stock solution was stored at 4 °C and was diluted to the desired final concentration for each experiment using deionized water. An aliquot of EDTA and contaminants were added to each batch reactor (tubes) and subsequently placed in a slow shaker for a time period up to 2 weeks. At the end of each time interval (15 min, 1h, 3h, 24 h, 48 h, 168 h and 336 h) the batch reactors were removed for sampling. Prior to sampling, the pH (pH_R) was determined for each sampling period using ThermoScientific Orion 9110DJWP electrode. The pH_R values were subsequently converted to pcH values by the equation below (Wall et al., 2002):

$$pcH = pH_R + (0.255 \cdot m_{NaCl}) \quad \text{Eq. 5}$$

Where m_{NaCl} is brine (NaCl) molality.

After pH measurements the batch samples were not filtered because previous studies reported losses of contaminants (especially Nd) to various filter materials (e.g. paper, cellulose ester, and PTFE filters) (Emerson et al., 2018). However, two separation methods - settling (15 minutes) and centrifugation (20 minutes, 8000 rpm) - were employed to assess the potential for colloid formation. The expected particle sizes remaining in solution after separation are estimated as follows: $<6 \times 10^6$ nm for settling and <80 nm for centrifugation, respectively. All samples were prepared in 2% HNO₃ and subsequently analyzed by an inductively coupled plasma optical emission spectrometer (ICP-OES, Perkin Elmer 7600) for concentrations of Ca and Mg, while inductively coupled plasma mass spectrometry (ICP-MS, Agilent 7900) was used for analysis of Nd, Th, and U.

Subtask 5.2: Results and Discussion

During FIU Year 10, the batch experiments investigating the impact of EDTA on the sorption of lanthanides and actinides onto dolomite in NaCl brines (0.1 and 5.0 M), GWB and ERDA-6 were completed and the results reported elsewhere (Sockwell et al., 2020).

The results of studies investigating the impact of EDTA and ionic strength (0.1-5.0 M) on the dissolution of dolomite are presented in Figure 72 - Figure 77. Batch experiments were used to evaluate dolomite (5 g/L) dissolution in NaNO₃ (0.1, 1.0, 5.0 M), CaCl₂ (5.0 M), Na₂SO₄ (1.0 M) and CsCl (1.0 M) solutions in the presence or absence of EDTA, a strong cation chelator. It has been demonstrated in previous studies that less than 2% of dolomite dissolved over 168 h at pH 8.5 in 0.1 and 1.0 M NaCl, CaCl₂, and MgCl₂ solutions (Emerson et al., 2018). Furthermore, it was observed that aqueous Ca concentration in the 1.0 M NaCl solution was higher than that in 0.1 M NaCl, implying that high ionic strength solution promoted increased dissolution rate of dolomite (Emerson et al., 2018).

Figure 72 A-D displays the results for dolomite dissolution in the presence and absence of EDTA in an unfiltered and filtered solutions of 0.1, 1.0 and 5.0 M NaNO₃. Dolomite dissolution over time in these varying ionic strength solutions was monitored by changes in aqueous Ca and Mg concentrations. The unfiltered 0.1 M NaNO₃ solution with EDTA exhibited higher Ca and Mg concentrations compared to the Ca and Mg concentrations in the unfiltered 0.1 M NaNO₃ system without EDTA. This increase was attributed to the strong complexation of EDTA with Ca and Mg in the low ionic strength solution. However, in the 1.0 and 5.0 M NaNO₃ unfiltered solutions complexation of EDTA with Ca and Mg was hindered likely due to strong competitions from copious hydroxyl ions present in the higher ionic strength systems. Filtration of these samples by centrifugation removed suspended particles or colloids from solutions, and resulted in lower aqueous Ca and Mg concentrations in the 0.1, 1.0 and 5.0 M NaNO₃ solutions (Figure 72 B, D). The apparent increase in dolomite dissolution observed with rising ionic strength (0.1 to 1.0 M) for both the unfiltered and filtered NaNO₃ solutions with or without EDTA is ambiguous and is attributed to higher measurement errors. Overall measured aqueous Ca was typically higher than aqueous Mg in the NaNO₃ solutions.

There was no discernable difference between aqueous Mg in the 5.0 M CaCl₂ solution with and without EDTA because complexation of Mg by EDTA was suppressed in the high ionic strength solution by competing ions (Figure 73 C, D). In the 5.0 M CaCl₂ solution aqueous Mg in the unfiltered solution was approximately two times higher than that in the filtered solution due to removal of colloidal or suspended particles from solution. The aqueous fraction, a measure of Ca and Mg released from dolomite surface was 0.28 and 0.60% for Mg²⁺ in the filtered and unfiltered 5.0 M CaCl₂ system with or without EDTA (data not shown).

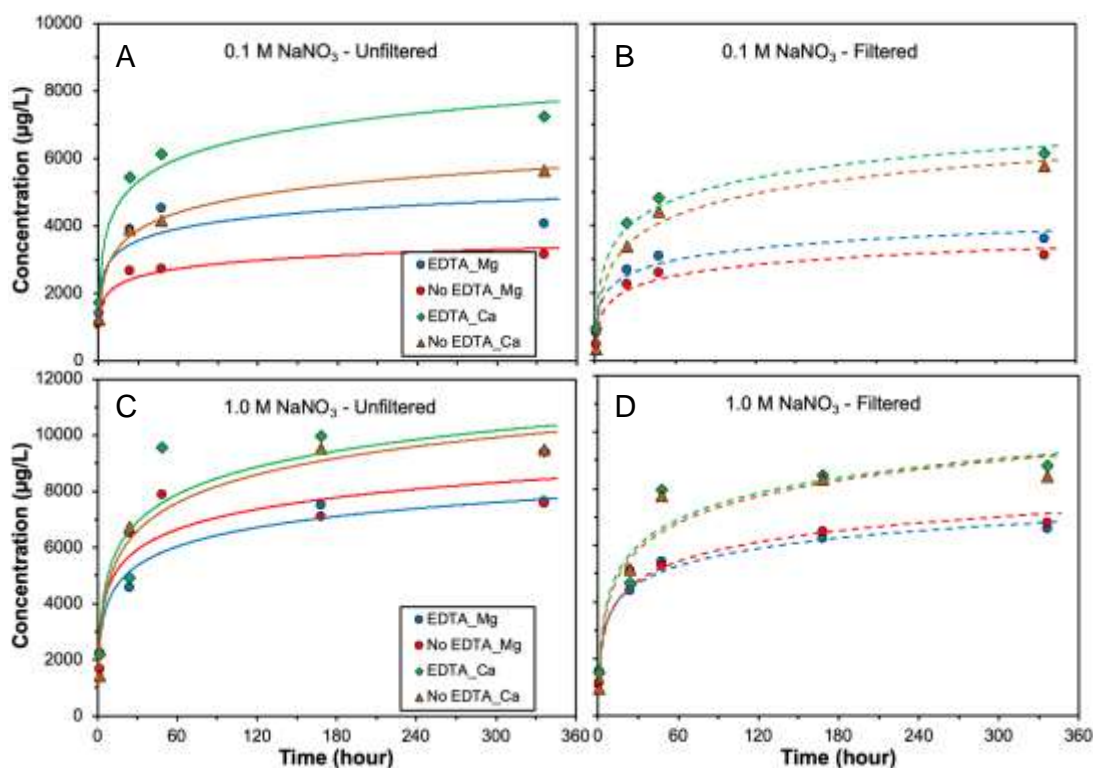


Figure 72. Dissolution of dolomite (5 g/L) with time as a function of EDTA and separation methods in 0.1 M NaNO₃ (A, B), 1.0 M NaNO₃ solutions (C, D). Error bars are based on one standard deviation of triplicate samples.

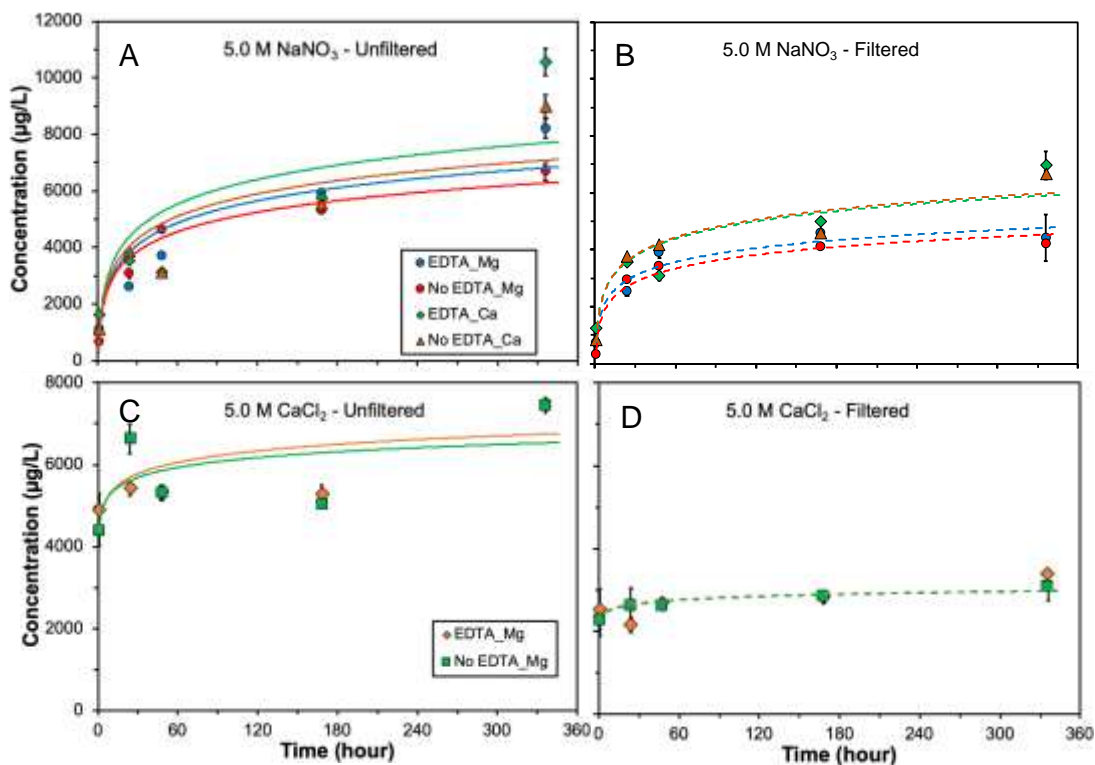


Figure 73. Dissolution of dolomite (5 g/L) with time as a function of EDTA and separation methods in in high ionic strength 5.0 M NaNO₃ (A, B) and 5.0 M CaCl₂ solutions (C, D). Error bars are based on one standard deviation of triplicate samples.

Figure 74 A-B illustrates the results of dolomite dissolution in 1.0 M Na₂SO₄ as a function of EDTA and filtration methods. There was no difference in aqueous Ca and Mg concentrations between the unfiltered samples with and without EDTA. However, the filtered samples with EDTA exhibited higher Ca and Mg concentrations compared to the filtered samples without EDTA. This is attributed to the strong complexation of EDTA with Ca and Mg in the 1.0 M Na₂SO₄ solution. Filtration of samples by centrifugation had little impact on decreasing aqueous Ca and Mg concentrations in the 1.0 M Na₂SO₄ solutions compared to the unfiltered samples (Figure 74 A-B). Measured Ca concentration was typically higher than Mg concentration in the 1.0 M Na₂SO₄ samples. The aqueous fraction reached approximately 0.02% for Ca and Mg in the filtered and unfiltered 1.0 M Na₂SO₄ systems with or without EDTA (Figure 75 A-B).

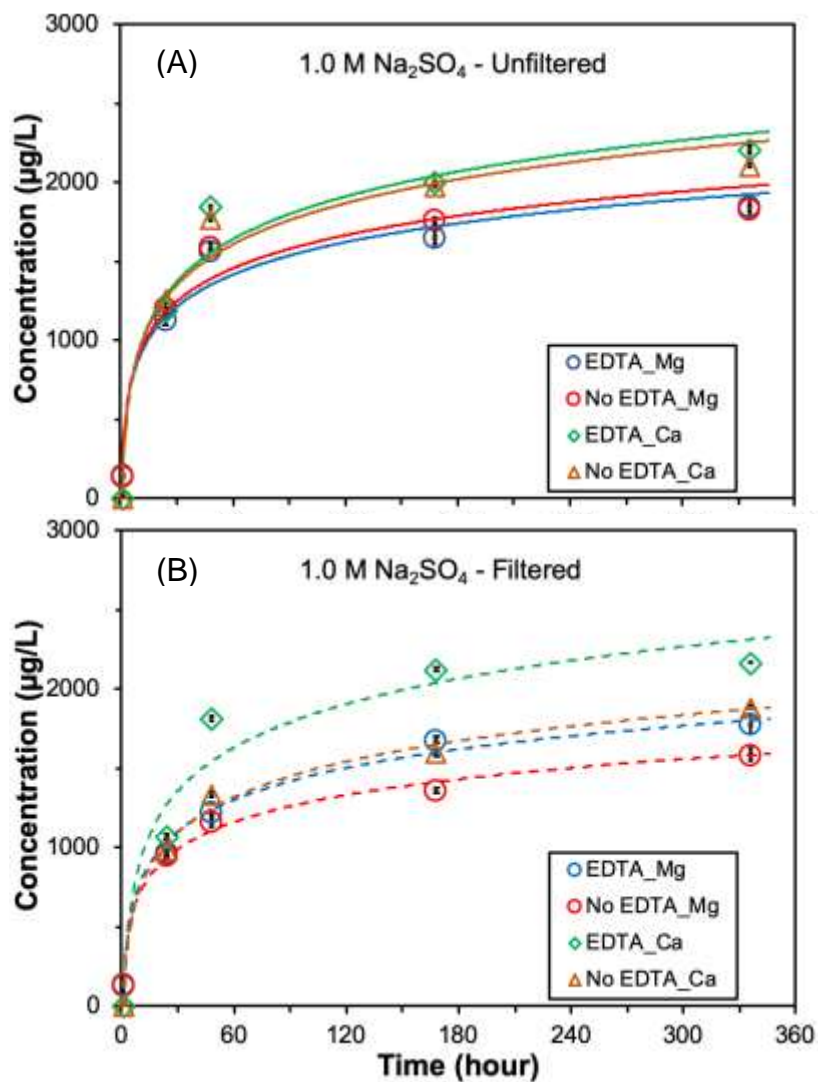


Figure 74. Dissolution of dolomite (5 g/L) with time as a function of EDTA and separation methods in 1.0 M Na₂SO₄. Error bars are based on one standard deviation of triplicate samples.

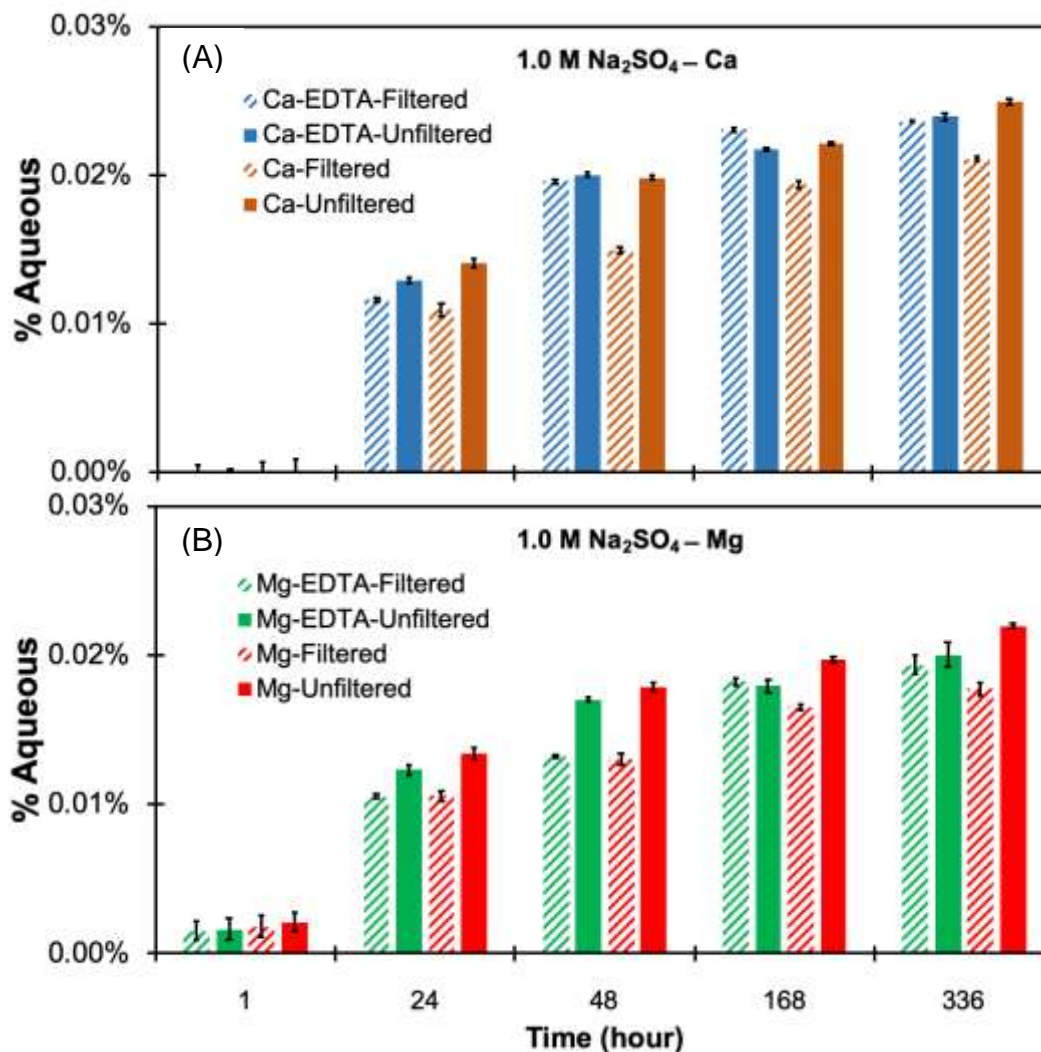


Figure 75. Dissolution of dolomite (5 g/L) with time as a function of EDTA and separation methods in 1.0 M Na₂SO₄. Error bars are based on one standard deviation of triplicate samples.

Presented in Figure 76 - Figure 77 are the results of dolomite dissolution in 1.0 M CsCl in the presence and absence of EDTA. Initially, dissolution of dolomite was slow, but gradually approached equilibration after 60 hours (Figure 76). The unfiltered samples with EDTA had higher Ca and Mg concentrations compared to concentrations of Ca and Mg in the unfiltered samples without EDTA due likely to the complexation of EDTA with Ca and Mg. Moreover, Ca concentration in the unfiltered samples with EDTA was higher than Mg concentration in the unfiltered samples without EDTA. Centrifugation of the samples led to lower Ca and Mg concentrations in the unfiltered samples containing EDTA compared to Ca and Mg unfiltered samples without EDTA, suggesting possible removal of Ca and Mg colloidal particles from the dissolve phase by this separation step. There were no discernable differences in Ca and Mg concentrations between the filtered samples with and without EDTA. However, the filtered samples with or without EDTA typically contained higher Ca compared to Mg concentrations (Figure 76). This may be due to EDTA higher complexing affinity for Ca compared to that of Mg.

The aqueous fraction of Ca and Mg released from the dolomite surface reached approximately 0.025% for Ca and Mg in the 1.0 M CsCl samples irrespective of filtration or EDTA addition (Figure 77).

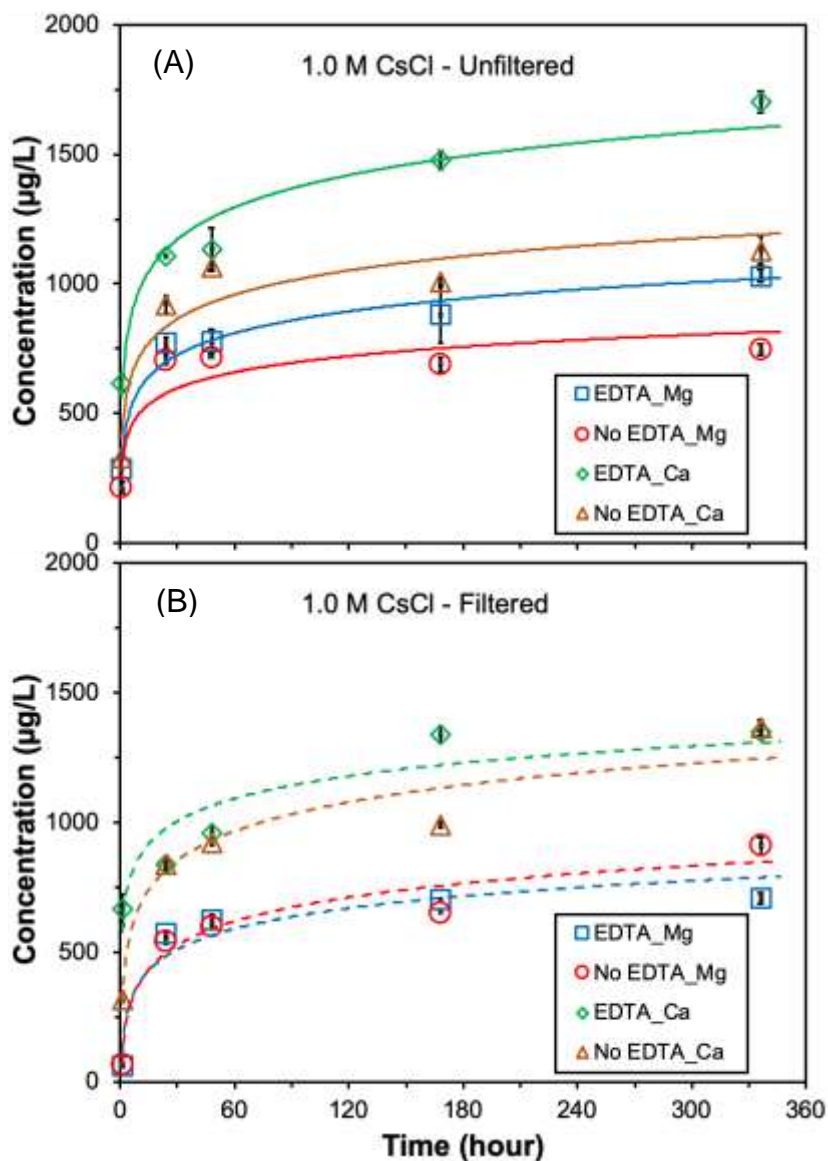


Figure 76. Dissolution of dolomite (5 g/L) over time as a function of EDTA and separation methods (unfiltered -A; Filtered – B) in 1.0 M CsCl solution. Error bars are based on one standard deviation of triplicate samples

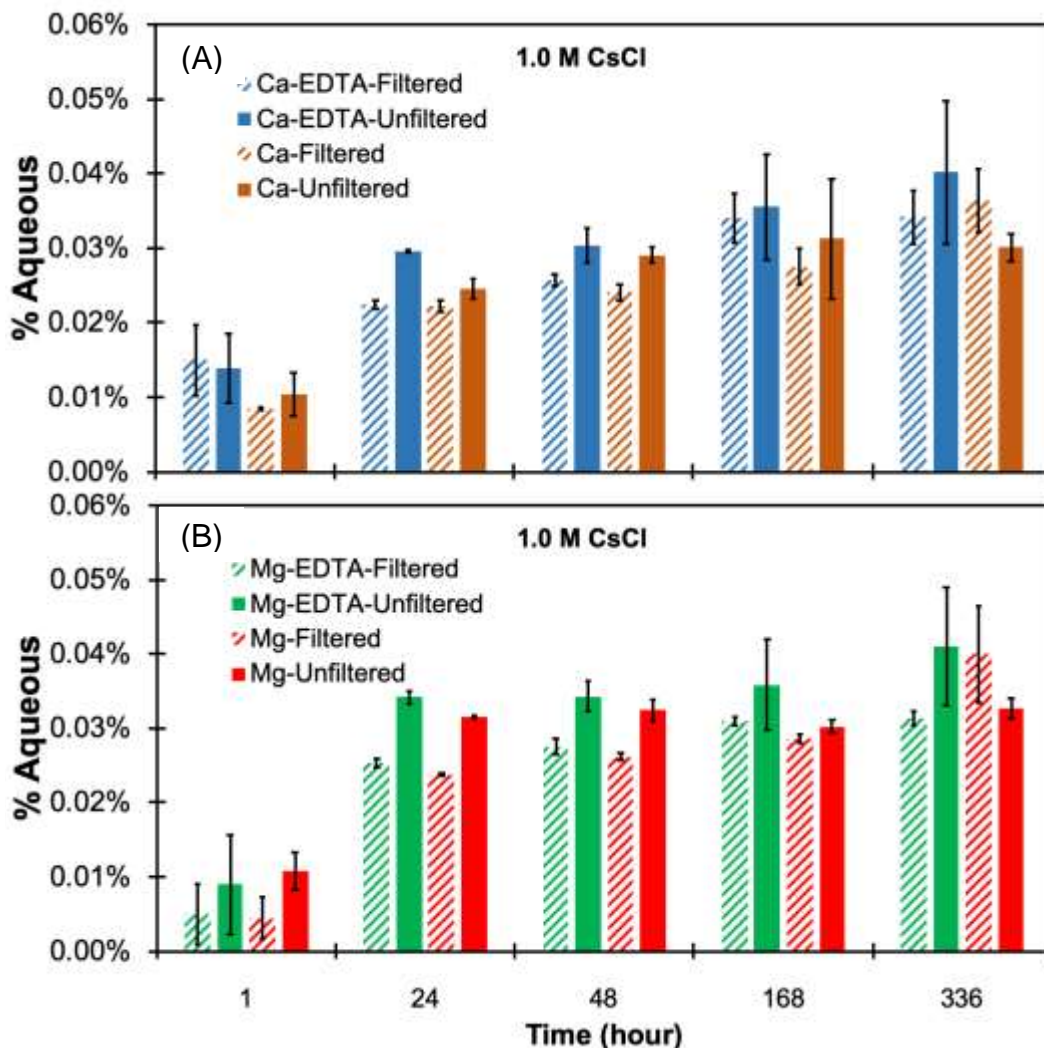


Figure 77. Aqueous Ca (A) and Mg (B) dissolved from dolomite (5 g/L) over time in 1.0 M CsCl solution. Error bars are based on one standard deviation of triplicate samples

Subtask 5.2: Conclusions

Study results showed that less than 1% of dolomite dissolved at pH 8.5 in solutions of NaNO₃ (0.1 -5.0 M), Na₂SO₄ (1.0 M), CaCl₂ (5.0M) and CsCl. The aqueous concentration of Ca in the 1.0 M NaNO₃ was higher than that in both the 0.1 M and 5.0 M NaNO₃ systems. Although previous studies reported that aqueous Ca concentration was higher in 1.0 M NaCl compared to that in 0.1 M NaCl, the observed trend in these current studies is attributed to error associated with measurements. Across the studied salts (1.0 M), the dolomite dissolution decreased in the following order: NaNO₃ > CsCl > Na₂SO₄. These studies suggest that the complexation impact of EDTA on dolomite dissolution was hindered with increasing high ionic strength. Overall, study results indicate negligible impact of EDTA on dolomite dissolution with increasing ionic strength.

Research work in support of WIPP performance assessment models will be continued by FIU ARC. Ligands of interest for the WIPP, such as gluconate (cement additive) and iron minerals (corrosion product) are potential targets for FIU’s study. Currently gluconate is not considered in risk assessments of the WIPP due to the expected low impact in WIPP conditions. However,

previous studies have shown the ability of actinides to form complexes with gluconate in a wide range of pH (Baston et al., 1992; Tits et al., 2005). An increase in Th solubility has been observed in alkaline conditions in the presence of gluconate (Colàs et al., 2011). Moreover, sorption of actinides onto WIPP-relevant iron minerals (corrosion product, e.g. magnetite) under anaerobic conditions relevant to the WIPP environment is well understood. Therefore, FIU will evaluate the impact of gluconate on the sorption of actinides onto pertinent iron minerals in WIPP conditions. Study results will be used to support and inform future development of risk assessment models for the WIPP site.

Subtask 5.2: References

- Baston, G. M. N., Berry, J. A., Bond, K. A., Brownsword, M., & Linklater, C. M. (1992). Effects of Organic Degradation Products on the Sorption of Actinides. *Radiochimica Acta*, 58-9(2), 349-356. <Go to ISI>://WOS:A1992KD61300024
- Beauheim, R. L., & Holt, R. M. (1990). Hydrogeology of the WIPP Site. *Geological and hydrological studies of evaporites in the northern Delaware Basin for the Waste Isolation Pilot Plant (WIPP), New Mexico: Geological Society of America (available from Dallas Geological Society), Field Trip, 14*, 131-179.
- Brady, P. V., Papenguth, H. W., & Kelly, J. W. (1999). Metal sorption to dolomite surfaces. *Applied Geochemistry*, 14(5), 569-579. <Go to ISI>://WOS:000080043300003
- Brown, G. O., Lucero, D. A., & Perkins, W. G. (1999). *Column Experiments for Radionuclide Adsorption Studies of the Culebra Dolomite: Retardation Parameter Estimation for Non-Eluted Actinide Species* (SAND98-1005; Other: ON: DE00002672 United States 10.2172/2672 Other: ON: DE00002672 SNL English). Retrieved from <https://www.osti.gov/servlets/purl/2672>
- Brush, L. H., & storz, L. J. (1996). *Revised Ranges and Probability Distributions of Kds for Dissolved Pu, Am, U, Th, and Np in the Culebra for the PA Calculations to Support the WIPP CCA*. Retrieved from Albuquerque, New Mexico:
- Chou, L., Garrels, R. M., & Wollast, R. (1989). Comparative study of the kinetics and mechanisms of dissolution of carbonate minerals. *Chemical Geology*, 78(3-4), 269-282. <http://www.sciencedirect.com/science/article/pii/0009254189900636>
<https://www.sciencedirect.com/science/article/abs/pii/0009254189900636?via%3Dihub>
- Colàs, E., Grivé, M., Rojo, I., & Duro, L. (2011). Solubility of ThO₂·xH₂O(am) in the presence of gluconate. *Radiochimica Acta*, 99(5), 269-273.
- Emerson, H. P., Zengotita, F., Richmann, M., Katsenovich, Y., Reed, D. T., & Dittrich, T. M. (2018). Retention of neodymium by dolomite at variable ionic strength as probed by batch and column experiments. *Journal of Environmental Radioactivity*, 190-191, 89-96. <https://dx.doi.org/10.1016/j.jenvrad.2018.05.007>
- Holt, R. M., Beauheim, R. L., & Powers, D. W. (2005). *Predicting Fractured Zones in the Culebra Dolomite*. Retrieved from

https://www.wipp.energy.gov/information_repository/information_repository_a/supplemental_information/Holt%20et%20al%202005.pdf

- Leigh, C. D., Trone, J. R., & Fox, B. (2005). TRU Waste Inventory for the 2004 Compliance Recertification Application Performance Assessment Baseline Calculation. *Sandia National Laboratories, Carlsbad, NM. ERMS, 541118*, 21.
- NAS-NRC. (1957). *The Disposal of Radioactive Waste on Land. Report by the Committee on Waste Disposal, Division of Earth Sciences*. Retrieved from Washington DC:
- Oviedo, C., & Rodríguez, J. (2003). EDTA: the chelating agent under environmental scrutiny. *Química Nova, 26*(6), 901-905. <https://dx.doi.org/10.1590/s0100-40422003000600020>
- Pokrovsky, O. S., & Schott, J. (2001). Kinetics and mechanism of dolomite dissolution in neutral to alkaline solutions revisited. *American Journal of Science, 301*(7), 597-626.
- Pokrovsky, O. S., Schott, J., & Thomas, F. (1999). Dolomite surface speciation and reactivity in aquatic systems. *Geochimica et Cosmochimica Acta, 63*(19-20), 3133-3143. [https://dx.doi.org/10.1016/s0016-7037\(99\)00240-9](https://dx.doi.org/10.1016/s0016-7037(99)00240-9)
- Sockwell, K. A., Zengotita, F., Vento, A., Swanson, J. S., Reed, D. T., Katsenovich, Y., & Emerson, H. P. (2020). *The impact of ethylenediaminetetraacetic acid (EDTA) on the sorption of Nd(III), Th(IV), and U(VI) onto dolomite in WIPP-relevant brines, GWB and ERDA-6*. Paper presented at the Waste Management, Phoenix, Arizona.
- Stein, C. L. (1985). *Mineralogy in the Waste Isolation Pilot Plant (WIPP) facility stratigraphic horizon* (SAND-85-0321; Other: ON: DE86000571 United States 10.2172/5203761 Other: ON: DE86000571 NTIS, PC A03/MF A01. SNL English). Retrieved from <https://www.osti.gov/servlets/purl/5203761>
- Stumm, W. (1992). *Chemistry of the solid-water interface: processes at the mineral-water and particle-water interface in natural systems*: John Wiley & Son Inc.
- Tits, J., Wieland, E., & Bradbury, M. H. (2005). The effect of isosaccharinic acid and gluconic acid on the retention of Eu(III), Am(III) and Th(IV) by calcite. *Applied Geochemistry, 20*(11), 2082-2096. <https://dx.doi.org/10.1016/j.apgeochem.2005.07.004>
- Tracy, C. L. (2019). Feasibility and Risks of Human Intrusion in WIPP. In. Belfer Center for Science and International Affairs, Kennedy School of Government, Harvard University, USA.
- Van Cappellen, P., Charlet, L., Stumm, W., & Wersin, P. (1993). A surface complexation model of the carbonate mineral-aqueous solution interface. *Geochimica et Cosmochimica Acta, 57*(15), 3505-3518.
- Wall, N. A., Borkowski, M., Chen, J., & Choppin, G. R. (2002). Complexation of americium with humic, fulvic and citric acids at high ionic strength. *Radiochimica Acta, 90*(9-11), 563-568.

TASK 6: HYDROLOGY MODELING FOR WIPP (NEW)

Task 6: Executive Summary

This task was initiated by FIU researchers at the Applied Research Center in collaboration with DOE personnel at Pacific Northwest National Laboratory (PNNL) and the Carsbad Field Office (CBFO) to support research and development activities at the WIPP site by developing a groundwater-basin model for the WIPP site using the DOE-developed Advanced Simulation Capability for Environmental Management (ASCEM) modeling toolset. ASCEM is a multi-laboratory initiative to promote a state-of-the-art scientific approach for understanding and predicting subsurface flow and contaminant transport behavior and is ideally suited for this task as its integrated toolset offers advanced modeling capabilities that can be used across the DOE complex. The proposed ASCEM groundwater-basin model will be used to improve the current understanding of regional and local groundwater flow at the WIPP site as there have been significant changes within the last several years, including increased water withdrawals outside the LWA boundary that have impacted water levels and chemistry in compliance monitoring wells on site. There are also questions which remain unanswered related to recharge to the Rustler Formation overlaying the Salado Formation that hosts the repository.

There is a need for an improved understanding of the regional water balance, particularly the relation between Culebra recharge and the intense, episodic precipitation events typical of the monsoon. This relationship is essential for understanding the rate of propagation of the shallow dissolution front, and the impact of land-use changes around the WIPP facility on water levels in compliance-monitoring wells. These types of analyses require a revision of the current site conceptual model to couple surface water and groundwater processes, a high resolution digital elevation model (DEM) including channels and sinkholes to account for surface water routing, and the development of a new mathematical model. The ASCEM hydrologic model cannot currently account for land surface hydrology, which is essential for computing the water balance. The proposed work will therefore also require the coupling of a state-of-the-art open-source land surface model (LSM) with the groundwater models (GWMs) within the ASCEM toolbox to simulate three-dimensional, unsaturated and saturated water flow. Candidate LSMs include the Community Land Model (CLM), which has been successfully coupled with the LBNL-developed ParFlow, and the UCAR-developed Noah and Noah-Multi-parameterization (Noah-MP) models. Noah-MP has been successfully coupled with the Weather Research and Forecasting (WRF) Model and used to predict the water cycle components including precipitation, soil moisture, snow pack, groundwater, streamflow, and inundation. Both the CLM and Noah-MP LSMs can be run as standalone codes, generating output that can be used to force ASCEM groundwater models while work is done within the ASCEM program to couple the LSM and GWMs.

The objective of this task is to develop a groundwater-basin model for the WIPP site using ASCEM coupled with a selected LSM to account for the surface and near-surface processes. These models will be used to compute the water balance across multiple scales and to reduce uncertainties in recharge estimates and propagation of the shallow dissolution front. This task will provide an extensible, multi-scale land-atmosphere modeling capability for conservative, coupled and uncoupled prediction of the hydrological cycle components. This will simplify the upper boundary condition for flow in Culebra that is currently externally specified without consideration of water fluxes due to surface processes like runoff, infiltration and evapotranspiration. Coupling of the

LSM with the ASCEM GWMs leads to more accurate predictions of groundwater flow patterns, including horizontal flow (e.g., potentiometric surface, flow direction, vertical flow into transmissive units, and the effect of density on flow direction). With improved estimates of the spatial and temporal patterns of recharge to force the GWM, predictions of halite dissolution and propagation of the shallow dissolution front will be made possible and the potential impact on repository performance quantified.

Subtask 6.1: Digital Elevation Model and Hydrologic Network

Subtask 6.1: Introduction

Development of a high resolution DEM will facilitate accurate delineation of hydrological and topographical features including drainage basins, brine lakes, channels, sinkholes, discharge points and other relevant hydrological features to account for surface water routing, ensuring that all features are hydrologically correct so that channels and drainage divides are in the correct places and that optimal monitoring and forecasting points can be identified. The geospatial data generated will be used in the selected LSM in order to derive parameters that account for the surface and near-surface hydrological processes and assist in computing the surface water balance across multiple scales to reduce uncertainties in recharge estimates at the WIPP site.

Subtask 6.1: Objectives

The purpose of this subtask is to develop the data layers for the terrestrial overland flow, channel routing, and subsurface flow processes of the LSM. FIU's assessment of available high-resolution DEM data revealed the absence of data in this study area that would produce the level of topographical detail and accuracy desired for this project. Therefore during FIU's Performance Year 10, a pilot study was conducted to: (1) capture high resolution aerial imagery of a representative section of Basin 6 in the Nash Draw adjacent to the WIPP site using a UAV equipped with a GPS and way-point tracking ability; (2) process the aerial images collected using photogrammetric techniques to build a high resolution DEM; and (3) utilize the developed DEM to delineate and extract the hydrological features of interest as mentioned above. The pilot study will serve as proof of concept that the proposed methodology is feasible and has practical applications at WIPP to generate high-resolution imagery for development of a DEM, which is essential for detailed delineation of hydrologic basins within and surrounding the WIPP LWA boundary. This research also provides FIU undergraduate and graduate students (DOE Fellows) with training on UAV photogrammetry methods in addition to mentorship and field experience, as well as an opportunity to participate in student summer internships in collaboration with PNNL and CBFO scientists.

Subtask 6.1: Methodology

In FIU Performance Year 10, FIU continued this subtask by collecting aerial imagery of a subset of the research area in Basin 6 covering an area of 5 km². The collected data was used to validate the workflow of photogrammetry for generating a submeter-resolution digital elevation model (DEM) of the land surface, as well as testing a number of vegetation removal techniques. This approach allowed us to better capture the ground surface topography and local features which will enable more accurate delineation and extraction of features such as drainage basins, brine lakes, channels, sink holes and discharge points in future. The information gathered will also aid in determination of the software, data and processing requirements required for this task.

In December 2019, a literature review for methodologies of vegetation removal from unmanned aerial vehicle (UAV)-based photogrammetric digital surface models was completed as FIU Performance Year 9 carryover scope. The full literature review was submitted as an appendix to the FIU Performance Year 9 end of year report. Due to the cost of acquiring and processing LiDAR data for DEM development, the use of unmanned aerial vehicles (UAVs) to acquire digital photos is becoming more common. However, UAV-based point clouds do not represent the bare earth surface as well as LiDAR. This literature review therefore serves to investigate various ground filtering and machine learning methodologies for vegetation identification and removal from UAV-based photogrammetric digital surface models (DSMs) in order to improve DEM accuracy. The use of UAV-based photogrammetric methods provides a more affordable approach for DEM development. In conjunction with the appropriate ground filtering or machine learning methodology, it can provide researchers with accurate representations of the bare earth for development of land surface and hydrological models. FIU intends to use an appropriate vegetation removal technique to process the UAV aerial images collected in Basin 6 during the pilot study.

During FIU Performance Year 10, FIU tested and compared two vegetation removal techniques from UAV-based photogrammetric digital surface/elevation models based on the literature review. The methodology employed can be seen in Figure 78 below.

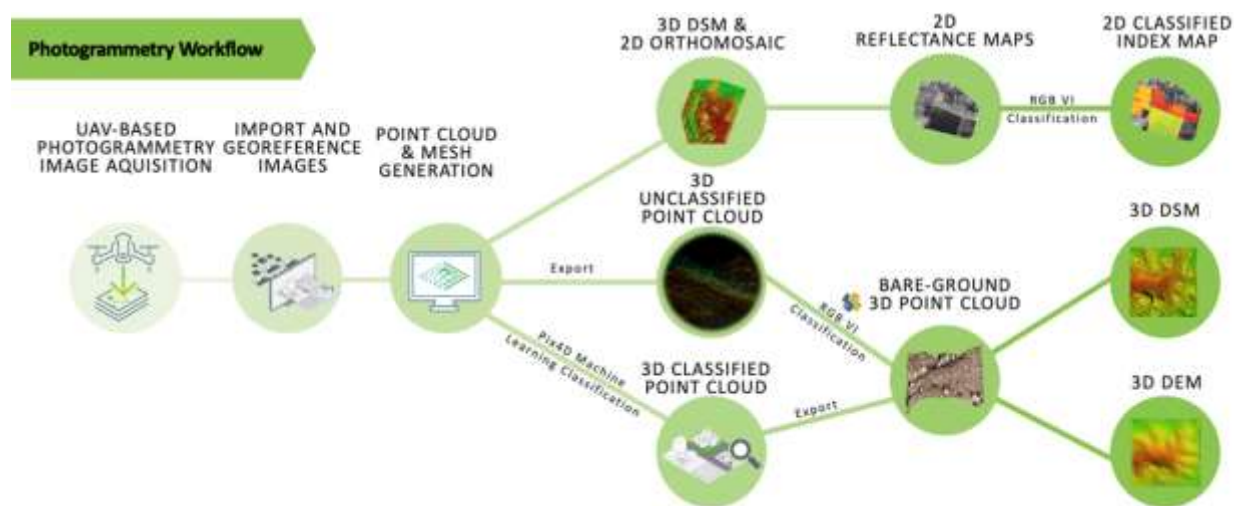


Figure 78. Photogrammetry workflow to produce bare ground DEMs from a point cloud of the study area using RGB-based vegetation indices and machine learning technology.

Digital images taken in Basin 6 during a trip to Carlsbad, NM in August 2019 were imported into the photogrammetry software Pix4D, which is able to automatically georeference the images and generate an unclassified 3D point cloud seen in Figure 79 below.

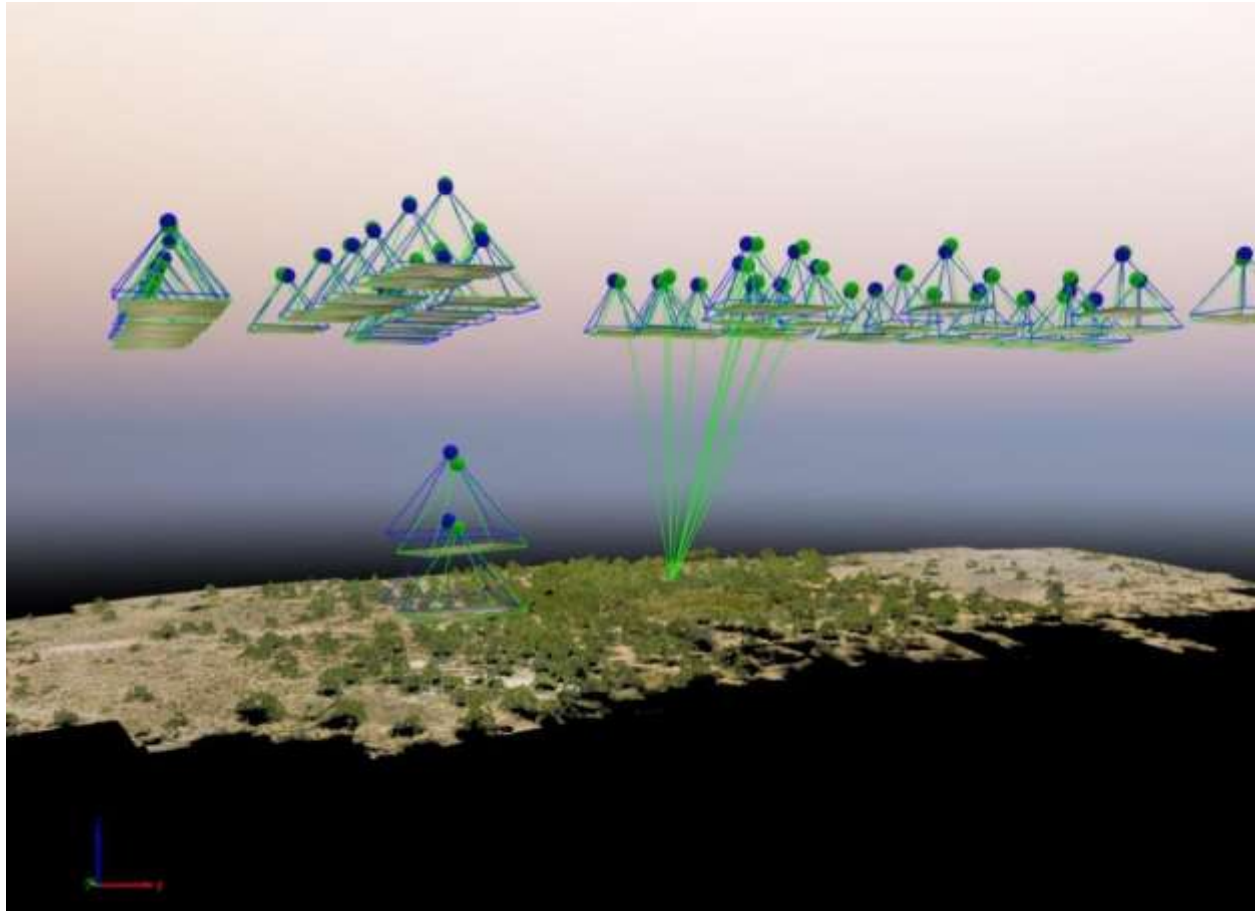


Figure 79. Ray cloud generated in Pix4D after importing aerial images taken in Basin 6, Carlsbad, NM.

A 2D digital orthomosaic and a 3D digital surface model (DSM) were also generated as seen below.

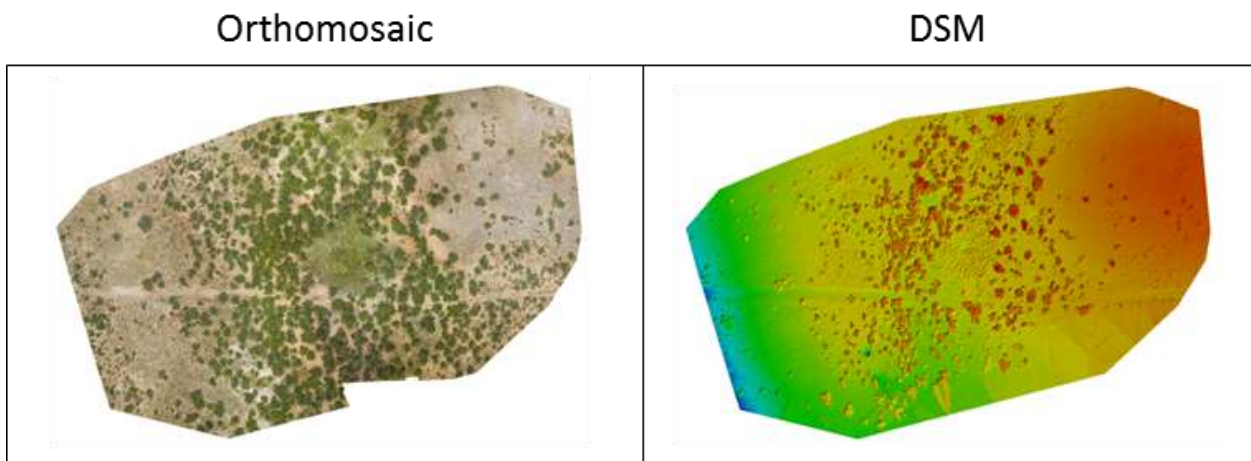


Figure 80. 2D orthomosaic and 3D DSM generated when Basin 6 aerial images were imported into Pix4D.

2D reflectance maps were then generated in Pix4D from the orthomosaic. Various RGB-based vegetation indices (VIs) (Table 31) derived from Themistocleous (2019) were then applied to the

reflectance maps to create 2D index maps which were each divided into two classes representing the bare ground and vegetation. The index maps provided a means for visual comparison with the orthomosaic to determine which of the RGB-based classifications might produce the closest representation of the bare-ground and vegetation in the study area.

Table 31. Vegetation Indices Applied to Pix4D-generated Reflectance Maps

Vegetation Indices	Equation
Red Green Index (RGI)	R_R / R_G
Red-Green-Blue Vegetation Index (RGBVI)	$(R_G * R_G) - (R_R * R_B) / (R_G * R_G) + (R_R * R_B)$
Green Leaf Index (GLI)	$(2 * R_G - R_R - R_B) / (2 * R_G + R_R + R_B)$
Visible Atmospherically Resistant Index (VARI)	$(R_G - R_R) / (R_G + R_R - R_B)$
Normalized Green Red Difference Index (NGRDI)	$(R_G - R_R) / (R_G + R_R)$
Enhanced Red-Green-Blue Vegetation Index (ERGBVE)	$\pi * ((R_G^2 - (R_R * R_B)) / (R_G^2 + (R_R * R_B)))$

The unclassified point cloud generated by Pix4D was exported as a .las file. Six different python scripts were then created, each one containing one of the algorithms of the six RGB-based VIs. The unclassified point cloud was then processed six times, each time using one of the six python scripts. This method allowed the point cloud to be separated in a three-dimensional manner into two classes, vegetation and bare ground, producing 2 separate vegetation and bare ground point clouds (.las files) for each vegetation index applied. The resultant bare ground .las files were then imported into ArcMap as LAS datasets and converted to rasters/DEMs using ArcGIS tools. The results of this method were then compared to the built-in machine learning method used by Pix4D. The unclassified point cloud created in Pix4D after importing the images of the study area was classified by selecting “Run Point Cloud Classification” under the Process tab in the program. The bare ground point cloud generated was then exported as a .las file and then imported into ArcMap as a LAS dataset and converted to a raster/DEM as in the former RGB method described above.

The 3D RGB-based point cloud classification using Python scripts was a modification of the procedure by Themistocleous (2019). The method using LibLAS classifies the point cloud three-dimensionally, whereas the method by Themistocleous (2019) is two-dimensional.

In February 2020, Dr. Yan Zhou and DOE Fellow Gisselle Gutierrez travelled to Carlsbad, NM to collect the aerial images of the subset of Basin 6 adjacent to the WIPP along both sides of Road 128 that cover most of the topographical and surface hydrological features of interest including brine lakes, sinkholes, roads, pumping wells, etc. The workload was spread into four days from February 22-28, 2020. Before and during the field trip to Carlsbad, Dr. Zhou trained Fellow Gutierrez on the piloting of the drone, automated way-tracking, and establishment of ground control points for geo-referencing. More than 7,000 aerial images were collected for an area of 1*5 km using a drone equipped with automated way-tracking capacity. Accurate coordinates of 87 ground control points were measured using a Trimble GPS receiver for proper scaling and calibration in the process of photogrammetry. Data collected from this field trip covered a complete workflow of photogrammetry including geo-referencing and supported tests of different

vegetation removal approaches. During this trip the team met with Dr. Anderson Ward, FIU's collaborator from the DOE Carlsbad Field Office (CBFO) to provide an update on the field trip result and discuss the future direction of this project.

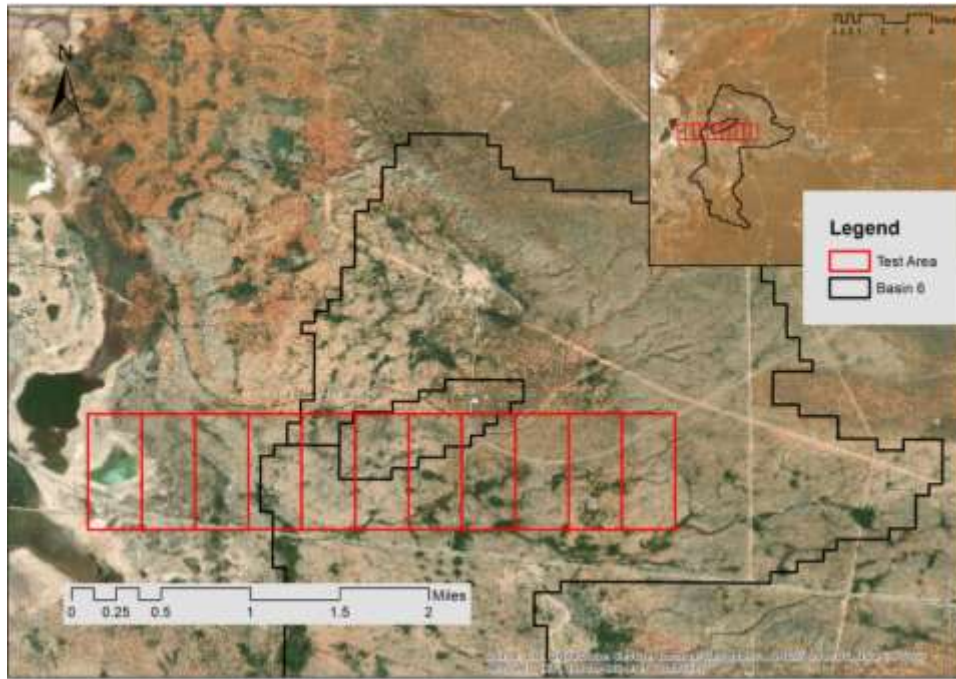


Figure 81. Coverage of aerial survey (in red) conducted by FIU in Basin 6, Carlsbad, NM.



Figure 82. FIU team marking ground control points using a Trimble GPS receiver in Basin 6, taking note of surface hydrological features of interest including brine lakes, sinkholes, and gullies.

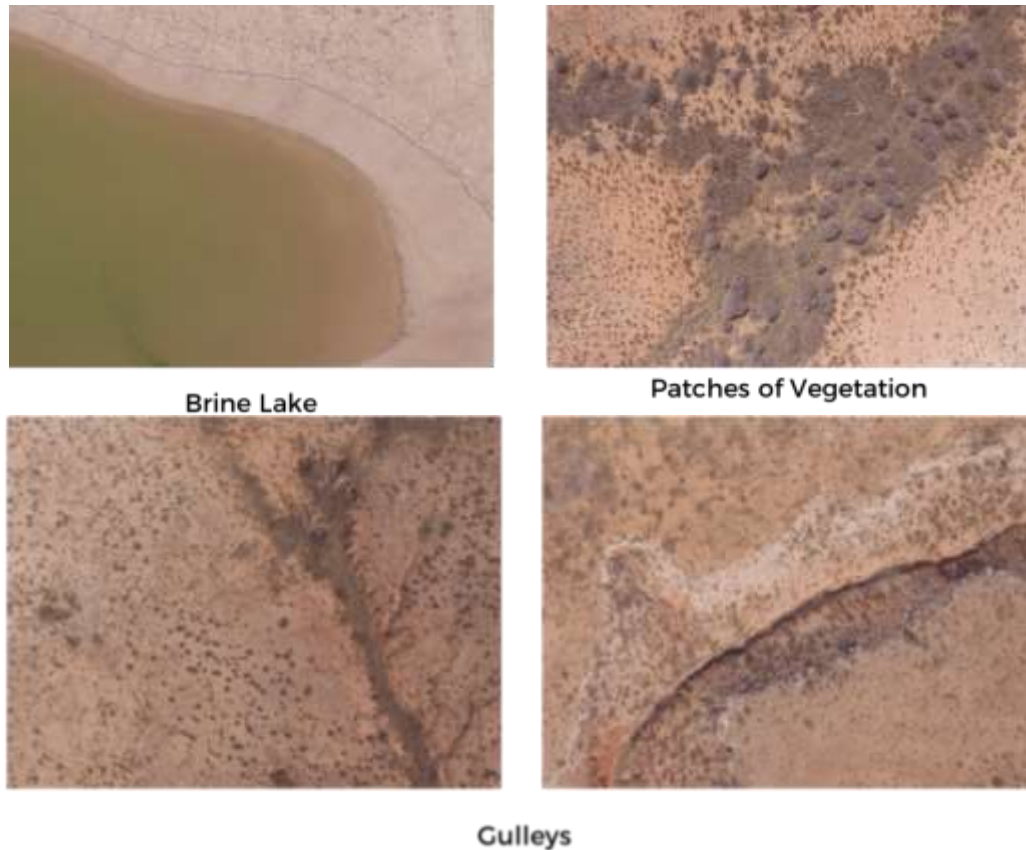


Figure 83. Drone images captured during the aerial survey conducted by FIU in Basin 6, Carlsbad, NM.

In February FIU also continued evaluating techniques for vegetation removal from UAV-based photogrammetry for creating a high-resolution digital elevation model. The methods evaluated included developing RGB-based index maps, using LibLAS in Python to generate a classified point cloud using the RGB vegetation indices, and using Pix4D's automatic machine learning classification. Aerial images collected from the August 2019 field trip to Carlsbad were imported into Pix4D where a point cloud was generated. From this, both a digital surface model and an orthomosaic were created and the first method to classify the point cloud and identify the vegetation was implemented. Method #1 consisted of generating a reflectance map from the DSM and orthomosaic and then applying six (6) different RGB-based vegetation indices that were used in a previous study to generate classified index maps. Methods #2 & 3 use the unclassified point cloud generated in Pix4D. Method #2 uses LibLAS toolkit to separate the bare ground from vegetation, using the .las file and the thresholds from the index maps derived from Method #1. The detailed procedure was provided in the January 2020 monthly report to DOE EM. DOE Fellow Gisselle Gutierrez also presented these results as a poster (seen below) during the student poster session of the Waste Management Symposia 2020, which was held in Phoenix, AZ in March 2020.

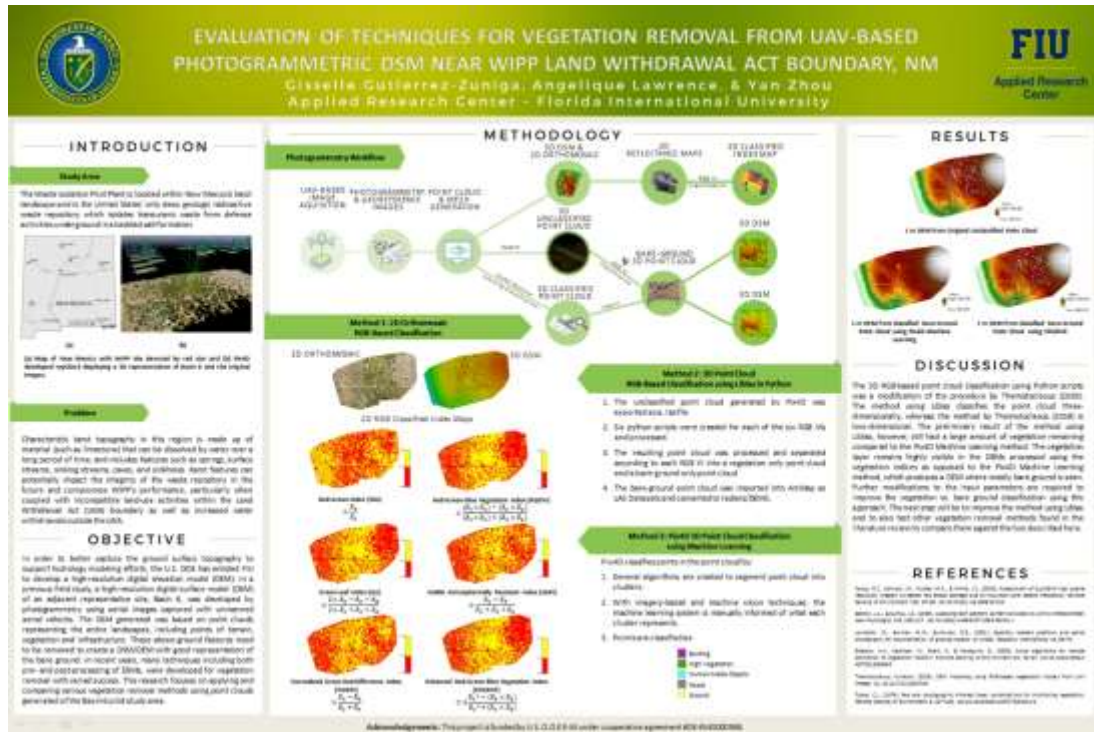


Figure 84. Waste Management Symposium 2020 poster being presented by DOE Fellow Gisselle Gutierrez based on the hydrological modeling research being conducted for the WIPP by FIU ARC.

In March, FIU began processing the aerial images collected in late February 2020 during the visit to Carlsbad, NM in pilot study area (Basin 6) adjacent to the WIPP. The geographical coordinates of the ground control points (GCPs) collected were transferred into an MS Excel spreadsheet, compiling and organizing the data in the format of latitude, longitude, and elevation for input into the photogrammetric program Pix4D. Image preparation and initial analysis with Pix4D was then initiated. All of the drone images that were taken were filtered to select favorable images within duplicated areas. This reduced the number of images from 7,407 to 5,242 and removed unsatisfactory images as well, i.e., images captured with a low light angle.

In April, the coordinates of the ground control points (GCPs) were input into the photogrammetry software Pix4D, with 15 out of 87 of them serving as check points (CPs) for error evaluation (Figure 85 and Figure 86).

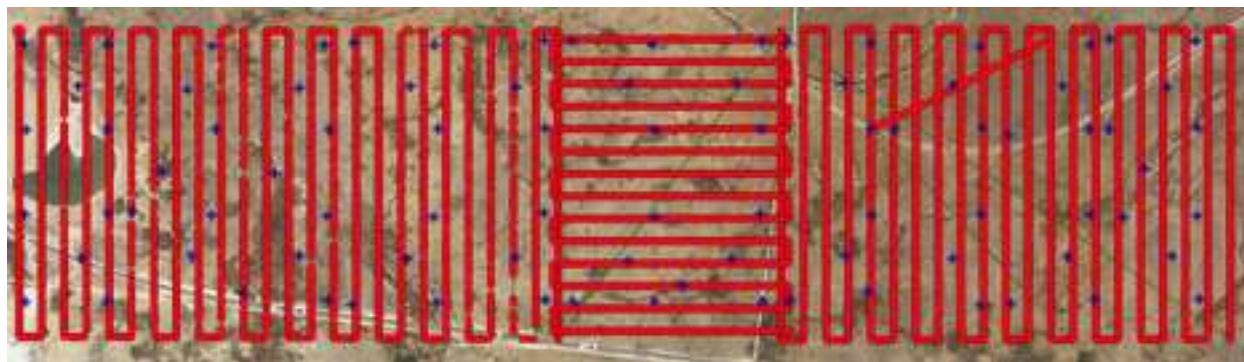


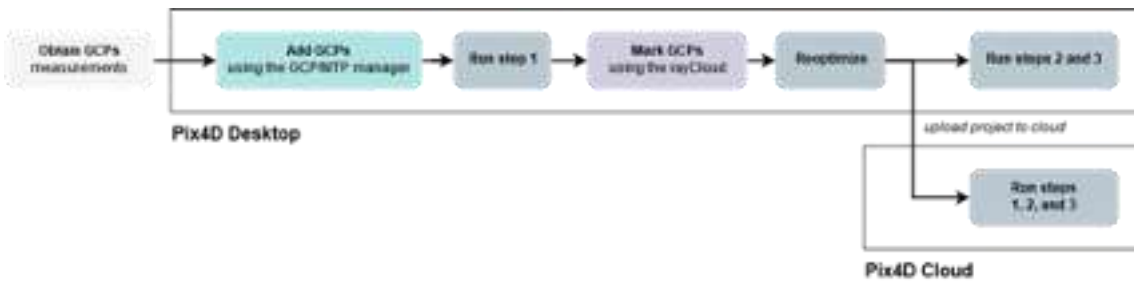
Figure 85. Location of 87 measured ground control points (GCPs) shown as blue-cross markers.



Figure 86. Location of 15 check points (CPs) shown as light blue markers vs. ground control points (GCPs) shown as dark blue markers.

Two geo-referencing workflows recommended by Pix4D were tested:

- Method A seen below depends on known coordinates of images and the GCPs. It allows the user to directly mark the GCPs on the images.



- Method B below can use images without a geotag. A fraction of the GCPs were used to match the images located in an arbitrary coordinate system with the GCPs in a known coordinate system. The rest of the GCPs will then be added during the geo-referencing process, similar to Method A.



Due to drifting of the vertical coordinates in the image geotags, the distance between the GCPs and images was deemed too far to be matched by Pix4D. Therefore, Method A could not be directly applied on the dataset even though the images have known coordinates. As a workaround, the average distance between the GCPs and images was evaluated, and an offset of GCP coordinates (-100 meter) was used to bring them closer to be matched. After offsetting the GCPs, Pix4D successfully established matches between the GCPs and images as shown in Figure 87.



Figure 87. Matches of GCP (1a) and images (DJI_0145- DJI_0167).

During the month of May DOE Fellow Gisselle Gutierrez completed marking all the ground control points (GCPs) using Pix4D, with the exception of six missing GCPs whose markings could not be clearly identified. The associated images adjacent to the GCPs would therefore require further examination with an image enhancement software such as Adobe Photoshop in order to more easily identify the orange markings on the ground.

The following outlines the procedure followed using Pix4D to mark the GCPs:

1. The rayCloud was opened by going to **View > rayCloud**
2. On the left sidebar that appears under the section *Layers*, **Tie Points** is clicked followed by **GCPs/ MTPs**. The coordinates of 87 measured locations in the field were input from the .csv file and 14 of them were used as check points (CPs) to calculate the accuracy of geo-referencing.
3. Each GCP/CP is chosen from the GCPs/MTPs section and a sidebar appears on the right listing its Properties and the images that it is visible in.
4. For each image, a blue circle shows the location of GCP/CP estimated automatically by Pix4D. The estimated GCP/CP locations are typically different from the exact locations of GCP/CP spray-marked on the ground, illustrating the error of automatic 3D reconstruction that need to be corrected by geo-referencing.
5. The exact position of each GCP/CP was found and marked with the left click on the mouse. The clicked position appears with a yellow cross and circle. The size of the circle varies depending on the zoom level at which it was clicked.
6. Once the GCP/CP is marked on at least two images, Pix4D recalculates the location of GCP/CP on the rest of the images and is indicated by a green cross mark. This assists the marking of the rest of images.
7. In the instances that the GCP/CP was not found in the image, the GCP name and image file was recorded onto a spreadsheet in order to further analyze the image with other programs such as Adobe Photoshop.

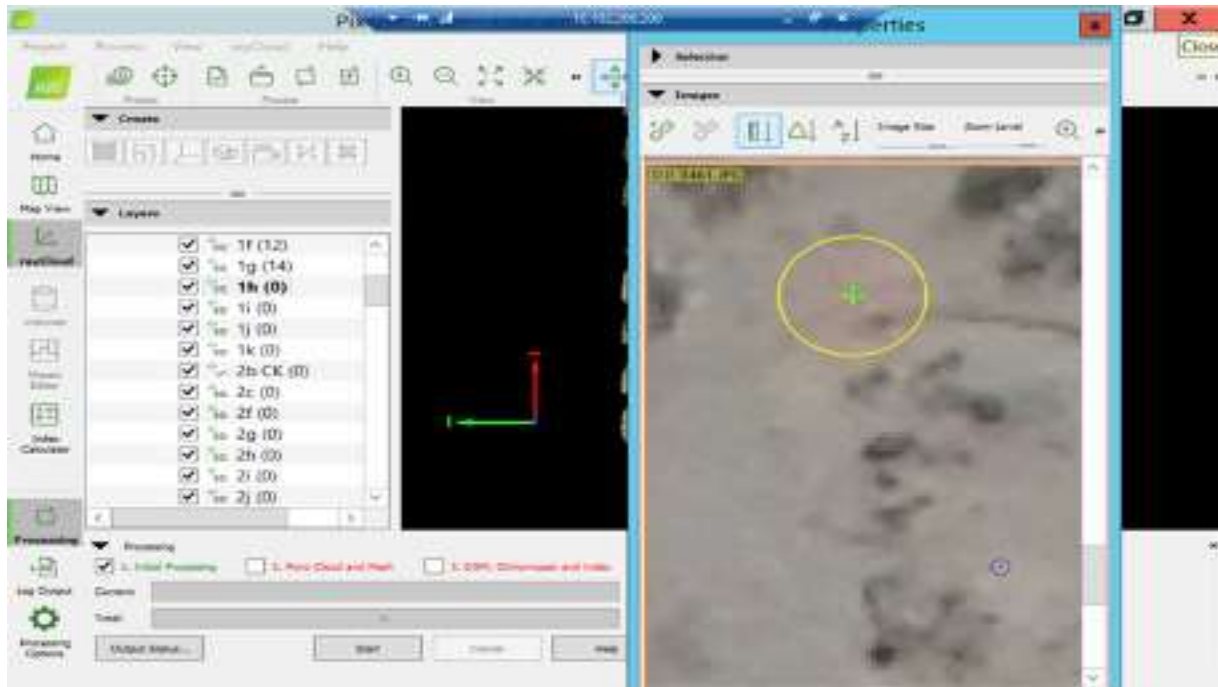
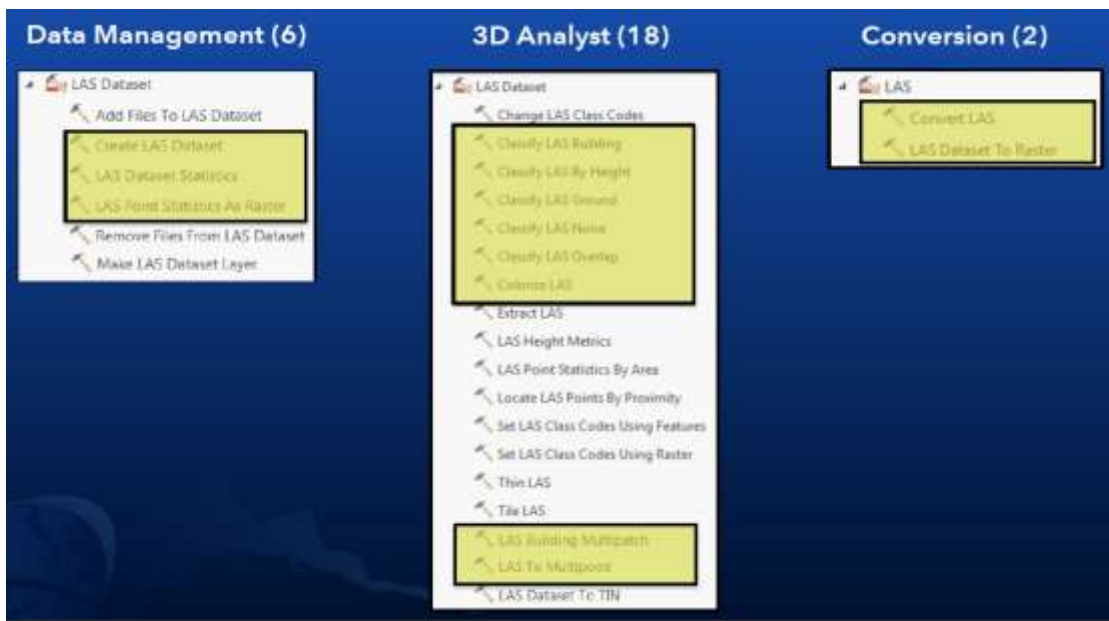


Figure 88. Marking of GCPs in the rayCloud on Pix4D.

ARC personnel attended the 2020 ESRI User Conference virtually which demonstrated the capability of ArcGIS Pro in point cloud (LAS data) processing and relevant toolboxes in three main categories: data management, 3D Analyst and data conversions as shown in the diagram below:



Compared to Pix4D automated processes, LAS toolboxes in ArcGIS allow more control in point cloud processing. Therefore, FIU initiated training and testing of cloud point manipulation

capacity in ArcGIS Pro which is expected to benefit post-processing in the photogrammetry workflow.

In August, FIU tested the 3D Analyst and data conversion toolboxes in ArcGIS Pro. The point clouds generated from Pix4D were input into ArcGIS Pro for visualization and processing. The automated point cloud classification was applied, and the result was visualized as seen in Figure 89.

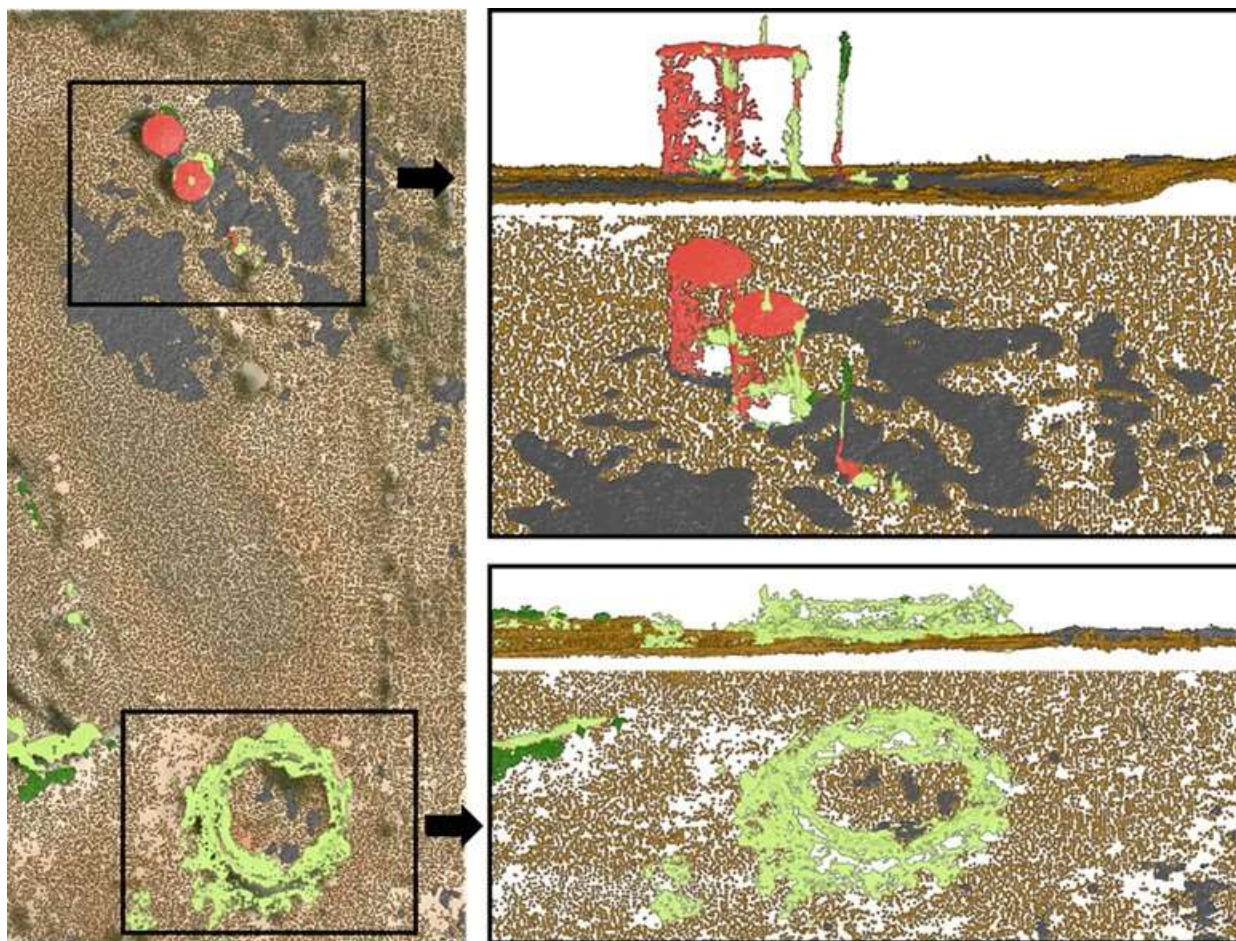


Figure 89. Automated point cloud classification showing land surface in brown, low vegetation in light green, high vegetation in dark green, road surface in grey and structure in red.

From Figure 89, one can see that the results showed limited success: the land surfaces were delineated with part of them being classified as road surface (in grey); the vegetation and structures were well identified even though not well separated; and a large number of points were unclassified (masked from Figure 89). Additional testing is needed to achieve a better classification result.

In September, images representing a subset of the surveyed area adjacent to the WIPP were selected to test a vegetation removal technique based on vegetation indices in order to compare it with the automated point cloud classification. DOE Fellow Gisselle Gutierrez submitted the following poster abstract to the Waste Management Symposia 2021 that outlines this effort in more detail.

Title: Comparison of Vegetation Filtering Methods for UAV-Based Photogrammetry to Generate High-Res Bare-Surface DEM Near the WIPP Land Withdrawal Act (LWA) Boundary, New Mexico.

Abstract: The Waste Isolation Pilot Plant (WIPP) in New Mexico is the United States' only deep geologic radioactive waste repository situated underground in a bedded salt formation, which isolates transuranic waste generated from national defense activities. Characteristic karst topography in this region consists of material (such as limestone) that can undergo dissolution over a long period of time due to surface/subsurface hydrologic variability related to seasonal water table fluctuation, as well as the presence of springs, surface streams, sinking streams, caves, and sinkholes that are within close proximity. As such, the integrity of the waste repository, and thus the WIPP's performance, can be impacted in the future by instability of the karst topography under hydrologic drivers, particularly when coupled with incompatible land-use activities within the Land Withdrawal Act (LWA) boundary, as well as increased water withdrawals outside the LWA. The U.S. Department of Energy (DOE) has a need for an improved understanding of the regional water balance and a means of estimating the rate of propagation of the shallow dissolution front. To better capture the ground surface topography to support hydrological modeling efforts, the U.S. DOE has enlisted researchers at Florida International University (FIU) to develop a high-resolution digital elevation model (DEM). A field study was conducted in February 2020, during which aerial images were collected with an unmanned aerial vehicle to support the development of a high-res DEM using photogrammetry. Images were then processed using Pix4D, which generates a point cloud from the imported imagery that represents entire landscapes, including points of terrain, vegetation and infrastructure, which all need to be removed to expose the ground surface. In recent years, many techniques including both pre- and post-processing of aerial imagery were developed for vegetation removal with varied success. The aim of this research therefore, is to test one of the most accepted vegetation removal methods, vegetation indices based classification via libLAS package in Python, and contrast it with the automated machine learning classification, and evaluate their effectiveness based on the resulting DEMs.

Subtask 6.1: Results and Discussion

In January, FIU calculated 2D reflectance maps in Pix4D from the orthomosaic. Various RGB-based VIs were applied and below are the results:

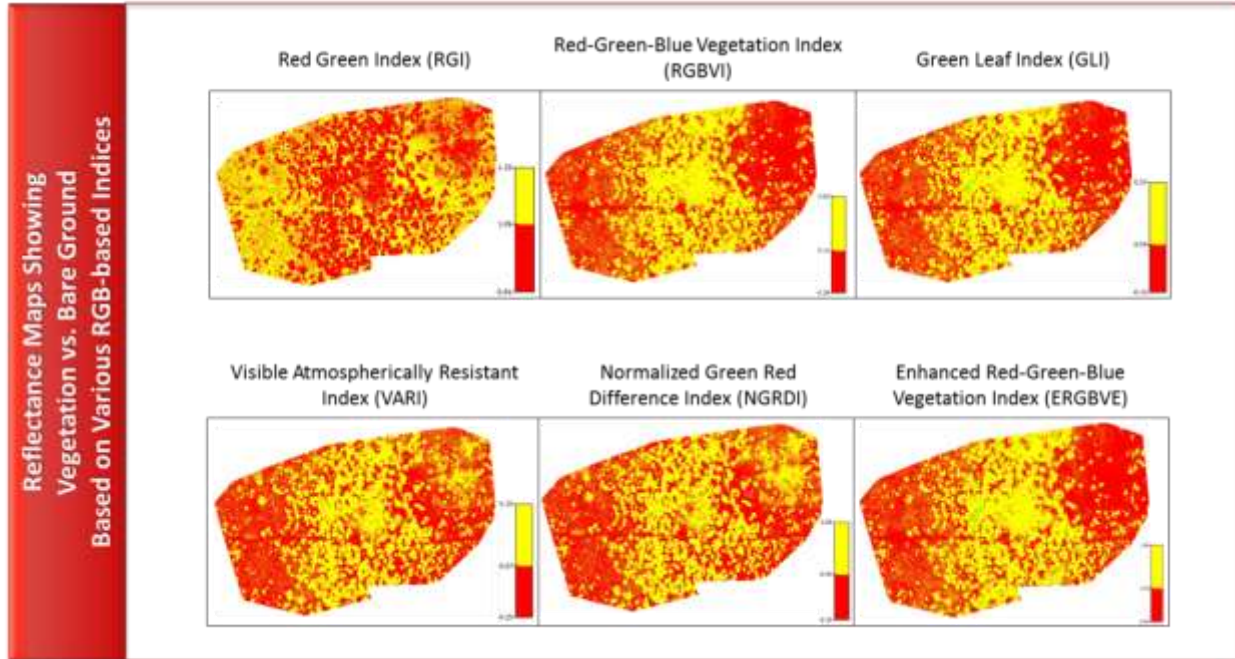


Figure 90. Reflectance/classified index maps showing vegetation vs. bare ground based on seven different RGB-based vegetation indices.

The 3D RGB-based point cloud classification using Python scripts was a modification of the procedure by Themistocleous (2019). The method using LibLAS classifies the point cloud three-dimensionally, whereas the method by Themistocleous (2019) is two-dimensional. The preliminary result of the method using LibLAS, however, still had a large amount of vegetation remaining compared to the Pix4D machine learning method seen in Figure 91 below.

From the LibLAS method, the vegetation layer remains highly visible in the DEMs processed using the vegetation indices as opposed to the Pix4D machine learning method, which produces a DEM where mostly bare ground is seen. Further modifications to the input parameters are required to improve the vegetation vs. bare ground classification using this approach. The next step will be to improve the method using LibLAS and to also test other vegetation removal methods found in the literature review to compare them against the two described here.

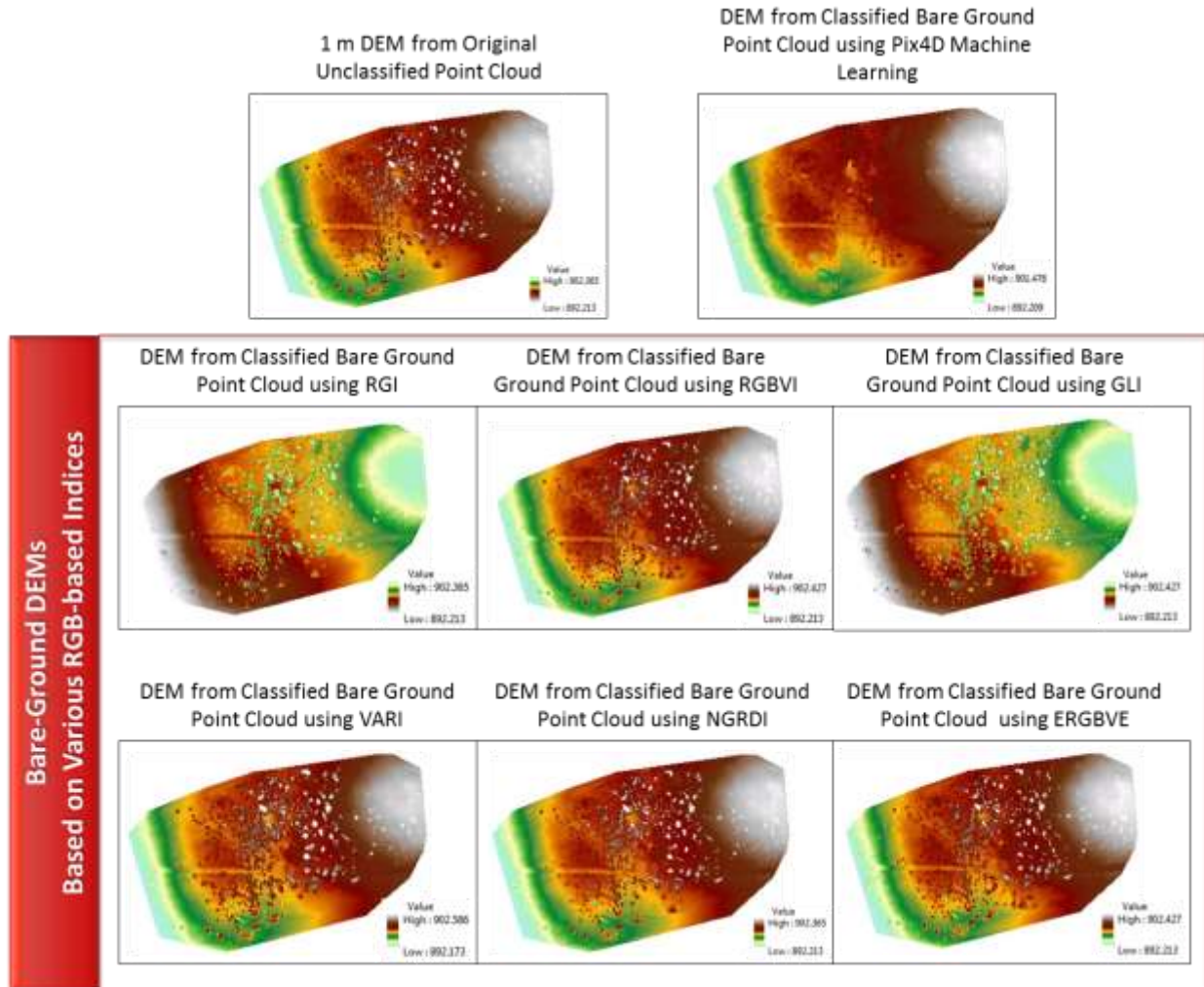


Figure 91. Rasters/DEMs created using ArcGIS tools after point cloud classification using an RGB-based method and a machine learning method.

In June, the DEM of the surveyed area in Basin 6 adjacent to the WIPP was generated by DOE fellow Gisselle Gutierrez and Dr. Yan Zhou. All the ground control points (GCPs) and check points (CPs) were successfully identified and marked (including the six missing GCPs/CPs), based on a combination of geo-marks in the image, coordinates measured during the field work and image enhancement using Adobe Photoshop. Re-optimization was then performed to improve the matching of land features and 3D reconstruction using marked GCPs/CPs. After re-optimization, Step 2 was executed to densify the point cloud followed by Step 3 to filter the vegetation and generate a digital elevation model (DEM) at a resolution of 0.17 meters, five times the pixel size (Figure 92).

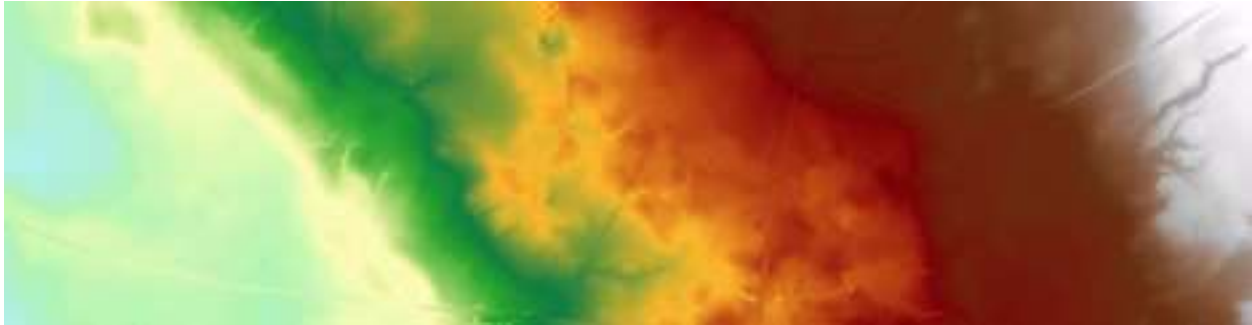
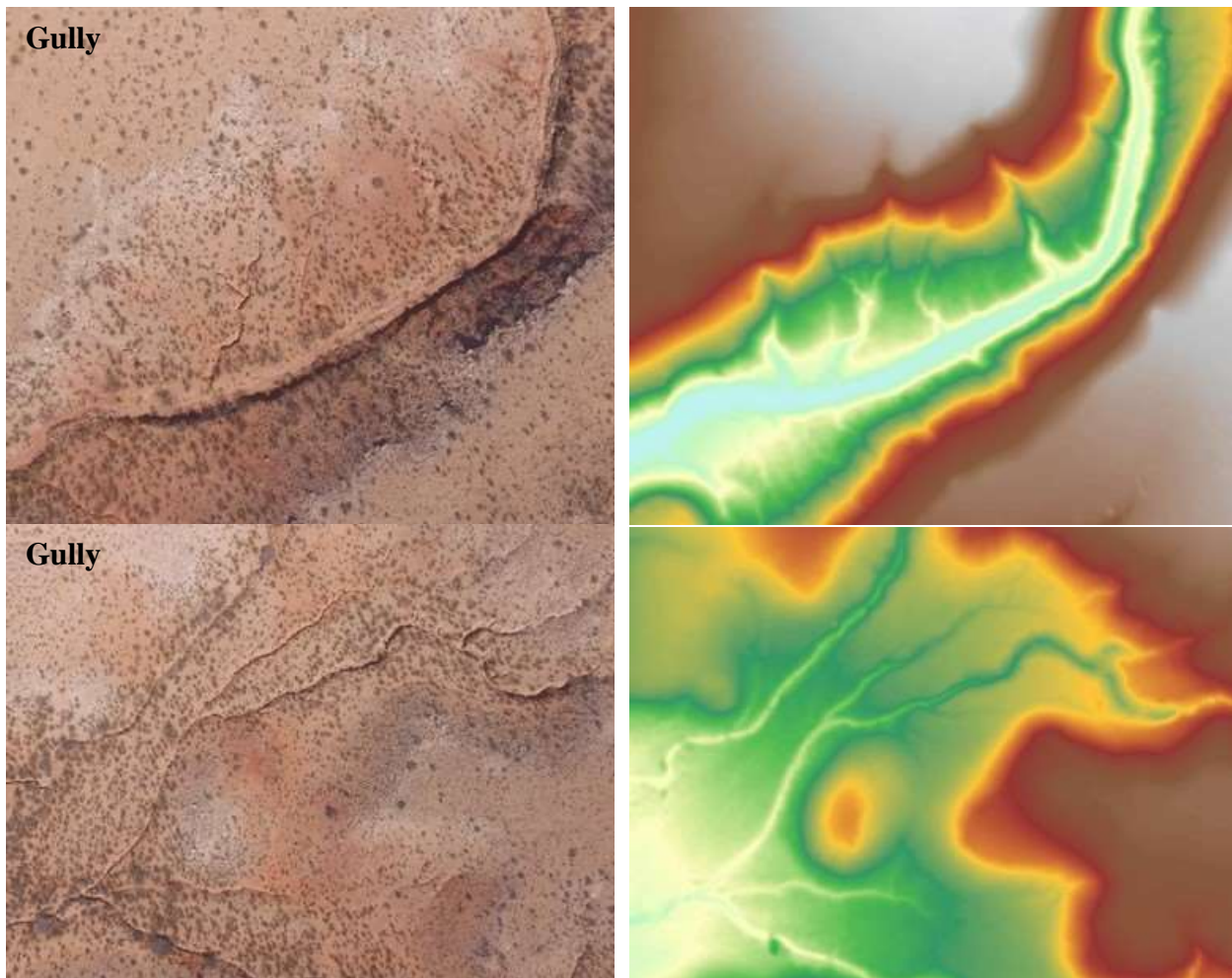


Figure 92. DEM of the surveyed area in Basin 6 adjacent to the WIPP.

The high-resolution DEM generated allows several land features to be easily identified, for example, a gully, brine lake, and land sink (Figure 93).



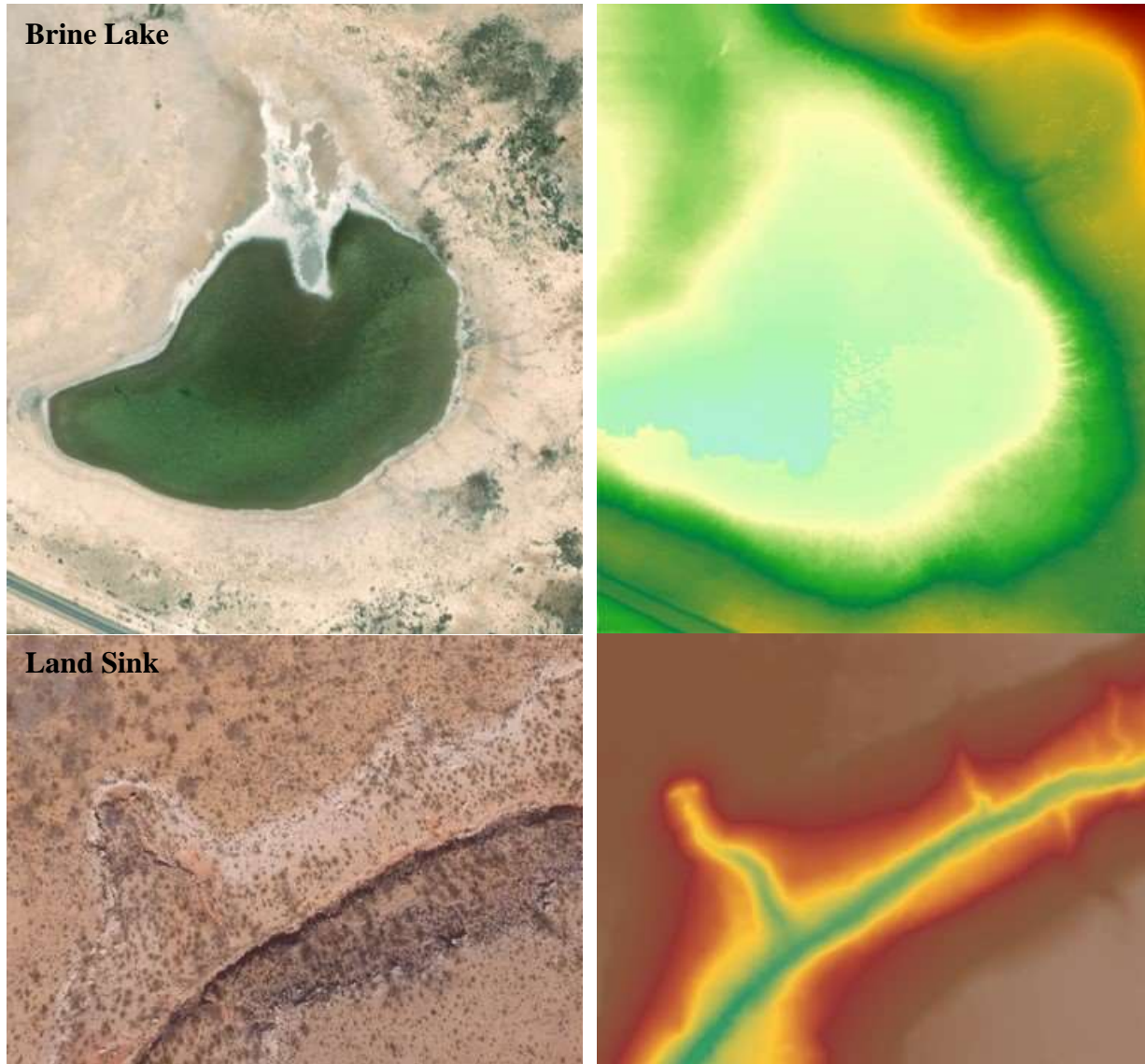


Figure 93. Land features shown on both DEM and aerial images.

In some instances, however, artifacts were noticed at the seam between image sets that were not only collected on two different days, but also at different times of the day (Figure 94). The set of images on the left were collected in the afternoon of Day 1, while those on the right were collected in the morning of Day 2. This resulted in a matching error caused by differing light angles, which can be minimized by planning accordingly to merge image sets at the same time of the day in future data collection.



Figure 94. DEM artifacts visible at the seam between image sets.

The accuracy of the DEM was assessed based on the error of the GCPs and CPs. The error of most of the GCPs/CPs were considered acceptable with the 95% confidence interval of (-0.1752, 0.1583), (-0.2028, 0.1078) and (-0.442, 0.234) meters for the x-, y-, and z-axes respectively, except for two outliers located within the area of the artifacts. The errors of the GCPs/CPs are presented in Figure 95.

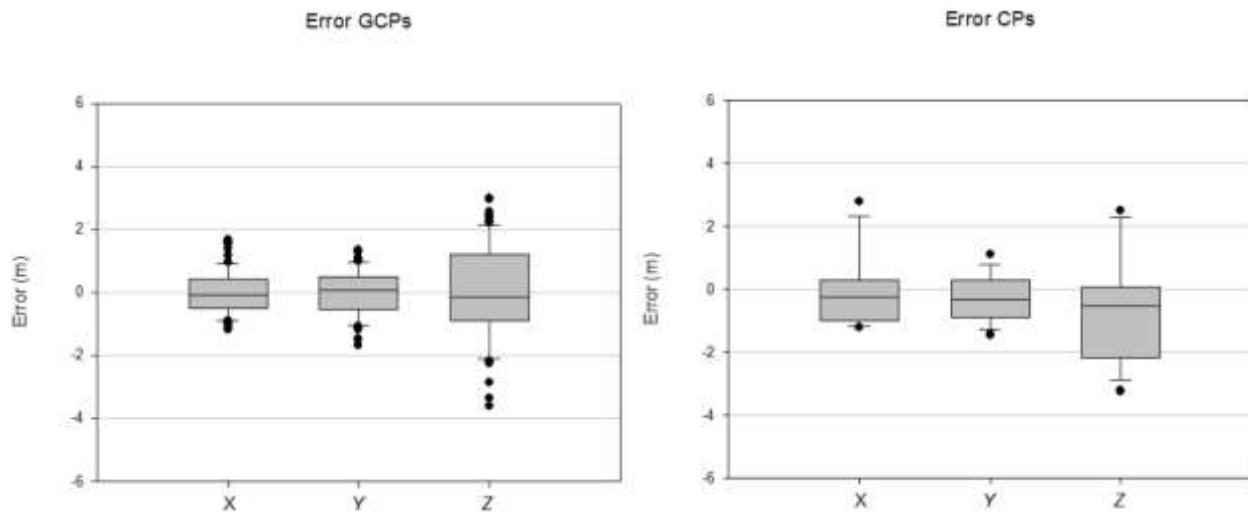


Figure 95. Error of GCPs and CPs in meters for x-, y-, and z-axes.

Subtask 6.1: Conclusions

The application of photogrammetry was successful in generating a DEM at the resolution of 0.17 meters that allows land features to be easily identified. This allow us to accurately delineate the local hydrologic features, such as sinkholes and brine lakes, that due to the karstic topography, play an essential role in the surface/subsurface water exchange in the target area. After the DEM was generated, it was then postprocessed for vegetation removal, revealing the true ground surface. FIU DOE Fellows were trained on the drone operation for image collection, use of photogrammetric software for image processing, and data post-processing for vegetation removal.

During FIU Performance Year 1 of the renewed DOE-FIU Cooperative Agreement, FIU will refine the aforementioned methodology for high-resolution DEM development based on the pilot study of UAV-based photogrammetry and extend the coverage area to the entire Basin 6 by collecting further aerial imagery. The generated DEM of Basin 6 will be used to delineate and extract topographical features such as drainage basins, brine lakes, channels, sink holes, discharge points and other relevant hydrological features using ArcGIS geoprocessing tools, which will be essential for LSM development. FIU will train undergraduate and graduate students (DOE Fellows) on UAV photogrammetry methods and provide mentorship and field experience through student summer internships in collaboration with Carlsbad Field Office (CBFO) and Pacific Northwest National Laboratory (PNNL) scientists.

Subtask 6.1: References

- Anders, N., Valente, J., Masselink, R., & Keesstra, S. (2019). Comparing Filtering Techniques for Removing Vegetation from UAV-Based Photogrammetric Point Clouds. *Drones*, 3(3), 61.
- Sadeghi-Tehran, P., Virlet, N., Sabermanesh, K., & Hawkesford, M. J. (2017). Multi-feature machine learning model for automatic segmentation of green fractional vegetation cover for high-throughput field phenotyping. *Plant methods*, 13(1), 103.
- Sandino, J., Gonzalez, F., Mengersen, K., & Gaston, K. J. (2018). UAVs and machine learning revolutionising invasive grass and vegetation surveys in remote arid lands. *Sensors*, 18(2), 605.
- Serifoglu Yilmaz, C., & Gungor, O. (2018). Comparison of the performances of ground filtering algorithms and DTM generation from a UAV-based point cloud. *Geocarto international*, 33(5), 522-537.
- Skarlatos, D., & Vlachos, M. (2018). Vegetation removal from UAV derived DSMS, using combination of RGB and NIR imagery.
- Yilmaz, V., Konakoglu, B., Serifoglu, C., Gungor, O., & Gökalp, E. (2018). Image classification-based ground filtering of point clouds extracted from UAV-based aerial photos. *Geocarto international*, 33(3), 310-320.
- Zhang, C., & Xie, Z. (2013). Object-based vegetation mapping in the Kissimmee River watershed using HyMap data and machine learning techniques. *Wetlands*, 33(2), 233-244.

Subtask 6.2: Model Development

Subtask 6.2: Introduction

This subtask involves the development of regional land surface and groundwater models for the WIPP site, using the DOE-developed ASCEM modeling toolset to improve the current

understanding of regional and local groundwater flow at the WIPP site and a selected open-source land surface model (LSM) to provide surface process parameters for input into the ASCEM model (e.g. infiltration rate) to compute the surface water balance, and derive estimates of groundwater recharge. This subtask will provide an extensible, multi-scale land-atmosphere modeling capability for conservative, coupled and uncoupled prediction of the hydrological cycle components in the WIPP area and surrounding region. This will simplify the upper boundary condition for flow in Culebra that is currently externally specified without consideration of water fluxes due to surface processes like runoff, infiltration and evapotranspiration. Coupling of the LSM with the ASCEM GWMs leads to more accurate predictions of groundwater flow patterns, including horizontal flow (e.g., potentiometric surface, flow direction, vertical flow into transmissive units, and the effect of density on flow direction). With improved estimates of the spatial and temporal patterns of recharge to force the GWM, predictions of halite dissolution and propagation of the shallow dissolution front will be made possible and the potential impact on repository performance quantified.

Subtask 6.2: Objectives

The objective of this subtask is to develop a groundwater-basin model for the WIPP site using ASCEM, as well as a selected LSM to account for the surface and near-surface processes. These models will be used to compute the water balance across multiple scales and to reduce uncertainties in recharge estimates and propagation of the shallow dissolution front. FIU's focus during FIU Performance Year 10 was primarily on training of FIU personnel and students on the use of the ASCEM modeling toolset by the DOE ASCEM team. The training will assist FIU researchers in learning how to use the ASCEM code, become familiar with the publicly available graphical user interface (GUI), and research existing case studies where ASCEM has been implemented at DOE sites to determine the best practices and lessons learned for implementing this modeling toolset. FIU also conducted a more in-depth literature review of candidate LSMs in order to identify an optimal LSM based on capacity and compatibility with ASCEM. Candidate LSMs include the Community Land Model (CLM), which has been successfully coupled with the LBNL-developed ParFlow, and the UCAR-developed Noah and Noah-Multi-parameterization (Noah-MP) models. Noah-MP has been successfully coupled with the Weather Research and Forecasting (WRF) Model and used to predict the water cycle components including precipitation, soil moisture, snow pack, groundwater, streamflow, and inundation. In future, the LSM of the WIPP region developed by FIU in collaboration with PNNL and CBFO scientists will be used to force the ASCEM GWMs to predict groundwater flow patterns. The spatial distribution of recharge, and groundwater flow rates and directions will be used to estimate the rate of halite dissolution and the rate of propagation of the shallow dissolution front, both of which have the potential to affect post-closure repository performance.

Subtask 6.2: Methodology

WIPP Groundwater Model Development: ASCEM Training

In FIU Performance Year 10, training on the ASCEM groundwater model was officially initiated using a number of existing model examples. The ASCEM modeling toolset will be used to develop a regional groundwater model for the WIPP and surrounding areas in order to simulate the fluctuation of groundwater levels in response to climate variability and pumping activities. The training which should have begun within the first quarter of the Year 10 period of performance

was delayed due to health and safety concerns and travel restrictions imposed as a result of the coronavirus (COVID-19) pandemic, as well as FIU’s transition of most of its employees to remote work. It was therefore agreed that FIU’s PNNL and CBFO collaborators would conduct the training remotely instead of on-site at FIU. The training kicked off in June 2020 with an introduction of the ASCEM modelling platform, Akuna, by Dr. Vicky Freedman from PNNL, within which the computational grid is defined and the model inputs are setup. The simulation engine Amanzi and other relevant simulators were also introduced and links to online resources to assist in setting up the program were provided. Dr. Freedman also provided a tutorial of the Akuna GUI and building the ASCEM model within Akuna, in addition to instructions for setting up the simulation specifications. FIU was also provided with user accounts to access the National Energy Research Scientific Computing Center (NERSC) simulation server and instructions on the configuration of the simulation engine, Amanzi, locally. Dr. Yan Zhou prepared a document and scripts for running the Amanzi simulator in a Windows environment.

In July, FIU received training by Dr. Freedman from PNNL on ASCEM model development and data visualization using an example of transient vadose zone flow and transport of Tc-99 from two surface point sources at the DOE Hanford BC Cribs and Trenches site. The example involves a two-dimensional heterogeneous three-layer subsurface system with time- and space-varying infiltration at the ground surface (Figure 96, Table 32). More information can be found at: https://amanzi.github.io/amanzi/UserGuide/tutorial/transient_infiltration/Tutorial_dvz.html.

Table 32. History of discharge.

	Recharge (mm/yr)	Tc-99 Concentration (mol/m ³)
General site, pre-1956	3.5	N/A
General site, post-1956	47	N/A
B-17, Jan 1956	8025	1.88E-06
B-18, Feb-Mar 1956	10439	2.27E-06

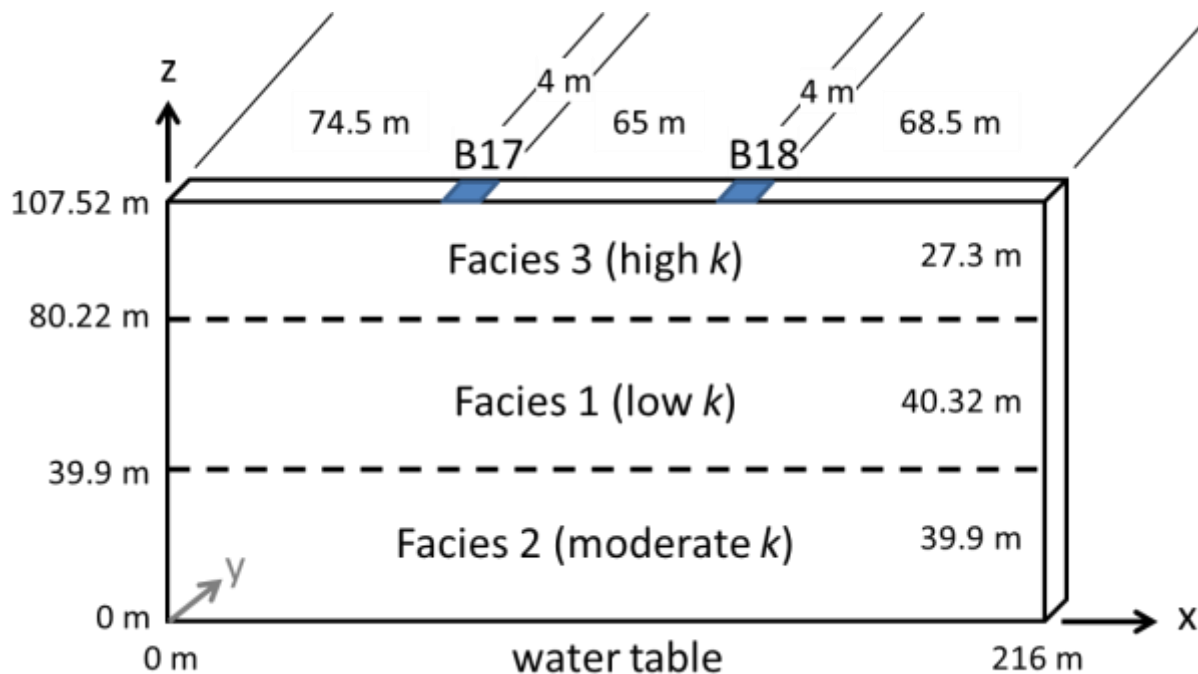


Figure 96. Model structure.

In August, FIU continued training on ASCEM model development and data visualization using an example of transient vadose zone flow and transport of Tc-99 from two surface point sources at the DOE Hanford BC Cribs and Trenches site. Continuous feedback was provided to PNNL collaborator, Dr. Vicky Freedman. During the training, a few unexpected model behaviors were encountered related to the solute transport component, including the test release of Tc-99 not being reflected at observations points. More testing is needed to evaluate the model’s response to parameters in the solute transport component, especially numerical control that may resolve the problem.

During the month of September, FIU focused efforts on conducting a literature review of existing models for the area around the WIPP as Dr. Vicky Freedman was unavailable for training and the NERSC Cori Server was offline. The training will be resumed in October as well as data collection for model development. The following publications found were helpful in providing information related to previous modeling efforts for the WIPP, particularly the MODFLOW groundwater model.

WIPP Land Surface Model (LSM) Development: Literature Review of Candidate LSMs

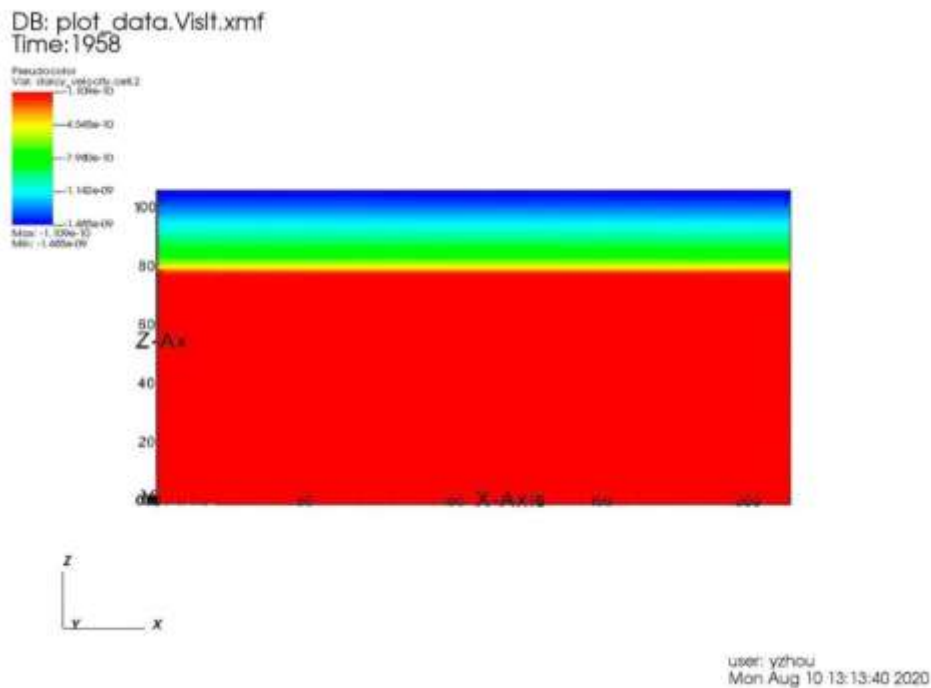
FIU conducted a literature review of candidate open-source land surface models during Performance Year 10 focusing primarily on the model applications, specifications and input requirements. The research findings are provided in the following section. Once a high-resolution DEM is developed for the representative pilot study area of the WIPP region, an open source LSM will be chosen and a land surface model of the study area will be created. Coupling of a LSM with the ASCEM GWMs in future will lead to more accurate predictions of groundwater flow patterns in the WIPP region, including horizontal flow (e.g., potentiometric surface, flow direction, vertical flow into transmissive units, and the effect of density on flow direction). With improved estimates of the spatial and temporal patterns of recharge to force the GWM, predictions of halite dissolution

and propagation of the shallow dissolution front will be made possible the potential impact on repository performance quantified.

Subtask 6.2: Results and Discussion

WIPP Groundwater Model Development: ASCEM Training

To date FIU’s ASCEM training has led to successful reproduction and visualization of the hydrologic response of test models. FIU successfully developed and executed the example using the HPC (high-performance computer) Cori provided by NERSC and visualized the result of the hydrologic components using VisIt, an open-source interactive parallel visualization and graphical analysis tool for viewing scientific data developed by LLNL. Visualization results are demonstrated in Figure 97.



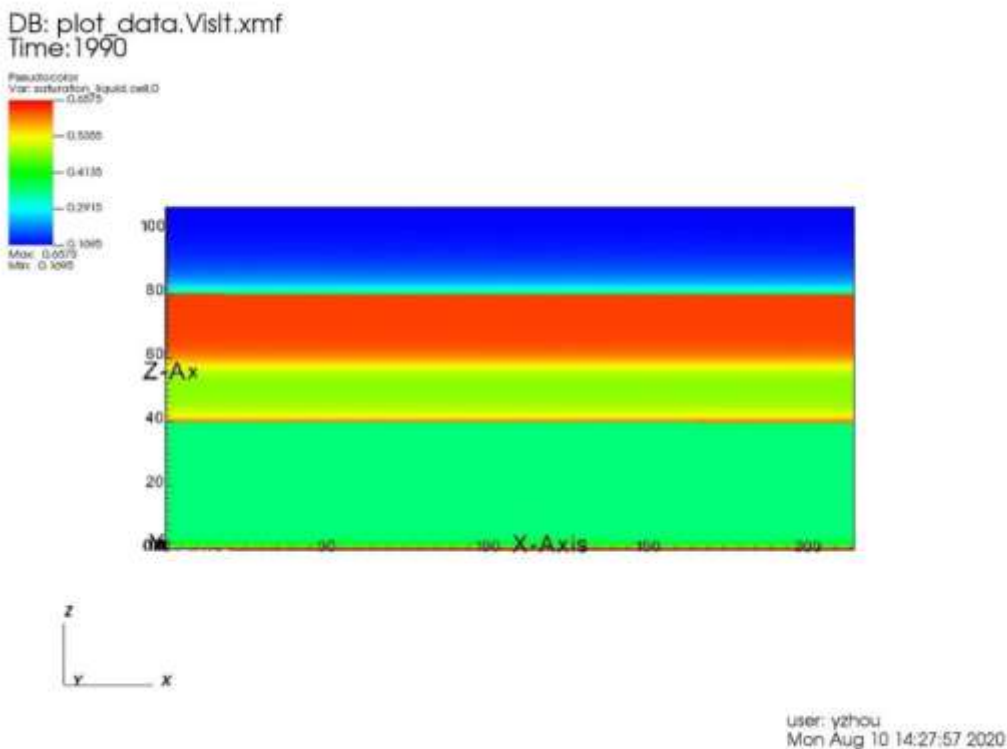


Figure 97. Visualization of the example model showing vertical Darcy velocity on the top and the saturation at the bottom.

Further training is needed to accommodate contaminant transport simulation test cases and to provide guidance and improve exception-handling capabilities. In addition, due to the nature of the evolving model status, communication with the DOE model developers will continue throughout the model development process. The ongoing ASCEM training designed and executed by PNNL will be held one day per week to support Basin 6 ASCEM model development. The remaining training will be reactive in nature, as it will be designed based on the technical needs of FIU.

WIPP Land Surface Model (LSM) Development: Literature Review of Candidate LSMs

The following represents FIU’s research findings for various open-source land surface models which will assist in the selection of an optimal product to be used to develop a regional land surface model of the WIPP region. FIU focused primarily on the model applications, specifications and input requirements. A few related publications are also described.

Community Land Model

The Community Land Model is the land model for the Community Earth System Model (CESM). This model formalizes and quantifies concepts of ecological climatology where the physical, chemical, and biological processes affect and are affected by the climate across spatial scales. The Community Land Model includes different aspects of the land surface and components related to

biogeophysics, the hydrologic cycle, and biogeochemistry are included. More specifically, processes include:

- Vegetation composition, structure, and phenology
- Absorption, reflection, and transmittance of solar radiation
- Absorption and emission of longwave radiation
- Momentum, sensible heat (ground and canopy), and latent heat (ground evaporation, canopy evaporation, transpiration) fluxes
- Heat transfer in soil and snow including phase change
- Canopy hydrology (interception, throughfall, and drip)
- Snow hydrology (snow accumulation and melt, compaction, water transfer between snow layers)
- Soil hydrology (surface runoff, infiltration, redistribution of water within the column, sub-surface drainage, groundwater)
- Plant hydrodynamics
- Stomatal physiology and photosynthesis
- Lake temperatures and fluxes
- Dust deposition and fluxes
- Routing of runoff from rivers to ocean
- Volatile organic compounds emissions
- Urban energy balance and climate
- Carbon-nitrogen cycling
- Dynamic landcover change
- Land management including crops and crop management and wood harvest
- Ecosystem Demography (FATES, optional)

Model configurations include satellite phenology, biogeochemical cycles with crops, and biogeochemical with no anthro. Many other options to reduce complexity are methane emissions, carbon isotopes, land-use change, VOC emissions, plant hydraulics, and soil structure. As well as option to increase complexity which include representative hillslopes, FATES, fire trace gas emissions, additional land management, flooding, ozone damage to plants. Features included in the most updated CLM5 are:

- Global crop model with eight basic crop types
- Crop irrigation
- Crop industrial fertilization
- Wood harvest
- Urban environments

From previous studies, CLM has been used for:

- Representing urban areas in climate models (urban heat island effect)
- Impacts of land use and land use change on climate, carbon, water, and extremes
- Modeling land cover change and land management (forest and agricultural)
- Water and food security in context of climate change, climate variability, and extreme weather

- Land-atmosphere interactions, hydrologic prediction, water and land management, data assimilation, model analysis
- Fire modeling

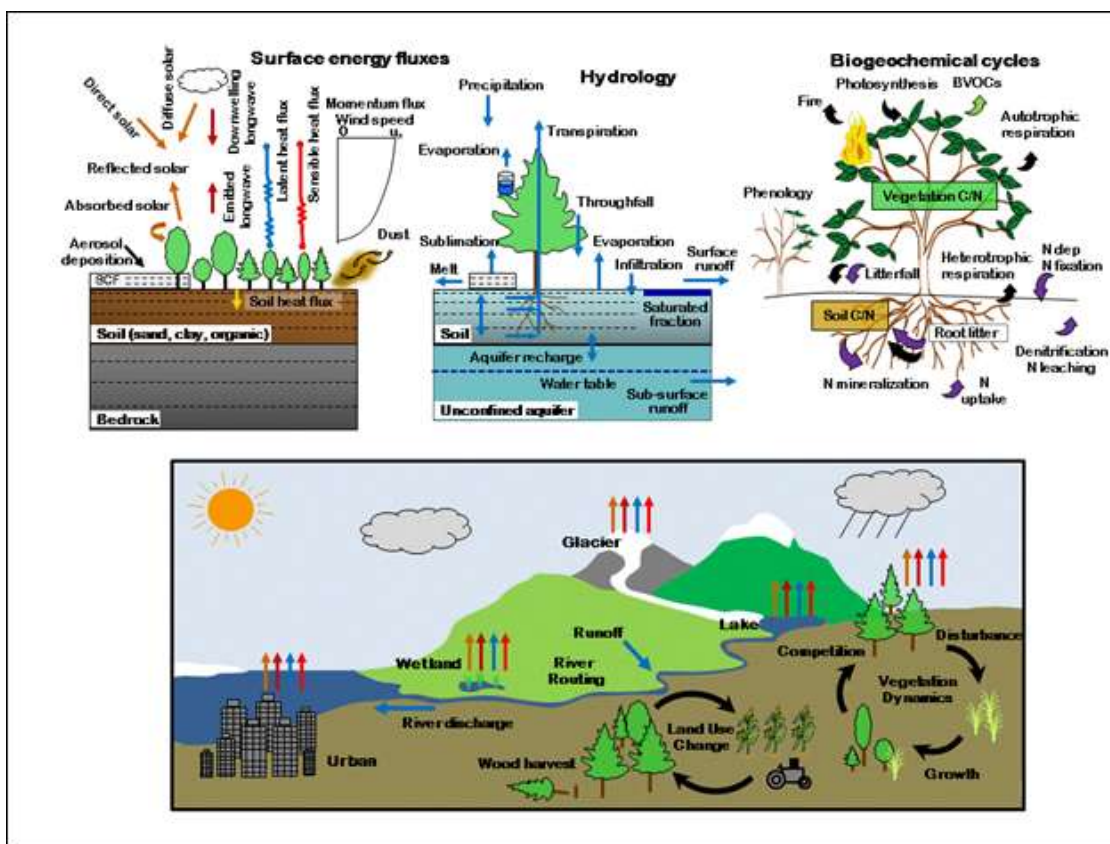


Figure 98. Figure from the CLM5.

Table 33. Key Processes in CLM

Processes	CLM
Plant	<ul style="list-style-type: none"> • Canopy hydrology (interception, throughfall, and drip) • Plant hydrodynamics • Stomatal physiology and photosynthesis
Land cover	<ul style="list-style-type: none"> • Vegetation composition, structure, and phenology • Dynamic landcover change • Land management including crops and crop management and wood harvest
Channel/ surface Routing	<ul style="list-style-type: none"> • Routing of runoff from rivers to ocean
Soil	<ul style="list-style-type: none"> • Soil hydrology (surface runoff, infiltration, redistribution of water within the column, sub-surface drainage, groundwater)
Add. Chem	<ul style="list-style-type: none"> • Volatile organic compounds emissions • Carbon-nitrogen cycling
Add. Heat	<ul style="list-style-type: none"> • Absorption, reflection, and transmittance of solar radiation

	<ul style="list-style-type: none"> • Absorption and emission of longwave radiation • Momentum, sensible heat (ground and canopy), and latent heat (ground evaporation, canopy evaporation, transpiration) fluxes • Heat transfer in soil and snow including phase change
Add. Others	<ul style="list-style-type: none"> • Snow hydrology (snow accumulation and melt, compaction, water transfer between snow layers) • Lake temperatures and fluxes • Dust deposition and fluxes • Urban energy balance and climate • Ecosystem Demography (FATES, optional)

NOAH-MP

According to many sources, the NOAH-Multiparametrization (MP) has been widely used by the National Centers for Environmental Protection (NCEP) in operational weather and climate predictions. It was originally developed in order to facilitate climate predictions with physically based ensembles and has been coupled with the NCEP Global Forecasting System (GFS) and Climate Forecasting System (CFS) in order to improve climate predictions. It has also been coupled with the Weather Research and Forecasting (WRF) modeling system to improve weather predictions.

The NOAH-MP contains a separate vegetation canopy defined by a canopy top and bottom, crown radius, and leaves with prescribed dimensions, orientation, density and radiometric properties. It also contains a multi-layer snowpack with liquid water storage and melt/refreeze capability and a snow-interception model which describes loading/unloading, melt/refreeze capability, and sublimation of canopy-intercepted snow. Along with multiple options for surface water infiltration and runoff and groundwater transfer and storage including water table depth to an unconfined aquifer.

Some features of the NOAH-MP include:

1. Major components include a 1-layer canopy; 3-layer snow; 4-layer soil
2. Subgrid scheme: semi-tile vegetation and bare soil (Niu et al. 2010a)
3. Interactive energy balance method to predict skin temperature of the canopy and snow/soil surface
4. Modified two-stream radiation transfer scheme to consider the 3-D structure of the canopy (Niu and Yang, 2004)
5. More realistic snow physics: a thin surface layer, liquid water retention and refreezing, and snowpack densification (Yang and Niu, 2003)
6. A TOPMODEL- based runoff scheme (Niu et al., 2005)
7. An unconfined aquifer interacting with soil (Niu et al., 2007)
8. More permeable frozen soil (Niu and Yang, 2006)
9. Ball-Berry stomatal resistance related to photosynthesis

10. A short-term leaf dynamic model. (Dickinson et al., 1998)

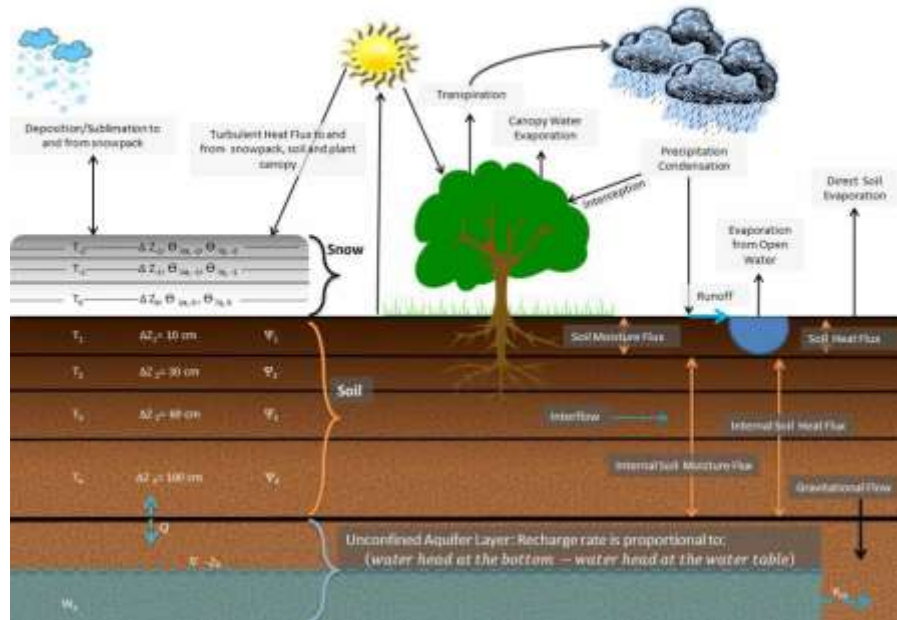


Figure 99. Figure from NOAA-MP.

Table 34. Key processes in Noah-MP

Processes	Noah-MP
Plant	<ul style="list-style-type: none"> • Green vegetation fraction • Rooting depth • Stomatal resistance • Minimum and maximum leaf area index through the year • Minimum and maximum background emissivity through the year • Minimum and maximum background albedo through the year • Maximum canopy water capacity
Land cover	<ul style="list-style-type: none"> • Land-use category representing bare ground • land-use category representative of the non-urban portion of urban land-use points
Channel/surface Routing	<ul style="list-style-type: none"> • Surface runoff
Soil	<ul style="list-style-type: none"> • Soil evaporation • Soil heat capacity • Lower boundary soil temperature • Soil thermal diffusivity/conductivity coefficient • Saturation soil moisture content

	<ul style="list-style-type: none"> • Saturation soil conductivity and diffusivity • Wilting point soil moisture
Add. Others	<ul style="list-style-type: none"> • Snow cover • Frozen ground • Threshold water-equivalent snow depth • Upper bound on maximum albedo over deep snow

WRF-HYDRO

The Weather Research and Forecasting Model Hydrological (WRF-Hydro) is a fully distributed modeling system which was developed as a community-based, open source, model coupling framework with the goal of linking multi-scale process models of the atmosphere and terrestrial hydrology. It was developed to enable improved versions of terrestrial hydrologic processes with the spatial redistribution of surface, subsurface, and channel waters of the land surface and to ease the coupling of atmospheric models and hydrologic models. Some features include:

- Multi-scale functionality to permit modeling of atmospheric, land surface and hydrological processes on different spatial grids
- Modularized component model coupling interfaces for various typical terrestrial hydrologic processes including surface runoff, channel flow, lake reservoir flow, sub-surface flow, land-atmosphere exchanges
- Parallel code development for application on commodity cluster and higher performance computing systems
- Stand-alone capabilities for hydrological prediction and research uncoupled to atmospheric models
- Coupling capability so it can be embedded with or coupled to other types of Earth system models such as NCAR Community Earth System Model (CESM)
- Use of variety of standard data formats for an efficient job evaluation
- Pre and post processing workflows

WRF-Hydro improves simulations of land surface hydrology and energy states and fluxes at high spatial resolutions of 1 km or less using different physics-based approaches. Some of the model physics options are:

- 1-dimensional (vertical) land surface parameterization
- Surface overland flow
- Channel routing
- Reservoir routing
- Conceptual/empirical baseflow

WRF-Hydro operates in two modes: coupled or uncoupled. Coupled mode is critical for land-atmosphere coupling research and long-term predictions and the uncoupled mode is for spinup, data assimilation and model calibration. The WRF-Hydro website provides a plethora of tutorial and materials on topics such as its system overview, system conceptualization, physics

components overview, Noah-MP column LSM overview, GIS Pre-processing tool, and implementation and best practices. Additionally, the Noah land surface and Noah-MP land surface model options can be used in the current version of WRF-Hydro.

Table 35. Primary Output data

Variable	Units
Surface latent heat flux	W m-2
Surface sensible heat flux	W m-2
Ground heat flux	W m-2
Ground surface and/or canopy skin temperature	K
Surface evaporation components (soil evaporation, transpiration, canopy water evaporation, snow sublimation and ponded water evaporation)	kg m-2 s-1
Soil moisture	m3 m-3
Soil temperature	K
Deep soil drainage	
Surface runoff	mm
Canopy moisture content	mm
Snow depth	m
Snow liquid water equivalent	mm
Stream channel inflow (optional with terrain routing)	mm
Channel flow rate (optional with channel routing)	m3 s-1
Channel flow depth (optional with channel routing)	mm
Reservoir height and discharge (optional with channel and reservoir routing)	

Past applications of WRF-Hydro have included flash flood prediction, regional hydroclimate impacts assessment, seasonal forecasting of water resources and land-atmosphere coupling studies.

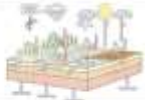
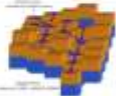
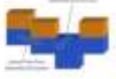

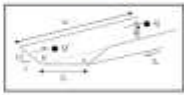
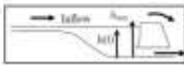
	WRF-Hydro Options	Current NWM Configuration
Column Land Surface Model	 3 up-to-date column land models: Noah, NoahMP (w/ built-in multi-physics options), Sac-HTET	NoahMP
Overland Flow Module	 3 surface routing schemes: diffusive wave, kinematic wave, direct basin aggregation	Diffusive wave
Lateral Subsurface Flow Module	 2 subsurface routing scheme: Boussinesq shallow saturated flow, 2d aquifer model	Boussinesq shallow saturated flow
Conceptual Baseflow Parameterizations	 2 groundwater schemes: direct aggregation storage-release; pass-through or exponential model	Exponential model
Channel Routing/Hydraulics	 5 channel flow schemes: diffusive wave, kinematic wave, RAPID, custom-network Muskingum or Muskingum-Cunge	Custom-network (NHDPlus) Muskingum-Cunge model
Lake/Reservoir Management	 1 lake routing scheme: level-pool management	Level-pool management

Figure 100. WRF-Hydro physics permutations.

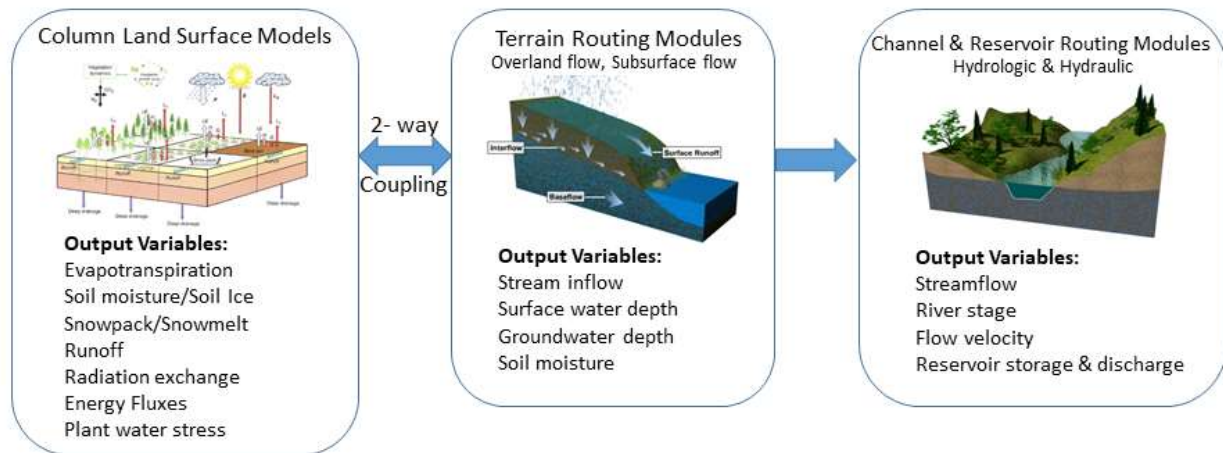


Figure 101. WRF-Hydro physics components.

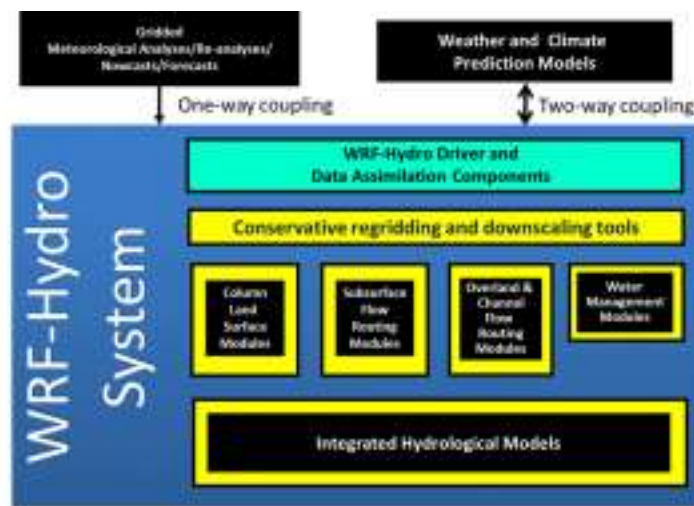


Figure 102. Schematic of the WRF-Hydro modeling framework displaying several categories of the model components.

Input data that must be provided when setting up WRF-Hydro includes:

- Geographical input data
 - Includes data such as topography and land use categories and can expand to about 10 gigabytes (GB).
- Domain coordinates
 - This will help produce GEOGRID files which will be used by WRF-Hydro
- Digital Elevation Model/ Elevation Data
 - The DEM/ elevation data must be in raster format, have a valid coordinate reference system, must cover the entire GEOGRID domain, in meters, and it is suggested that it be hydrologically corrected (i.e. processed to ensure that rivers and drainage divides are in the correct locations)
- Meteorological Forcing Data

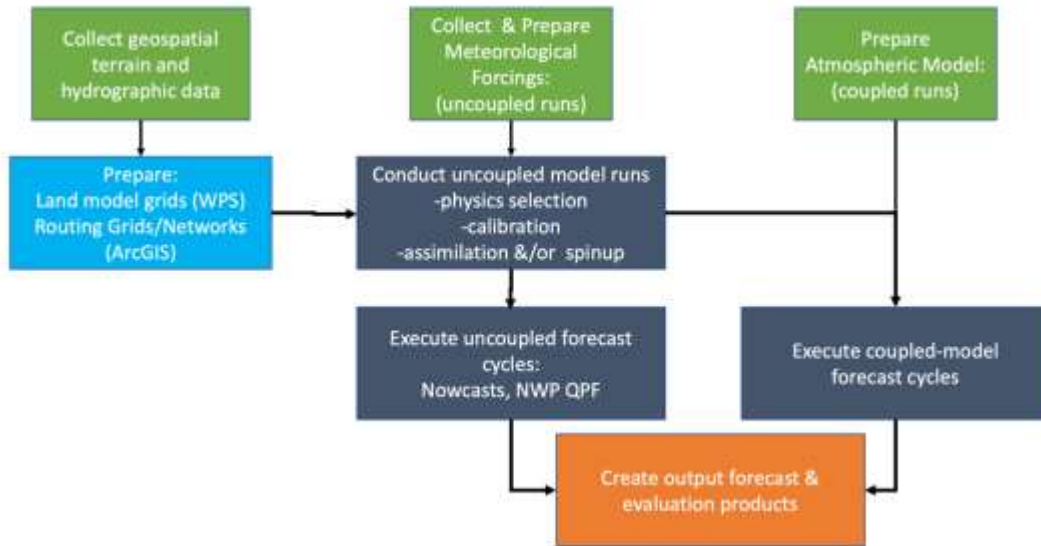


Figure 103. WRF-Hydro implementation workflow.

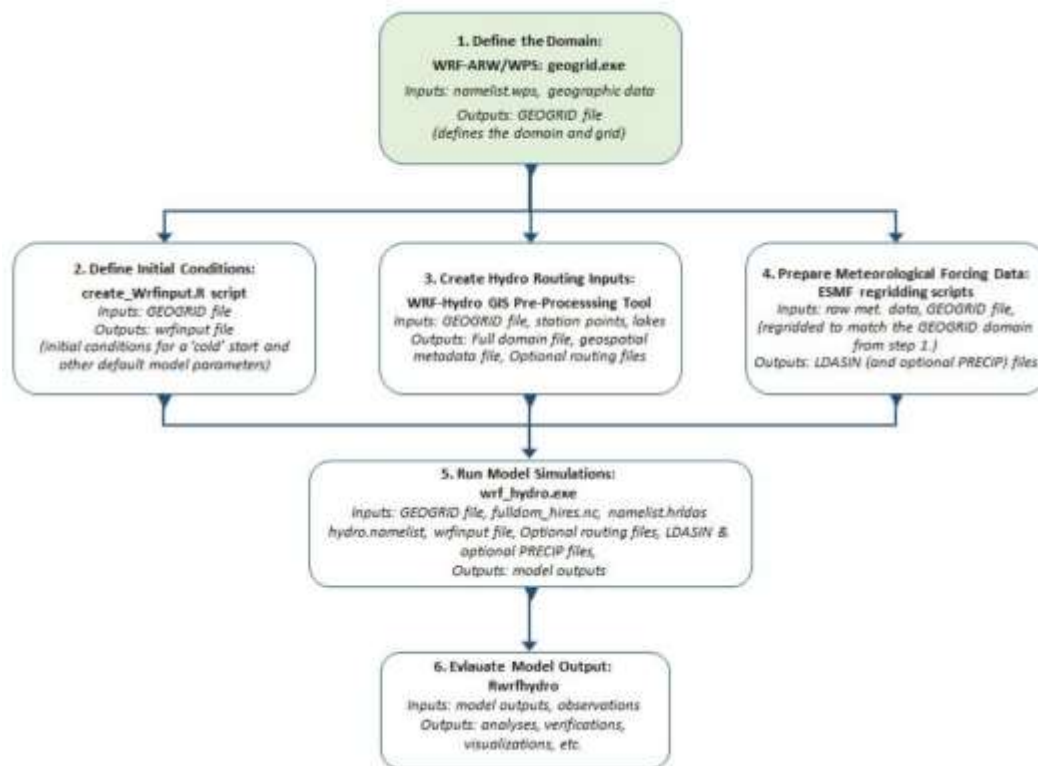


Figure 104. WRF-Hydro setup workflow.

Table 36. Key processes in WRF-Hydro

Processes	<ul style="list-style-type: none"> • WRF-Hydro
Plant	<ul style="list-style-type: none"> • Ground surface and/or canopy skin temperature • Canopy water evaporation

	<ul style="list-style-type: none"> • Pondered water evaporation • Canopy moisture content • Sediment transport/ deposition
Land cover	<ul style="list-style-type: none"> • Land cover change due fire, urbanization, ag/silviculture
Channel/ surface Routing	<ul style="list-style-type: none"> • Surface overland flow • Saturated subsurface flow • Channel routing • Reservoir routing • Surface runoff • Stream channel inflow (optional with channel routing) • Channel flow rate (optional with channel routing) • Channel flow depth (optional with channel routing)
Soil	<ul style="list-style-type: none"> • Soil hydrology (surface runoff, channel flow, lake/reservoir flow, sub-surface flow, land-atmosphere exchanges) • Soil evaporation • Soil transpiration • Soil moisture • Soil temperature • Deep soil drainage
Add. Chem	<ul style="list-style-type: none"> • Surface latent, surface sensible, and ground heat flux
Add. Heat	<ul style="list-style-type: none"> • Energy and moisture fluxes • Turbulent heat flux to/from snowpack/soil/plant/canopy
Add. Others	<ul style="list-style-type: none"> • Snow sublimation • Snow depth • Snow liquid water equivalent

PARFLOW

ParFlow is a numerical model that simulates the hydrologic cycle from the bedrock to the top of the plant canopy. It integrates three-dimensional groundwater flow with overland flow and plant processes using physically based equations to simulate fluxes of water and energy. It can also be characterized as a parallel, integrated hydrology model which can simulate spatially distributed surface and subsurface flow as well as other land surface processes such as evapotranspiration. ParFlow solves saturated and varied saturated flow in three dimensions with either orthogonal or terrain following, semi-structured mesh which allows for fine vertical resolution near the land surface and deep (approximately 1 km) confined and unconfined aquifers. Additionally, the model uses robust linear and nonlinear solution methods and exhibits efficient parallel scaling to large processor counts, more than 100K cores which allows for large simulations with fine resolution. ParFlow has been coupled to other land surface and atmospheric models such as CLM, WRF, and TerrSysMP.

Some features of ParFlow include:

- Richards' equation for variably saturated 3D subsurface flow

- Shallow water equations for surface flow
- Modular, coupled land model that represents full energy budget, vegetative and snow processes
- Robust nonlinear solvers (using the Kinsol Newton-Krylov package) and efficient multigrid linear solver (using the HyPre package)
- Parallel implementation using multiple approaches and architectures
- Excellent parallel scalability with production runs of more than 30k processors
- Support for OpenMP and CUDA for use on accelerator architectures such as GPUs
- Data formats such as SILO and NetCDF4
- Implementation on different architectures and operating systems from "Laptop to Supercomputer" (single CPU, Linux clusters, highly scalable systems such as IBM Blue Gene) with the same source code and input on all platforms
- Widespread use on many institutional computer systems including many of the fastest supercomputers in the world (e.g. Edison, Cori, Yellowstone, JUQUEEN)
- Application to a wide range of hydrology problems and basins from small headwaters catchment to the continent
- Broad community development and use
- Extensive automated testing framework that follows best software practices
- Implementation as a Docker instance for easy and efficient deployments
- Large set of utilities for pre- and postprocessing and diagnostics calculations
- Flexible and portable cmake built environment

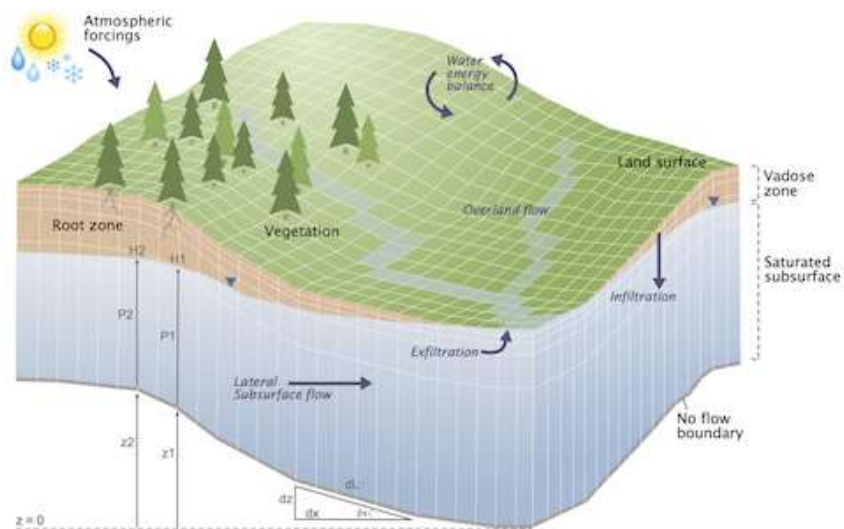


Figure 105. Figure from ParFlow.

Table 37. Key processes in ParFlow

Processes	• WRF-Hydro
Plant	• Bio-geochemistry (plant/water interactions)

Channel/ surface Routing	<ul style="list-style-type: none"> • Integrated overland flow • Saturated subsurface flow • Surface runoff • Groundwater flow • Vadose zone flow • Unsaturated flow
Soil	<ul style="list-style-type: none"> • Spatial and temporal variability of soil burn severity
Add. Heat	<ul style="list-style-type: none"> • Shallow heat transport
Add. Others	<ul style="list-style-type: none"> • Land energy budget

Some example applications include:

- Transient, integrated simulation of groundwater and surface water over the continental US
- Groundwater-surface water interaction in the San Joaquin River Basin
- Groundwater-land surface-atmosphere feedbacks during the European 2003 heat wave
- Continental water residence times
- Effects of insect-induced tree mortality on water and energy in mountain headwaters
- Scale dependent parameterization in integrated hydrologic modeling
- Moisture dependent irrigation and its feedbacks with integrated hydrology

RELATED PUBLICATIONS

Calibration and Evaluation of a Flood Forecasting System: Utility of Numerical Weather Prediction Model, Data Assimilation and Satellite-Based Rainfall (Yucel et al, 2015)

This study uses WRF-Hydro model to assess the potential for skillful flood forecasting based on precipitation inputs. Ten rainfall-runoff events in the Black Sea region were used for evaluation and calibration. The WRF model domains were set at 12 km and 4 km resolutions. Following model calibration, WRF-Hydro was able to reproduce observed flood hydrographs in terms of the runoff volume produced and the overall shape of the hydrograph.

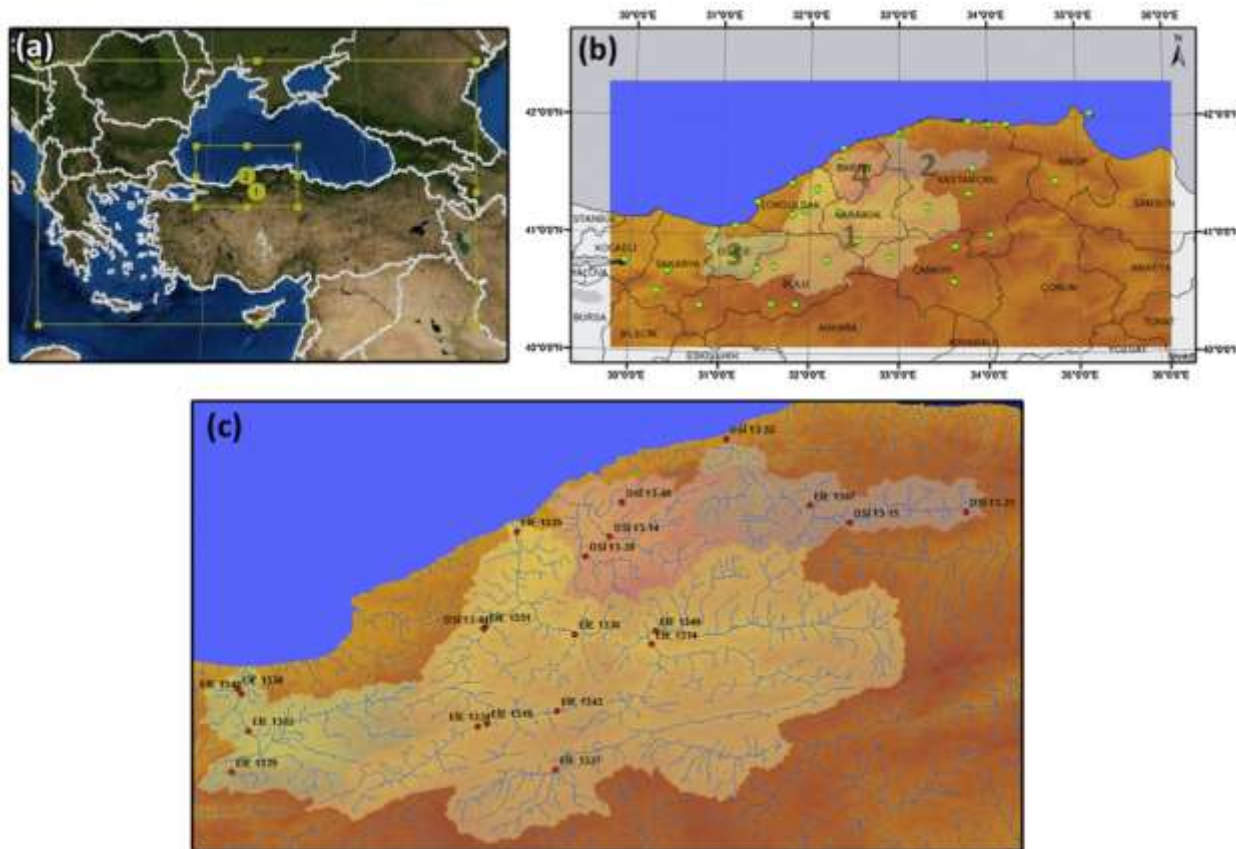


Figure 106. Study area in Black Sea Region

Four sub-basins were selected in the Black Sea region and contained 21 streamflow gauge stations. The WRF model uses the 3-dimensional VARIational data assimilation technique (3DVAR) and selected physics options of large-scale precipitation, cumulus, radiation, boundary layer, and land surface. Initial conditions and lateral boundaries for the course domain comes from the 25 km, 3 hr analysis fields from the European Centre for Medium Range Weather Forecasts. Additionally, the Noah LSM in WRF has the capacity to simulate frozen and liquid soil moisture, soil temperature, skin temperature, snowpack water equivalent, canopy water content, energy and moisture fluxes at surface of the Earth.

Hydrological components are throughfall, re-evaporation of rainfall intercepted by the canopy, soil infiltration, direct soil evaporation, vertical soil water movement, transpiration, surface and subsurface runoff. Infiltration capacity exceedance is allowed to stay in the model domain as ‘ponded water’ which is then available for lateral redistribution. After lateral redistribution, the remaining ponded water is then combined with new precipitation before the infiltration amount is calculated. Within Noah LSM, for each hour the column moisture is disaggregated from the LSM grid (the 4 km WRF model grid) to the high resolution-routing grid using a sub-grid, spatial-weighting method. The 4 km grid disaggregation produced 256 grids at 250 m resolution within each 4 km grid. The relevant input fields from Noah LSM to routing modules include maximum soil moisture for each soil type, infiltration capacity excess, lateral saturated hydraulic conductivity for each soil type, and soil moisture content for each soil layer. Apart from topography, land cover,

soil type, WRF Hydro needs high resolution topography and channel network in order to accurately route water across landscape via overland, subsurface, or channel flows.

Analysis of an Extreme Weather Event in A Hyper-Arid Region Using WRF-Hydro Coupling, Station, and Satellite Data (Wehbe et Al, 2019)

This study focuses on three nested domains with the parent domain covering the Arabian Peninsula, Iran, Iraq, Afghanistan, and parts of Pakistan, Syria, and Ethiopia, covering a broad range of weather systems. In this study, two simulations were carried out: one using the standalone WRF version and the other with the coupled WRF-WRF Hydro version. In both simulations, the initial and lateral boundary conditions of the parent domain were from the Global Operational Analysis and Forecast Products of the National Center for Environmental Prediction at 0.5° spatial resolution and 6 h intervals. Whereas, the static terrain attributes and topography used in the WRF preprocessing system (WPS) derived from USGS datasets.

The Noah MP LSM in the standalone WRF considers single vertical columns of one dimension of terrain properties at each overland grid cell. But it does not take into account the horizontal interactions between adjacent grid cells to calculate soil moisture, temperature profiles, runoff, and water and energy fluxes at the land surface. Whereas WRF-Hydro uses Noah MP LSM 1-D representations in an attempt to improve the simulation of terrestrial hydrologic processes at high spatial and temporal resolutions by including lateral redistribution of overland and saturated subsurface flows for runoff prediction. It can be concluded that WRF-Hydro and the standalone WRF model differs in the lateral distribution of surface runoff and feedback of surface fluxes to the atmosphere.

Coupled WRF | WRF-Hydro V5 Test Case User Guide (WRF-Hydro Dev. Team, 2018)

In this study, a fully distributed three-dimensional overland surface flow model configuration was used. GIS Python-based preprocessing was used to derive the WRF-Hydro LSM and routing grids. The WPS GEOGRID file was used as input of the static terrain properties as well as the high-resolution (30 m) ASTER DEM. A re-gridding factor of 10 was used in order to reach the 100 m LSM resolution from the 1 km GEOGRID resolution. The minimum basin size was defined by a threshold of 20 pixels per stream.

Subtask 6.2: Conclusions

In FIU Performance Year 10, FIU continued their collaboration with PNNL and CBFO in search of an appropriate open-source LSM, which will be used to derive parameters that account for the surface and near-surface hydrological processes and assist in computing the surface water balance across multiple scales to reduce uncertainties in recharge estimates at the WIPP site. During FIU Performance Year 1 of the renewed DOE-FIU Cooperative Agreement, FIU will finalize the review of open-source LSMs to determine the best option and initiate development of a LSM of the WIPP study domain using the data derived from Subtask 6.1. Hydrological, climate and topography datasets will be collected from DOE and various national database platforms. A LSM will be developed using the modeling platform selected based on the outcome of the literature review.

In Performance Year 10, the FIU team also began training on the ASCEM model under the guidance of PNNL and CBFO collaborators. This is an ongoing subtask that will extend into

Performance Year 1 of the new contractual agreement between DOE and FIU. A groundwater model will be developed using the ASCEM modelling platform for the Culebra Dolomite Member (Culebra) of the Permian Rustler Formation which is a potential radionuclide release pathway from the WIPP. The extent of the model domain will be Basin 6 which was identified as a pilot study area. The fluctuation of groundwater levels in response to climate variability and pumping activities will be simulated using the developed Basin 6 groundwater model. Training on ASCEM will continue periodically as the model development progresses based on the technical needs of FIU.

Subtask 6.2: References

- Beauheim, R. L. (2009). Collection and integration of geoscience information to revise the WIPP hydrology conceptual model. In *Approaches and challenges for the use of geological information in the safety case for deep disposal of radioactive waste*.
- Corbet, T. F., & Knupp, P. M. (1996). *The role of regional groundwater flow in the hydrogeology of the Culebra Member of the Rustler Formation at the Waste Isolation Pilot Plant (WIPP), southeastern New Mexico* (No. SAND-96-2133). Sandia National Lab, Albuquerque, NM (United States).
- Hart, D. B., McKenna, S. A., & Beauheim, R. L. (2009). *Calibration of the WIPP culebra transmissivity fields* (No. SAND2009-7334C). Sandia National Lab.(SNL-NM), Albuquerque, NM (United States); Sandia National Laboratories,, Carlsbad, NM.
- Hayes, A. (2019). *Culebra Hydrologic Model in WIPP Performance Assessment* (No. SAND2019-4432PE). Sandia National Lab.(SNL-NM), Albuquerque, NM (United States).
- Sampson, K., & Gochis, D. (2018). *WRF Hydro GIS Pre-Processing Tools, Version 5.0 Documentation*. Boulder, CO: National Center for Atmospheric Research, Research Applications Laboratory.
- Wehbe, Y., Temimi, M., Weston, M., Chaouch, N., Branch, O., Schwitalla, T., Wulfmeyer, V., Zhan, X., Liu, J. and Al Mandous, A. (2019). *Analysis of an extreme weather event in a hyper-arid region using WRF-Hydro coupling, station, and satellite data*. Natural Hazards & Earth System Sciences, 19(6).
- Yucel, I., Onen, A., Yilmaz, K. K., & Gochis, D. J. (2015). *Calibration and evaluation of a flood forecasting system: Utility of numerical weather prediction model, data assimilation and satellite-based rainfall*. Journal of Hydrology, 523, 49-66.
- Zeitler, T. R. (2016). *WIPP Performance Assessment* (No. SAND2016-8142PE). Sandia National Lab.(SNL-NM), Albuquerque, NM (United States).

ACKNOWLEDGEMENTS

Funding for this research was provided by U.S. DOE Cooperative Agreement #DE-EM0000598. FIU's Applied Research Center would like to acknowledge the commitment of DOE-EM to this specific workforce development project and to all the research being conducted as part of the Cooperative Agreement. The partnership between DOE EM and FIU has resulted in the development and training of outstanding minority STEM students that will benefit this country as a whole.

CONFERENCE PARTICIPATION, PUBLICATIONS & AWARDS

Peer-reviewed Publications

Di Pietro, S.A., Emerson, H.P, Katsenovich, Y, Qafoku, N. P, and J. E.Szecsody. Phyllosilicate mineral dissolution upon alkaline treatment under aerobic and anaerobic conditions, 2020. *Applied Clay Science*, v.189, p.105520

Under review:

Katsenovich Y.P., Trimino Gort,R., Gudavalli, R., Szecsody, J., Freedman, V., and Nikolla P. Qafoku, Silicon concentration and pH controls over competitive or simultaneous incorporation of iodate and chromate into calcium carbonate phases (under review in *Applied Geochemistry*)

Garcia, A., Katsenovich, Y., Lee, B., Roguer Placencia-Gomez, E., Thomle, J., and D. Whitman. Geophysical indicators on uranium release from autunite mineral in biotic sediment systems (Under review in *Geophysical Journal International*).

Gonzalez-Raymat, H., Gudavalli, R., Denham, M., Cai, Y, and Y. Katsenovich. *In situ* sequestration of uranium from contaminated groundwater using a low-cost unrefined humic substance (In preparation).

Oral Presentations (presenter is underlined)

Iodine Co-Precipitation with Calcium Carbonate in the Presence of Silica Ions. Katsenovich, Y., Trimino Gort, R. (DOE Fellow), Lugo, X., (DOE Fellow), Gudavalli R., Qafoku, N.P., Freedman, V., and L. Lagos. WM2020 Conference Proceedings, March 8-12, 2020, Phoenix AZ.

Di Pietro, S., Emerson, HP, Qafoku,N, and JE Szecsody, *Effects of Variable Redox Conditions and Alkaline Treatment in Phyllosilicate Minerals.* Presented at 57th Clay Mineral Society Conference held virtually in Richland, WA, October 18-23, 2020.

Katsenovich, Y., Trimino Gort, R., Gudavalli, R., Qafoku, N. P., Szecsody, J., and V.Freedman, *Iodine Co-Precipitation with Calcium Carbonate in the Presence of Silica Ions.* Presented at 57th Clay Mineral Society Conference held virtually in Richland, WA, October 18-23, 2020.

Sockwell, AK, F Zengotita, A Vento, D Reed, J Swanson, J Dickson, Y Katsenovich, and H Emerson: Mobility of Actinides (+3, +4, and +6) in the Presence of Dolomite - Effect of EDTA and Ionic Strength. Presented at 57th Clay Mineral Society Conference held virtually in Richland, WA, October 18-23, 2020.

S. Kandel, Y. Katsenovich, D. Boglaienko, H.P. Emerson, T. Levitskaia. Effect of Tc-99 on Zero Valent Iron Performance at Neutral pH, WM2020 Conference, March 8-12, 2020, Phoenix, Arizona, USA

Kandel, S., Katsenovich Y., Asmussen R. M., Sockwell, A. K. and R. Gudavalli. *Effect of grout impacted groundwater on the ORLEC28 glass dissolution behavior at various temperature* Abstract submitted to the WM2021 Conference Proceedings, March 7- 11, 2021.

Poster Presentations (presenter is underlined)

Gudavalli, R., Emerson, H., Garcia, S., Gonzalez Raymat, H., Katsenovich, Y., and L. Lagos. *Impact of UV-light and pH on the Fate of Tc, I, and U in Wetlands at Savannah River Site*, WM2020 Conference, March 8-12, 2020, Phoenix, Arizona, USA

A. Kirstin Sockwell, Frances Zengotita, Alexis Vento, Juliet S. Swanson, Donald T. Reed, Yelena Katsenovich, Hilary P. Emerson. *The impact of ethylenediaminetetraacetic acid (EDTA) on the sorption of Nd(III), Th(IV), and U(VI) onto dolomite in WIPP-relevant brines, GWB and ERDA-6*, WM2020 Conference, March 8-12, 2020, Phoenix, Arizona, USA

Rocio Trimino Gort, Yelena Katsenovich, *Iodine co-precipitation with calcium carbonate in the presence of silica ions*, WM 2020 Symposia, March 8-12, Phoenix, AZ 2020. [Student poster].

Silvina Di Pietro, Hilary P. Emerson, Yelena Katsenovich, *Uranium partitioning upon ammonia gas treatment on phyllosilicate minerals*, WM 2020 Symposia, March 8-12, Phoenix, AZ 2020. [Student poster].

Alexis Vento, Hilary P. Emerson, A. Kirstin Sockwell, and Frances Zengotita, *Culebra dolomite dissolution of relevance to the Waste Isolation Pilot Plant*, Waste Management Symposia 2020, Phoenix, AZ, Mar. 8-12, 2020. [Student poster].

Ravi Gudavalli, Katherine Delarosa, Hansell Gonzalez Raymat, Brian Looney, Yelena Katsenovich, Leonel Lagos, *Study of an Unrefined Humate Solution as a Possible Attenuation-based Remedy for Uranium Contamination in Acidic Groundwater*, WM2020 Conference Proceedings, March 8-12, 2020, Phoenix, AZ.

Silvina Di Pietro, Claudia Joseph, Mavrik Zavarin, *Neptunium (IV) Diffusion through Bentonite Clay DOE Fellows Poster Competition - Applied Research Center, Florida International University - Miami, FL, November 7th, 2019*.

Katsenovich, Y.P., Trimino Gort, R., Gudavalli, R., Qafoku, N.P., Szecsody, J., Freedman, V. and L. Lagos, *Incorporation of Iodate and Chromate in Calcium Carbonate Phases at Variable pH and Si Concentrations*. Abstract submitted to the WM2021 Conference Proceedings, March 7- 11, 2021 Virtual.

Doughman, M., Katsenovich Y., *Evaluation of Competing Attenuation Processes for Mobile Contaminants in Hanford Sediments*. Abstract submitted to the WM2021 Conference, March 7- 11, 2021 Virtual. [Student poster].

Gudavalli, R., De La Rosa, K., Pham, P., Gonzalez, H., Looney, B., Katsenovich, Y., and L.Lagos. *Low Cost Humate as an Amendment for Uranium Remediation*. Abstract submitted to the WM2021 Conference Proceedings, March 7- 11, 2021 Virtual.

Di Pietro, S., Emerson H. P., and Y.Katsenovich. *Solid phase characterization of physicochemical mineral phase alterations upon NH₃ gas treatment*. Abstract submitted to the WM2021 Conference, March 7- 11, 2021 Virtual. [Student poster].

Dickson, J., Vento, A., Katsenovich, Y., and K. Sackwell, Swanson, J., and D.Reed. *Organic Ligand Control on Mineral Stability in High Ionic Strength Matrices: Implication for Actinide Mobility in WIPP-relevant Environment*. Abstract submitted to the WM2021 Conference Proceedings, March 7- 11, 2021.

Tuya, N., and R. Gudavalli. *Influence of Environmental Factors on Iodine Attenuation and Release in Savannah River Site Wetlands Sediments*. Abstract submitted to the WM2021 Conference, March 7- 11, 2021 Virtual. [Student poster].

De La Rosa, K., Gudavalli, R., Pham, P., and Y. Katsenovich. *Effect of Modified-HA on the Sequestration of Uranium in Acidic Groundwater at the Savannah River Site*. Abstract submitted to the WM2021 Conference, March 7- 11, 2021 Virtual. [Student poster].

Pham, P., Gonzalez, H., and R. Gudavalli. *Characterization of KW-15 Modified Humic Acid - A Potential In-Situ Technology for Uranium Remediation at the SRS*. Abstract submitted to the WM2021 Conference, March 7- 11, 2021 Virtual. [Student poster].

Vento, A., Katsenovich, Y., Stockwell, K. and H. Emerson. *The Impact of Ethylenediaminetetraacetic acid on Actinides Adsorption onto Dolomite Mineral in WIPP-relevant Environment*. Abstract submitted to the WM2021 Conference, March 7- 11, 2021 Virtual. [Student poster].

Gutierrez, G., Zhou, Y. and A. Lawrence. *Evaluation of Vegetation Removal Methods for UAV-Based Photogrammetry within the WIPP Land Withdrawal Act Boundary, NM*. Abstract submitted to the WM2021 Conference, March 7- 11, 2021 Virtual. [Student poster].

Morales, J., Bramer, L., Lagos, L., and K. Waters. *Investigation of Heavy Metal Biomarkers for the Assessment of Remediated Surface Waters*. Abstract submitted to the WM2021 Conference, March 7- 11, 2021 Virtual. [Student poster].

Stevens, C., Alam, M., Zhou, Y., Lawrence, A., Looney, B. and J. Seaman. *Examining the Variation in the Sediment Transport process under different Erosion and Precipitation Criteria*. Abstract submitted to the WM2021 Conference, March 7- 11, 2021 Virtual. [Student poster].

Student Awards

2020 WM Symposia - Roy G. Post Foundation Scholarship recipients (Gisselle Gutierrez, Amanda Yancoski and Frances Zengotita).

Fall 2019 - FIU World's Ahead Graduate (Frances Zengotita).

APPENDIX

The following documents are available at the DOE Research website for the Cooperative Agreement between the U.S. Department of Energy Office of Environmental Management and the Applied Research Center at Florida International University: <https://doeresearch.fiu.edu>

FIU Year 10 Annual Research Review Presentations:

1. FIU Research Review - Project 1
2. FIU Research Review - Project 2
3. FIU Research Review - Project 3 - DnD
4. FIU Research Review - Project 3 - IT
5. FIU Research Review - Project 4 - 5
6. FIU Research Review - Project 4 - DOE Fellow Derek Gabaldon
7. FIU Research Review - Project 4 - DOE Fellow Gisselle Gutierrez-Zuniga
8. FIU Research Review - Project 4 - DOE Fellow Aurelien Meray
9. FIU Research Review - Project 4 - DOE Fellow Jeff Navidad
10. FIU Research Review - Project 4 - DOE Fellow Silvina De Pietro
11. FIU Research Review - Project 5 - DOE Fellow Olivia Bustillo
12. FIU Research Review - Project 5 - DOE Fellow Eduardo Rojas
13. FIU Research Review - Wrap Up - Project 1
14. FIU Research Review - Wrap Up - Project 2
15. FIU Research Review - Wrap Up - Project 3 - DnD
16. FIU Research Review - Wrap Up - Project 3 - IT
17. FIU Research Review - Wrap Up - Project 4 - 5

In addition, the following documents have been uploaded to OSTI.gov:

Date Submitted to OSTI (mm/dd/yyyy)	OSTI ID	*STI PRODUCT TITLE:	Publication/ Issue Date
09/09/2020	1658912	PROJECT TECHNICAL PLAN - Project 1: Chemical Process Alternatives for Radioactive Waste	12/13/2019
09/09/2020	1658920	Literature Review of Adhesion Mechanisms For Mobile Platforms	4/10/2020
09/15/2020	1660375	Summary of Testing for the Miniature Rover with Integrated UT Sensor	7/24/2020
09/15/2020	1660379	Initial Testing for the H-Canyon Study	8/14/2020
09/15/2020	1660434	FIU PROJECT 1: Chemical Process Alternatives for Radioactive Waste	8/25/2020
09/15/2020	1660389	PROJECT TECHNICAL PLAN - Project 2: Environmental Remediation Science & Technology	12/13/2019

09/15/2020	1660396	FIU PROJECT 2: Environmental Remediation Science & Technology	8/25/2020
09/16/2020	1660534	PROJECT TECHNICAL PLAN - Project 3: Waste and D&D Engineering and Technology Development	12/13/2019
09/16/2020	1660535	EXPERIMENTAL DESIGN: Quantifying / Certifying the Effects of Radiological Fixating Materials & Technologies ISO Source Term Calculations and Open Air Demolition	1/31/2020
09/16/2020	1660536	FIU PROJECT 3: Waste and D&D Engineering and Technology Development	8/25/2020
09/16/2020	1660539	PROJECT TECHNICAL PLAN - Project 4: DOE-FIU Science and Technology Workforce Development Program	12/13/2019
09/16/2020	1660538	Subtle Process Anomalies Detection using Machine Learning Methods	12/20/2019
09/16/2020	1660543	Neptunium (IV) Diffusion through Bentonite Clay	12/20/2019
09/16/2020	1660544	Amplicon Sequencing Assessment to Measure Microbial Community Response from Heavy Metal Contaminated Soils in Savannah River Site, Tims Branch Watershed	12/20/2019
09/16/2020	1660714	An Assessment of Long-Term Monitoring Strategies and Developing Technologies	12/20/2019
09/16/2020	1660717	Mechanical Properties Permanent Foaming Fixatives for D&D Activities	12/20/2019
09/16/2020	1660721	Contributing to the DOE EM 4.1 and 4.12, Office of Groundwater and Subsurface Closure	12/20/2019
09/17/2020	1660918	Double Shelled Tank Visual Inspections	12/20/2019
09/17/2020	1660919	H-6bR Water density Stratification Investigation	12/20/2019
09/17/2020	1660921	2D Dam-Break Analysis of L Lake and PAR Pond Dams Using HEC-RAS	12/20/2019
09/17/2020	1660922	Plutonium Migration from Estuary Sediments (Ravenglass, UK)	12/20/2019
09/17/2020	1660923	FIU PROJECTS 4 & 5: DOE-FIU Science and Technology Workforce Development Program	8/25/2020
09/17/2020	1660925	PROJECT TECHNICAL PLAN - Project 5: DOE-FIU Science and Technology Workforce Development Initiative for Office of Legacy Management (NEW)	12/13/2019

09/17/2020	1660926	DOE-FIU Science and Technology Workforce Development Initiative for Office of Legacy Management	4/30/2020
09/18/2020	1661159	Biotic dissolution of autunite under anaerobic conditions: effect of bicarbonates and <i>Shewanella oneidensis</i> MR1 microbial activity.	Environmental Geochemistry and Health/12/19/2019. https://doi.org/10.1007/s10653-019-00480-7